

REVOLUTION IN AUTONOMOUS ORBITAL NAVIGATION (RAON)

by

Rachit Bhatia

A dissertation submitted in partial fulfillment
of the requirements for the degree

of

DOCTOR OF PHILOSOPHY

in

Aerospace Engineering

Approved:

David K. Geller, Ph.D.
Major Professor

Stephen A. Whitmore, Ph.D.
Committee Member

Charles M. Swenson, Ph.D.
Committee Member

Douglas Hunsaker, Ph.D.
Committee Member

Geordie Richards, Ph.D.
Committee Member

Richard S. Inouye, Ph.D.
Vice Provost for Graduate Studies

UTAH STATE UNIVERSITY
Logan, Utah

2019

Copyright © Rachit Bhatia 2019

All Rights Reserved

ABSTRACT

Revolution in Autonomous Orbital Navigation (RAON)

by

Rachit Bhatia

Utah State University, 2019

Major Professor: David K. Geller, Ph.D.
Department: Mechanical and Aerospace Engineering

The future of deep space exploration depends upon technological advancement towards improving spacecraft's autonomy and versatility. This study aims to examine the feasibility of autonomous orbit determination using advanced accelerometer measurements. The objective of this research is to ascertain specific sensor requirements to meet pre-defined mission navigation error budgets. Traditional inertial navigation (dead reckoning and external aiding) is not considered. Instead, measurements from pairs of advanced, highly sensitive accelerometers (e.g. cold atom accelerometers) are used on-board, to determine gravity field gradients which are then correlated to onboard gravity maps and used to determine orbital information. Linear Covariance Theory helps to efficiently conduct an error budget analysis of the system. This error budget analysis helps to determine the effect of specific error sources in the sensor measurements, thereby providing information to rank and compare relevant sensor parameters and determine an optimal sensor configuration for a given space mission. The procedure is repeated to evaluate different accelerometer configurations, and sensor parameters, for a range of space missions.

(219 pages)

PUBLIC ABSTRACT

Revolution in Autonomous Orbital Navigation (RAON)

Rachit Bhatia

Spacecraft navigation is a critical component of any space mission. Space navigation uses on-board sensors and other techniques to determine the spacecraft's current position and velocity, with permissible accuracy. It also provides requisite information to navigate to a desired position, while following the desired trajectory. Developments in technology have resulted in new techniques of space navigation. However, inertial navigation systems have consistently been the bedrock for space navigation.

Recently, the successful space mission GOCE used on-board gravity gradiometer for mapping Earth's gravitational field. This has motivated the development of new techniques like cold atom accelerometers, to create ultra-sensitive gravity gradiometers, specifically suited for space applications, including autonomous orbital navigation.

This research aims to highlight the existing developments in the field of gravity gradiometry and its potential space navigation applications. The study aims to use the Linear Covariance Theory to determine specific sensor requirements to enable autonomous space navigation for different flight regimes.

ACKNOWLEDGMENTS

I believe gaining knowledge is the absolute goal of one's life. I have been fortunate enough to pursue this goal with the utmost support of my teachers, family, and friends. I hope to continue to pursue this goal.

This dissertation is a stepping stone towards this lifelong goal. A number of people have been part of this effort and I am heartily grateful to everyone who have helped me become a better version of myself. Although, it is seldom that words do justice when conveying gratitude of this magnitude, I would like to acknowledge a few of these good people without whom this work would not have been possible.

Foremost, I am immensely indebted to my major advisor, Dr. David K. Geller. I am grateful to him for sharing his immense knowledge with me and for giving me a chance to pursue research under his guidance. His incredible pedagogical skills, extensive experience, and excellent mentorship has always been a source of inspiration. His continuous support towards innovative research ideas was the driving force for selecting this research topic. It has been an honor to be his student and I feel fortunate to have him as my mentor and icon.

Next, I would like to acknowledge the sustained support and love from my grandparents, parents, siblings, and friends during this endeavor. Their best wishes have always provided me with the necessary thrust to achieve success.

I also want to thank my committee members Dr. Stephen A. Whitmore, Dr. Charles M. Swenson, Dr. Douglas Hunsaker, and Dr. Geordie Richards for their substantial guidance and suggestions to bring this work to the present form.

I have been fortunate to have received valuable suggestions and timely advice from Dr. Kieran Carroll, Chief Technology Officer at Gedex Inc. His immense knowledge about gravity gradiometers and his extensive work on this innovative technology has been very conducive in understanding some of the parts of this research. I am immensely grateful to him for sharing his knowledge with me.

Special thanks to all the members of Space Awareness, Guidance, and Navigation (SAGN) Lab and USU GN&C group, especially Dr. Randall Christensen, Dr. Ben Rose. Thanks to all of you, I have always enjoyed our weekly GN&C meetings and our discussion on various research projects.

Heartfelt thanks to my friends and colleagues Dr. Nicholas Ortolano, John Laney, Akhter Mahmud Nafi, Simon Shuster, Arun Bernard, and Sheril Ak. Thank you for your invaluable ideas, helpful suggestions, and most importantly constant friendship.

Sincere thanks to Utah State University (USU) and Cache Valley, for providing a home to me for last four years. As an international student traveling to the United States for the first time, with limited money and little knowledge about the future, I was supported to the maximum. This work would not have been possible without the supportive and caring people at USU, especially my friend Dr. Troy Munro.

I also extend heartfelt acknowledgement to the staff of Mechanical and Aerospace Engineering Department at Utah State University for admitting me as a doctoral student and giving me the opportunity to conduct this research. I am very grateful to Research and Graduate Studies Department (USU) for recognizing me as a Presidential Doctoral Research Fellow (PDRF) for the class of 2015-2019, it has been an honor and privilege to be part of this elite group. I am also thankful to International Space Safety Foundation for recognizing me as a Graduate Student Fellow and partially funding this research project.

In the end, I would like to mention again that this effort would not have been possible without the support of my family members, especially bade pa, badi ma, nanaji, naniji, papa, mummy, and Ani. Thank you very much!!

- Rachit Bhatia

August 2019

CONTENTS

	Page
ABSTRACT	iii
PUBLIC ABSTRACT	iv
ACKNOWLEDGMENTS	v
LIST OF TABLES	xi
LIST OF FIGURES	xv
1 Introduction	1
1.1 Research Objective	3
1.2 Dissertation Overview	3
2 Literature Survey and Related Works	4
2.1 Gravity Gradiometry	4
2.2 Gravity Gradiometer - History, Development and Classification	7
2.3 Applications and Challenges of Gravity Gradiometry	14
2.4 Extended Kalman Filter and Linear Covariance Analysis Techniques	17
2.5 Literature Review Summary	19
3 Dissertation Overview	20
3.1 Chapter Overview	20
3.2 Scope	20
3.3 Objective	21
3.4 Approach	22
3.4.1 Key Problem Parameters and Reference frames	22
3.4.2 Non-Linear Modeling	24
3.4.3 Linear Modeling	28
3.4.4 Observability Analysis	29
3.4.5 Linear Covariance Analysis	29
3.4.6 Performance Metrics	29
3.5 Summary	30
4 Coordinate Frames, Transformations, and Gravity Field Models	31
4.1 Chapter Overview	31
4.2 Coordinate Frames	31
4.2.1 Earth-Centered Inertial Frame (ECI)	31
4.2.2 Local Vertical and Local Horizontal Frame (LVLH)	33
4.2.3 Nominal Reference Frame (NRF)	34
4.3 LAGEOS Spacecraft	35
4.4 Gravity Field Models	36

4.5	Summary	38
5	Problem Parameters and System Modeling	39
5.1	Chapter Overview	39
5.2	State Vector and Reference Frames	39
5.3	Environmental Models	41
5.3.1	Spherical Harmonics Gravity Model	42
5.3.2	Atmospheric Drag Model	42
5.3.3	Solar Radiation Pressure Model	43
5.3.4	Third-body Perturbation model	44
5.3.5	Gravity Gradient Torque	45
5.4	Non-Linear Dynamics Modeling	46
5.4.1	Translational Dynamics	46
5.4.2	Rotational Dynamics	50
5.4.3	Instrument Error Dynamics	51
5.5	Nonlinear Measurement Modeling	54
5.6	Linear Dynamics Modeling	63
5.6.1	Linearized Translational Dynamics	63
5.6.2	Linearized Rotational Dynamics	66
5.6.3	Linearized Instrument Error Dynamics	69
5.7	Linearized Measurement Equation	71
5.8	Summary of Linearized Dynamics & Measurement Model	77
5.9	Summary	81
6	Observability Analysis	82
6.1	Chapter Overview	82
6.2	Theoretical Setup	82
6.3	Mathematical Setup	86
6.4	Results	90
6.5	Summary	94
7	Linear Covariance (LinCov) Analysis Tool Development	95
7.1	Chapter Overview	95
7.2	LinCov Models - Theory & Setup	95
7.2.1	Propagation	96
7.2.2	Update - Accelerometer Measurements	98
7.2.3	Update - Star Camera Measurements	99
7.2.4	Performance Evaluation	101
7.3	Error Budget Analysis	101
7.4	Summary	103
8	LinCov Simulation Testing	104
8.1	Chapter Overview	104
8.2	Reference Trajectory Testing	104
8.2.1	Test Case 1 - Check Orbital Dynamics	106
8.2.2	Test Case 2 - Check Effect of J2 & Rotating Spacecraft	108
8.2.3	Test Case 3 - Check Atmospheric Drag Model	110

8.3	LinCov Propagation Testing	112
8.3.1	Test Case 1 - Check State Dynamics & Propagation Equations	115
8.3.2	Test Case 2 - Find Appropriate Process Noise	116
8.4	LinCov Update Testing	116
8.4.1	Test Case 1 - Verify State Dynamics & Update Equations	117
8.4.2	Test Case 2 - With Process Noise	122
8.4.3	Test Case 3 - With Error Groups	124
8.5	Numerical Instability & Limitations	125
8.5.1	Overview	125
8.5.2	Prospective Solutions	125
8.6	Summary	127
9	LinCov Simulation Results and Analysis	128
9.1	Chapter Overview	128
9.2	Initial Setup	128
9.3	Low Earth Orbit (50 degree Inclination)	132
9.3.1	Reference Trajectory	132
9.3.2	High Sensor Grade & Precise System Model	137
9.3.3	Moderate Sensor Grade & Moderately Precise System Model	154
9.3.4	Low Sensor Grade & Less Precise System Model	158
9.4	Polar Low Earth Orbit (P-LEO)	159
9.4.1	Reference Trajectory	159
9.4.2	High Sensor Grade & Precise System Model	164
9.4.3	Moderate Sensor Grade & Moderately Precise System Model	171
9.4.4	Low Sensor Grade & Less Precise System Model	175
9.5	Summary	176
10	Conclusion	177
10.1	Summary of the Contributions & Results	177
10.2	Proposed Future Work	178
	REFERENCES	180
	APPENDICES	184
A	Matrix Partial Derivatives	185
A.1	Overview	185
A.2	Partial Of Gravitational Acceleration With Respect To Spacecraft Position	185
A.3	Partial Of Acceleration Due To Atmospheric Drag With Respect To Spacecraft Position	185
A.4	Partial Of Acceleration Due To Atmospheric Drag With Respect To Spacecraft Velocity	185
A.5	Partial Of Acceleration Due To Atmospheric Drag With Respect To Spacecraft Ballistic Coefficient	185
A.6	Partial Of Acceleration Due To Atmospheric Drag With Respect To Reference Atmospheric Density	186

A.7	Partial Of Acceleration Due To Atmospheric Drag With Respect To Scale Height	186
A.8	Partial Of Solar Radiation Pressure Perturbation With Respect To Spacecraft Position	186
A.9	Partial Of Third-Body Perturbation With Respect To Spacecraft Position	187
A.10	Partial Of Gravity Gradient Torque With Respect To Spacecraft Position	187
A.11	Partial Of Gravity Gradient Torque With Respect To Spacecraft Rotation Vector	188
A.12	Partial of Accelerometer Measurement With Respect To Spacecraft Rotation Vector	189
A.13	Partial Of Acceleration Measurement With Respect To Spacecraft Angular Velocity	193
A.14	Partial Of Accelerometer Measurement With Respect To Spacecraft's Center Of Mass Position	193
A.15	Partial Of Accelerometer Measurement With Respect To Accelerometer Position	194
B	Semi-Major Axis Time Derivative	196
B.1	Overview	196
B.2	Derivation	196
	CURRICULUM VITAE	198

LIST OF TABLES

Table	Page
2.1 An example of differencing and intrinsic gravity gradiometers. Their sensitivity axes are chosen to be aligned along the X direction. However, a gradiometer can have multiple sensitivity axes and measure all five independent gravity gradient tensor components. Adapted from Veryaskin, Gravity, Magnetic and Electromagnetic Gradiometry (2018) [1].	13
2.2 Gravity Gradiometer Instruments. Adapted from Richeson, Gravity gradiometer aided inertial navigation within non-GNSS environments (2008) [2].	14
4.1 Spacecraft (s/c) Parameters	35
6.1 Orbit and Attitude Observability (O)/Unobservability (U) using three 3-axis accelerometers	91
6.2 Orbit and Attitude Observability (O)/Unobservability (U) using one 3-axis accelerometer	91
6.3 Orbit and Attitude Observability (O)/Unobservability (U) using one 2-axis accelerometer	91
6.4 Orbit and Attitude Observability (O)/Unobservability (U) using one single-axis accelerometer	92
6.5 Orbit-Only Observability (O)/Unobservability (U) using three 3-axis accelerometers	93
6.6 Orbit-Only Observability (O)/Unobservability (U) using one 3-axis accelerometer	93
6.7 Orbit-Only Observability (O)/Unobservability (U) using one 2-axis accelerometer	93
6.8 Orbit Observability (O)/Unobservability (U) using one single-axis accelerometer	94
8.1 LEO Orbital parameters	105
8.2 Spacecraft (s/c) Specifications and Nominal Value of Atmospheric Drag Parameters	105

8.3	Time Constants (T denotes the orbital period)	113
8.4	Initial Conditions - Spacecraft (s/c) position, velocity, attitude, and angular velocity	113
8.5	Accelerometer (AC) Parameters	114
8.6	Star Camera (SC) Parameters	114
8.7	Environmental Uncertainties	114
9.1	Spacecraft (s/c) Specifications and Nominal Value of Atmospheric Drag Parameters	129
9.2	Initial Conditions - Spacecraft (s/c) Position, Velocity, Attitude, and Angular Velocity	129
9.3	Time Constants (T denotes the orbital period)	130
9.4	Accelerometer (AC) Parameters	130
9.5	Star Camera (SC) Parameters	130
9.6	Environmental Uncertainties	131
9.7	LEO (50 degree Inclination) Orbital Parameters	132
9.8	Error budget of the maximum steady-state true navigation error 1σ standard deviation	139
9.9	Error budget of the maximum steady-state true navigation error 1σ standard deviation	142
9.10	Error budget of the maximum steady-state true navigation error 1σ standard deviation	143
9.11	Error budget of the maximum steady-state true navigation error 1σ standard deviation	144
9.12	Error budget of the maximum steady-state true navigation error 1σ standard deviation	145
9.13	Error budget of the maximum steady-state true navigation error 1σ standard deviation	145
9.14	Error budget of the maximum steady-state true navigation error 1σ standard deviation	146

9.15 Error budget of the maximum steady-state true navigation error 1σ standard deviation	146
9.16 Error budget of the maximum steady-state true navigation error 1σ standard deviation	147
9.17 Error budget of the maximum steady-state true navigation error 1σ standard deviation	147
9.18 Error budget of the maximum steady-state true navigation error 1σ standard deviation	148
9.19 Error budget of the maximum steady-state true navigation error 1σ standard deviation	148
9.20 Error budget of the maximum steady-state true navigation error 1σ standard deviation	149
9.21 Error budget of the maximum steady-state true navigation error 1σ standard deviation	150
9.22 Error budget of the maximum steady-state true navigation error 1σ standard deviation	150
9.23 Error budget of the maximum steady-state true navigation error 1σ standard deviation	151
9.24 Error budget of the maximum steady-state true navigation error 1σ standard deviation	152
9.25 Error budget of the maximum steady-state true navigation error 1σ standard deviation	152
9.26 Error budget of the maximum steady-state true navigation error 1σ standard deviation	153
9.27 Error budget of the maximum steady-state true navigation error 1σ standard deviation	153
9.28 Error budget of the maximum steady-state true navigation error 1σ standard deviation	156
9.29 Error budget of the maximum steady-state true navigation error 1σ standard deviation	158
9.30 Polar LEO Orbital Parameters	159

9.31 Error budget of the maximum steady-state true navigation error 1σ standard deviation	166
9.32 Error budget of the maximum steady-state true navigation error 1σ standard deviation	169
9.33 Error budget of the maximum steady-state true navigation error 1σ standard deviation	170
9.34 Error budget of the maximum steady-state true navigation error 1σ standard deviation	170
9.35 Error budget of the maximum steady-state true navigation error 1σ standard deviation	173
9.36 Error budget of the maximum steady-state true navigation error 1σ standard deviation	175

LIST OF FIGURES

Figure	Page
1.1 Autonomous Space Navigation using Advanced Accelerometer Measurements	2
2.1 Block Diagram of the GGT Inversion Positioning System (Image taken from Chen et al. - “Gravity gradient tensor eigendecomposition for spacecraft positioning” (2015)) [3].	7
2.2 The RMGG developed at the Hughes Aircraft Research Laboratory. (a) Two orthogonal dumbbells are set to rotate uniformly around a mutual pivot representing a torsional spring. (b) A real RMGG prototype (Image taken from Veryaskin, Gravity, Magnetic and Electromagnetic Gradiometry (2018)) [1].	9
2.3 Classification of Differencing Gradiometers based on the measurement sensor type, operating principle, and operating temperature. Adapted from Veryaskin, Gravity, Magnetic and Electromagnetic Gradiometry (2018) [1].	12
2.4 Classification of Intrinsic Gradiometers based on the measurement sensor type, operating principle, and operating temperature. Adapted from Veryaskin, Gravity, Magnetic and Electromagnetic Gradiometry (2018). [1]	13
2.5 Comparison of gravity gradiometry applications, based on a sensitivity scale (Image taken from Evstifeev, The state of the art in the development of onboard gravity gradiometers (2017)) [4].	15
2.6 Kalman Filter Flow Diagram	18
2.7 Generic Closed-Loop GN&C Simulation (Image taken from Christensen and Geller, Linear covariance techniques for closed-loop guidance navigation and control system design and analysis (2014)) [5].	18
3.1 Gravity Gradiometer Instrument - Schematic Diagram (only 2 of the 6 accelerometer are shown). Adapted from Cesare, Performance Requirements and budgets for gradiometric mission (2002). [6]	28
4.1 Earth-Centered Inertial Frame (ECI) [7]	33
4.2 Local Vertical and Local Horizontal frame (LVLH) and ECI frame	34
5.1 Accelerometer Nominal Reference Frame (ANRF) and Accelerometer Actual Reference Frame (AARF) frame	41

5.2	Position vectors for n-body system [8].	45
5.3	Spacecraft's center of mass position vector relative to inertial reference frame (IRF) and spacecraft body-fixed reference frame (SBRF)	54
5.4	Schematic Model (only 2 of the 6 accelerometer are shown)[6].	61
6.1	Gravity field near a position \mathbf{r} (left); gravity-gradient tensor at a position \mathbf{r} (right)	83
6.2	Position of the center-of-mass of a spacecraft with respect to an inertial frame, and position of the i th accelerometer with respect to the center-of-mass	84
6.3	Field of gravity-gradient tensors, and satellite measurement of the gravity gradient tensor in the body frame	85
6.4	Different satellite orientations with the same measurement of the gravity-gradient tensor in the body frame	86
8.1	Accelerometer Configuration	106
8.2	Test case 1 - Spacecraft Position in ECI frame	107
8.3	Test case 1 - Accelerometer measurements (in Spacecraft body-fixed reference frame) for accelerometer 1, 2, & 3	107
8.4	Test case 2 - LEO orbital elements	108
8.5	Test case 2 - Euler angles denoting attitude of the spacecraft body-fixed reference frame with respect to the ECI frame	109
8.6	Test case 2 - Accelerometer measurements (in Spacecraft body-fixed reference frame) for accelerometer 1, 2, & 3	109
8.7	Test case 3 - Change in semi-major axis for the given LEO orbit	110
8.8	Test case 3 - Euler angles denoting attitude of the spacecraft body-fixed reference frame with respect to the ECI frame	111
8.9	Test case 3 - Accelerometer measurements (in Spacecraft body-fixed reference frame) for accelerometer 1, 2, & 3	112
8.10	Test case 1 - Spacecraft's center of mass position (with respect to the origin of the spacecraft body-fixed frame and expressed in spacecraft body-fixed frame) filter navigation error - (a) For 2 orbits, (b) Zoomed view for first 350 seconds	119

8.11	Test case 1 - Accelerometer 1 position (with respect to the origin of the spacecraft body-fixed frame and expressed in spacecraft body-fixed frame) filter navigation error - (a) For 2 orbits, (b) Zoomed view for first 350 seconds	120
8.12	Test case 1 - Accelerometer bias, misalignment, and scale factor (expressed in accelerometer actual reference frame) filter navigation error - (a) For Accelerometer 1, (b) For Accelerometer 2	121
8.13	Test case 1 - Spacecraft position (expressed in LVLH frame) filter navigation error	122
8.14	Test case 1 - Spacecraft attitude (expressed in ECI frame) filter navigation error	123
8.15	Test case 1 - Filter navigation error on ballistic coefficient, reference atmospheric density, and scale height	124
8.16	UDU Covariance Propagation and Update Flow Diagram. Based on the algorithm given in Maybeck (1979), Stochastic Models, Estimation, and Control [9]	126
9.1	Accelerometer Configuration	131
9.2	Reference Trajectory (Non-rotating spacecraft) - LEO (50 degree Inclination) orbital elements	133
9.3	Reference Trajectory (Non-rotating spacecraft) - Spacecraft Position in ECI frame	134
9.4	Reference Trajectory (Non-rotating spacecraft) - Euler angles denoting attitude of the spacecraft body-fixed frame with respect to the ECI frame	134
9.5	Reference Trajectory (Non-rotating spacecraft) - Accelerometer measurements (in Spacecraft body-fixed frame) for accelerometer 1, 2, & 3	135
9.6	Reference Trajectory (Rotating spacecraft) - Euler angles denoting attitude of the spacecraft body-fixed frame with respect to the ECI frame	136
9.7	Reference Trajectory (Rotating spacecraft) - Accelerometer measurements (in Spacecraft body-fixed frame) for accelerometer 1, 2, & 3	136
9.8	True navigation error 1σ standard deviation on spacecraft position components (expressed in LVLH frame) and magnitude	137
9.9	True navigation error 1σ standard deviation on spacecraft attitude magnitude	138
9.10	True navigation error 1σ standard deviation on spacecraft position components (expressed in LVLH frame) and magnitude	140

9.11 True navigation error 1σ standard deviation on spacecraft attitude magnitude	141
9.12 True navigation error 1σ standard deviation on spacecraft position magnitude	154
9.13 True navigation error 1σ standard deviation on spacecraft attitude magnitude	155
9.14 True navigation error 1σ standard deviation on spacecraft position magnitude	156
9.15 True navigation error 1σ standard deviation on spacecraft attitude magnitude	157
9.16 Reference Trajectory (Non-rotating spacecraft) - Polar LEO orbital elements	160
9.17 Reference Trajectory (Non-rotating spacecraft) - Spacecraft Position in ECI frame	160
9.18 Reference Trajectory (Non-rotating spacecraft) - Euler angles denoting attitude of the spacecraft body-fixed frame with respect to the ECI frame	161
9.19 Reference Trajectory (Non-rotating spacecraft) - Accelerometer measurements (in Spacecraft body-fixed frame) for accelerometer 1, 2, & 3	162
9.20 Reference Trajectory (Rotating spacecraft) - Euler angles denoting attitude of the spacecraft body-fixed frame with respect to the ECI frame	163
9.21 Reference Trajectory (Rotating spacecraft) - Accelerometer measurements (in Spacecraft body-fixed frame) for accelerometer 1, 2, & 3	163
9.22 True navigation error 1σ standard deviation on spacecraft position components (expressed in LVLH frame) and magnitude	164
9.23 True navigation error 1σ standard deviation on spacecraft attitude magnitude	165
9.24 True navigation error 1σ standard deviation on spacecraft position components (expressed in LVLH frame) and magnitude	167
9.25 True navigation error 1σ standard deviation on spacecraft attitude magnitude	168
9.26 True navigation error 1σ standard deviation on spacecraft position magnitude	172
9.27 True navigation error 1σ standard deviation on spacecraft attitude magnitude	172
9.28 True navigation error 1σ standard deviation on spacecraft position magnitude	174
9.29 True navigation error 1σ standard deviation on spacecraft attitude magnitude	174

CHAPTER 1

Introduction

Revolution in Autonomous Orbital Navigation (RAON) is a study to investigate the feasibility and requirements for an autonomous navigation that can potentially apply to all flight regimes. For any space mission, navigation relies primarily on external aids such as the Global Positioning Systems (GPS), the Tracking and Data Relay Satellite (TDRSS), or the Deep Space Network (DSN). These traditional space navigation techniques limit the range of space exploration capability, and require specialized communication and ground-based navigation systems to achieve acceptable levels of spaceflight safety. These additional systems not only require precious onboard resources, but are also subject to failures that can result in the Loss of Crew or Loss of Vehicle condition. For next generation space navigation, there is a need to relieve the traditional navigation techniques by implementing autonomous navigation system onboard and thus reduce the risk level of Loss of Crew or Loss of Vehicle condition.

This research aims to explore the viability of using pairs of advanced accelerometers and onboard gravity field maps to autonomously determine orbital position and velocity for Low Earth Orbit (LEO) regime. This study will evaluate the role of advanced accelerometers, used in recent gravity-mapping missions like GRACE-2 (Gravity Recovery and Climate Experiment) and GOCE (Gravity Field and Steady-State Ocean Circulation Explorer), in developing and executing autonomous orbital navigation for different mission requirements.

Gravity gradiometry has been in use since mid 20th century and has applications in wide ranging fields like mineral exploration, field survey, submarine navigation, and gravitational mapping [2, 6, 10]. The technology has been used for many airborne and terrestrial surveys, predominantly to image subsurface geology to aid hydrocarbon and mineral exploration [2]. Over 2.5-million-line km has been surveyed using the technique [10]. During the Cold War, US Navy submarines used gravity gradiometry for covert navigation [2].

In recent years, the technology has matured and requisite instruments have evolved and been upgraded. Because of this, there is renewed interest in space applications for this technique. Recently, engineers and scientists have used various measurement principles based on electrostatics, superconductivity, and cold atom interferometry, to considerably advance the measurement sensitivity and precision of accelerometers [2].

Future autonomous orbital navigation architectures need to be suitable and reliable for varying space environments. The navigation approach addressed in this study has the potential to satisfy these requirements. Considering the universal nature of gravity, this approach provides a generic solution for autonomous navigation in almost all types of space environment. Thus, giving the RAON concept an edge over other potential autonomous orbital navigation techniques.

The idea of autonomous space navigation (see Figure 1.1), as presented in this study, is to reverse the problem of precision gravitational mapping (as achieved during European Space Agency’s GOCE mission) and have this high fidelity gravity map on-board along with a pair of ultra-precise accelerometers. The accelerometer measurements can be correlated to the on-board gravity map to navigate autonomously in the LEO regime.

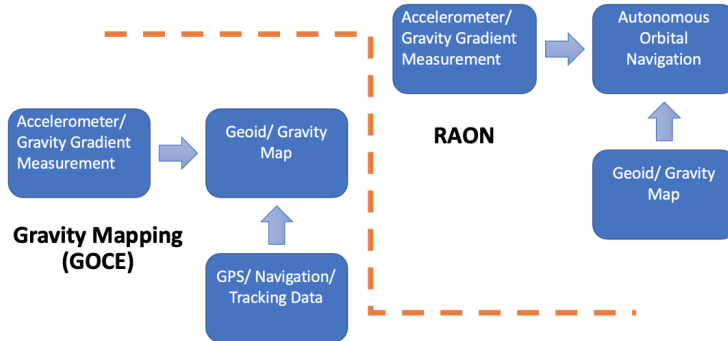


Fig. 1.1: Autonomous Space Navigation using Advanced Accelerometer Measurements

1.1 Research Objective

The objective of this research is to use the Linear Covariance theory to investigate the feasibility and sensor requirements for an autonomous orbit determination using advanced accelerometer measurements and onboard gravity field maps, for different sensor and orbit configurations.

1.2 Dissertation Overview

Chapter 2 covers associated literature and previous work, relevant to the topic of research. Chapter 3 covers the scope, objectives, and approach for the research. Chapters 4 and 5 review the problem setup, important parameters and system modeling. Observability analysis theory and results are discussed in Chapter 6, and Linear Covariance analysis tool theory, testing, and results are covered in Chapters 7 to 9. Lastly, Chapter 10 offers the conclusion of this study, and highlights important contributions.

CHAPTER 2

Literature Survey and Related Works

This chapter provides an overview of the literature related to the gravity gradiometry, its history, and the development of the existing gravity gradiometer instruments. A literature review of the gravity gradiometry applications has been examined, primarily in the light of its potential application for autonomous orbital navigation. At the end of this chapter, a brief account of the Extended Kalman Filter (EKF) theory and the Linear Covariance theory is discussed. Throughout this chapter, effort has been made to provide insight about the previous work in the field of gravity gradiometry and its application in autonomous orbital navigation. In the summary section, a concise review of this literature survey has been presented, so as to help the reader gauge the application of this theory, in regard to the objective of this dissertation.

The purpose of this chapter is to help the reader assess the existing developments in the field of gravity gradiometry, and thereby, understand the importance of the research and its prospective influence on the future of gravity gradiometry.

2.1 Gravity Gradiometry

The study and measurement of the changes in the gravitational acceleration, with respect to the change in spatial position, is termed *gravity gradiometry*. The measurement of gravity gradiometry is a gravity gradient tensor, measured over the given spatial distance.

Hungarian physicist Baron Loránd (Roland) von Eötvös is credited for inventing the first gravity gradiometer instrument, in the late 1880s [1, 11]. While working on series of experiments on the proportionality of inertial and gravitational masses, Eötvös' specialized torsion balance was used to measure gravitational gradient [11]. To recognize his ingenious invention, the unit of the gravitational gradient has been named after him [11]. One Eötvös (Eö) is equal to $10^{-9}s^{-2}$ [12]. The gravity gradient tensor (GGT) is the 3x3 matrix, con-

sisting of 9 components of the derivative of the gravitational vector with respect to position vector.

$$\nabla g = \begin{bmatrix} \nabla g_{XX} & \nabla g_{XY} & \nabla g_{XZ} \\ \nabla g_{YX} & \nabla g_{YY} & \nabla g_{YZ} \\ \nabla g_{ZX} & \nabla g_{ZY} & \nabla g_{ZZ} \end{bmatrix} \quad (2.1)$$

$$\nabla g_{ij} = \frac{\partial^2 U}{\partial \mathbf{r}_i \partial \mathbf{r}_j}, \quad i, j = X, Y, Z \quad (2.2)$$

where U is the gravitational potential at the given position vector \mathbf{r} . The conservative nature and the continuity of the gravitation field ensures that the gravity gradient matrix is symmetric ($\nabla g_{ij} = \nabla g_{ji}$), and by Laplace's equation it has zero trace ($\sum_i \nabla g_{ii} = 0$) [3, 13, 14]. Thus, only five out of nine components are independent [6].

Gravity gradient measurement is a significant tool as it emphasizes the short-wavelength characteristics of the field, and enhances fine structures, such as geological edges and faults [15]. The components of the gravity gradient matrix contain encoded information about the curvature of the potential [15]. This information about the curvature of the potential can be used to model the subsurface features, estimate the position and velocity of the measuring instrument, and determine the directions of the principal axes of source bodies, respectively. [15].

A number of studies have analytically and mathematically decoded the geophysical, gravitational and spatial information ciphered in the gravity gradient measurements. A publication by Christopher Jekeli on Gravity Gradiometry, in 2011, beautifully highlights the rich mathematical foundations of the gravity gradiometry [15]. He presents the basic mathematical equations leading up to the derivation of gravity gradient tensor, and the formulas to compute the minimum and maximum curvature of an equipotential surface, using gravity gradient measurements.

In his paper, Jekeli presents an interesting account of the measurement error analysis of the gravity gradient measurement, specifically the analysis of the required gyroscope and gradiometer noise levels adequate enough to separate the gravity gradient from non-

gravitational components. Further, Jekeli briefly discuss the minimum number of accelerometer measurements required to make the “full tensor gradiometer”, and their corresponding configuration. This is interesting as one of the objectives of this research includes the study of optimal accelerometer configurations for an on-board gravity gradiometer.

A more recent effort to extract the positional information of a spacecraft from the gravity gradient matrix includes a paper titled “Gravity Gradient Eigen-Decomposition for Spacecraft Positioning” (2015), by Pei Chen, Sun, and Han. In this paper, they comprehensively describe the method to isolate the attitudinal, latitudinal and longitudinal information from the gravity gradient matrix, assuming that the true gravity field is known [3].

Chen and others present an Eigen-Decomposition algorithm for spacecraft positioning using gravity gradient measurements (Figure 2.1) [3]. This provides a powerful technique, when attitudinal states of the spacecraft are known within permissible limits, and a high resolution gravity field model of the primary body is available onboard. Interestingly, this technique does not require any prediction or initial guess. Hence, it is believed that this technique can be significant for dead reckoning and help provide initial guesses for Kalman Filters. To formulate this Eigen-Decomposition algorithm, Chen and others use J2 spherical harmonics gravity model only. It is believed that this theory can be extended to higher spherical harmonics models, or different gravity models, as well.

Other attempts made to analytically extract useful information from gravity gradient matrix include the study titled “Measuring Attitude with Gradiometer” (1994) by David Sonnabend, and Thomas G. Gardner (University of Colorado), and the article titled “The gradient tensor of potential field anomalies: Some implications on data collection and data processing of maps” (1990) by Pedersen and Rasmussen [16, 17].

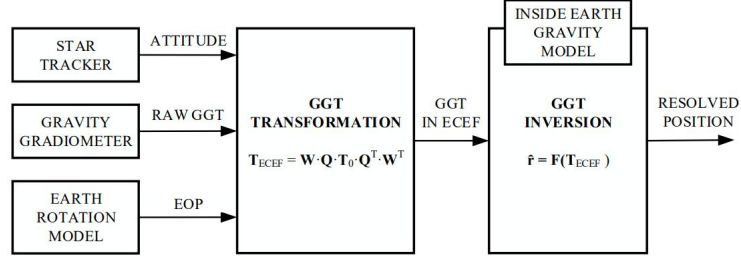


Fig. 2.1: Block Diagram of the GGT Inversion Positioning System (Image taken from Chen et al. - “Gravity gradient tensor eigendecomposition for spacecraft positioning” (2015)) [3].

Detailed mathematical analysis of gravity gradient is also found in “Geophysical Exploration” (1963) by Carl August Heiland, and “Physical Geodesy” (2005) by Bernhard Hofmann-Wellenhof and Helmut Moritz. The abundant and useful knowledge, conveyed by the gravity gradient measurements, has rendered gravity gradiometry as a favorite tool for the geologists, and archeologists. Unsurprisingly, scientists (specifically physicists) and engineers have been equally interested in the developments of gravity gradiometry. A brief history of the development of the gravity gradiometer instruments, and their classification is presented in the next section, followed by the real-world applications of the gravity gradiometry.

2.2 Gravity Gradiometer - History, Development and Classification

A number of publications have extensively highlighted the technical history and mathematical details on the setup and the operating principles of different gravity gradiometers. Some of the prominent studies are cited in this document. These include W.C. Wells’ article on “Spaceborne gravity gradiometers” (1984), Christopher Jekeli’s paper on “A review of gravity gradiometer survey system data analyses” (1993), Richeson’s thesis on “Gravity gradiometer aided inertial navigation within non-GNSS Environments” (2008), a paper on “Gravity gradiometer systems—advances and challenges” by Daniel DiFrancesco et al., (2008), a paper by DiFrancesco on “Gravity gradiometry - today and tomorrow” (2009), an

article by Jekeli on “Gravity Gradiometry” (2011), and a very recent book titled “Gravity, Magnetic and Electromagnetic Gradiometry - Strategic technologies in the 21st century” (Feb 2018) by Alexey V Veryaskin [1, 2, 10, 15, 18, 19, 20].

In this subsection, technical details and operating principles of prominent gravity gradiometers is provided and an attempt has been made to classify the gradiometers, based on operating principle and other characteristics, respectively.

Experiments with gravity sensors have been performed since late 1700s [19]. Henry Cavendish, in 1798, determined the universal gravitational constant (G) using a torsion balance [19]. In the quest to test the equivalence principle, Eötvös continued to improve the sensitivity of the torsion balance by careful manufacturing increasingly sensitive instruments [11].

Around 1888, Eötvös improved his instrument to precisely measure the universal gravitational constant, and soon realized the potential of this simple device to measure gravity gradients with a sensitivity of $10^{-9} s^{-2}$ or 1Eö [11]. The gravity gradiometer developed by Eötvös was a working torsion balance [11]. Christopher Jekeli, in his paper on Gravity Gradiometry (2011), presents detailed mathematical equations for measuring gravity gradients using the Eötvös torsion balance [15].

In the early 1900s, Eötvös’ gradiometer along with the next-generation Oertling gradiometer, were widely used to map oil and gas [19]. After World War 1, geologists tried to use the Eötvös’ gradiometer to find geologic structures called salt domes [21]. Technological development of gravity gradiometry slowed down until 1960s [22].

During 1960s, with the heightened space race and cold war, the need for improvements in inertial navigation and methods to accurately measure the vertical deflection of the gravity vector was felt [19, 22]. Around the 1960s and the 1970s, U.S. Navy and Air Force Geophysics Laboratory became interested in the applications of gravity gradiometer [2, 19]. This led to a competition between Hughes Aircraft, C.S. Draper Laboratory and Bell Aerospace Textron, with Bell Aerospace finally getting the contract to develop the gradiometer for U.S. Navy [19].

During this period, Robert Forward of the Hughes Aircraft Research Laboratory invented the first prototype of a rotating gravity gradiometer (RGG) [1, 23]. This is one of the earliest modern gradiometers [15]. It has two centrally pivoted arms, in a cross-shaped arrangement, with proof masses on each end (refer Figure 2.2) [1, 2, 15, 23]. These types of gravity gradiometers can be called resonant rotating gravity gradiometers (RRGG) or resonant modulating gravity gradiometers (RMGG) [1]. The RGG's operating principle is that at a sufficiently high frequency, the error contribution, towards gravity gradient measurements, due to the linear and angular motions are negligible and hence, the useful signal can be modulated-demodulated from the error and noise sources [1, 2, 15, 23].

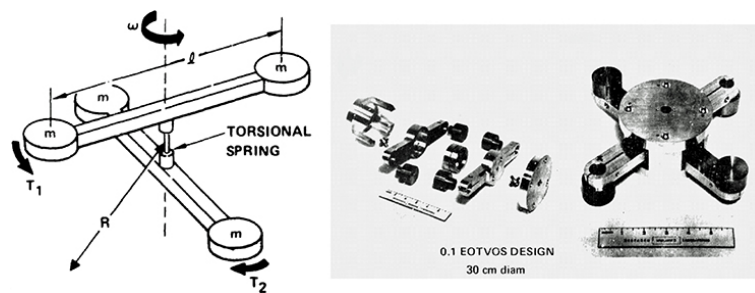


Fig. 2.2: The RMGG developed at the Hughes Aircraft Research Laboratory. (a) Two orthogonal dumbbells are set to rotate uniformly around a mutual pivot representing a torsional spring. (b) A real RMGG prototype (Image taken from Veryaskin, Gravity, Magnetic and Electromagnetic Gradiometry (2018)) [1].

In 1970s, the development of the floated gravity gradiometer (FGG) by Milton Trageser of Charles Stark Draper Laboratory (Cambridge, Massachusetts) was another novel attempt to design stable gravity gradiometers [1, 2, 15]. Some of the advantages of FGG included quick time response, low self-noise, relative insensitivity to angular vibration, low fluid unbalance, and reasonably low sensitivity to linear vibration, temperature and magnetic fields [1].

During 1980s, Ernest Metzger of Bell Aerospace / Textron designed a rotating finite differenced accelerometer gravity gradiometer, to measure the full-tensor of gravity gradients (FTGs) [1, 2]. It operates on the principle of measuring gravity gradients by adding two finite differenced accelerometer pairs, mounted diametrically opposite on a rotating disk [1, 2, 19].

In the mid 2000s, improvements to this concept were made by digitizing the critical signals, so as to decrease the noise, increase reliability, and reduce the size and weight of the installed system [19]. Eventually, the Bell / Textron instrument technology was acquired by Lockheed Martin, which has since developed the current-generation of rotating GGIs [1, 2, 19]. Subsequent developments made by Bell Aerospace and Lockheed Martin to improve the current generation of gravity gradiometers are discussed in detail by Richeson (2008), DiFrancesco (2009), Jekeli (2011), and Veryaskin (2018), respectively [1, 2, 15, 19].

Difficulties associated in using rotating gravity gradiometers for surface and airborne surveillance systems stimulated the search for technological concepts and ideas that can enhance gravity gradiometer accuracy and make instrumentation easier for application in dynamic environments. Four potential candidates for progressing the future of gradiometer technology emerged from this search. These include the string (ribbon) gravity gradiometer, superconducting gravity gradiometer, MEMS gravity gradiometer and quantum gravity gradiometer (cold atom accelerometer based technology).

The string (ribbon) gravity gradiometer is an 'intrinsic' class gravity gradiometer (IGG), which has been under development, since 1995, by Gravitec Instruments Ltd [1]. In 2005, Gravitec Instruments collaborated with University of Western Australia to develop an intrinsic string magnetic gradiometer [1]. String gravity gradiometer concept does not follow torsional (dumbbell) or accelerometric operating principle [1]. Instead, string gravity gradiometer use a single sensing element (a ribbon) that responds to gravity gradient forces [1, 19]. Because these types of gradiometers do not difference the signals from paired sensors such as accelerometers or gravimeters, they are called intrinsic gravity gradiometers [1].

Another potential future gravity gradiometer is the superconducting gravity gradiometer. The gravity gradiometer instruments developed using superconducting technology have an order-of-magnitude improvement in noise sensitivity, reduced thermal noise, near perfect magnetic shielding, high degree of mechanical and electrical stability, virtual elimination of thermal gradients and unprecedented mechanical displacement measurement sensitivity [1, 2].

The first superconducting gravity gradiometer (SGG) were developed independently, in the 1980s, by Ho Jung Paik of the University of Maryland (UMD), and Frank van Kann of the University of Western Australia (UWA) [1, 2, 24]. The operating principle of SGG is based on sensing the proof mass displacement by the change in superconducting current [1].

The European Space Agency's Gravity Field and Steady-State Ocean Circulation Explorer (ESA GOCE, 2008) satellite carried an Electrostatic Gravity Gradiometer (EGG) on-board to achieve its objective to map Earth's gravitational field spatially and temporally [2]. The EGG on-board GOCE satellite used capacitance (i.e., voltage) to measure the accelerometer's proof mass displacements, unlike UMD's SGG which used inductance (i.e., current) to sense proof mass displacement [2].

A third potential future gravity gradiometer is a MEMS-based gravity gradiometer. MEMS or Micro-machined Electro-Mechanical Systems are micro machined state of the art structures [1]. Owing to this extraordinary sensitivity, and their ultra-miniature size, they are counted as a potential technology for space applications [1].

The Quantum gravity gradiometer works on the principle of atom interferometry, which use the concepts of wave-particle duality, and the superposition principle [1, 22, 25]. The first quantum gravity gradiometer was based on laser-manipulated atom interferometry and was developed by Mark Kasevich's laboratory (Yale University) [1]. Since the proof mass in this gradiometer are individual atoms and absolute acceleration is being measured simultaneously at both positions, errors due to sensor misalignment, scale factor, null bias errors, material instabilities due to temperature variations, and any other 'classic' systematic errors are virtually eliminated [1].

Some considerable efforts have been made in the past to classify different types of gravity gradiometers based on their working principles, measurement noise level, and other parameters [1]. One such attempt includes the efforts made by Soviet-era physicist Victor Nazarenko, in 1982 [1]. Based on Nazarenko's classification, as published by Veryaskin (2018), a horizontal tree diagram is shown in Figures 2.3 and 2.4 [1].

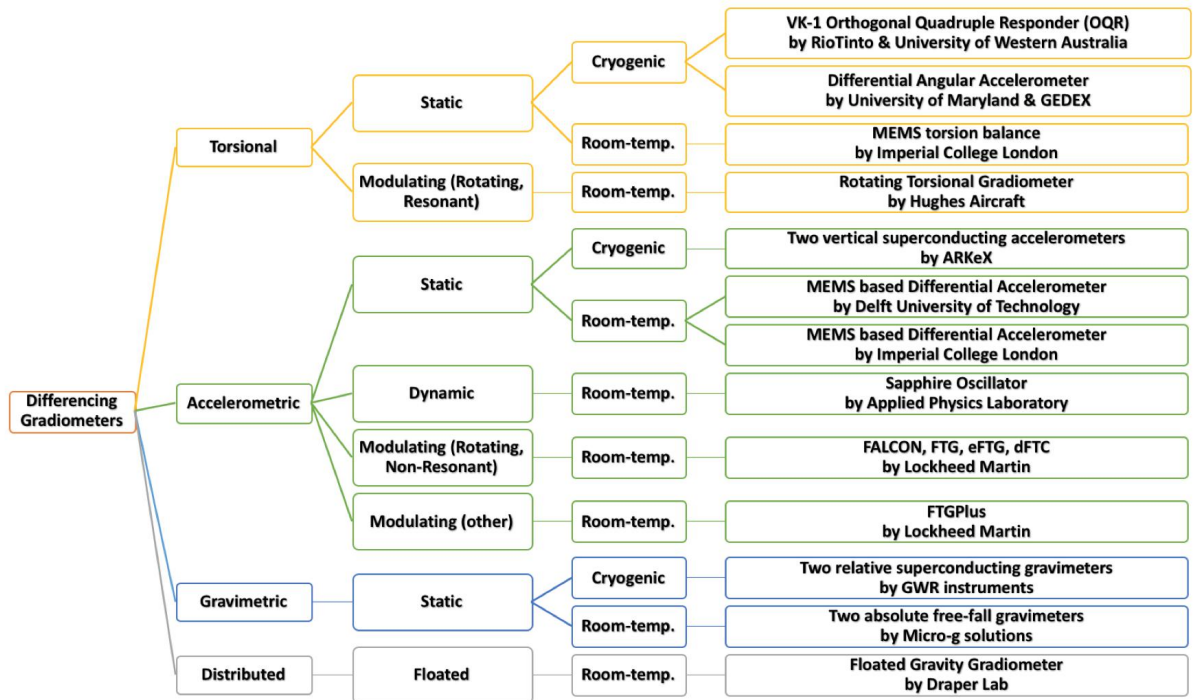


Fig. 2.3: Classification of Differencing Gradiometers based on the measurement sensor type, operating principle, and operating temperature. Adapted from Veryaskin, Gravity, Magnetic and Electromagnetic Gradiometry (2018) [1].

Gravity gradiometers can be classified as two basic types (refer Table 2.1) [1]. Firstly, differencing Gradiometers, which use differencing method, i.e., subtracting the real-time output signals from a pair of sensors [1]. Secondly, intrinsic gradiometers, which use a single sensing element to make gravity gradient measurements directly [1]. The measurement

model used in this study will be based on differencing type (i.e. cold atom accelerometer, electrostatic gravity accelerometer, etc.) gradiometers only.

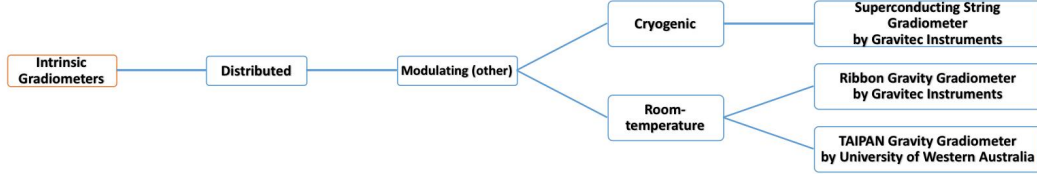


Fig. 2.4: Classification of Intrinsic Gradiometers based on the measurement sensor type, operating principle, and operating temperature. Adapted from Veryaskin, Gravity, Magnetic and Electromagnetic Gradiometry (2018). [1]

GGI type	Measured quantity	Major problem
Differencing	$\frac{g_{z_2} - g_{z_1}}{x_2 - x_1}$	Misalignment of sensing elements
Intrinsic	$G_{zx} = \frac{\partial g_z}{\partial x} = \frac{\partial g_x}{\partial z}$	Read-out sensitivity limitations

Table 2.1: An example of differencing and intrinsic gravity gradiometers. Their sensitivity axes are chosen to be aligned along the X direction. However, a gradiometer can have multiple sensitivity axes and measure all five independent gravity gradient tensor components. Adapted from Veryaskin, Gravity, Magnetic and Electromagnetic Gradiometry (2018) [1].

Finally, Table 2.2 summarizes the chronological evolution of the gravity gradiometer instruments and parallel improvement in their sensitivity, respectively [2].

Gradiometer	Developer	Noise ($1\text{-}\sigma$ Eö)	Data Rate (sec)
Rotating Accelerometer GGI	Bell Aerospace/Textron	2 (Lab), 10 (Air)	10
Rotating Torque GGI	Hughes Research Lab	0.5 (Goal)	10
Floated GGI	Draper Lab	1 (Lab)	10
Falcon AGG	LM/BHP Billiton	3	Post Survey
ACVGG	Lockheed Martin(LM)	1	1
3D FTG	LM/Bell Geospace	5	Post Survey
FTGeX	LM/ARKeX	10 (Goal)	1
UMD SGG (Space)	UMD	0.02 (Lab)	1
UMD SAA (Air)	UMD	0.3 (Lab)	1
UWA OQR	UWA	1 (Lab)	1
Exploration GGI	ARKeX	1 (Goal)	1
HD-AGG	Gedex/UMD/UWA	1(Goal)	1
Electrostatic GGI	ESA	0.001 (Goal)	10
Cold Atom Interferometer	Stanford/JPL	30 (Lab)	1

Table 2.2: Gravity Gradiometer Instruments. Adapted from Richeson, Gravity gradiometer aided inertial navigation within non-GNSS environments (2008) [2].

2.3 Applications and Challenges of Gravity Gradiometry

The gravity gradient measurement is significant as it can detect small geological features, and contain spatial and attitudinal information. This renders the gravity gradiometry as an important tool in a plethora of real-world applications. Some of the prominent applications of gravity gradiometry have been highlighted in Figure 2.5 [4].

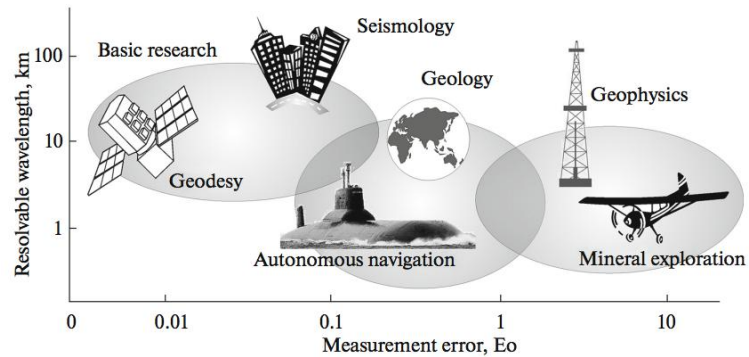


Fig. 2.5: Comparison of gravity gradiometry applications, based on a sensitivity scale (Image taken from Evstifeev, The state of the art in the development of onboard gravity gradiometers (2017)) [4].

Since mid 20th century, gravity gradiometry has become an important industrial tool in many fields, ranging from oil and mineral exploration to archeology to geophysics and geology. However, the major part of the technological development in gravity gradiometry can be associated with its use in oil and mineral exploration. With the necessary technological development, the potential of using gravity gradiometry in commercial and defense applications has steadily increased, which has stimulated mainstream interest and has opened up new research fronts in this field. Apart from oil, gas, and mineral exploration, gravity gradiometry has found applications in gravity gradiometer surveying, underground tunnels and void detection, cargo hidden masses detection, nuclear non proliferation, terrestrial GPS denied navigation, and space missions to map Earth's gravitational field [1, 12]. There has also been an on-going effort to further develop gradiometer technology to make measurements possible during sub-surface explorations [1].

According to Veryaskin (2018), the first passive navigation system, which employed gravity gradient map matching techniques, was discussed by Clive Affleck and Albert Jircitano of Bell Aerospace Textron (USA) [1, 2, 26]. Affleck and Jircitano presented a parametric study for an airborne system operating over land and ocean areas for varying navigation

system quality, gradiometer quality, altitude above terrain, etc. [26].

Many other studies like the technical report on “Superconducting gravity gradiometer mission” by Paik and Morgan (1993), the article titled “Satellite orbit determination using satellite gravity gradiometry observations in GOCE mission perspective” by Bobojć (2003), the dissertation on “Gravity gradiometer aided inertial navigation within non-GNSS environments” by Richeson (2008), two papers titled “Low-Earth Orbit Determination from Gravity Gradient Measurements” , and “Autonomous Orbit Determination via Kalman Filtering of Gravity Gradients” by Sun et al (2016), and lastly, a paper on “Autonomous Orbit Determination Using Epoch-Differenced Gravity Gradients and Starlight Refraction” by Pei et al (2017) discuss different approaches and methods for airborne and terrestrial navigation using GPS integrated gravity gradiometer system [2, 24, 27, 28, 29, 30].

Some studies only discuss terrestrial or airborne navigation, while others only discuss techniques to estimate spacecraft’s position and velocity. Most of the studies consider integrated inertial navigation system (INS) based on gravity gradient measurements and GPS updates. Most of these studies do not include the objective to compute the required measurement sensitivity to enable gravity gradiometer based navigation. During the literature survey, no study has been found to discuss the techniques to provide real-time estimate of the spacecraft’s position, velocity, and attitude using gravity gradient measurements only. Further, most of the studies used analytical approaches or Monte Carlo analysis to conduct the measurement error analysis for gravity gradient measurements. No study has been conducted to analyze the effects of gravity gradiometer measurement sensitivity on the final navigation solution, for different mission requirements. This research will be the first to conduct a Linear Covariance analysis and provide error budgets for gravity gradiometer measurements, for different sensor requirements.

This research offers to complement the existing literature. The contribution of this research will include the determination of specific sensor requirements and optimal sensor configuration for different mission types. This will help guide the development of future advanced accelerometers.

Today, as the technological development of gravity gradiometer instruments enhance their measurement sensitivity, one of the biggest challenge is to isolate the gravity gradient measurements from the disturbing sources [10, 19]. This is because with the enhanced measurement sensitivity the resolution of a gravity gradient measurement improves, however this also improves the resolution of disturbing sources by the same amount [10, 19]. Some of the major challenges impacting the full use of gravity gradiometry include the difficulty in obtaining gravity gradient measurements in a dynamic environment, limitations of gradiometer measurement bandwidth for moving-base gravity gradiometers, difficulty in processing gravity gradient measurements and isolating useful measurements from the disruptive noise sources, and lastly, hardware and data export controls limit the growth of this field [10, 19].

2.4 Extended Kalman Filter and Linear Covariance Analysis Techniques

The Extended Kalman Filter and Linear Covariance Analysis Techniques are mathematical/statistical tools used for estimating and predicting the future states of a dynamic system, and studying the complexities of closed-loop GN&C systems (refer Figure 2.7) [9, 31].

The Extended Kalman Filter is an optimal recursive data processing algorithm used to estimate the current and future value of the variables of interest [9]. An Extended Kalman filter is an “extended” version of a standard Kalman filter, in a sense that the Kalman filter is extended to use non-linear models and process non-linear dynamics, and discrete non-linear measurement models to estimate the states of the system [9, 32]. It consists of two stages, firstly, propagation of the states and state covariance, and secondly, the update of the state and state covariance [9, 32, 33]. The flowchart depicting the two stage process for a discrete linearized model is shown in Figure 2.6.

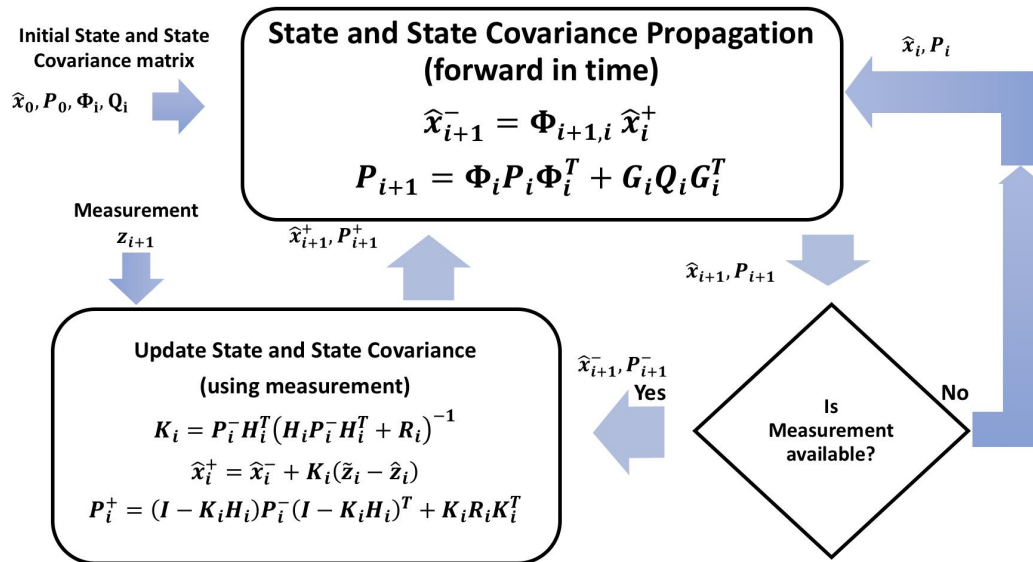


Fig. 2.6: Kalman Filter Flow Diagram .

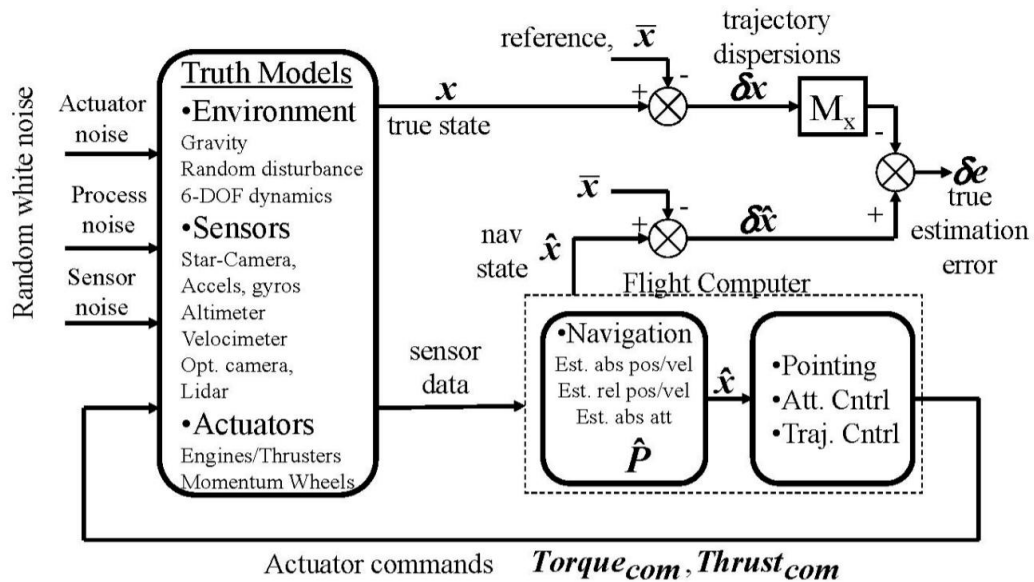


Fig. 2.7: Generic Closed-Loop GN&C Simulation (Image taken from Christensen and Geller, Linear covariance techniques for closed-loop guidance navigation and control system design and analysis (2014)) [5].

Linear covariance (LinCov) analysis for closed-loop GN&C analysis is used to determine the expected performance of a Kalman filter by evaluating the covariance of the true state estimation errors [5, 9, 31]. For linear covariance analysis, it is important to linearize the system dynamics about a nominal or desired reference trajectory and then use linear stochastic system theory to determine the state covariance [9, 31].

2.5 Literature Review Summary

In this chapter, a holistic overview of gravity gradiometry, chronological development of gravity gradiometer instruments, their classification, potential applications, and corresponding challenges needed to be solved to make progress in the future, have been presented. This chapter covered the basics of gravity gradiometry, and the literature highlighting the analytical approaches available to deduce spatial and attitudinal information from a gravity gradient matrix.

The working principle of different gravity gradiometer instruments were explained and their advantages were highlighted. A brief overview of the applications of gravity gradiometry and the existing challenges towards achieving the full potential was discussed. Lastly, a summary of important mathematical tools, like the Extended Kalman Filter and Linear Covariance Theory, has been presented.

CHAPTER 3

Dissertation Overview

3.1 Chapter Overview

This chapter aims to define the scope and objectives of the study, and help understand the real-world applications of this research. The approach and introduction to the important mathematical tools required to achieve the pre-defined objectives are described. Performance metrics to validate the final results, of this study, are defined.

3.2 Scope

This research is focussed on investigating the feasibility of using advanced accelerometer measurements and onboard gravity field maps for autonomous orbit determination in LEO regime. This study does not consider traditional inertial navigation (dead reckoning and external aiding). Instead, the study focuses on identifying the required range of measurement sensitivity for advanced accelerometers, for different sensor and orbit configurations.

Linear Covariance Theory is used as a tool to determine the sensitivity of the final navigation error to specific error sources. The error budgets are then used to determine specific sensor requirements and, thereby, calculate the optimal sensor configuration required to satisfy given mission requirements. One of the key objectives of this study is to determine the sensitivities of the final navigation solution to system uncertainties.

The final outcome of this research aims to answer the following realm of questions:

- Which type of advanced accelerometer with what level of measurement sensitivity is best suited for autonomous navigation, for a given mission objective?
- Can highly sensitive accelerometers solve both the orbit determination and the attitude determination problem?
- What are the best system solutions for LEO regime?

- What is the optimal sensor configuration required to determine position, velocity, and attitude of the spacecraft in a specified orbit and for a given mission objective?
- What levels of accelerometer bias and alignment error can be tolerated?
- What is the optimal accelerometer separation and to what accuracy must the separation be known?

To answer these questions and achieve the goals of this study, Linear Covariance analysis is used to study various sensor configurations for different orbital configurations. High-fidelity dynamics models include rotational and translational dynamics. Environment models include higher-order gravity models, solar radiation pressure, drag, and high-fidelity planetary ephemerides. Sensor models include uncertainties in scale-factors, biases, noise (colored as applicable), and sensor location.

This study does not include the development of hardware or sensor architecture. The scope of this research is restricted to test the hypothesis by computer simulations only and does not include field trials. The research plan is to evaluate and guide the development of the family of advanced accelerometers with an objective of their potential for space applications.

Based on this research, the required range of measurement sensitivity for advanced accelerometers, using different measurement principles for different flight regimes, will be determined.

3.3 Objective

This research includes differencing type (i.e. cold atom accelerometer, electrostatic gravity accelerometer, etc.) gradiometer measurement model only. The main objectives of this research are

- Conduct observability analysis to investigate the feasibility of using advanced accelerometer measurements to determine position, velocity, and attitude of the spacecraft.

- Develop a Linear Covariance tool to determine the sensitivity of the final orbit navigation error to specific error sources for different orbital configurations.
- Determine specific sensor requirements and calculate the optimal sensor configuration required to satisfy given mission requirements.

3.4 Approach

In the following subsections, an outline of the approach pursued for setting up the problem is discussed. The details of this approach are presented in Chapter 5.

3.4.1 Key Problem Parameters and Reference frames

The key problem parameters are defined by the following state vector (\mathbf{x})

$$\mathbf{x} = (\mathbf{x}_s, \mathbf{x}_p, \mathbf{x}_a)^T \quad (3.1)$$

It consists of 16 spacecraft states (\mathbf{x}_s), 3 environmental parameter states (\mathbf{x}_p), and $12n$ (n = number of accelerometers) accelerometer states (\mathbf{x}_a). The spacecraft states are given by

$$\mathbf{x}_s = \left(\mathbf{r}_{CM/E}^I, \mathbf{v}_{CM/E}^I, \mathbf{q}_{I \rightarrow B}, \boldsymbol{\omega}_{B/I}^B, \mathbf{r}_{CM/O}^B \right)^T \quad (3.2)$$

where $\mathbf{r}_{CM/E}^I$ and $\mathbf{v}_{CM/E}^I$ denote the position and velocity of the spacecraft's center of mass with respect to the center of the Earth, expressed in inertial frame, $\mathbf{q}_{I \rightarrow B}$ denotes the spacecraft's attitude quaternion, such that it defines the attitude/orientation of the spacecraft body-fixed reference frame with respect to the inertial reference frame, $\boldsymbol{\omega}_{B/I}^B$ is the angular velocity of the spacecraft with respect to the inertial frame, expressed in spacecraft body-fixed frame, and $\mathbf{r}_{CM/O}^B$ denotes the spacecraft center of mass position with respect to the origin of the spacecraft body-fixed reference frame.

The three environmental parameter states are given by

$$\mathbf{x}_p = (\beta, \rho_r, h_s)^T \quad (3.3)$$

where β is the ballistic coefficient for the spacecraft, ρ_r is the reference sea level atmospheric density, and h_s is the scale height for exponentially decaying atmospheric drag model.

The accelerometer parameter states are given by

$$\mathbf{x}_a = \left(\mathbf{r}_{a_i/O}^B, \mathbf{b}_i^{\tilde{a}_i}, \mathbf{f}_i^{\tilde{a}_i}, \boldsymbol{\epsilon}_i^{\tilde{a}_i} \right)^T \quad (3.4)$$

where $\mathbf{r}_{a_i/O}^B$ denotes the i^{th} accelerometer position with respect to the origin of spacecraft body-fixed reference frame, and $\mathbf{b}_i^{\tilde{a}_i}$, $\mathbf{f}_i^{\tilde{a}_i}$, and $\boldsymbol{\epsilon}_i^{\tilde{a}_i}$ denote the accelerometer bias, scale factor and accelerometer misalignment, respectively.

The relevant reference frames (all right-handed and orthogonal) used in this study are the Inertial Reference Frame (IRF), Spacecraft Body-fixed Reference Frame (SBRF), Accelerometer Nominal Reference Frame (ANRF), and Accelerometer Actual Reference Frame (AARF). The first 3 frames are generally known, while the AARF is generally unknown.

The fundamental Inertial Reference Frame (IRF) for this study is defined by an origin located at the centre of the Earth, x-axis at the intersection of the mean ecliptic plane with the mean equatorial plane at the date of 1st January 2000 and pointing positively towards the vernal equinox, z-axis orthogonal to the mean equatorial plane at the date 1st January 2000, and y-axis completing a right-handed reference frame.

The Spacecraft Body-fixed Reference Frame (SBRF) is an arbitrarily defined reference frame whose center coincides with the nominal center of mass of the spacecraft. The transformation from IRF to SBRF is denoted as $T_{I \rightarrow B}$ or $q_{I \rightarrow B}$.

The Accelerometer Nominal Reference Frame (ANRF) is the accelerometer reference frame defined by the manufacturer or as per the accelerometer model. The transformation from SBRF to ANRF is denoted as $T_{B \rightarrow a_i^N}$.

The Accelerometer Actual Reference Frame (AARF) is the same as Accelerometer Nominal Reference Frame (ANRF), except that it takes into account the misalignments (ϵ_i) in-

roduced while securing the accelerometer on the spacecraft structure. The transformation from ANRF to AARF is a small angle transformation defined by

$$T_{a_i^N \rightarrow \tilde{a}_i} = I_{3 \times 3} - \left[\epsilon_i^{\tilde{a}_i} \times \right] \quad (3.5)$$

where $\epsilon_i^{\tilde{a}_i}$ is a vector of three small angle rotations.

In this study, a spherical harmonic gravity model is used to simulate Earth's gravity model. Perturbations like atmospheric drag, solar radiation pressure, third-body effect (due to the sun and moon), and gravity gradient torques are included in the dynamical model. Detailed environmental model is discussed in Chapter 5.

3.4.2 Non-Linear Modeling

The non-linear dynamics of the spacecraft and the measurements are defined as presented below

The dynamics for the given system can be defined in the general form

$$\dot{\mathbf{x}} = \mathbf{f}(\mathbf{x}, t) + G\mathbf{w} \quad (3.6)$$

where \mathbf{x} is the true state vector, G is a matrix to map the noise vector to the state dynamics, and \mathbf{w} is a vector of zero-mean white noise processes. The dynamics can then be segmented into three broad categories: (1) translational dynamics, (2) rotational dynamics, and (3) dynamics of the uncertainties inherent to system/environmental model.

The translational dynamics are defined as

$$\dot{\mathbf{r}}_{CM/E}^I = \mathbf{v}_{CM/E}^I \quad (3.7)$$

$$\dot{\mathbf{v}}_{CM/E}^I = \mathbf{g}_e^I \left(\mathbf{r}_{CM/E}^I \right) + \mathbf{a}_{Third-body}^I \left(\mathbf{r}_{CM/E}^I, \boldsymbol{\rho}_{Sun}, \boldsymbol{\rho}_{Moon} \right)$$

$$+\mathbf{a}_{aero}^I\left(\mathbf{r}_{CM/E}^I, \mathbf{v}_{CM/E}^I, \beta, \rho_r, h_s\right) + \mathbf{a}_{SRP}^I\left(\mathbf{r}_{CM/E}^I, \boldsymbol{\rho}_{Sun}\right) + \mathbf{w}_T + \mathbf{w}_{aero} \quad (3.8)$$

where $\mathbf{g}_e(\mathbf{r})$ denotes the Earth's gravitational acceleration at position $\mathbf{r}_{CM/E}^I$, and \mathbf{a}_{aero} is the aerodynamic acceleration at position $\mathbf{r}_{CM/E}^I$, velocity $\mathbf{v}_{CM/E}^I$, and for ballistic coefficient β , reference atmospheric density ρ_r , and scale height h_s . In Eq(3.8), \mathbf{w}_T and \mathbf{w}_{aero} denote the translational disturbance acceleration and unmodeled aerodynamic acceleration, modeled as zero-mean white Gaussian noise. The dynamics for three environmental parameters (β, ρ_r, h_s) are modeled as 1st-order Markov processes, also known as Exponentially Correlated Random Variables (ECRVs), given as follow

$$\dot{\mathbf{x}}_p = \frac{\mathbf{x}_p}{\tau_{\mathbf{x}_p}} + \omega_{\mathbf{x}_p} \quad (3.9)$$

where \mathbf{x}_p are the parameters, $\tau_{\mathbf{x}_p}$ is the time-constant of the corresponding parameters, and $\omega_{\mathbf{x}_p}$ is the unmodeled zero-mean white Gaussian noise in the dynamics.

The rotational dynamics are defined by the quaternion representing the orientation of the spacecraft body-fixed reference frame (SBRF) with respect to the inertial reference frame (IRF), denoted as $\mathbf{q}_{I \rightarrow B}$. The corresponding kinematics and dynamics will be defined as [31]

$$\dot{\mathbf{q}}_{I \rightarrow B} = \frac{1}{2} \boldsymbol{\omega}_{B/I}^B \otimes \mathbf{q}_{I \rightarrow B} \quad (3.10)$$

where $\boldsymbol{\omega}_{B/I}^B$ is the angular velocity of the spacecraft, expressed in spacecraft-fixed body frame. Correspondingly, spacecraft's angular acceleration can be defined as [31]

$$\dot{\boldsymbol{\omega}}_{B/I}^B = J^{-1} \left[\mathbf{M}_{gg} \left(\mathbf{r}_{CM/E}^I, \mathbf{q}_{I \rightarrow B} \right) - \boldsymbol{\omega}_{B/I}^B \times \left(J \boldsymbol{\omega}_{B/I}^B \right) \right] + \mathbf{w}_R \quad (3.11)$$

where J is the moment of inertia of the spacecraft, and \mathbf{M}_{gg} is the gravity gradient torque. In Eq(3.11), \mathbf{w}_R is the rotational disturbance acceleration, modeled as zero-mean white

Gaussian noise.

Instrument error dynamics are defined by uncertainty and process (unmodeled) noise of the center of mass position $\mathbf{r}_{CM/O}^B$ (with respect to the spacecraft fixed body frame), accelerometer position $\mathbf{r}_{a_i/O}^B$ (with respect to the spacecraft fixed body frame), accelerometer measurement bias $\mathbf{b}_i^{\tilde{a}_i}$, accelerometer measurement scale-factor bias $\mathbf{f}_i^{\tilde{a}_i}$, and lastly, accelerometer misalignment $\boldsymbol{\epsilon}_i^{\tilde{a}_i}$. The dynamics of these parameters $(\mathbf{r}_{CM/O}^B, \mathbf{r}_{a_i/O}^B, \mathbf{b}_i^{\tilde{a}_i}, \mathbf{f}_i^{\tilde{a}_i}, \boldsymbol{\epsilon}_i^{\tilde{a}_i})$ are modeled as 1st-order Markov processes, also known as Exponentially Correlated Random Variables (ECRVs), and generally defined by Eq. 3.9.

The accelerometer measurements for a system can be generically defined as

$$\tilde{a}_i^{\tilde{a}_i} = \mathbf{h}(\mathbf{x}) + \boldsymbol{\eta}_i^{\tilde{a}_i} \quad (3.12)$$

where \mathbf{x} is the true state vector, and $\boldsymbol{\eta}_i$ is a vector of zero-mean white Gaussian noise. The subscript i represents the i^{th} accelerometer.

In terms of the state vector, the non-linear model for the accelerometer measurements, will be modeled as

$$\mathbf{h}(\mathbf{x}) = \left[I + D(\mathbf{f}_i^{\tilde{a}_i}) \right] \mathbf{a}_{d_i}^{\tilde{a}_i} + \mathbf{b}_i^{\tilde{a}_i} \quad (3.13)$$

where I denotes a 3×3 identity matrix and $D(\mathbf{f}_i^{\tilde{a}_i})$ is a matrix with $\mathbf{f}_i^{\tilde{a}_i}$ as diagonal elements and $\mathbf{b}_i^{\tilde{a}_i}$ is the accelerometer bias.

$$\mathbf{a}_{d_i}^{\tilde{a}_i} = T_{a_i^N \rightarrow \tilde{a}_i} T_{B \rightarrow a_i^N} T_{I \rightarrow B}(\mathbf{q}_{I \rightarrow B}) \mathbf{a}_{d_i}^I \quad (3.14)$$

$$\mathbf{a}_{d_i}^I = \mathbf{g}^I(\mathbf{r}_{CM/E}^I) - \mathbf{g}^I(\mathbf{r}_{a_i/E}^I) + \mathbf{N}^I(\mathbf{r}_{CM/E}^I, \mathbf{v}_{CM/E}^I, \beta, \rho_r, h_s)$$

$$+ T_{B \rightarrow I}(\mathbf{q}_{B \rightarrow I}) \left[\boldsymbol{\omega}_{B/I}^B \times (\boldsymbol{\omega}_{B/I}^B \times \mathbf{r}_{a_i/CM}^B) \right] \quad (3.15)$$

where all the vectors with superscript I, \tilde{a}_i , and \tilde{a}_i^N are coordinatized in inertial reference frame, accelerometer actual reference frame, and accelerometer nominal reference frame, respectively. In Eq. 3.15, \tilde{a}_i denotes the accelerometer measurement, $\boldsymbol{\eta}_i^{\tilde{a}_i}$ is the accelerometer measurement noise modeled as zero-mean white Gaussian noise, $\mathbf{a}_{d_i}^{\tilde{a}_i}$ denotes the detected acceleration in the accelerometer frame, $\mathbf{a}_{d_i}^I$ is the detected acceleration in the inertial reference frame, and $\mathbf{g}\left(\mathbf{r}_{CM/E}^I\right)$ denotes the total gravitational acceleration $\left(\mathbf{g}_e\left(\mathbf{r}_{CM/E}^I\right) + \mathbf{a}_{3^{rd}body}\left(\mathbf{r}_{CM/E}^I\right)\right)$ at position $\mathbf{r}_{CM/E}^I$. Further, $\mathbf{r}_{a_i/CM}^B$, $\dot{\mathbf{r}}_{a_i/CM}^B$, and $\ddot{\mathbf{r}}_{a_i/CM}^B$ are the accelerometer position, velocity, and acceleration with respect to the spacecraft center of mass (and is expressed in spacecraft fixed body frame), and \mathbf{N} denotes the non-gravitational acceleration (i.e., acceleration due to atmospheric drag and solar radiation pressure) as a function of spacecraft position $\mathbf{r}_{CM/E}^I$, velocity $\mathbf{v}_{CM/E}^I$, ballistic coefficient β , reference atmospheric density ρ_r , and scale height h_s . It can be noted that the last three terms in Eq(3.15) are very small, this is because spacecraft structure is assumed to be rigid (i.e., $\dot{\mathbf{r}}_{a_i/CM}^B \approx 0$, and, $\ddot{\mathbf{r}}_{a_i/CM}^B \approx 0$), the accelerometer position vector $\left(\mathbf{r}_{a_i/CM}^B\right)$ is assumed to be relatively small, and the spacecraft is assumed to have very small angular acceleration, such that the cross product (i.e., $\dot{\boldsymbol{\omega}}_{B/I}^B \times \mathbf{r}_{a_i/CM}^B$) is approximately equal to zero. Thus, these terms are absorbed into the bias and noise terms in Eq(3.13). The accelerometer set-up is shown in Figure 3.1.

Only the differencing type (i.e. cold atom accelerometer, electrostatic gravity accelerometer, etc.) gradiometer measurement model are studied for this research. This is because of the market predominance of differencing type gradiometers relative to the intrinsic type. And since most of the gradiometers are based on the differencing model, which includes the gradiometer on-board GOCE mission and the promising cold atom accelerometer based gradiometer, it is more pertinent to study and analyze the differencing type gradiometers.

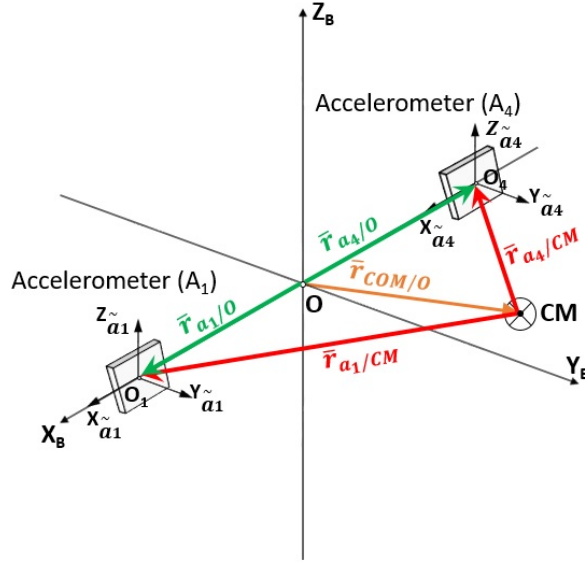


Fig. 3.1: Gravity Gradiometer Instrument - Schematic Diagram (only 2 of the 6 accelerometers are shown). Adapted from Cesare, Performance Requirements and budgets for gradiometric mission (2002). [6]

Measurements from an on-board star camera are used to improve the estimation of the states and thereby enhance the overall fidelity of the navigation system. The measurement model for the star camera measurements is presented in Chapter 5.

3.4.3 Linear Modeling

The aforementioned non-linear models and equations are linearized about the reference state vector ($\bar{\mathbf{x}}$) so as to formulate the linear covariance model for the given system. The reference state includes the desired trajectory (i.e., given LEO orbit). Note that for formulating an Extended Kalman Filter, linearization is done about the estimated state vector ($\hat{\mathbf{x}}$). The linearized equations of motion (Jacobian) and measurement partials are derived in Chapter 5.

3.4.4 Observability Analysis

Next, the observability analysis of the system is conducted. The observability of the given linearized time-varying discrete-time model can be deduced by computing the observability gramian $\mathcal{O}_k(0, M)$ for M measurements, as

$$\mathcal{O}_k(0, M) \triangleq \sum_{i=1}^M \phi^T(i, 0) H^T(i) H(i) \phi(i, 0) \quad (3.16)$$

where ϕ is the state transition matrix, and H is the measurement partial. The model is said to be completely observable if and only if any of the following criteria are met after some finite M measurements : (1) the null space of $\mathcal{O}_k(0, M)$ is $\mathbf{0} \in R^n$, (2) $\mathcal{O}_k(0, M)$ is non-singular, i.e., invertible, (3) $\mathcal{O}_k(0, M)$ is positive definite, (4) the determinant of $\mathcal{O}_k(0, M)$ is non-zero [9].

3.4.5 Linear Covariance Analysis

Finally, the Linear Covariance Analysis is conducted and the corresponding results are used to develop an error budget model for the system, which in turn is used to deduce specific sensor requirements and optimal sensor configuration. This approach is repeated for different flight regimes and mission types so as to build a measurement sensitivity requirement chart based on the mission requirements.

Performance analysis is conducted by studying important modeling parameters like filter gravity model, measurement noise, measurement frequency, number of accelerometers, gradiometer baseline length, orbital regime, and initial state covariance. This helps to obtain the preliminary results for determining the role and importance of each modeling parameter in designing an autonomous orbital navigation system.

3.4.6 Performance Metrics

Performance metrics for this research are the navigation solution at the final time, i.e., the standard deviation (3-sigma values) for the spacecraft position, velocity, attitude, angular velocity, center of mass position, accelerometer positions, and accelerometer parameters

(bias, scale factor, and misalignment). Final navigation requirements are defined based on the mission type, and these requirements are compared to the performance metrics of the autonomous navigation system based on advanced accelerometers.

Final navigation requirements are defined in the Local Vertical and Local Horizontal (LVLH) frame, and the final navigation solution in the LVLH frame is compared with the pre-defined requirements (as described in mission objective). Error budgets are used to show the contribution of each source of error to the final orbit navigation error, which in turn is compared against the reference solution, for different mission types.

MATLAB is used to develop the required algorithm and generate results for this study.

3.5 Summary

In this chapter, the scope and the objective of the proposed research were presented. The approach and important mathematical tools required to achieve the pre-defined objectives were outlined. Performance metrics to validate the final results, of this study, was also defined.

CHAPTER 4

Coordinate Frames, Transformations, and Gravity Field Models

4.1 Chapter Overview

Detailed problem setup and relevant mathematical quantities require detailed review of coordinate frames and corresponding transformations. This chapter provides an overview of the significant coordinate frames used during this study. The aim of this chapter is to help create the foundation for a detailed problem setup in later chapters, and elucidate the specifics of coordinate transformations and gravity field models.

4.2 Coordinate Frames

Defining relevant coordinate frames is integral to any navigation system, and expressing mathematical quantities in appropriate coordinates helps to better represent dynamical systems. All the coordinate frames used in this study are right-handed Cartesian/orthogonal coordinates. Coordinate frames used in this study are described next.

4.2.1 Earth-Centered Inertial Frame (ECI)

Earth-Centered Inertial Frame (ECI) is one of the most fundamental coordinate frames, used frequently to define systems that obey Newton's laws of motion. An inertial frame is a non-rotating frame, defined to be fixed in space or moving with no acceleration [34, 35]. This frame is generally preferred to define a satellites' motion in an orbit.

The origin of this frame coincides with the center of the Earth, and the X-axis and Z-axis are aligned with the Earth's vernal equinox axis and polar axis, respectively. The Y-axis completes the right handed coordinate system. The X-Y axes of this frame lie in Earth's equatorial plane, and are non-rotating with respect to fixed stars.

The direction of the vernal equinox is defined as the apparent direction from Earth to the Sun at the time of vernal equinox, i.e., when the length of day and night are equal and

when the Sun appears to cross the equatorial plane into the northern hemisphere. The polar axis of Earth is defined as the rotation axis of the Earth, through the conventional terrestrial pole (CTP). The ECI frame is shown in Figure 4.1.

However, in reality, all the inertial frames are actually “quasi-inertial”. This is because the reference directions like Earth’s polar axis or Earth’s vernal equinox axis, used to define an inertial frame, have some precession rate. For example, the inertial direction of the Earth’s vernal equinox is changing slowly at about 50 arc seconds per year, while the inertial direction of the rotation axis of Earth has a rotation rate of about 1.6×10^{-6} deg/h [7]. Because the rate of this precession is very small and over a large time period, with respect to most of the navigation problems, the defined coordinate frame can be treated as a reference frame. Further, to improve consistency of these models, the inertial directions are usually corrected by giving a particular date and time for the assumed value of the mean equatorial plane [7].

Currently, according to International Earth Rotation and Reference Systems Service (IERS) convention, ECI is referenced to the J2000 ECI reference frame and the Earth’s mean equator and equinox at 12:00 terrestrial time on 1 January 2000 are used as the inertial directions to define the axes of the reference frame.

Thus to define the ECI frame, it is necessary to calculate the days past the J2000 epoch. For this Julian date is computed. For all the results presented in this document, time of start has been defined as 2 a.m. on January 1st, 2019.

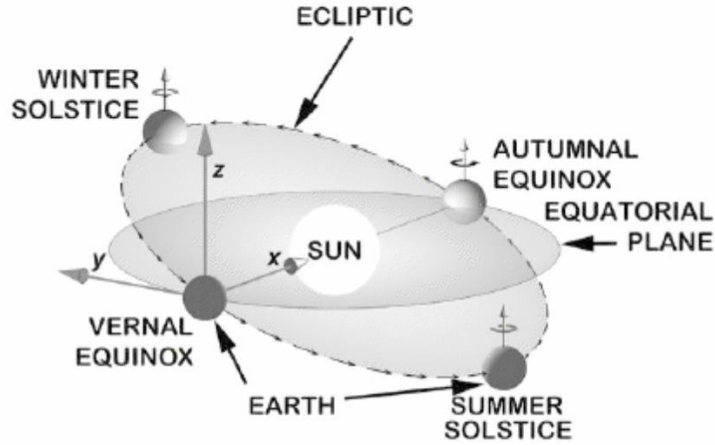


Fig. 4.1: Earth-Centered Inertial Frame (ECI) [7] .

4.2.2 Local Vertical and Local Horizontal Frame (LVLH)

Local Vertical and Local Horizontal Frame (LVLH) is a common reference frame used to define the motion of the spacecraft, in reference to the spacecraft's orbit. This frame also offers convenient representation of spacecraft's attitude, especially for an Earth-pointing spacecraft.

The three axes of the LVLH frame are defined in an inertial frame, as follow

$$\hat{\mathbf{L}}_z^I = \frac{\mathbf{r}_{CM/E}^I}{\|\mathbf{r}_{CM/E}^I\|} \quad (4.1)$$

$$\hat{\mathbf{L}}_y^I = \frac{\mathbf{r}_{CM/E}^I \times \mathbf{v}_{CM/E}^I}{\|\mathbf{r}_{CM/E}^I \times \mathbf{v}_{CM/E}^I\|} \quad (4.2)$$

$$\hat{\mathbf{L}}_x^I = \hat{\mathbf{L}}_y^I \times \hat{\mathbf{L}}_z^I \quad (4.3)$$

where $\mathbf{r}_{CM/E}^I$ and $\mathbf{v}_{CM/E}^I$ are the position and velocity of the spacecraft's center of mass with respect to the center of the Earth, expressed in the ECI frame. In Eqs. 4.1-4.3, $\hat{\mathbf{L}}_z^I$ is the radial axis of the LVLH frame and it points in the radially outward, i.e. in the direction from the center of the Earth to the origin of the LVLH frame along the position vector

of the spacecraft. Further, $\hat{\mathbf{L}}_y^I$ is defined as the cross-track axis of the LVLH frame and it points along the orbit normal, and $\hat{\mathbf{L}}_x^I$ is the along-track axis of the LVLH frame and it completes the right-handed coordinate system. The origin of the LVLH frame coincides with the nominal center of mass of the spacecraft. The LVLH frame is shown in Figure 4.2. Note that when the spacecraft is in a circular orbit, the along-track axis is aligned with the velocity vector $\mathbf{v}_{CM/E}^I$ of the spacecraft.

The rotation matrix from the LVLH frame to ECI frame can be expressed as

$$T_{LVLH \rightarrow ECI} = \begin{bmatrix} \hat{\mathbf{L}}_x^I & \hat{\mathbf{L}}_y^I & \hat{\mathbf{L}}_z^I \end{bmatrix} \quad (4.4)$$

For this study, to better estimate and determine orientation of a rotating spacecraft, the body-fixed frame of the spacecraft is defined to be aligned with the LVLH frame. When a case for a non-rotating spacecraft is considered, the body-fixed frame of the spacecraft is defined to be aligned with the ECI frame. This is done to ease the interpretation of the orbital motion of the spacecraft and its' orientation for the results presented in Chapter 9.

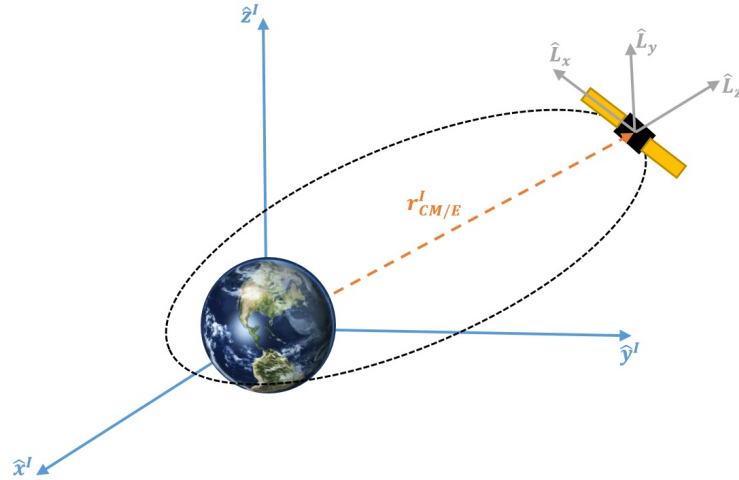


Fig. 4.2: Local Vertical and Local Horizontal frame (LVLH) and ECI frame .

4.2.3 Nominal Reference Frame (NRF)

To effectively define the measurements from the on-board sensors like accelerometers

and star camera, a nominal reference frame is defined for each sensor. This is important for operational reasons, because large forces during launch, unmodeled structural forces like thermal deformations, or some planned motion of gimballed instruments while on-orbit, can complicate the ability to accurately express measurements from on-board sensors.

For this study, the nominal reference frame for all on-board sensors is defined to be always aligned with the spacecraft's body fixed frame.

4.3 LAGEOS Spacecraft

For this study, specification of the LAsEr GEODynamic Satellite (LAGEOS) has been used for setting up the simulation. LAGEOS is a passive research satellite, designed by NASA and launched on May 4, 1976. This spacecraft is an aluminum sphere with a brass core, and has a diameter of 60 cm and a mass of 411 kg.

The primary reason to select LAGEOS as the basis for deciding the specifications (refer Table 4.1) of the spacecraft, simulated in this study, is because it is a spherically symmetric spacecraft, and hence a simplistic atmospheric drag model can be implemented with reasonable fidelity. In fact, recent research by Pilinski and Palo has highlighted the techniques to measure the atmospheric drag on small satellites, and this study has used a spherically symmetric spacecraft for the basis of the model [36].

Name	Value	Units
s/c radius	0.3	m
s/c mass	406.965	kg
s/c coefficient of diffuse reflection	2	unit-less
s/c inertia (along X-X)	11.4	kg.m ²
s/c inertia (along Y-Y)	10.93	kg.m ²
s/c inertia (along Z-Z)	10.93	kg.m ²
s/c coefficient of drag	2	unit-less

Table 4.1: Spacecraft (s/c) Parameters .

4.4 Gravity Field Models

Understanding gravity field models of a planetary body is important for designing any orbital mission, and also, for accurate tracking and orbital determination of a satellite. This section provides a brief overview of the history and techniques behind the modeling of gravitation field.

Before the Space Age began, terrestrial gravimetry was predominantly used to measure Earth's gravitational field [37]. However, the measurements were sparse and evidently inadequate. Space technology and the ability to place satellites in Earth orbit opened a gateway to measure and observe the gravity field with unprecedented precision.

A straightforward technique to measure gravitational field is to measure the orbital period and semi-major axis of either a small natural moon or a small satellite orbiting about the given body [38]. Various techniques, ranging from telescopic observations to radio tracking, are used to estimate the velocity and position of the orbiting satellite [38]. The primary body's mass can then be easily deduced with the knowledge of Kepler's third law or measured data [38]. And in the fortunate case, when the primary body's mass is spherically symmetric, knowledge of body's mass provides sufficient insight about its gravitational field, otherwise spherical harmonic functions are used to estimate a model of the gravitational field [38].

The fundamental expression for the primary body's gravitational potential acting on a satellite is derived as the integral solution to Laplace's equation [37]

$$\nabla^2 U = 0 \tag{4.5}$$

where the unit potential U is defined as

$$U = G \int_{Volume} \left(\frac{dm}{r_s} \right) \tag{4.6}$$

where r_s is the distance from an arbitrary incremental mass dm inside the primary body to the satellite (considered as a point mass), and G is the universal gravitation constant

[37]. Noting that \mathbf{r}_s is the vector difference of two vectors, i.e., $\mathbf{r} - \mathbf{R}$, where \mathbf{R} is the vector from the center of mass of the primary body to the arbitrary incremental mass dm inside the primary body, and \mathbf{r} is the vector from the center of mass of the primary body to the satellite, thus [37]

$$r_s = \sqrt{(\mathbf{r} - \mathbf{R}) \cdot (\mathbf{r} - \mathbf{R})} = r \sqrt{1 - 2R \frac{\cos \theta}{r} + \left(\frac{R}{r}\right)^2} \quad (4.7)$$

Using Eqs. 4.5-4.7, Laplace formulated Earth's gravitational potential (valid external to the Earth) as [37]

$$U = \frac{G}{r} \int \sum_{n=0}^{\infty} P_n(\cos \theta) \left(\frac{R}{r}\right)^n dm \quad (4.8)$$

where P_n are the Legendre polynomials in $\cos \theta$, and θ is the angle between the position vector to the mass increment (\mathbf{R}) and the position vector to the satellite (\mathbf{r}), respectively [37]. A familiar form of the Earth's gravitational potential can be obtained by converting coordinates in Eq. 4.8 to spherical coordinates (r, ϕ, λ) and applying Rodrigues' formula, followed by evaluation of the integrals, such that [37]

$$U = \frac{\mu}{r} \left[1 + \sum_{n=1}^{\infty} \sum_{m=0}^n \left(\frac{R_E}{r}\right)^n P_{n,m}(s_\lambda) (C_{n,m} \cos(m\phi) + S_{n,m} \sin(m\phi)) \right] \quad (4.9)$$

where μ is the universal gravitational parameter, \mathbf{r} is the position vector from a point O fixed in body E (say Earth) to a generic point Q, r denotes the magnitude of \mathbf{r} , R_E is a scaling radius for body E. $P_{n,m}$ is the associated Legendre function of the first kind, of degree n and order m , and has as its argument s_λ , the sine of λ , the latitude of Q [39, 40]. The longitude of Q is denoted by ϕ . $C_{n,m}$ and $S_{n,m}$ are unnormalized gravitational coefficients of degree n and order m [39, 40]. If point O is coincident with the mass center of E, then $C_{1,0}$, $C_{1,1}$, and $S_{1,1}$ all become zero [39, 40, 41].

In geodetic applications, the Legendre polynomials are called zonals, sectorials, and tesserals, determined by their exclusive dependency on latitude ($m=0$), longitude ($n=m$), or both latitude and longitude ($n \neq m$), respectively [37].

Details about gravity field models, required for this study, have been covered in this

section. However, for readers interested in more details, studies by Vetter (1994) and Carrol (2018) are recommended. The paper titled “The Evolution of Earth Gravitational Models used in Astrodynamics” by Jerome R. Vetter provides detailed history and mathematical background for modeling Earth’s gravitational field, and the study by Carroll and Faber, titled “Asteroid Orbital Gravity Gradiometry”, highlights relevant techniques for measuring gravity and gravity gradient from orbit [37, 38].

For this study, Goddard Earth Model (GEM-T1) coefficients have been used [42]. However, the algorithm has been setup that the simulation can be run by feeding coefficients from any other Spherical Harmonics gravity model as well.

4.5 Summary

This chapter provided an overview of the significant coordinate frames used during this study. This chapter helped create the foundation for a detailed problem setup in later chapters, and elucidate the specifics of coordinate transformations and gravity field models.

CHAPTER 5

Problem Parameters and System Modeling

5.1 Chapter Overview

This chapter aims to formulate, develop and detail the non-linear dynamics and measurement equations for onboard autonomous orbital navigation based on accelerometer measurement model. The chapter also describes in detail the corresponding linearized dynamics and measurement models for the given system. Detailed derivations of important equations, required to conduct Linear Covariance (LinCov) analysis are presented.

5.2 State Vector and Reference Frames

For the given model, the state vector (\mathbf{x}) has been defined as follow

$$\mathbf{x} = (\mathbf{x}_s, \mathbf{x}_p, \mathbf{x}_a)^T \quad (5.1)$$

It consists of 16 spacecraft states (\mathbf{x}_s), 3 environmental parameter states (\mathbf{x}_p), and $12n$ (n = number of accelerometers) accelerometer states (\mathbf{x}_a), such that

$$\mathbf{x}_s = \left(\mathbf{r}_{CM/E}^I, \mathbf{v}_{CM/E}^I, \mathbf{q}_{I \rightarrow B}, \boldsymbol{\omega}_{B/I}^B, \mathbf{r}_{CM/O}^B \right)^T \quad (5.2)$$

where $\mathbf{r}_{CM/E}^I$ and $\mathbf{v}_{CM/E}^I$ denote the position and velocity of the spacecraft's center of mass with respect to the center of the Earth, expressed in inertial frame, $\mathbf{q}_{I \rightarrow B}$ denote the spacecraft's attitude quaternion, such that it defines the attitude/orientation of the spacecraft body-fixed reference frame with respect to the inertial reference frame, $\boldsymbol{\omega}_{B/I}^B$ is the angular velocity of the spacecraft with respect to the inertial frame, expressed in spacecraft body-fixed frame, and $\mathbf{r}_{CM/O}^B$ denote the spacecraft center of mass position with respect to the origin of the spacecraft body-fixed reference frame.

The three environmental parameter states are given by

$$\mathbf{x}_p = (\beta, \rho_r, h_s)^T \quad (5.3)$$

where β is the ballistic coefficient for the spacecraft, ρ_r is the reference sea level atmospheric density, and h_s is the scale height for exponentially decaying atmospheric drag model.

The accelerometer parameter states are given by

$$\mathbf{x}_a = \left(\mathbf{r}_{a_i/O}^B, \mathbf{b}_i^{\tilde{a}_i}, \mathbf{f}_i^{\tilde{a}_i}, \boldsymbol{\epsilon}_i^{\tilde{a}_i} \right)^T \quad (5.4)$$

where $\mathbf{r}_{a_i/O}^B$ denote the i^{th} accelerometer position with respect to the origin of spacecraft body-fixed reference frame, and lastly, $\mathbf{b}_i^{\tilde{a}_i}$, $\mathbf{f}_i^{\tilde{a}_i}$, and $\boldsymbol{\epsilon}_i^{\tilde{a}_i}$ denote the accelerometer bias, scale factor and misalignment, respectively.

The relevant reference frames (all right-handed and orthogonal) used in this study are the Inertial Reference Frame (IRF), Spacecraft Body-fixed Reference Frame (SBRF), Accelerometer Nominal Reference Frame (ANRF), and Accelerometer Actual Reference Frame (AARF). The first 3 frames are generally known, while the AARF is generally unknown.

Inertial Reference Frame (IRF) The fundamental inertial reference frame for this study is defined by an origin located at the centre of the Earth, x-axis at the intersection of the mean ecliptic plane with the mean equatorial plane at the date of 1st January 2000 and pointing positively towards the vernal equinox, z-axis orthogonal to the mean equatorial plane at the date 1st January 2000, and y-axis completing a right-handed reference frame.

Spacecraft Body-fixed Reference Frame (SBRF) This is an arbitrarily defined reference frame, whose center coincides with the nominal center of mass of the spacecraft. The transformation from IRF to SBRF is denoted as $T_{I \rightarrow B}$ or $q_{I \rightarrow B}$.

Accelerometer Nominal Reference Frame (ANRF) This is the accelerometer reference frame, as defined by the manufacturer or as per the accelerometer model. The transformation from SBRF to ANRF is denoted as $T_{B \rightarrow a_i^N}$.

Accelerometer Actual Reference Frame (AARF) This reference frame is the same as Accelerometer Nominal Reference Frame (ANRF), except that it takes into account the misalignments (ϵ_i) introduced while securing the accelerometer on the spacecraft structure. The transformation from ANRF to AARF is a small angle transformation defined by

$$T_{a_i^N \rightarrow \tilde{a}_i} = I_{3 \times 3} - \left[\epsilon_i^{\tilde{a}_i} \times \right] \quad (5.5)$$

where $\epsilon_i^{\tilde{a}_i}$ is a vector of three small angle rotations. AARF and ANRF are shown in Figure 5.1.

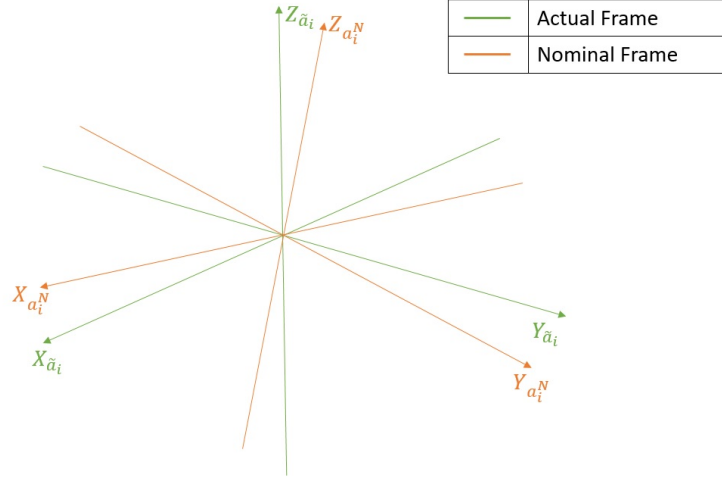


Fig. 5.1: Accelerometer Nominal Reference Frame (ANRF) and Accelerometer Actual Reference Frame (AARF) frame .

5.3 Environmental Models

In this section, relevant environmental models are presented and correspondingly appropriate perturbations acting on the spacecraft are mathematically represented. There are in general two classifications of the perturbations: (1) those that arise from the gravitational potential functions and (2) those that are not derivable from gravitational potential functions [8]. Perturbations like third-body effect (due to the sun, the moon, and other massive space objects), gravity gradient torques, or the tidal potential perturbations are

classified under first category, as all of these effects can be derived from potential functions [8]. However, perturbations due to atmospheric drag, solar radiation pressure, and other perturbations that involve some “contact” with the spacecraft are classified under the second category [8].

5.3.1 Spherical Harmonics Gravity Model

Spherical harmonics gravity model is used to simulate Earth’s gravity model. It is computed analytically by evaluating the first derivative of gravitational potential $U(\mathbf{r})$ with respect to the position vector \mathbf{r} .

$$U = \frac{\mu}{r} \left[1 + \sum_{n=1}^{\infty} \sum_{m=0}^n \left(\frac{R_E}{r} \right)^n P_{n,m}(s_\lambda) (C_{n,m} \cos(m\phi) + S_{n,m} \sin(m\phi)) \right] \quad (5.6)$$

where gravitational potential $U(\mathbf{r})$ is given by Eq. 5.6, such that μ is the universal gravitational parameter, \mathbf{r} is the position vector from a point O fixed in body E (say Earth) to a generic point Q, r denotes the magnitude of \mathbf{r} , R_E is a scaling radius for body E. $P_{n,m}$ is the associated Legendre function of the first kind, of degree n and order m , and has as its argument s_λ , the sine of λ , the latitude of Q [39, 40]. The longitude of Q is denoted by ϕ . $C_{n,m}$ and $S_{n,m}$ are unnormalized gravitational coefficients of degree n and order m [39, 40]. If point O is coincident with the mass center of E, then $C_{1,0}$, $C_{1,1}$, and $S_{1,1}$ all become zero [39, 40, 41].

5.3.2 Atmospheric Drag Model

Spacecraft in the lower altitudes (approx. 400 km or below) of the low earth orbit, experience an opposing force or drag due to the interaction with the upper atmosphere. A simplified exponentially decaying atmospheric drag model is used for this study, defined as follow [43]

$$\mathbf{a}_{aero}^I = -\frac{1}{2}\rho \left(\mathbf{r}_{CM/E}^I, \rho_r, h_s \right) \beta \left\| \mathbf{v}_{CM/E}^I \right\| \mathbf{v}_{CM/E}^I \quad (5.7)$$

$$\rho \left(\mathbf{r}_{CM/E}^I, \rho_r, h_s \right) = \rho_r e^{-\left(\frac{\|\mathbf{r}_{CM/E}^I\| - h_{ref}}{h_s} \right)} \quad (5.8)$$

$$h_{ref} = 400000 + R_E \quad (5.9)$$

where \mathbf{a}_{aero} is the aerodynamic acceleration due to atmospheric drag, at spacecraft position $\mathbf{r}_{CM/E}^I$, velocity $\mathbf{v}_{CM/E}^I$, and for ballistic coefficient β , reference atmospheric density ρ_r , and scale height h_s . Further, ρ is the atmospheric density at spacecraft position $\mathbf{r}_{CM/E}^I$, h_{ref} is the reference altitude in meters, at which reference atmospheric density ρ_r and scale height h_s have been defined, and lastly, R_E is the radius of the Earth [34, 43].

5.3.3 Solar Radiation Pressure Model

Due to the incident solar radiation, a force is exerted on the spacecraft and this is modeled based on three main factors: (1) the intensity and spectral distribution of the incident radiation, (2) the geometry of the surface and its optical properties, and (3) the orientation of the Sun vector relative to the spacecraft [43]. Here, a simple radiation model is considered, i.e., a constant solar radiation has been assumed (the Earth's albedo and the radiation emitted from the Earth and its atmosphere have been ignored) [43]. The mathematical model of the acceleration due to the solar radiation pressure on a spherical spacecraft can be defined as follows [43]

$$\mathbf{a}_{SRP}^I = -P_{flux} \left(\frac{3}{r_{sc}\rho_{sc}} \right) \left(\frac{1}{4} + \frac{1}{9}c_d \right) \hat{\mathbf{s}} \quad (5.10)$$

$$\hat{\mathbf{s}} = -\frac{\mathbf{d}_j}{\|\mathbf{d}_j\|} = -\frac{\mathbf{r} - \boldsymbol{\rho}_j}{\|\mathbf{r} - \boldsymbol{\rho}_j\|} = -\frac{\mathbf{r}_{CM/E}^I - \boldsymbol{\rho}_{Sun}}{\|\mathbf{r}_{CM/E}^I - \boldsymbol{\rho}_{Sun}\|} = \hat{\boldsymbol{\rho}}_{Sun} \quad (5.11)$$

where \mathbf{a}_{SRP} is the acceleration due to solar radiation pressure, P_{flux} is the mean momentum flux acting on a surface normal to the Sun's radiation (refer Eq. 5.12), r_{sc} is the radius of the spherical spacecraft, ρ_{sc} is the density of the spherical spacecraft, c_d denote the coefficient

of diffuse reflection, i.e. the fraction of the incident radiation that is diffusely reflected, $\hat{\mathbf{s}}$ is the unit vector from the spacecraft to the Sun (refer Figure 5.2 and Eq. 5.11), \mathbf{d}_j denote the vector from the sun to the spacecraft, $\mathbf{r}_{CM/E}^I$ is the vector from the Earth to the spacecraft, and $\boldsymbol{\rho}_j$ is the vector from the Earth to the sun [43]. The mean momentum flux is defined as follows [43]

$$P_{flux} = \frac{F_e}{c} \quad (5.12)$$

$$F_e = \frac{1358}{1.0004 + 0.0334 \cos D} W/m^2 \quad (5.13)$$

where F_e is the solar constant (modeled with $1358 W/m^2$, i.e. the mean flux at 1 AU, and the denominator is a correction for the true Earth distance), D is the "phase" of the year measured from July 4 (the day of Earth aphelion), and c is the speed of light [43]. It should be noted that the solar constant depends on the radiation wavelength and the eccentricity of the Earth's orbit about the Sun [43]. The variations in this flux (based on the above model) are always less than 0.5%, and solar radiation is largely emitted in the visible and near-infrared portions of the spectrum [43]. For this study, a constant mean momentum flux of $4.4 \times 10^{-6} kg \cdot m^{-1} \cdot s^{-2}$ has been considered (see page 130 in reference [43]).

5.3.4 Third-body Perturbation model

The perturbing acceleration (\mathbf{a}_{3rd}^I), acting on the spacecraft, due to the gravitational force of the massive space objects (Sun and Moon) can be modeled as follows [8]

$$\mathbf{a}_{3rd}^I = -Gm_{Sun} \left(\frac{\mathbf{d}_{Sun}}{\|\mathbf{d}_{Sun}\|^3} + \frac{\boldsymbol{\rho}_{Sun}}{\|\boldsymbol{\rho}_{Sun}\|^3} \right) - Gm_{Moon} \left(\frac{\mathbf{d}_{Moon}}{\|\mathbf{d}_{Moon}\|^3} + \frac{\boldsymbol{\rho}_{Moon}}{\|\boldsymbol{\rho}_{Moon}\|^3} \right) \quad (5.14)$$

Since, the vector (\mathbf{d}_j) from the Sun and Moon to the spacecraft can be defined as (refer Figure 5.2) [8]

$$\mathbf{d}_j = \mathbf{r} - \boldsymbol{\rho}_j \quad (5.15)$$

this implies

$$\begin{aligned} \mathbf{a}_{3rd}^I = & -Gm_{Sun} \left(\frac{\mathbf{r}_{CM/E}^I - \boldsymbol{\rho}_{Sun}}{\|\mathbf{r}_{CM/E}^I - \boldsymbol{\rho}_{Sun}\|^3} + \frac{\boldsymbol{\rho}_{Sun}}{\|\boldsymbol{\rho}_{Sun}\|^3} \right) \\ & -Gm_{Moon} \left(\frac{\mathbf{r}_{CM/E}^I - \boldsymbol{\rho}_{Moon}}{\|\mathbf{r}_{CM/E}^I - \boldsymbol{\rho}_{Moon}\|^3} + \frac{\boldsymbol{\rho}_{Moon}}{\|\boldsymbol{\rho}_{Moon}\|^3} \right) \end{aligned} \quad (5.16)$$

where m_{Sun} and m_{Moon} are the mass of the Sun and the Moon, and G is the universal gravitational constant.

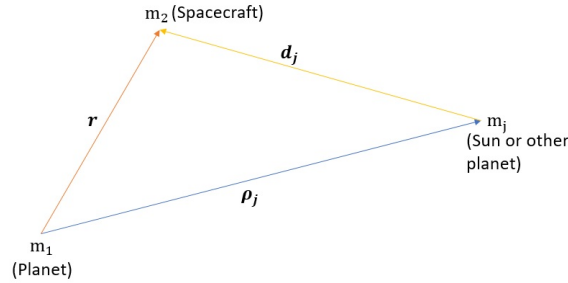


Fig. 5.2: Position vectors for n-body system [8].

5.3.5 Gravity Gradient Torque

The gravity gradient torque, due to point-mass gravitational field of the Earth, acting on the spacecraft is given as follow [43]

$$\mathbf{M}_{gg} = \frac{3\mu}{\|\mathbf{r}_{O/E}^B\|^5} \left[\mathbf{r}_{O/E}^B \times \left(\mathbf{J} \cdot \mathbf{r}_{O/E}^B \right) \right] \quad (5.17)$$

where $\mathbf{r}_{O/E}^B$ is the position vector of the spacecraft's geometric center with respect to the center of the Earth, $\mu = GM_E$ is the Earth's gravitational constant, and J is the spacecraft moment-of-inertia tensor [43]. Note that the above expression is valid only if it is assumed that the center of mass of the spacecraft coincide with its geometric center [43].

5.4 Non-Linear Dynamics Modeling

The non-linear dynamical and measurement models are presented in this section.

The dynamics for the given system can be defined as

$$\dot{\mathbf{x}} = \mathbf{f}(\mathbf{x}, t) + G\mathbf{w} \quad (5.18)$$

where \mathbf{x} is the true state vector, G is a matrix to map the noise vector to the state dynamics, and \mathbf{w} is a vector of zero-mean white noise processes. The dynamics can be segmented into three broad categories: (1) Translational dynamics, (2) Rotational dynamics, and (3) Dynamics of the uncertainties/errors (inherent to system/environmental model).

5.4.1 Translational Dynamics

The position and velocity of the spacecraft's center of mass with respect to the center of the Earth, expressed in inertial frame, are denoted as $\mathbf{r}_{CM/E}^I$ and $\mathbf{v}_{CM/E}^I$. All vectors with superscript I are coordinatized in the inertial reference frame (IRF).

Correspondingly, spacecraft dynamics can be defined as

$$\dot{\mathbf{r}}_{CM/E}^I = \mathbf{v}_{CM/E}^I \quad (5.19)$$

$$\dot{\mathbf{v}}_{CM/E}^I = \mathbf{g}_E^I(\mathbf{r}_{CM/E}^I) + \mathbf{a}_{3rd}^I(\mathbf{r}_{CM/E}^I, \boldsymbol{\rho}_{Sun}, \boldsymbol{\rho}_{Moon})$$

$$+\mathbf{a}_{aero}^I \left(\mathbf{r}_{CM/E}^I, \mathbf{v}_{CM/E}^I, \beta, \rho_r, h_s \right) + \mathbf{a}_{SRP}^I \left(\mathbf{r}_{CM/E}^I, \boldsymbol{\rho}_{Sun} \right) + \mathbf{w}_T + \mathbf{w}_{aero} \quad (5.20)$$

where $\mathbf{g}_E(\mathbf{r})$ denotes the Earth's gravitational acceleration at position $\mathbf{r}_{CM/E}^I$, and \mathbf{a}_{aero} is the aerodynamic acceleration at position $\mathbf{r}_{CM/E}^I$, velocity $\mathbf{v}_{CM/E}^I$, and for ballistic coefficient β , reference atmospheric density ρ_r , and scale height h_s . In Eq. 5.20, \mathbf{w}_T and \mathbf{w}_{aero} are the translational disturbance acceleration and unmodeled aerodynamic acceleration, modeled as zero-mean white Gaussian noise

$$E[\mathbf{w}_T(t) \mathbf{w}_T(t')^T] = Q_T \delta(t - t') \quad (5.21)$$

$$E[\mathbf{w}_{aero}(t) \mathbf{w}_{aero}(t')^T] = Q_{aero} \delta(t - t') \quad (5.22)$$

where Q_T is the strength of the translational disturbance acceleration, Q_{aero} is the strength of the unmodeled aerodynamic acceleration, and δ is the Dirac delta function. The initial position and velocity uncertainty are defined as,

$$\mathbf{r}_{CM/E}^I(t_0) \sim N(\bar{\mathbf{r}}_{CM/E}(t_0), P_{rr}(t_0)) \quad (5.23)$$

$$\mathbf{v}_{CM/E}^I(t_0) \sim N(\bar{\mathbf{v}}_{CM/E}(t_0), P_{vv}(t_0)) \quad (5.24)$$

where $P_{rr}(t_0)$ and $P_{vv}(t_0)$ are initial covariance of spacecraft's position and velocity, and $\bar{\mathbf{r}}_{CM/E}^I(t_0)$ and $\bar{\mathbf{v}}_{CM/E}^I(t_0)$ are the initial nominal position and velocity of the spacecraft.

Further, the aerodynamic acceleration \mathbf{a}_{aero}^I is modeled by Eq. 5.7, where the ballistic coefficient β is defined as follows

$$\beta = \bar{\beta} + \delta\beta \quad (5.25)$$

where $\bar{\beta}$ is the nominal value of the ballistic coefficient β , and $\delta\beta$ is a small deviation of the ballistic coefficient β from its nominal value. The dynamics of $\delta\beta$ is modeled as a 1st-order Markov process (ECRV)

$$\delta\dot{\beta} = \frac{-\delta\beta}{\tau_\beta} + w_\beta \quad (5.26)$$

$$\delta\beta(t_0) \sim N(0, \sigma_\beta^2) \quad (5.27)$$

$$E[w_\beta(t) w_\beta(t')^T] = q_\beta \delta(t - t') = \frac{2\sigma_\beta^2}{\tau_\beta} \delta(t - t') \quad (5.28)$$

where σ_β denote the steady state standard deviation of ballistic coefficient, and w_β is the unmodeled noise in the dynamics of ballistic coefficient, modeled as zero-mean white Gaussian noise with a strength denoted by q_β .

Similarly, the reference atmospheric density ρ_r is defined as follows

$$\rho_r = \bar{\rho}_r + \delta\rho_r \quad (5.29)$$

where $\bar{\rho}_r$ is the nominal value of the reference atmospheric density ρ_r , and $\delta\rho_r$ is a small deviation of the reference atmospheric density ρ_r from its nominal value. The dynamics of $\delta\rho_r$ is modeled as a 1st-order Markov process (ECRV)

$$\delta\dot{\rho}_r = \frac{-\delta\rho_r}{\tau_{\rho_r}} + w_{\rho_r} \quad (5.30)$$

$$\delta\rho_r(t_0) \sim N(0, \sigma_{\rho_r}^2) \quad (5.31)$$

$$E[w_{\rho_r}(t) w_{\rho_r}(t')^T] = q_{\rho_r} \delta(t - t') = \frac{2\sigma_{\rho_r}^2}{\tau_{\rho_r}} \delta(t - t') \quad (5.32)$$

where σ_{ρ_r} denote the steady state standard deviation of reference atmospheric density, and w_{ρ_r} is the unmodeled noise in the dynamics of reference atmospheric density, modeled as zero-mean white Gaussian noise with a strength denoted by q_{ρ_r} .

Lastly, the scale height h_s is defined as follows

$$h_s = \bar{h}_s + \delta h_s \quad (5.33)$$

where \bar{h}_s is the nominal value of the scale height h_s , and δh_s is a small deviation of the scale height h_s from its nominal value. The dynamics of δh_s is modeled as a 1st-order Markov process (ECRV)

$$\delta \dot{h}_s = \frac{-\delta h_s}{\tau_{h_s}} + w_{h_s} \quad (5.34)$$

$$\delta h_s(t_0) \sim N(0, \sigma_{h_s}^2) \quad (5.35)$$

$$E[w_{h_s}(t) w_{h_s}(t')^T] = q_{h_s} \delta(t - t') = \frac{2\sigma_{h_s}^2}{\tau_{h_s}} \delta(t - t') \quad (5.36)$$

where σ_{h_s} denote the steady state standard deviation of scale height, and w_{h_s} is the unmodeled noise in the dynamics of scale height, modeled as zero-mean white Gaussian noise with a strength denoted by q_{h_s} .

5.4.2 Rotational Dynamics

The quaternion representing the orientation of the spacecraft body-fixed reference frame (SBRF) with respect to the inertial reference frame (IRF) is defined as $\mathbf{q}_{I \rightarrow B}$, and the corresponding kinematics are defined as [31]

$$\dot{\mathbf{q}}_{I \rightarrow B} = \frac{1}{2} \boldsymbol{\omega}_{B/I}^B \otimes \mathbf{q}_{I \rightarrow B} \quad (5.37)$$

where $\boldsymbol{\omega}_{B/I}^B$ is the angular velocity of the spacecraft with respect to the inertial frame, expressed in spacecraft-fixed body frame. Correspondingly, the spacecraft's angular acceleration is defined as [31]

$$\dot{\boldsymbol{\omega}}_{B/I}^B = J^{-1} \left[\mathbf{M}_{gg} \left(\mathbf{r}_{CM/E}^I, \mathbf{q}_{I \rightarrow B} \right) - \boldsymbol{\omega}_{B/I}^B \times \left(J \boldsymbol{\omega}_{B/I}^B \right) \right] + \mathbf{w}_R \quad (5.38)$$

where J is the moment of inertia of the spacecraft, and \mathbf{M}_{gg} is the gravity gradient torque. In Eq. 5.38, \mathbf{w}_R is the rotational disturbance acceleration, modeled as zero-mean white Gaussian noise

$$E[\mathbf{w}_R(t) \mathbf{w}_R(t')^T] = Q_R \delta(t - t') \quad (5.39)$$

where Q_R is the strength of the rotational disturbance acceleration. Further, the initial uncertainty in spacecraft's quaternion is modeled as [31]

$$\mathbf{q}_{I \rightarrow B}(t_0) = \delta \mathbf{q}(\boldsymbol{\theta}) \otimes \bar{\mathbf{q}}_{I \rightarrow B}(t_0) \quad (5.40)$$

where $\delta \mathbf{q}(\boldsymbol{\theta})$ is the quaternion representing any small rotation, $\boldsymbol{\theta}$ is the incremental rotation vector of the spacecraft, and $\bar{\mathbf{q}}_{I \rightarrow B}(t_0)$ is the reference quaternion at initial time. Further, the initial uncertainty in spacecraft's rotation vector and angular velocity are modeled as

$$\boldsymbol{\theta}(t_0) \sim N(\mathbf{0}_{3 \times 1}, P_{\boldsymbol{\theta}\boldsymbol{\theta}}(t_0)) \quad (5.41)$$

$$\boldsymbol{\omega}_{B/I}^B(t_0) \sim N\left(\bar{\boldsymbol{\omega}}_{B/I}^B(t_0), P_{\boldsymbol{\omega}\boldsymbol{\omega}}(t_0)\right) \quad (5.42)$$

where $\boldsymbol{\theta}(t_0)$ and $\boldsymbol{\omega}_{B/I}^B(t_0)$ are the initial nominal spacecraft's rotation vector and angular velocity, and $P_{\boldsymbol{\theta}\boldsymbol{\theta}}(t_0)$ and $P_{\boldsymbol{\omega}\boldsymbol{\omega}}(t_0)$ are the initial covariance of the spacecraft's rotation vector and angular velocity, respectively.

The convention used in this document for quaternion is that the first three elements are known as the vector component, whereas the fourth element is the scalar component.

5.4.3 Instrument Error Dynamics

The center of mass position $\mathbf{r}_{CM/O}^B$, with respect to the spacecraft fixed body frame, can also be defined as a 1st-order Markov process (ECRV)

$$\dot{\mathbf{r}}_{CM/O}^B = \frac{-\mathbf{r}_{CM/O}^B}{\tau_{\mathbf{r}_{CM/O}}} + \mathbf{w}_{\mathbf{r}_{CM/O}} \quad (5.43)$$

$$\mathbf{r}_{CM/O}^B(t_0) \sim N\left(\mathbf{0}_{3 \times 1}, \sigma_{\mathbf{r}_{CM/O}}^2 I_{3 \times 3}\right) \quad (5.44)$$

$$E[\mathbf{w}_{\mathbf{r}_{CM/O}}(t) \mathbf{w}_{\mathbf{r}_{CM/O}}(t')^T] = q_{\mathbf{r}_{CM/O}} \delta(t - t') I_{3 \times 3} \quad (5.45)$$

$$q_{\mathbf{r}_{CM/O}} = \frac{2\sigma_{\mathbf{r}_{CM/O}}^2}{\tau_{\mathbf{r}_{CM/O}}} \quad (5.46)$$

where $\sigma_{\mathbf{r}_{CM/O}}$ denotes the steady state standard deviation of center of mass position, and $\mathbf{w}_{\mathbf{r}_{CM/O}}$ is the unmodeled noise in the center of mass position, modeled as zero-mean white Gaussian noise with a strength denoted by $q_{\mathbf{r}_{CM/O}}$.

Similarly, the accelerometer position $\mathbf{r}_{a_i/O}^B$, with respect to the spacecraft fixed body frame, can be defined as follow

$$\mathbf{r}_{a_i/O}^B = \bar{\mathbf{r}}_{a_i/O}^B + \delta\mathbf{r}_{a_i/O}^B \quad (5.47)$$

where $\bar{\mathbf{r}}_{a_i/O}^B$ is the nominal value of the accelerometer position $\mathbf{r}_{a_i/O}^B$, and $\delta\mathbf{r}_{a_i/O}^B$ is a small deviation of the accelerometer position $\mathbf{r}_{a_i/O}^B$ from its nominal value. The dynamics of $\delta\mathbf{r}_{a_i/O}^B$ is modeled as a 1st-order Markov process (ECRV)

$$\delta\dot{\mathbf{r}}_{a_i/O}^B = \frac{-\delta\mathbf{r}_{a_i/O}^B}{\tau_{\mathbf{r}_{a_i/O}^B}} + \mathbf{w}_{\mathbf{r}_{a_i/O}^B} \quad (5.48)$$

$$\delta\mathbf{r}_{a_i/O}^B(t_0) \sim N(\mathbf{0}_{3 \times 1}, \sigma_{\mathbf{r}_{a_i/O}^B}^2 I_{3 \times 3}) \quad (5.49)$$

$$E[\mathbf{w}_{\mathbf{r}_{a_i/O}^B}(t) \mathbf{w}_{\mathbf{r}_{a_i/O}^B}(t')^T] = q_{\mathbf{r}_{a_i/O}^B} \delta(t - t') I_{3 \times 3} \quad (5.50)$$

$$q_{\mathbf{r}_{a_i/O}^B} = \frac{2\sigma_{\mathbf{r}_{a_i/O}^B}^2}{\tau_{\mathbf{r}_{a_i/O}^B}} \quad (5.51)$$

where $\sigma_{\mathbf{r}_{a_i/O}^B}$ denotes the steady state standard deviation of accelerometer position, and $\mathbf{w}_{\mathbf{r}_{a_i/O}^B}$ is the unmodeled noise in the accelerometer position, modeled as zero-mean white Gaussian noise with a strength denoted by $q_{\mathbf{r}_{a_i/O}^B}$.

Similarly, the accelerometer measurement bias $\mathbf{b}_i^{\tilde{a}_i}$ can be defined as a 1st-order Markov process (ECRV)

$$\dot{\mathbf{b}}_i^{\tilde{a}_i} = \frac{-\mathbf{b}_i^{\tilde{a}_i}}{\tau_{\mathbf{b}_i^{\tilde{a}_i}}} + \mathbf{w}_{\mathbf{b}_i^{\tilde{a}_i}} \quad (5.52)$$

$$\mathbf{b}_i^{\tilde{a}_i}(t_0) \sim N(\mathbf{0}_{3 \times 1}, \sigma_{\mathbf{b}_i^{\tilde{a}_i}}^2 I_{3 \times 3}) \quad (5.53)$$

$$E[\mathbf{w}_{\mathbf{b}_i^{\tilde{a}_i}}(t) \mathbf{w}_{\mathbf{b}_i^{\tilde{a}_i}}(t')^T] = q_{\mathbf{b}_i^{\tilde{a}_i}} \delta(t - t') I_{3 \times 3} \quad (5.54)$$

$$q_{\mathbf{b}_i^{\tilde{a}_i}} = \frac{2\sigma_{\mathbf{b}_i^{\tilde{a}_i}}^2}{\tau_{\mathbf{b}_i^{\tilde{a}_i}}} \quad (5.55)$$

where $\sigma_{\mathbf{b}_i}$ denotes the steady state standard deviation of accelerometer measurement bias, and $\mathbf{w}_{\mathbf{b}_i}$ is the unmodeled noise in the accelerometer measurement bias, modeled as zero-mean white Gaussian noise with a strength denoted by $q_{\mathbf{b}_i}$. All vectors with superscript \tilde{a}_i are coordinatized in the actual i^{th} accelerometer frame, and the subscript i represents the i^{th} accelerometer.

Similarly, the accelerometer measurement scale-factor $\mathbf{f}_i^{\tilde{a}_i}$ can be defined as a 1st-order Markov process (ECRV)

$$\dot{\mathbf{f}}_i^{\tilde{a}_i} = \frac{-\mathbf{f}_i^{\tilde{a}_i}}{\tau_{\mathbf{f}_i}} + \mathbf{w}_{\mathbf{f}_i} \quad (5.56)$$

$$\mathbf{f}_i^{\tilde{a}_i}(t_0) \sim N(\mathbf{0}_{3 \times 1}, \sigma_{\mathbf{f}_i}^2 I_{3 \times 3}) \quad (5.57)$$

$$E[\mathbf{w}_{\mathbf{f}_i}(t) \mathbf{w}_{\mathbf{f}_i}(t')^T] = q_{\mathbf{f}_i} \delta(t - t') I_{3 \times 3} \quad (5.58)$$

$$q_{\mathbf{f}_i} = \frac{2\sigma_{\mathbf{f}_i}^2}{\tau_{\mathbf{f}_i}} \quad (5.59)$$

where $\sigma_{\mathbf{f}_i}$ denotes the steady state standard deviation of accelerometer measurement scale-factor, and $\mathbf{w}_{\mathbf{f}_i}$ is the unmodeled noise in the accelerometer measurement scale-factor, modeled as zero-mean white Gaussian noise with a strength denoted by $q_{\mathbf{f}_i}$.

Lastly, the accelerometer misalignment $\epsilon_i^{\tilde{a}_i}$ can be defined as a 1st-order Markov process (ECRV)

$$\dot{\epsilon}_i^{\tilde{a}_i} = \frac{-\epsilon_i^{\tilde{a}_i}}{\tau_{\epsilon_i}} + \mathbf{w}_{\epsilon_i} \quad (5.60)$$

$$\epsilon_i^{\tilde{a}_i}(t_0) \sim N(\mathbf{0}_{3 \times 1}, \sigma_{\epsilon_i}^2 I_{3 \times 3}) \quad (5.61)$$

$$E[\mathbf{w}_{\epsilon_i}(t) \mathbf{w}_{\epsilon_i}(t')^T] = q_{\epsilon_i} \delta(t - t') I_{3 \times 3} \quad (5.62)$$

$$q_{\epsilon_i} = \frac{2\sigma_{\epsilon_i}^2}{\tau_{\epsilon_i}} \quad (5.63)$$

where σ_{ϵ_i} denotes the steady state standard deviation of accelerometer misalignment, and \mathbf{w}_{ϵ_i} is the unmodeled noise in the accelerometer misalignment, modeled as zero-mean white Gaussian noise with a strength denoted by q_{ϵ_i} .

5.5 Nonlinear Measurement Modeling

The accelerometer measurements for a system can be generically defined as

$$\tilde{a}_i^{\tilde{a}_i} = \mathbf{h}(\mathbf{x}) + \boldsymbol{\eta}_i^{\tilde{a}_i} \quad (5.64)$$

where \mathbf{x} is the true state vector, $\mathbf{h}(\cdot)$ is a non-linear function which maps state vector to the accelerometer measurements, and $\boldsymbol{\eta}_i^{\tilde{a}_i}$ is a vector of zero-mean white Gaussian noise on the accelerometer measurements. In this document, the subscript i represents the quantities/vectors related to the i^{th} accelerometer, and the superscript I, B, and \tilde{a}_i denote the vectors coordinatized in the inertial reference frame (IRF), spacecraft body-fixed reference frame (SBRF), and accelerometer actual reference frame (AARF), respectively.

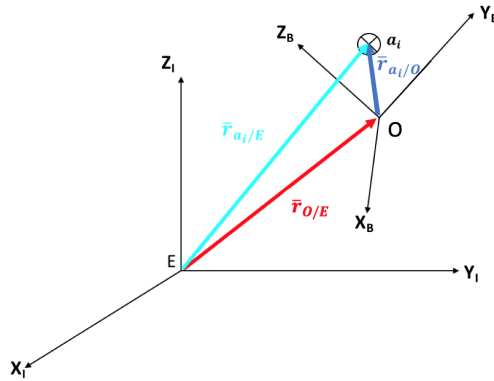


Fig. 5.3: Spacecraft's center of mass position vector relative to inertial reference frame (IRF) and spacecraft body-fixed reference frame (SBRF) .

According to Figure 5.3, the position of the i^{th} accelerometer, with respect to the center of the Earth, can be defined as follow

$$\mathbf{r}_{a_i/E} = \mathbf{r}_{O/E} + \mathbf{r}_{a_i/O} \quad (5.65)$$

where $\mathbf{r}_{a_i/E}$ is the position of the i^{th} accelerometer with respect to the center of the Earth, $\mathbf{r}_{O/E}$ is the position of the origin of the spacecraft body-fixed reference frame with respect to the center of the Earth, and $\mathbf{r}_{a_i/O}$ is the position of the i^{th} accelerometer with respect to the origin of the spacecraft body-fixed reference frame. On differentiating Eq. 5.65,

$$\mathbf{v}_{a_i/E} = \dot{\mathbf{r}}_{a_i/E} = \dot{\mathbf{r}}_{O/E} + \dot{\mathbf{r}}_{a_i/O} \quad (5.66)$$

where $\mathbf{v}_{a_i/E}$ is the velocity of the i^{th} accelerometer with respect to the center of the Earth, and the derivatives on the right hand side of Eq. 5.66 are calculated from the view point of an observer in the inertial reference frame. Now using the transport theorem, the relationship between the time derivatives of $\mathbf{r}_{a_i/O}$ from the view point of an observer in the inertial reference frame and the spacecraft body-fixed reference frame, is given as follow

$$\dot{\mathbf{r}}_{a_i/O} = (\dot{\mathbf{r}}_{a_i/O})_{rel} + \boldsymbol{\omega}_{B/I} \times \mathbf{r}_{a_i/O} \quad (5.67)$$

where $\boldsymbol{\omega}_{B/I}$ is the angular velocity of the spacecraft body-fixed reference frame with respect to the inertial frame. Substituting the result from Eq. 5.67 in the Eq. 5.66, gives

$$\mathbf{v}_{a_i/E} = \dot{\mathbf{r}}_{a_i/E} = \dot{\mathbf{r}}_{O/E} + (\dot{\mathbf{r}}_{a_i/O})_{rel} + \boldsymbol{\omega}_{B/I} \times \mathbf{r}_{a_i/O} \quad (5.68)$$

Now differentiating Eq. 5.68, from the view point of an observer in the inertial reference frame, and using transport theorem again, gives

$$\ddot{\mathbf{r}}_{a_i/E} = \ddot{\mathbf{r}}_{O/E} + (\ddot{\mathbf{r}}_{a_i/O})_{rel} + 2\boldsymbol{\omega}_{B/I} \times (\dot{\mathbf{r}}_{a_i/O})_{rel} + \dot{\boldsymbol{\omega}}_{B/I} \times \mathbf{r}_{a_i/O} + \boldsymbol{\omega}_{B/I} \times (\boldsymbol{\omega}_{B/I} \times \mathbf{r}_{a_i/O}) \quad (5.69)$$

Now assuming that the origin O of the spacecraft body-fixed reference frame is fixed to the spacecraft's center of mass CM , then the inertial acceleration of the i^{th} accelerometer is given as follow

$$\ddot{\mathbf{r}}_{a_i/E} = \ddot{\mathbf{r}}_{CM/E} + \left(\ddot{\mathbf{r}}_{a_i/CM}\right)_{rel} + 2\boldsymbol{\omega}_{B/I} \times \left(\dot{\mathbf{r}}_{a_i/CM}\right)_{rel} + \dot{\boldsymbol{\omega}}_{B/I} \times \mathbf{r}_{a_i/CM} + \boldsymbol{\omega}_{B/I} \times (\boldsymbol{\omega}_{B/I} \times \mathbf{r}_{a_i/CM}) \quad (5.70)$$

An electrostatic accelerometer is designed to detect the difference between the acceleration of center of mass of the spacecraft, and that of the proof mass of the i^{th} accelerometer, by measuring the electrostatic force required to keep the proof mass in the center of the accelerometer. Using Eq. 5.70, the acceleration of the proof mass $\mathbf{a}_{p_i}^I$ of the i^{th} accelerometer, expressed in the inertial reference frame, can be given as

$$\begin{aligned} \mathbf{a}_{p_i}^I = \ddot{\mathbf{r}}_{a_i/E} = \ddot{\mathbf{r}}_{CM/E}^I + \left(\ddot{\mathbf{r}}_{a_i/CM}^I\right)_{rel} + 2\boldsymbol{\omega}_{B/I}^I \times \left(\dot{\mathbf{r}}_{a_i/CM}^I\right)_{rel} \\ + \dot{\boldsymbol{\omega}}_{B/I}^I \times \mathbf{r}_{a_i/CM}^I + \boldsymbol{\omega}_{B/I}^I \times \left(\boldsymbol{\omega}_{B/I}^I \times \mathbf{r}_{a_i/CM}^I\right) \end{aligned} \quad (5.71)$$

where $\mathbf{a}_{p_i}^I$ is the acceleration of the i^{th} accelerometer' proof mass, $\ddot{\mathbf{r}}_{CM/E}^I$ is the acceleration of the spacecraft, $\left(\ddot{\mathbf{r}}_{a_i/CM}^I\right)_{rel}$ is the acceleration of the i^{th} accelerometer' proof mass with respect to the spacecraft, as viewed relative to the rotating spacecraft body-fixed reference frame, $\left(\dot{\mathbf{r}}_{a_i/CM}^I\right)_{rel}$ denotes the velocity of the i^{th} accelerometer' proof mass with respect to the spacecraft, as viewed relative to the rotating spacecraft body-fixed reference frame, and $\mathbf{r}_{a_i/CM}^I$ is the position of the i^{th} accelerometer' proof mass with respect to the spacecraft.

Using Newton's second law

$$\mathbf{F}_v^I = m_v \ddot{\mathbf{r}}_{CM/E}^I \quad (5.72)$$

$$\mathbf{F}_{p_i}^I = m_{p_i} \mathbf{a}_{p_i}^I \quad (5.73)$$

where \mathbf{F}_v^I is the total force acting on the spacecraft, m_v is mass of the spacecraft, $\mathbf{F}_{p_i}^I$ is the total force acting on the i^{th} accelerometer' proof mass, and m_{p_i} is mass of the i^{th} accelerometer' proof mass.

Force analysis of the i^{th} accelerometer' proof mass yields

$$\mathbf{F}_{p_i} = \mathbf{F}_{g_{p_i}} + \mathbf{F}_{emf_i} \quad (5.74)$$

where $\mathbf{F}_{g_{p_i}}$ is the force acting on the i^{th} accelerometer' proof mass due to gravitational field, and \mathbf{F}_{emf_i} is the electro-motive force acting on the i^{th} accelerometer' proof-mass, to keep the proof mass at the center of the accelerometer frame.

Force analysis of the vehicle yields

$$\mathbf{F}_v = \mathbf{F}_{g_v} + \mathbf{N} - \mathbf{F}_{emf_i} \quad (5.75)$$

where \mathbf{F}_{g_v} is the force acting on the spacecraft due to gravitational field, \mathbf{N} is the force acting on the spacecraft due to non-gravitational forces, like atmospheric drag, and \mathbf{F}_{emf_i} is the equal and opposite electro-motive force acting on the spacecraft.

Using free body analysis of the vehicle and i^{th} accelerometer' proof mass, the acceleration of the spacecraft and the acceleration of the i^{th} accelerometer' proof mass can be expressed as below

$$\mathbf{a}_v^I = \mathbf{g}^I(\mathbf{r}_{CM/E}^I) + \frac{\mathbf{N}^I(\mathbf{r}_{CM/E}^I, \mathbf{v}_{CM/E}^I, \beta, \rho_r, h_s)}{m_v} - \frac{\mathbf{F}_{emf_i}^I}{m_v} \quad (5.76)$$

$$\mathbf{a}_{p_i}^I = \mathbf{g}^I(\mathbf{r}_{CM/E}^I + \mathbf{r}_{a_i/CM}^I) + \frac{\mathbf{F}_{emf_i}^I}{m_{p_i}} \quad (5.77)$$

where $\mathbf{r}_{CM/E}^I$ is the inertial position of the spacecraft, $\mathbf{v}_{CM/E}^I$ is the inertial velocity of the spacecraft, $\mathbf{g}^I(\mathbf{r}_{CM/E}^I)$ is the gravitational acceleration at the position $\mathbf{r}_{CM/E}^I$, and

$\mathbf{g}^I \left(\mathbf{r}_{CM/E}^I + \mathbf{r}_{a_i/CM}^I \right)$ is the gravitational acceleration at the position $\left(\mathbf{r}_{CM/E}^I + \mathbf{r}_{a_i/CM}^I \right)$. Further,

$$\mathbf{r}_{CM/E}^I + \mathbf{r}_{a_i/CM}^I = \mathbf{r}_{a_i/E}^I \quad (5.78)$$

where $\mathbf{r}_{a_i/E}^I$ is the inertial position of the i^{th} accelerometer's proof mass.

The difference between the acceleration of center of mass of the spacecraft, and that of the proof mass of the i^{th} accelerometer is defined as the detected acceleration, and is denoted by $\mathbf{a}_{d_i}^I$. The detected acceleration is equal to the sum of all non-gravitational accelerations acting on the proof mass. Thus using Eq. 5.77 and Eq. 5.78, the detected acceleration is given as

$$\mathbf{a}_{d_i}^I = \frac{\mathbf{F}_{emf_i}^I}{m_{p_i}} = \mathbf{a}_{p_i}^I - \mathbf{g}^I \left(\mathbf{r}_{a_i/E}^I \right) \quad (5.79)$$

To re-state this rigorously, substituting Eqs. 5.76-5.78 in Eq. 5.71, and noting that the detected acceleration measurement is proportional to $\mathbf{F}_{emf_i}^I \left(\frac{1}{m_{p_i}} + \frac{1}{m_v} \right)$, the detected acceleration is given as

$$\begin{aligned} \mathbf{a}_{d_i}^I &= \mathbf{F}_{emf_i}^I \left(\frac{1}{m_{p_i}} + \frac{1}{m_v} \right) = \mathbf{g}^I \left(\mathbf{r}_{CM/E}^I \right) - \mathbf{g}^I \left(\mathbf{r}_{a_i/E}^I \right) + \\ &\mathbf{N}^I \left(\mathbf{r}_{CM/E}^I, \mathbf{v}_{CM/E}^I, \beta, \rho_r, h_s \right) + \boldsymbol{\omega}_{B/I}^I \times \left(\boldsymbol{\omega}_{B/I}^I \times \mathbf{r}_{a_i/CM}^I \right) + \\ &\boldsymbol{\omega}_{B/I}^I \times \mathbf{r}_{a_i/CM}^I + 2\boldsymbol{\omega}_{B/I}^I \times \left(\dot{\mathbf{r}}_{a_i/CM}^I \right)_{rel} + \left(\ddot{\mathbf{r}}_{a_i/CM}^I \right)_{rel} \end{aligned} \quad (5.80)$$

Since, quantities like position, velocity, and acceleration of the i^{th} accelerometer's proof mass, and the spacecraft angular velocity are traditionally measured in spacecraft body-fixed

reference frame (SBRF), these terms are transformed using a transformation matrix from SBRF to IRF.

$$\begin{aligned}
\mathbf{a}_{d_i}^I &= \mathbf{g}^I \left(\mathbf{r}_{CM/E}^I \right) - \mathbf{g}^I \left(\mathbf{r}_{a_i/E}^I \right) + \mathbf{N}^I \left(\mathbf{r}_{CM/E}^I, \mathbf{v}_{CM/E}^I, \beta, \rho_r, h_s \right) \\
&+ T_{B \rightarrow I} \left[\boldsymbol{\omega}_{B/I}^B \times \left(\boldsymbol{\omega}_{B/I}^B \times \mathbf{r}_{a_i/CM}^B \right) \right] + T_{B \rightarrow I} \left[\dot{\boldsymbol{\omega}}_{B/I}^B \times \mathbf{r}_{a_i/CM}^B \right] \\
&+ 2T_{B \rightarrow I} \left[\boldsymbol{\omega}_{B/I}^B \times \dot{\mathbf{r}}_{a_i/CM}^B \right] + T_{B \rightarrow I} \left[\ddot{\mathbf{r}}_{a_i/CM}^B \right]
\end{aligned} \tag{5.81}$$

where $\mathbf{g} \left(\mathbf{r}_{CM/E}^I \right)$ denotes the total gravitational acceleration at position $\mathbf{r}_{CM/E}^I$, and \mathbf{N} denotes the non-gravitational acceleration (includes acceleration due to atmospheric drag and solar radiation pressure) as a function of spacecraft position $\mathbf{r}_{CM/E}^I$, velocity $\mathbf{v}_{CM/E}^I$, ballistic coefficient β , reference atmospheric density ρ_r , and scale height h_s .

For this measurement model, Eq. 5.64 is expanded and, the accelerometer measurements are given by the detected acceleration in the accelerometer frame $\mathbf{a}_{d_i}^{\tilde{a}_i}$ plus errors due to bias and noise

$$\tilde{a}_i^{\tilde{a}_i} = \mathbf{a}_{d_i}^{\tilde{a}_i} + \mathbf{b}_i^{\tilde{a}_i} + \boldsymbol{\eta}_i^{\tilde{a}_i} \tag{5.82}$$

where $\boldsymbol{\eta}_i^{\tilde{a}_i}$ is the accelerometer measurement noise modeled as zero-mean white Gaussian noise with a strength denoted by $Q_{\boldsymbol{\eta}_i}$, such that

$$E[\boldsymbol{\eta}_i^{\tilde{a}_i}(t) \boldsymbol{\eta}_i^{\tilde{a}_i}(t')^T] = Q_{\boldsymbol{\eta}_i} \delta(t - t') \tag{5.83}$$

This means that if the accelerometer measurement noise resolution is $\boldsymbol{\eta}_i^{\tilde{a}_i} \left(\frac{m}{s^2 \sqrt{Hz}} \right)$, then the power spectral density of the accelerometer noise can be defined as $Q_{\boldsymbol{\eta}_i} \left(\frac{m^2}{s^4 Hz} \text{ or } \frac{m^2}{s^3 2\pi rad} \right)$

Thus, the measurement covariance $R \left(\frac{m^2}{s^4 2\pi rad} \right)$ is given as

$$R = \frac{Q_{\eta_i}}{\delta t_{meas}} \quad (5.84)$$

where δt_{meas} is measurement update time in seconds. All vectors with superscript \tilde{a}_i are coordinatized in the actual i^{th} accelerometer frame. In Eq. 5.82, $\mathbf{a}_{d_i}^{\tilde{a}_i}$ denotes the detected acceleration in the accelerometer frame, defined as

$$\mathbf{a}_{d_i}^{\tilde{a}_i} = \left[I + D \left(\mathbf{f}_i^{\tilde{a}_i} \right) \right] T_{a_i^N \rightarrow \tilde{a}_i} T_{B \rightarrow a_i^N} T_{I \rightarrow B} \left[\mathbf{a}_{d_i}^I \right] \quad (5.85)$$

where $D \left(\mathbf{f}_i^{\tilde{a}_i} \right)$ denotes the matrix with accelerometer measurement scale-factors on the diagonal. All vectors with superscript a_i^N are coordinatized in the nominal i^{th} accelerometer frame. The nominal i^{th} accelerometer frame and the actual i^{th} accelerometer frame are different because of the inherent misalignments that occur while setting up the accelerometer in the spacecraft frame. These accelerometer misalignments $\left(\boldsymbol{\epsilon}_i^{\tilde{a}_i} \right)$ are accounted for by defining the following small angle rotation

$$T_{a_i^N \rightarrow \tilde{a}_i} = I - \left[\boldsymbol{\epsilon}_i^{\tilde{a}_i} \times \right] \quad (5.86)$$

It can be noted that with reasonable assumptions of nearly constant spacecraft angular velocity and a rigid body spacecraft with accelerometers firmly fixed to the spacecraft structure, the last three terms in Eq. 5.81 are very small and can be absorbed into the bias and noise terms in Eq. 5.82.

Further, using vector algebra (refer Figure 5.4), the relationship between accelerometer position $\left(\mathbf{r}_{a_i/E}^I \right)$ with respect to the center of the Earth, expressed in inertial frame, and accelerometer position $\left(\mathbf{r}_{a_i/CM}^B \right)$ with respect to the spacecraft center of mass, expressed in spacecraft fixed body frame, can be written as

$$\mathbf{r}_{a_i/E}^I = \mathbf{r}_{CM/E}^I + T_{I \rightarrow B}^T \left[\mathbf{r}_{a_i/CM}^B \right] \quad (5.87)$$

where accelerometer position $\left(\mathbf{r}_{a_i/CM}^B\right)$ with respect to the spacecraft center of mass, expressed in spacecraft fixed body frame, is given as

$$\mathbf{r}_{a_i/CM}^B = \mathbf{r}_{a_i/O}^B - \mathbf{r}_{CM/O}^B \quad (5.88)$$

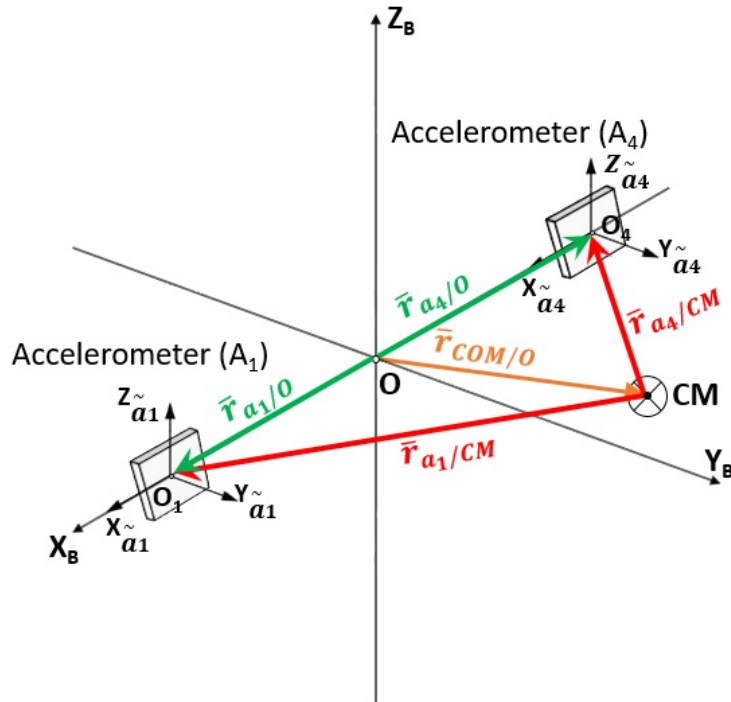


Fig. 5.4: Schematic Model (only 2 of the 6 accelerometer are shown)[6].

Now using Eq. 5.86 in Eq. 5.85 , gives

$$\mathbf{a}_{d_i}^{\tilde{a}_i} = \left[I + D \left(\mathbf{f}_i^{\tilde{a}_i} \right) \right] \left(I - \left[\boldsymbol{\epsilon}_i^{\tilde{a}_i} \times \right] \right) T_{B \rightarrow a_i^N} T_{I \rightarrow B} \left[\mathbf{a}_{d_i}^I \right] \quad (5.89)$$

where the detected acceleration $\left(\mathbf{a}_{d_i}^I\right)$, in the inertial frame, can be rewritten using Eqs. 5.87-5.88 and ignoring the linear acceleration $\left(\dot{\boldsymbol{\omega}}_{B/I}^B \times \mathbf{r}_{a_i/CM}^B\right)$, Coriolis acceleration $\left(2\bar{\boldsymbol{\omega}}_{B/I}^B \times \dot{\mathbf{r}}_{a_i/CM}^B\right)$, and acceleration with respect to the spacecraft $\left(\ddot{\mathbf{r}}_{a_i/CM}^B\right)$

$$\begin{aligned} \mathbf{a}_{d_i}^I = & \mathbf{g}^I \left(\mathbf{r}_{CM/E}^I \right) - \mathbf{g}^I \left(\mathbf{r}_{CM/E}^I + T_{B \rightarrow I} \left[\mathbf{r}_{a_i/O}^B - \mathbf{r}_{CM/O}^B \right] \right) + \mathbf{a}_{aero}^I \left(\mathbf{r}_{CM/E}^I, \mathbf{v}_{CM/E}^I, \beta, \rho_r, h_s \right) \\ & + \mathbf{a}_{SRP}^I \left(\mathbf{r}_{CM/E}^I, \boldsymbol{\rho}_{Sun} \right) + T_{B \rightarrow I} \left\{ \boldsymbol{\omega}_{B/I}^B \times \left(\boldsymbol{\omega}_{B/I}^B \times \left[\mathbf{r}_{a_i/O}^B - \mathbf{r}_{CM/O}^B \right] \right) \right\} \end{aligned} \quad (5.90)$$

This provides the necessary relationship between the measurement \tilde{a}_i and the state \mathbf{x} .

Measurements from an on-board star camera are used to improve the estimation of the states and thereby enhance the overall fidelity of the navigation system. The star camera measurements \tilde{s} are generically defined as

$$\tilde{s}^{\tilde{s}} = \mathbf{l}(\mathbf{x}) + \boldsymbol{\eta}_{sc}^{\tilde{s}} \quad (5.91)$$

where superscript \tilde{s} denotes the vectors coordinatized in the actual star-camera reference frame (ASRF), \mathbf{x} is the true state vector, $\mathbf{l}(\cdot)$ is a non-linear function which maps state vector to the star camera measurements, and $\boldsymbol{\eta}_{sc}^{\tilde{s}}$ is a vector of zero-mean white Gaussian noise on the star camera measurements with the covariance of the noise denoted by $Q_{\boldsymbol{\eta}_{sc}}$ (rad^2), such that

$$E[\boldsymbol{\eta}_{sc,i}^{\tilde{s}} \boldsymbol{\eta}_{sc,j}^{\tilde{s}T}] = Q_{\boldsymbol{\eta}_{sc}} \delta_{ij} \quad (5.92)$$

where δ_{ij} is a Kronecker delta function.

The star camera measurements \tilde{s} are modeled as

$$\tilde{s}^{\tilde{s}} = T_{B \rightarrow \tilde{s}} \boldsymbol{\theta}_{I \rightarrow B} + \boldsymbol{\eta}_{sc}^{\tilde{s}} \quad (5.93)$$

where $T_{B \rightarrow \tilde{s}}$ is the transformation matrix from spacecraft body-fixed reference frame (SBRF) to the actual star-camera reference frame (ASRF) and $\boldsymbol{\theta}_{I \rightarrow B}$ is the true orientation of the

spacecraft body-fixed reference frame (SBRF) with respect to the inertial reference frame (IRF).

For this study, actual star-camera reference frame (ASRF) is aligned with the spacecraft body-fixed reference frame (SBRF). This means that the misalignments in the setting up of the star camera on the rigid body of the spacecraft have been ignored. Thus, $T_{B \rightarrow \bar{s}}$ is a 3×3 identity matrix.

5.6 Linear Dynamics Modeling

In this section, the aforementioned non-linear models and equations are linearized about the reference state vector ($\bar{\mathbf{x}}$) so as to formulate the linear covariance model for the given system. Note that for formulating an Extended Kalman Filter, linearization needs to be done about the estimated state vector ($\hat{\mathbf{x}}$). All the nominal values are decorated with an over-bar.

Also note that the state vector is “modified” to formulate the linear model. [44] The 4-dimensional quaternion state $\mathbf{q}_{I \rightarrow B}$ is replaced by the 3-dimensional rotation vector $\boldsymbol{\theta}_{I \rightarrow B}$ and the quaternion kinematics are replaced by the Bortz equation, given as [45]

$$\dot{\boldsymbol{\theta}} = \boldsymbol{\omega} + \frac{1}{2} \boldsymbol{\theta} \times \boldsymbol{\omega} + \frac{1}{\|\boldsymbol{\theta}\|} \left[1 - \frac{\|\boldsymbol{\theta}\| \sin \|\boldsymbol{\theta}\|}{2(1 - \cos \|\boldsymbol{\theta}\|)} \right] \boldsymbol{\theta} \times (\boldsymbol{\theta} \times \boldsymbol{\omega}) \quad (5.94)$$

Linearization of the rotational dynamics is presented in detail in Section 1.5.2, respectively.

5.6.1 Linearized Translational Dynamics

The linearized dynamics of the spacecraft position in inertial frame ($\mathbf{r}_{CM/E}^I$) is given as

$$\delta \dot{\mathbf{r}}_{CM/E}^I = \delta \mathbf{v}_{CM/E}^I \quad (5.95)$$

Discretized form of Eq. 5.95 is given as

$$\delta \mathbf{r}_{CM/E,k+1}^I = \delta \mathbf{r}_{CM/E,k}^I + \delta \mathbf{v}_{CM/E,k}^I \Delta t \quad (5.96)$$

where subscript k denote the state at a particular discrete time-step and Δt is the discretization time step.

The linearized dynamics of the spacecraft velocity in inertial frame ($\mathbf{v}_{CM/E}^I$) is given as

$$\begin{aligned} \delta \dot{\mathbf{v}}_{CM/E}^I = & \frac{\partial \mathbf{g}_E^I(\mathbf{r}_{CM/E}^I)}{\partial \mathbf{r}_{CM/E}^I} \Big|_{\bar{\mathbf{x}}} \delta \mathbf{r}_{CM/E}^I + \frac{\partial \mathbf{a}_{3rd}^I}{\partial \mathbf{r}_{CM/E}^I} \Big|_{\bar{\mathbf{x}}} \delta \mathbf{r}_{CM/E}^I + \frac{\partial \mathbf{a}_{aero}^I}{\partial \mathbf{r}_{CM/E}^I} \Big|_{\bar{\mathbf{x}}} \delta \mathbf{r}_{CM/E}^I + \\ & \frac{\partial \mathbf{a}_{SRP}^I}{\partial \mathbf{r}_{CM/E}^I} \Big|_{\bar{\mathbf{x}}} \delta \mathbf{r}_{CM/E}^I + \frac{\partial \mathbf{a}_{aero}^I}{\partial \mathbf{v}_{CM/E}^I} \Big|_{\bar{\mathbf{x}}} \delta \mathbf{v}_{CM/E}^I + \frac{\partial \mathbf{a}_{aero}^I}{\partial \beta} \Big|_{\bar{\mathbf{x}}} \delta \beta \\ & + \frac{\partial \mathbf{a}_{aero}^I}{\partial \rho_r} \Big|_{\bar{\mathbf{x}}} \delta \rho_r + \frac{\partial \mathbf{a}_{aero}^I}{\partial h_s} \Big|_{\bar{\mathbf{x}}} \delta h_s + \mathbf{w}_T + \mathbf{w}_{aero} \end{aligned} \quad (5.97)$$

where the partial derivatives in Eq. 5.97 are given in Appendix A, respectively.

Similarly, the discretized form of Eq. 5.97 is given as

$$\begin{aligned} \delta \mathbf{v}_{CM/E,k+1}^I = & \delta \mathbf{v}_{CM/E,k}^I + \frac{\partial \mathbf{g}_E^I(\mathbf{r}_{CM/E,k}^I)}{\partial \mathbf{r}_{CM/E,k}^I} \Big|_{\bar{\mathbf{x}},k} \delta \mathbf{r}_{CM/E,k}^I \Delta t + \frac{\partial \mathbf{a}_{3rd,k}^I}{\partial \mathbf{r}_{CM/E,k}^I} \Big|_{\bar{\mathbf{x}},k} \delta \mathbf{r}_{CM/E,k}^I \Delta t + \\ & \frac{\partial \mathbf{a}_{aero,k}^I}{\partial \mathbf{r}_{CM/E,k}^I} \Big|_{\bar{\mathbf{x}},k} \delta \mathbf{r}_{CM/E,k}^I \Delta t + \frac{\partial \mathbf{a}_{SRP,k}^I}{\partial \mathbf{r}_{CM/E,k}^I} \Big|_{\bar{\mathbf{x}},k} \delta \mathbf{r}_{CM/E,k}^I \Delta t + \frac{\partial \mathbf{a}_{aero,k}^I}{\partial \mathbf{v}_{CM/E,k}^I} \Big|_{\bar{\mathbf{x}},k} \delta \mathbf{v}_{CM/E,k}^I \Delta t + \end{aligned}$$

$$\frac{\partial \mathbf{a}_{aero,k}^I}{\partial \beta_k} \bigg|_{\bar{\mathbf{x}},k} \delta \beta_k \Delta t + \frac{\partial \mathbf{a}_{aero,k}^I}{\partial \rho_{r,k}} \bigg|_{\bar{\mathbf{x}},k} \delta \rho_{r,k} \Delta t +$$

$$\frac{\partial \mathbf{a}_{aero,k}^I}{\partial h_{s,k}} \bigg|_{\bar{\mathbf{x}},k} \delta h_{s,k} \Delta t + \mathbf{w}_{d,T,k} \Delta t + \mathbf{w}_{d,aero,k} \Delta t \quad (5.98)$$

where subscript k denote the state at a particular discrete time-step, $\mathbf{w}_{d,T,k}$ and $\mathbf{w}_{d,aero,k}$ are the discretized translational disturbance acceleration and discretized unmodeled aerodynamic acceleration, such that $Q_{d,T}$ is the variance of the discretized translational disturbance acceleration and $Q_{d,aero}$ is the variance of the discretized unmodeled aerodynamic acceleration, given as

$$Q_{d,T} = \frac{Q_T}{\Delta t} \quad (5.99)$$

$$Q_{d,aero} = \frac{Q_{aero}}{\Delta t} \quad (5.100)$$

Since the dynamics of ballistic coefficient, reference atmospheric density, and scale height are already linear, refer Eqs. 5.26, 5.30, and 5.34, the discretized form of the corresponding equations is given below.

The discretized dynamics of the small deviation in the ballistic coefficient ($\delta\beta$), for exponentially decaying atmospheric drag, is given as

$$\delta\beta_{k+1} = e^{-\Delta t/\tau_\beta} \delta\beta_k + \mathbf{w}_{d,\beta} \quad (5.101)$$

where subscript k denote the state at a particular discrete time-step, and $\mathbf{w}_{d,\beta}$ is the discretized unmodeled noise in the dynamics of the small deviation in the ballistic coefficient

with variance $Q_{d,\beta}$ given as

$$Q_{d,\beta} = E[\mathbf{w}_{d,\beta} [t_1] \mathbf{w}_{d,\beta} [t_2]^T] = \sigma_\beta^2 \left\{ 1 - \exp\left(\frac{-2\Delta t}{\tau_\beta}\right) \right\} \quad (5.102)$$

where σ_β denote the steady state standard deviation of the spacecraft ballistic coefficient, and Δt is the discretization time step.

The discretized dynamics of the small deviation in the reference atmospheric density ($\delta\rho_r$), for exponentially decaying atmospheric drag, is given as

$$\delta\rho_{r,k+1} = e^{-\Delta t/\tau_{\rho_r}} \delta\rho_{r,k} + \mathbf{w}_{d,\rho_r} \quad (5.103)$$

where \mathbf{w}_{d,ρ_r} is the discretized unmodeled noise in the dynamics of the small deviation in the reference atmospheric density with variance Q_{d,ρ_r} given as

$$Q_{d,\rho_r} = E[\mathbf{w}_{d,\rho_r} [t_1] \mathbf{w}_{d,\rho_r} [t_2]^T] = \sigma_{\rho_r}^2 \left\{ 1 - \exp\left(\frac{-2\Delta t}{\tau_{\rho_r}}\right) \right\} \quad (5.104)$$

where σ_{ρ_r} denote the steady state standard deviation of the reference atmospheric density.

The discretized dynamics of the small deviation in the scale height (δh_s), for exponentially decaying atmospheric drag, is given as

$$\delta h_{s,k+1} = e^{-\Delta t/\tau_{h_s}} \delta h_{s,k} + \mathbf{w}_{d,h_s} \quad (5.105)$$

where \mathbf{w}_{d,h_s} is the discretized unmodeled noise in the dynamics of the small deviation in the scale height with variance Q_{d,h_s} given as

$$Q_{d,h_s} = E[\mathbf{w}_{d,h_s} [t_1] \mathbf{w}_{d,h_s} [t_2]^T] = \sigma_{h_s}^2 \left\{ 1 - \exp\left(\frac{-2\Delta t}{\tau_{h_s}}\right) \right\} \quad (5.106)$$

where σ_{h_s} denote the steady state standard deviation of the scale height.

5.6.2 Linearized Rotational Dynamics

Noting that the time derivative of the nominal quaternion, refer Eq. 5.37, is given as

$$\dot{\mathbf{q}}_{I \rightarrow B} = \frac{1}{2} \bar{\boldsymbol{\omega}}_{B/I}^B \otimes \bar{\mathbf{q}}_{I \rightarrow B} \quad (5.107)$$

Now for a small quaternion $\delta \mathbf{q}_{I \rightarrow B}$, quaternion kinematics can be rewritten as

$$\frac{d}{dt} [\delta \mathbf{q}_{I \rightarrow B} \otimes \bar{\mathbf{q}}_{I \rightarrow B}] = \frac{1}{2} \boldsymbol{\omega}_{B/I}^B \otimes \mathbf{q}_{I \rightarrow B} \quad (5.108)$$

$$\delta \dot{\mathbf{q}}_{I \rightarrow B} \otimes \bar{\mathbf{q}}_{I \rightarrow B} + \delta \mathbf{q}_{I \rightarrow B} \otimes \dot{\bar{\mathbf{q}}}_{I \rightarrow B} = \frac{1}{2} \boldsymbol{\omega}_{B/I}^B \otimes (\delta \mathbf{q}_{I \rightarrow B} \otimes \bar{\mathbf{q}}_{I \rightarrow B}) \quad (5.109)$$

Using Eq. 5.107, gives

$$\delta \dot{\mathbf{q}}_{I \rightarrow B} \otimes \bar{\mathbf{q}}_{I \rightarrow B} + \delta \mathbf{q}_{I \rightarrow B} \otimes \left(\frac{1}{2} \bar{\boldsymbol{\omega}}_{B/I}^B \otimes \bar{\mathbf{q}}_{I \rightarrow B} \right) = \frac{1}{2} \boldsymbol{\omega}_{B/I}^B \otimes (\delta \mathbf{q}_{I \rightarrow B} \otimes \bar{\mathbf{q}}_{I \rightarrow B}) \quad (5.110)$$

Since nominal quaternion $\bar{\mathbf{q}}_{I \rightarrow B}$ is a unit quaternion, eliminating $\bar{\mathbf{q}}_{I \rightarrow B}$ from both sides in Eq. 5.110. Further, noting that a small quaternion and corresponding time derivative is defined as

$$\delta \mathbf{q}_{I \rightarrow B} = \begin{bmatrix} \delta \boldsymbol{\theta} / 2 \\ 1 \end{bmatrix}, \quad \delta \dot{\mathbf{q}}_{I \rightarrow B} = \begin{bmatrix} \delta \dot{\boldsymbol{\theta}} / 2 \\ 0 \end{bmatrix} \quad (5.111)$$

where $\delta \boldsymbol{\theta}$ is an error rotation vector defining the small change in the spacecraft's attitude.

Now using Eq. 5.111 in Eq. 5.110 and expanding the quaternion cross-product, yields

$$\begin{aligned} & \begin{bmatrix} -\frac{1}{2} [\delta \dot{\boldsymbol{\theta}} \times] & \frac{1}{2} \delta \dot{\boldsymbol{\theta}} \\ -\frac{1}{2} \delta \dot{\boldsymbol{\theta}}^T & 0 \end{bmatrix} + \frac{1}{2} \begin{bmatrix} I_{3 \times 3} - \frac{1}{2} [\delta \boldsymbol{\theta} \times] & \frac{1}{2} \delta \boldsymbol{\theta} \\ -\frac{1}{2} \delta \boldsymbol{\theta}^T & 1 \end{bmatrix} \begin{bmatrix} -[\bar{\boldsymbol{\omega}}_{B/I}^B \times] & \bar{\boldsymbol{\omega}}_{B/I}^B \\ -(\bar{\boldsymbol{\omega}}_{B/I}^B)^T & 0 \end{bmatrix} = \\ & \frac{1}{2} \begin{bmatrix} -[\boldsymbol{\omega}_{B/I}^B \times] & \boldsymbol{\omega}_{B/I}^B \\ -(\boldsymbol{\omega}_{B/I}^B)^T & 0 \end{bmatrix} \begin{bmatrix} I_{3 \times 3} - \frac{1}{2} [\delta \boldsymbol{\theta} \times] & \frac{1}{2} \delta \boldsymbol{\theta} \\ -\frac{1}{2} \delta \boldsymbol{\theta}^T & 1 \end{bmatrix} \end{aligned} \quad (5.112)$$

Now to get linearized form of the spacecraft's rotation vector, evaluating the 3×1 upper right corner of the matrices on both sides in Eq. 5.112, such that

$$\delta\dot{\boldsymbol{\theta}} + \bar{\boldsymbol{\omega}}_{B/I}^B - \frac{1}{2} [\delta\boldsymbol{\theta} \times] \bar{\boldsymbol{\omega}}_{B/I}^B = -\frac{1}{2} [\boldsymbol{\omega}_{B/I}^B \times] \delta\boldsymbol{\theta} + \boldsymbol{\omega}_{B/I}^B \quad (5.113)$$

On rearranging Eq. 5.113 resembles closely to Bortz equation Eq. 5.94, and on ignoring the second-order term this equation reduces to [45]

$$\delta\dot{\boldsymbol{\theta}} = \delta\boldsymbol{\omega}_{B/I}^B - \bar{\boldsymbol{\omega}}_{B/I}^B \times \delta\boldsymbol{\theta} \quad (5.114)$$

Discretized form of Eq. 5.114 is given as

$$\delta\boldsymbol{\theta}_{k+1} = \delta\boldsymbol{\theta}_k + \delta\boldsymbol{\omega}_{B/I,k}^B \Delta t - [\bar{\boldsymbol{\omega}}_{B/I,k}^B \times] \delta\boldsymbol{\theta}_k \Delta t \quad (5.115)$$

where subscript k denote the state at a particular discrete time-step and Δt is the discretization time step.

The linearized dynamics of the spacecraft's angular velocity ($\boldsymbol{\omega}_{B/I}^B$) is given as [31]

$$\delta\dot{\boldsymbol{\omega}}_{B/I}^B = J^{-1} \left[\frac{\partial M_{gg}}{\partial \mathbf{r}_{CM/E}^I} \Big|_{\bar{\mathbf{x}}} \delta \mathbf{r}_{CM/E}^I + \frac{\partial M_{gg}}{\partial \boldsymbol{\theta}} \Big|_{\bar{\mathbf{x}}} \delta \boldsymbol{\theta} - \frac{\partial \left(\boldsymbol{\omega}_{B/I}^B \times [J \boldsymbol{\omega}_{B/I}^B] \right)}{\partial \boldsymbol{\omega}_{B/I}^B} \Big|_{\bar{\mathbf{x}}} \delta \boldsymbol{\omega}_{B/I}^B \right] + \mathbf{w}_R \quad (5.116)$$

where

$$\frac{\partial \left(\boldsymbol{\omega}_{B/I}^B \times [J \boldsymbol{\omega}_{B/I}^B] \right)}{\partial \boldsymbol{\omega}_{B/I}^B} \Big|_{\bar{\mathbf{x}}} = - \left[(J \bar{\boldsymbol{\omega}}_{B/I}^B) \times \right] + [\bar{\boldsymbol{\omega}}_{B/I}^B \times] J \quad (5.117)$$

The partial derivatives of the gravity gradient torque with respect to the spacecraft position vector and the rotation vector, are given in Appendix A, respectively.

Discretized form of Eq. 5.116 is given as

$$\delta\boldsymbol{\omega}_{B/I,k+1}^B = \delta\boldsymbol{\omega}_{B/I,k}^B + J_k^{-1} \left[\frac{\partial M_{gg,k}}{\partial \mathbf{r}_{CM/E,k}^I} \bigg|_{\bar{\mathbf{x}}_k} \delta\mathbf{r}_{CM/E,k}^I \Delta t + \frac{\partial M_{gg,k}}{\partial \boldsymbol{\theta}_k} \bigg|_{\bar{\mathbf{x}}_k} \delta\boldsymbol{\theta}_k \Delta t - \frac{\partial \left(\boldsymbol{\omega}_{B/I,k}^B \times \left[J_k \boldsymbol{\omega}_{B/I,k}^B \right] \right)}{\partial \boldsymbol{\omega}_{B/I,k}^B} \bigg|_{\bar{\mathbf{x}}_k} \delta\boldsymbol{\omega}_{B/I,k}^B \Delta t \right] + \mathbf{w}_{d,R,k} \Delta t \quad (5.118)$$

where $\mathbf{w}_{d,R,k}$ is the discretized rotational disturbance acceleration, such that $Q_{d,R}$ is the variance of the discretized rotational disturbance acceleration, given as

$$Q_{d,R} = \frac{Q_R}{\Delta t} \quad (5.119)$$

5.6.3 Linearized Instrument Error Dynamics

Since the dynamics of center of mass position with respect to the spacecraft body-fixed frame $\left(\mathbf{r}_{CM/O}^B\right)$, i^{th} accelerometer position with respect to the spacecraft body-fixed frame $\left(\delta\mathbf{r}_{a_i/O}^B\right)$, accelerometer bias $\left(\mathbf{b}_i^{\tilde{a}_i}\right)$, accelerometer scale factor $\left(\mathbf{f}_i^{\tilde{a}_i}\right)$, and accelerometer misalignment $\left(\boldsymbol{\epsilon}_i^{\tilde{a}_i}\right)$ are already linear, refer Eqs. 5.43, 5.48, 5.52, 5.56, and 5.60, the discretized form of the corresponding equations is given below.

The discretized dynamics of the center of mass position with respect to the spacecraft body-fixed frame $\left(\mathbf{r}_{CM/O}^B\right)$ is given as

$$\mathbf{r}_{CM/O,k+1}^B = I_{3 \times 1} e^{-\Delta t / \tau_{r_{CM/O}}} \mathbf{r}_{CM/O,k}^B + \mathbf{w}_{d,r_{CM/O}} \quad (5.120)$$

where subscript k denote the state at a particular discrete time-step, and $\mathbf{w}_{d,r_{CM/O}}$ is the discretized unmodeled noise in the dynamics of the center of mass position with variance $Q_{d,r_{CM/O}}$ given as

$$Q_{d,\mathbf{r}_{CM/O}} = E[\mathbf{w}_{d,\mathbf{r}_{CM/O}} [t_1] \mathbf{w}_{d,\mathbf{r}_{CM/O}} [t_2]^T] = \sigma_{\mathbf{r}_{CM/O}}^2 \left\{ 1 - \exp\left(\frac{-2\Delta t}{\tau_{\mathbf{r}_{CM/O}}}\right) \right\} \quad (5.121)$$

where $\sigma_{\mathbf{r}_{CM/O}}$ denote the steady state standard deviation of center of mass position, and Δt is the discretization time step.

The discretized dynamics of the small deviation in the i^{th} accelerometer position with respect to the spacecraft body-fixed frame $(\delta\mathbf{r}_{a_i/O}^B)$ is given as

$$\delta\mathbf{r}_{a_i/O,k+1}^B = I_{3 \times 1} e^{-\Delta t/\tau_{\mathbf{r}_{CM/O}}} \delta\mathbf{r}_{a_i/O,k}^B + \mathbf{w}_{d,\mathbf{r}_{a_i/O}} \quad (5.122)$$

where $\mathbf{w}_{d,\mathbf{r}_{a_i/O}}$ is the discretized unmodeled noise in the dynamics of the small deviation in the i^{th} accelerometer position with variance $Q_{d,\mathbf{r}_{a_i/O}}$ given as

$$Q_{d,\mathbf{r}_{a_i/O}} = E[\mathbf{w}_{d,\mathbf{r}_{a_i/O}} [t_1] \mathbf{w}_{d,\mathbf{r}_{a_i/O}} [t_2]^T] = \sigma_{\mathbf{r}_{a_i/O}}^2 \left\{ 1 - \exp\left(\frac{-2\Delta t}{\tau_{\mathbf{r}_{a_i/O}}}\right) \right\} \quad (5.123)$$

where $\sigma_{\mathbf{r}_{a_i/O}}$ denote the steady state standard deviation of the i^{th} accelerometer position.

The discretized dynamics of the accelerometer bias $(\mathbf{b}_i^{\tilde{a}_i})$ is given as

$$\mathbf{b}_{i,k+1}^{\tilde{a}_i} = I_{3 \times 1} e^{-\Delta t/\tau_{\mathbf{b}_i}} \mathbf{b}_{i,k}^{\tilde{a}_i} + \mathbf{w}_{d,\mathbf{b}_i} \quad (5.124)$$

where $\mathbf{w}_{d,\mathbf{b}_i}$ is the discretized unmodeled noise in the dynamics of the accelerometer bias with variance Q_{d,\mathbf{b}_i} given as

$$Q_{d,\mathbf{b}_i} = E[\mathbf{w}_{d,\mathbf{b}_i} [t_1] \mathbf{w}_{d,\mathbf{b}_i} [t_2]^T] = \sigma_{\mathbf{b}_i}^2 \left\{ 1 - \exp\left(\frac{-2\Delta t}{\tau_{\mathbf{b}_i}}\right) \right\} \quad (5.125)$$

where $\sigma_{\mathbf{b}_i}$ denote the steady state standard deviation of the accelerometer bias.

The discretized dynamics of the accelerometer scale factor $(\mathbf{f}_i^{\tilde{a}_i})$ is given as

$$\mathbf{f}_{i,k+1}^{\tilde{a}_i} = I_{3 \times 1} e^{-\Delta t/\tau_{\mathbf{f}_i}} \mathbf{f}_{i,k}^{\tilde{a}_i} + \mathbf{w}_{d,\mathbf{f}_i} \quad (5.126)$$

where $\mathbf{w}_{d,\mathbf{f}_i}$ is the discretized unmodeled noise in the dynamics of the accelerometer scale factor with variance Q_{d,\mathbf{f}_i} given as

$$Q_{d,\mathbf{f}_i} = E[\mathbf{w}_{d,\mathbf{f}_i}[t_1] \mathbf{w}_{d,\mathbf{f}_i}[t_2]^T] = \sigma_{\mathbf{f}_i}^2 \left\{ 1 - \exp\left(\frac{-2\Delta t}{\tau_{\mathbf{f}_i}}\right) \right\} \quad (5.127)$$

where $\sigma_{\mathbf{f}_i}$ denote the steady state standard deviation of the accelerometer scale factor.

The discretized dynamics of the accelerometer misalignment $(\epsilon_i^{\tilde{a}_i})$ is given as

$$\epsilon_{i,k+1}^{\tilde{a}_i} = I_{3 \times 1} e^{-\Delta t / \tau_{\epsilon_i}} \epsilon_{i,k}^{\tilde{a}_i} + \mathbf{w}_{d,\epsilon_i} \quad (5.128)$$

where $\mathbf{w}_{d,\epsilon_i}$ is the discretized unmodeled noise in the dynamics of the accelerometer misalignment with variance Q_{d,ϵ_i} given as

$$Q_{d,\epsilon_i} = E[\mathbf{w}_{d,\epsilon_i}[t_1] \mathbf{w}_{d,\epsilon_i}[t_2]^T] = \sigma_{\epsilon_i}^2 \left\{ 1 - \exp\left(\frac{-2\Delta t}{\tau_{\epsilon_i}}\right) \right\} \quad (5.129)$$

where σ_{ϵ_i} denote the steady state standard deviation of the accelerometer misalignment.

5.7 Linearized Measurement Equation

Now, Eq. 5.64 is linearized as

$$\delta \tilde{a}_i^{\tilde{a}_i} = H_x \delta \mathbf{x} + \boldsymbol{\eta}_i^{\tilde{a}_i} \quad (5.130)$$

where H_x is the measurement partial due to the accelerometer measurements, defined as

$$H_x = \left. \frac{\partial \mathbf{h}}{\partial \mathbf{x}} \right|_{\bar{\mathbf{x}}} \quad (5.131)$$

$$H_x = \left[\begin{array}{cccccc} \left. \frac{\partial \mathbf{h}_{3n}}{\partial \mathbf{r}_{CM/E}^I} \right|_{\bar{\mathbf{x}}} & \left. \frac{\partial \mathbf{h}_{3n}}{\partial \mathbf{v}_{CM/E}^I} \right|_{\bar{\mathbf{x}}} & \left. \frac{\partial \mathbf{h}_{3n}}{\partial \boldsymbol{\theta}_{I \rightarrow B}} \right|_{\bar{\mathbf{x}}} & \left. \frac{\partial \mathbf{h}_{3n}}{\partial \boldsymbol{\omega}_{B/I}^B} \right|_{\bar{\mathbf{x}}} & \left. \frac{\partial \mathbf{h}_{3n}}{\partial \mathbf{r}_{CM/O}^B} \right|_{\bar{\mathbf{x}}} & \left. \frac{\partial \mathbf{h}_{3n}}{\partial \beta} \right|_{\bar{\mathbf{x}}} \\ \left. \frac{\partial \mathbf{h}_{3n}}{\partial \rho_r} \right|_{\bar{\mathbf{x}}} & \left. \frac{\partial \mathbf{h}_{3n}}{\partial h_s} \right|_{\bar{\mathbf{x}}} & \left. \frac{\partial \mathbf{h}_{3n}}{\partial \mathbf{r}_{a_i/O}^B} \right|_{\bar{\mathbf{x}}} & \left. \frac{\partial \mathbf{h}_{3n}}{\partial \mathbf{b}_i^{\tilde{a}_i}} \right|_{\bar{\mathbf{x}}} & \left. \frac{\partial \mathbf{h}_{3n}}{\partial \mathbf{f}_i^{\tilde{a}_i}} \right|_{\bar{\mathbf{x}}} & \left. \frac{\partial \mathbf{h}_{3n}}{\partial \epsilon_i^{\tilde{a}_i}} \right|_{\bar{\mathbf{x}}} \end{array} \right]_{3n \times (18+12n)} \quad (5.132)$$

Noting that the total number of states is $18 + 12n$ (where n is the number of accelerometers), the measurement partial H_x is a matrix of dimension size $3n \times (18 + 12n)$. Measurement partials with respect to each state are given below.

Measurement partials with respect to the spacecraft position in inertial frame $(\mathbf{r}_{CM/E}^I)$ are given as

$$\left. \frac{\partial \mathbf{h}}{\partial \mathbf{r}_{CM/E}^I} \right|_{\bar{\mathbf{x}}} = \left[I + D(\bar{\mathbf{f}}_i^{\tilde{a}_i}) \right] \left(I - [\bar{\boldsymbol{\epsilon}}_i^{\tilde{a}_i} \times] \right) T_{B \rightarrow a_i^N} T_{I \rightarrow B} \left. \frac{\partial \mathbf{a}_{d_i}^I}{\partial \mathbf{r}_{CM/E}^I} \right|_{\bar{\mathbf{x}}} \quad (5.133)$$

where

$$\begin{aligned} \left. \frac{\partial \mathbf{a}_{d_i}^I}{\partial \mathbf{r}_{CM/E}^I} \right|_{\bar{\mathbf{x}}} &= \left. \frac{\partial \mathbf{g}^I(\mathbf{r}_{CM/E}^I)}{\partial \mathbf{r}_{CM/E}^I} \right|_{\bar{\mathbf{x}}} - \left. \frac{\partial \mathbf{g}^I(\mathbf{r}_{CM/E}^I + T_{B \rightarrow I} [\mathbf{r}_{a_i/O}^B - \mathbf{r}_{CM/O}^B])}{\partial \mathbf{r}_{CM/E}^I} \right|_{\bar{\mathbf{x}}} + \left. \frac{\partial \mathbf{a}_{aero}^I}{\partial \mathbf{r}_{CM/E}^I} \right|_{\bar{\mathbf{x}}} \\ &+ \left. \frac{\partial \mathbf{a}_{SRP}^I}{\partial \mathbf{r}_{CM/E}^I} \right|_{\bar{\mathbf{x}}} + \left. \frac{\partial T_{B \rightarrow I} \left\{ \boldsymbol{\omega}_{B/I}^B \times \left(\boldsymbol{\omega}_{B/I}^B \times [\mathbf{r}_{a_i/O}^B - \mathbf{r}_{CM/O}^B] \right) \right\}}{\partial \mathbf{r}_{CM/E}^I} \right|_{\bar{\mathbf{x}}} \end{aligned} \quad (5.134)$$

where $\mathbf{g}(\mathbf{r})$ denote the total gravitational acceleration (i.e. gravitational acceleration due to Earth plus three body perturbations) at position \mathbf{r}

$$\begin{aligned} \left. \frac{\partial \mathbf{a}_{d_i}^I}{\partial \mathbf{r}_{CM/E}^I} \right|_{\bar{\mathbf{x}}} &= \nabla \bar{\mathbf{g}}^I(\bar{\mathbf{r}}_{CM/E}^I) - \nabla \bar{\mathbf{g}}^I(\bar{\mathbf{r}}_{a_i/E}^I) + \frac{1}{2} \bar{\rho}_r e^{-\left(\frac{\|\bar{\mathbf{r}}_{CM/E}^I\|}{h_s} \right)^{-h_{ref}}} \bar{\beta} \left\| \bar{\mathbf{v}}_{CM/E}^I \right\| \bar{\mathbf{v}}_{CM/E}^I \frac{\hat{\mathbf{i}}_{\bar{\mathbf{r}}_{CM/E}^I}^T}{\bar{h}_s} \\ &+ \frac{F_e}{c} \left[\frac{3}{r_{sc} \rho_{sc}} \right] \left[\frac{1}{4} + \frac{1}{9} c_d \right] \frac{\left[I_{3 \times 3} - \hat{\mathbf{i}}_{(\bar{\mathbf{r}}_{CM/E}^I - \bar{\boldsymbol{\rho}}_{Sun})}^I \left(\hat{\mathbf{i}}_{(\bar{\mathbf{r}}_{CM/E}^I - \bar{\boldsymbol{\rho}}_{Sun})}^I \right)^T \right]}{\left\| \bar{\mathbf{r}}_{CM/E}^I - \bar{\boldsymbol{\rho}}_{Sun} \right\|} \end{aligned} \quad (5.135)$$

Detailed derivation of partial derivatives used in Eq. 5.135 are given in Appendix A.

Measurement partials with respect to the spacecraft velocity in inertial frame ($\mathbf{v}_{CM/E}^I$) are given as

$$\left. \frac{\partial \mathbf{h}}{\partial \mathbf{v}_{CM/E}^I} \right|_{\bar{\mathbf{x}}} = \left[I + D \left(\bar{\mathbf{f}}_i^{\tilde{a}_i} \right) \right] \left(I - \left[\bar{\boldsymbol{\epsilon}}_i^{\tilde{a}_i} \times \right] \right) T_{B \rightarrow a_i^N} T_{I \rightarrow B} \left. \frac{\partial \mathbf{a}_{d_i}^I}{\partial \mathbf{v}_{CM/E}^I} \right|_{\bar{\mathbf{x}}} \quad (5.136)$$

where

$$\left. \frac{\partial \mathbf{a}_{d_i}^I}{\partial \mathbf{v}_{CM/E}^I} \right|_{\bar{\mathbf{x}}} = \left. \frac{\partial \mathbf{a}_{aero}^I}{\partial \mathbf{v}_{CM/E}^I} \right|_{\bar{\mathbf{x}}} = -\frac{1}{2} \bar{\rho}_r e^{-\left(\frac{\|\bar{\mathbf{r}}_{CM/E}^I\|^{-h_{ref}}}{h_s} \right)} \bar{\beta} \left(\bar{\mathbf{v}}_{CM/E}^I \hat{\mathbf{v}}_{CM/E}^I + \|\bar{\mathbf{v}}_{CM/E}^I\| I_{3 \times 3} \right) \quad (5.137)$$

Measurement partials with respect to the spacecraft's rotation vector ($\boldsymbol{\theta}_{I \rightarrow B}$) are given as

$$\left. \frac{\partial \mathbf{h}}{\partial \boldsymbol{\theta}_{I \rightarrow B}} \right|_{\bar{\mathbf{x}}} = \left[I + D \left(\bar{\mathbf{f}}_i^{\tilde{a}_i} \right) \right] \left(I - \left[\bar{\boldsymbol{\epsilon}}_i^{\tilde{a}_i} \times \right] \right) T_{B \rightarrow a_i^N} \left. \frac{\partial \mathbf{a}_{d_i}^B}{\partial \boldsymbol{\theta}_{I \rightarrow B}} \right|_{\bar{\mathbf{x}}} \quad (5.138)$$

where

$$\left. \frac{\partial \mathbf{a}_{d_i}^B}{\partial \boldsymbol{\theta}_{I \rightarrow B}} \right|_{\bar{\mathbf{x}}} = \left[\{ T_{I \rightarrow \bar{B}}(\bar{\boldsymbol{\theta}}) \bar{\mathbf{a}}_{d_i}^I(\bar{\boldsymbol{\theta}}) \} \times \right] + T_{I \rightarrow \bar{B}}(\bar{\boldsymbol{\theta}}) \nabla \mathbf{g}^I \left(\bar{\mathbf{r}}_{a_i/E}^I \right) T_{I \rightarrow \bar{B}}^T(\bar{\boldsymbol{\theta}}) \left[\bar{\mathbf{r}}_{a_i/CM}^B \times \right] \quad (5.139)$$

Detailed derivation of partial derivatives used in Eq. 5.139 are given in Appendix A.

Thus, measurement partial with respect to the spacecraft's rotation vector ($\boldsymbol{\theta}_{I \rightarrow B}$) is given as

$$\left. \frac{\partial \mathbf{h}}{\partial \boldsymbol{\theta}_{I \rightarrow B}} \right|_{\bar{\mathbf{x}}} = \left[I + D \left(\bar{\mathbf{f}}_i^{\tilde{a}_i} \right) \right] \left(I - \left[\bar{\boldsymbol{\epsilon}}_i^{\tilde{a}_i} \times \right] \right) T_{B \rightarrow a_i^N} \left(\left[\{ T_{I \rightarrow \bar{B}}(\bar{\boldsymbol{\theta}}) \bar{\mathbf{a}}_{d_i}^I(\bar{\boldsymbol{\theta}}) \} \times \right] \right)$$

$$+T_{I \rightarrow \bar{B}}(\bar{\boldsymbol{\theta}}) \nabla \bar{\mathbf{g}}^I \left(\bar{\mathbf{r}}_{a_i/E}^I \right) T_{I \rightarrow \bar{B}}^T(\bar{\boldsymbol{\theta}}) \left[\bar{\mathbf{r}}_{a_i/CM}^B \times \right] \quad (5.140)$$

where $\bar{\mathbf{a}}_{d_i}^I$ is given by Eq. 5.90

Measurement partials with respect to the spacecraft's angular velocity $(\boldsymbol{\omega}_{B/I}^B)$ are given as

$$\left. \frac{\partial \mathbf{h}}{\partial \boldsymbol{\omega}_{B/I}^B} \right|_{\bar{\mathbf{x}}} = \left[I + D \left(\bar{\mathbf{f}}_i^{\tilde{a}_i} \right) \right] \left(I - \left[\bar{\boldsymbol{\epsilon}}_i^{\tilde{a}_i} \times \right] \right) T_{B \rightarrow a_i^N} T_{I \rightarrow B}(\bar{\boldsymbol{\theta}}_{I \rightarrow B}) \left. \frac{\partial \mathbf{a}_{d_i}^I}{\partial \boldsymbol{\omega}_{B/I}^B} \right|_{\bar{\mathbf{x}}} \quad (5.141)$$

where

$$\left. \frac{\partial \mathbf{a}_{d_i}^I}{\partial \boldsymbol{\omega}_{B/I}^B} \right|_{\bar{\mathbf{x}}} = -T_{B \rightarrow I} \left\{ \left[\left(\bar{\boldsymbol{\omega}}_{B/I}^B \times \left[\bar{\mathbf{r}}_{a_i/O}^B - \bar{\mathbf{r}}_{CM/O}^B \right] \right) \times \right] + \left[\bar{\boldsymbol{\omega}}_{B/I}^B \times \right] \left[\left(\bar{\mathbf{r}}_{a_i/O}^B - \bar{\mathbf{r}}_{CM/O}^B \right) \times \right] \right\} \quad (5.142)$$

Detailed derivation of partial derivatives used in Eq. A.49 are given in Appendix A.

Measurement partials with respect to the center of mass position, in spacecraft body-fixed frame and with respect to the origin of the spacecraft body-fixed frame $(\mathbf{r}_{CM/O}^B)$, are given as

$$\left. \frac{\partial \mathbf{h}}{\partial \mathbf{r}_{CM/O}^B} \right|_{\bar{\mathbf{x}}} = \left[I + D \left(\bar{\mathbf{f}}_i^{\tilde{a}_i} \right) \right] \left(I - \left[\bar{\boldsymbol{\epsilon}}_i^{\tilde{a}_i} \times \right] \right) T_{B \rightarrow a_i^N} T_{I \rightarrow B}(\bar{\boldsymbol{\theta}}_{I \rightarrow B}) \left. \frac{\partial \mathbf{a}_{d_i}^I}{\partial \mathbf{r}_{CM/O}^B} \right|_{\bar{\mathbf{x}}} \quad (5.143)$$

where

$$\left. \frac{\partial \mathbf{a}_{d_i}^I}{\partial \mathbf{r}_{CM/O}^B} \right|_{\bar{\mathbf{x}}} = \nabla \bar{\mathbf{g}}^I \left(\bar{\mathbf{r}}_{a_i/E}^I \right) T_{B \rightarrow I} - T_{B \rightarrow I} \left(\left[\bar{\boldsymbol{\omega}}_{B/I}^B \times \right] \left[\bar{\boldsymbol{\omega}}_{B/I}^B \times \right] \right) \quad (5.144)$$

Detailed derivation of partial derivatives used in Eq. A.52 are given in Appendix A.

Measurement partials with respect to the ballistic coefficient (β), for exponentially decaying atmospheric drag, are given as

$$\left. \frac{\partial \mathbf{h}}{\partial \beta} \right|_{\bar{\mathbf{x}}} = \left[I + D \left(\bar{\mathbf{f}}_i^{\tilde{a}_i} \right) \right] \left(I - \left[\bar{\boldsymbol{\epsilon}}_i^{\tilde{a}_i} \times \right] \right) T_{B \rightarrow a_i^N} T_{I \rightarrow B} \left(\bar{\boldsymbol{\theta}}_{I \rightarrow B} \right) \left. \frac{\partial \mathbf{a}_{d_i}^I}{\partial \beta} \right|_{\bar{\mathbf{x}}} \quad (5.145)$$

where

$$\left. \frac{\partial \mathbf{a}_{d_i}^I}{\partial \beta} \right|_{\bar{\mathbf{x}}} = \left. \frac{\partial \mathbf{a}_{aero}^I}{\partial \beta} \right|_{\bar{\mathbf{x}}} = -\frac{1}{2} \bar{\rho}_r e^{-\left(\frac{\| \bar{\mathbf{r}}_{CM/E}^I \|}{h_s} - h_{ref} \right)} \left\| \bar{\mathbf{v}}_{CM/E}^I \right\| \bar{\mathbf{v}}_{CM/E}^I \quad (5.146)$$

Measurement partials with respect to the reference atmospheric density (ρ_r), for exponentially decaying atmospheric drag, are given as

$$\left. \frac{\partial \mathbf{h}}{\partial \rho_r} \right|_{\bar{\mathbf{x}}} = \left[I + D \left(\bar{\mathbf{f}}_i^{\tilde{a}_i} \right) \right] \left(I - \left[\bar{\boldsymbol{\epsilon}}_i^{\tilde{a}_i} \times \right] \right) T_{B \rightarrow a_i^N} T_{I \rightarrow B} \left(\bar{\boldsymbol{\theta}}_{I \rightarrow B} \right) \left. \frac{\partial \mathbf{a}_{d_i}^I}{\partial \rho_r} \right|_{\bar{\mathbf{x}}} \quad (5.147)$$

where

$$\left. \frac{\partial \mathbf{a}_{d_i}^I}{\partial \rho_r} \right|_{\bar{\mathbf{x}}} = \left. \frac{\partial \mathbf{a}_{aero}^I}{\partial \rho_r} \right|_{\bar{\mathbf{x}}} = -\frac{1}{2} e^{-\left(\frac{\| \bar{\mathbf{r}}_{CM/E}^I \|}{h_s} - h_{ref} \right)} \bar{\beta} \left\| \bar{\mathbf{v}}_{CM/E}^I \right\| \bar{\mathbf{v}}_{CM/E}^I \quad (5.148)$$

Measurement partials with respect to the scale height (h_s), for exponentially decaying atmospheric drag, are given as

$$\left. \frac{\partial \mathbf{h}}{\partial h_s} \right|_{\bar{\mathbf{x}}} = \left[I + D \left(\bar{\mathbf{f}}_i^{\tilde{a}_i} \right) \right] \left(I - \left[\bar{\boldsymbol{\epsilon}}_i^{\tilde{a}_i} \times \right] \right) T_{B \rightarrow a_i^N} T_{I \rightarrow B} \left(\bar{\boldsymbol{\theta}}_{I \rightarrow B} \right) \left. \frac{\partial \mathbf{a}_{d_i}^I}{\partial h_s} \right|_{\bar{\mathbf{x}}} \quad (5.149)$$

where

$$\left. \frac{\partial \mathbf{a}_{d_i}^I}{\partial h_s} \right|_{\bar{\mathbf{x}}} = \left. \frac{\partial \mathbf{a}_{aero}^I}{\partial h_s} \right|_{\bar{\mathbf{x}}} = -\frac{\left(\left\| \bar{\mathbf{r}}_{CM/E}^I \right\| - h_{ref} \right)}{2\bar{h}_s^2} \bar{\rho}_r e^{-\left(\frac{\| \bar{\mathbf{r}}_{CM/E}^I \|}{h_s} - h_{ref} \right)} \bar{\beta} \left\| \bar{\mathbf{v}}_{CM/E}^I \right\| \bar{\mathbf{v}}_{CM/E}^I \quad (5.150)$$

Measurement partials with respect to the i^{th} accelerometer position, in spacecraft body-fixed frame and with respect to the origin of the spacecraft body-fixed frame $(\mathbf{r}_{a_i/O}^B)$, are given as

$$\left. \frac{\partial \mathbf{h}}{\partial \mathbf{r}_{a_i/O}^B} \right|_{\bar{\mathbf{x}}} = \left[I + D(\bar{\mathbf{f}}_i^{\tilde{a}_i}) \right] \left(I - [\bar{\boldsymbol{\epsilon}}_i^{\tilde{a}_i} \times] \right) T_{B \rightarrow a_i^N} T_{I \rightarrow B} (\bar{\boldsymbol{\theta}}_{I \rightarrow B}) \left. \frac{\partial \mathbf{a}_{d_i}^I}{\partial \mathbf{r}_{a_i/O}^B} \right|_{\bar{\mathbf{x}}} \quad (5.151)$$

where

$$\left. \frac{\partial \mathbf{a}_{d_i}^I}{\partial \mathbf{r}_{a_i/O}^B} \right|_{\bar{\mathbf{x}}} = -\nabla \bar{\mathbf{g}}^I(\bar{\mathbf{r}}_{a_i/E}^I) T_{B \rightarrow I} + T_{B \rightarrow I} \left([\bar{\boldsymbol{\omega}}_{B/I}^B \times] [\bar{\boldsymbol{\omega}}_{B/I}^B \times] \right) \quad (5.152)$$

Detailed derivation of partial derivatives used in Eq. A.55 are given in Appendix A.

Measurement partials with respect to the accelerometer bias $(\mathbf{b}_i^{\tilde{a}_i})$ are given as

$$\left. \frac{\partial \mathbf{h}}{\partial \mathbf{b}_i^{\tilde{a}_i}} \right|_{\bar{\mathbf{x}}} = I_{3 \times 3} \quad (5.153)$$

Measurement partials with respect to the accelerometer scale factor $(\mathbf{f}_i^{\tilde{a}_i})$ are given as

$$\left. \frac{\partial \mathbf{h}}{\partial \mathbf{f}_i^{\tilde{a}_i}} \right|_{\bar{\mathbf{x}}} = D(\bar{\mathbf{a}}_{d_i}^{\tilde{a}_i}) \quad (5.154)$$

where $\bar{\mathbf{a}}_{d_i}^{\tilde{a}_i}$ is given by Eq. 5.89

Measurement partials with respect to the accelerometer misalignment $(\boldsymbol{\epsilon}_i^{\tilde{a}_i})$ is given as

$$\left. \frac{\partial \mathbf{h}}{\partial \boldsymbol{\epsilon}_i^{\tilde{a}_i}} \right|_{\bar{\mathbf{x}}} = \left(I + D(\bar{\mathbf{f}}_i^{\tilde{a}_i}) \right) \left\{ \left[\left(T_{B \rightarrow a_i^N} T_{I \rightarrow B} (\bar{\boldsymbol{\theta}}_{I \rightarrow B}) \bar{\mathbf{a}}_{d_i}^I \right) \times \right] \right\} \quad (5.155)$$

where $\bar{\mathbf{a}}_{d_i}^I$ is given by Eq. 5.90

Now star camera measurement model, as given in Eq. 5.93, is linearized as

$$\delta \tilde{\mathbf{s}}^{\tilde{s}} = L_x \delta \mathbf{x} + \boldsymbol{\eta}_{sc}^{\tilde{s}} \quad (5.156)$$

where L_x is the measurement partial due to star camera measurements, defined as

$$L_x = \left. \frac{\partial \mathbf{l}}{\partial \mathbf{x}} \right|_{\bar{\mathbf{x}}} \quad (5.157)$$

Noting that, for this study only one star camera has been included and because the total number of states is $18 + 12n$ (where n is the number of accelerometers), the measurement partial L_x is a matrix of dimension size $3 \times (18 + 12n)$. Since, using Eq. 5.93 it is easy to note that the star camera measurement is only the function of spacecraft rotation vector, this implies

$$\left. \frac{\partial \mathbf{l}}{\partial \boldsymbol{\theta}_{I \rightarrow B}} \right|_{\bar{\mathbf{x}}} = T_{B \rightarrow \bar{s}} = I_{3 \times 3} \quad (5.158)$$

As stated earlier, for this study, the misalignments in the setting up of the star camera on the rigid body of the spacecraft have been ignored. Thus, $T_{B \rightarrow \bar{s}}$ is a 3×3 identity matrix.

5.8 Summary of Linearized Dynamics & Measurement Model

The linearized dynamics in Eq. 5.18 can be summarized as follow

$$\delta \dot{\mathbf{x}} = F_x \delta \mathbf{x} + G \mathbf{w} \quad (5.159)$$

where uppercase characters denote partial derivatives taken with respect to the variable indicated by subscript and evaluated along the reference state vector (e.g. $F_x = \partial \mathbf{f} / \partial \mathbf{x} |_{\bar{\mathbf{x}}}$), and G is a matrix to map the noise vector to the state dynamics.

Now let the state vector be segmented in two parts such that

$$\mathbf{x} = \begin{bmatrix} \mathbf{x}_1 \\ \mathbf{x}_2 \end{bmatrix} \quad (5.160)$$

$$\dot{\mathbf{x}} = \begin{bmatrix} \dot{\mathbf{x}}_1 \\ \dot{\mathbf{x}}_2 \end{bmatrix} = \begin{bmatrix} \mathbf{f}_1(\mathbf{x}_1, t) \\ \mathbf{f}_2(\mathbf{x}_2, t) \end{bmatrix} \quad (5.161)$$

where \mathbf{x} is the true state vector, and \mathbf{x}_1 and \mathbf{x}_2 are defined as

$$\mathbf{x}_1 = \left(\mathbf{r}_{CM/E}^I, \mathbf{v}_{CM/E}^I, \boldsymbol{\theta}_{I \rightarrow B}, \boldsymbol{\omega}_{B/I}^B \right)^T \quad (5.162)$$

$$\mathbf{x}_2 = \left(\mathbf{r}_{CM/O}^B, \beta, \rho_r, h_s, \mathbf{r}_{a_i/O}^B, \mathbf{b}_i^{\bar{a}_i}, \mathbf{f}_i^{\bar{a}_i}, \boldsymbol{\epsilon}_i^{\bar{a}_i} \right)^T \quad (5.163)$$

where \mathbf{x}_2 denotes all the ECRV.

Thus, based on Eqs. 5.159-5.163, F_x can be defined as

$$F_x = \left. \frac{\partial \mathbf{f}}{\partial \mathbf{x}} \right|_{\bar{\mathbf{x}}} = \begin{bmatrix} F_{x_1x_1} & F_{x_1x_2} \\ F_{x_2x_1} & F_{x_2x_2} \end{bmatrix} \quad (5.164)$$

where F_x is a $(18 + 12n) \times (18 + 12n)$ Jacobian matrix, while $F_{x_1x_1}$ is 12×12 , $F_{x_1x_2}$ and $F_{x_2x_1}$ are $12 \times (6 + 12n)$ and $(6 + 12n) \times 12$, and lastly, $F_{x_2x_2}$ is $(6 + 12n) \times (6 + 12n)$, respectively. Number of accelerometers is denoted by n .

$$F_{x_1x_1} = \left. \frac{\partial \mathbf{f}_1}{\partial \mathbf{x}_1} \right|_{\bar{\mathbf{x}}} = \begin{bmatrix} 0_{3 \times 3} & I_{3 \times 3} & 0_{3 \times 3} & 0_{3 \times 3} \\ F_{VR} & F_{VV} & 0_{3 \times 3} & 0_{3 \times 3} \\ 0_{3 \times 3} & 0_{3 \times 3} & -\Omega_{\otimes} & I_{3 \times 3} \\ F_{WR} & 0_{3 \times 3} & F_{W\theta} & F_{WW} \end{bmatrix}_{12 \times 12} \quad (5.165)$$

where

$$F_{VR} = \left. \frac{\partial \mathbf{g}_E^I(\mathbf{r}_{CM/E}^I)}{\partial \mathbf{r}_{CM/E}^I} \right|_{\bar{\mathbf{x}}} + \left. \frac{\partial \mathbf{a}_{Third-body}^I}{\partial \mathbf{r}_{CM/E}^I} \right|_{\bar{\mathbf{x}}} + \left. \frac{\partial \mathbf{a}_{aero}^I}{\partial \mathbf{r}_{CM/E}^I} \right|_{\bar{\mathbf{x}}} + \left. \frac{\partial \mathbf{a}_{SRP}^I}{\partial \mathbf{r}_{CM/E}^I} \right|_{\bar{\mathbf{x}}} \quad (5.166)$$

$$F_{VV} = \left. \frac{\partial \mathbf{a}_{aero}^I}{\partial \mathbf{v}_{CM/E}^I} \right|_{\bar{\mathbf{x}}} \quad (5.167)$$

$$F_{WR} = J^{-1} \left. \frac{\partial M_{gg}}{\partial \mathbf{r}_{CM/E}^I} \right|_{\bar{\mathbf{x}}} \quad (5.168)$$

$$F_{W\theta} = J^{-1} \frac{\partial M_{gg}}{\partial \theta} \Big|_{\bar{\mathbf{x}}} \quad (5.169)$$

$$F_{WW} = -J^{-1} \frac{\partial \left(\boldsymbol{\omega}_{B/I}^B \times [J \boldsymbol{\omega}_{B/I}^B] \right)}{\partial \boldsymbol{\omega}_{B/I}^B} \Big|_{\bar{\mathbf{x}}} = -J^{-1} \left(- \left[(J \bar{\boldsymbol{\omega}}_{B/I}^B) \times \right] + \left[\bar{\boldsymbol{\omega}}_{B/I}^B \times \right] J \right) \quad (5.170)$$

Detailed derivation of partial derivatives used in Eqs. 5.166 - 5.169 are given in Appendix A.

$$F_{x_1 x_2} = \frac{\partial \mathbf{f}_1}{\partial \mathbf{x}_2} \Big|_{\bar{\mathbf{x}}} = \begin{bmatrix} \mathbf{0}_{3 \times 3} & \mathbf{0}_{3 \times 1} & \mathbf{0}_{3 \times 1} & \mathbf{0}_{3 \times 1} & \mathbf{0}_{3 \times 3n} & \mathbf{0}_{3 \times 3n} & \mathbf{0}_{3 \times 3n} & \mathbf{0}_{3 \times 3n} \\ \mathbf{0}_{3 \times 3} & F_{V\beta} & F_{V\rho_r} & F_{Vh_s} & \mathbf{0}_{3 \times 3n} & \mathbf{0}_{3 \times 3n} & \mathbf{0}_{3 \times 3n} & \mathbf{0}_{3 \times 3n} \\ \mathbf{0}_{3 \times 3} & \mathbf{0}_{3 \times 1} & \mathbf{0}_{3 \times 1} & \mathbf{0}_{3 \times 1} & \mathbf{0}_{3 \times 3n} & \mathbf{0}_{3 \times 3n} & \mathbf{0}_{3 \times 3n} & \mathbf{0}_{3 \times 3n} \\ \mathbf{0}_{3 \times 3} & \mathbf{0}_{3 \times 1} & \mathbf{0}_{3 \times 1} & \mathbf{0}_{3 \times 1} & \mathbf{0}_{3 \times 3n} & \mathbf{0}_{3 \times 3n} & \mathbf{0}_{3 \times 3n} & \mathbf{0}_{3 \times 3n} \end{bmatrix}_{12 \times (6+12n)} \quad (5.171)$$

where

$$F_{V\beta} = \frac{\partial \mathbf{a}_{aero}^I}{\partial \beta} \Big|_{\bar{\mathbf{x}}} \quad (5.172)$$

$$F_{V\rho_r} = \frac{\partial \mathbf{a}_{aero}^I}{\partial \rho_r} \Big|_{\bar{\mathbf{x}}} \quad (5.173)$$

$$F_{Vh_s} = \frac{\partial \mathbf{a}_{aero}^I}{\partial h_s} \Big|_{\bar{\mathbf{x}}} \quad (5.174)$$

Detailed derivation of partial derivatives used in Eqs. 5.172 - 5.174 are given in Appendix A.

$$F_{x_2 x_1} = \frac{\partial \mathbf{f}_2}{\partial \mathbf{x}_1} \Big|_{\bar{\mathbf{x}}} = \mathbf{0}_{(6+12n) \times 12} \quad (5.175)$$

$$F_{x_2x_2} = \left. \frac{\partial \mathbf{f}_2}{\partial \mathbf{x}_2} \right|_{\bar{\mathbf{x}}} \quad (5.176)$$

That is,

$$F_{x_2x_2} = \begin{bmatrix} -\frac{I_{3 \times 3}}{\tau_{\mathbf{r}_{CM/O}}} & \mathbf{0}_{3 \times 1} & \mathbf{0}_{3 \times 1} & \mathbf{0}_{3 \times 1} & \mathbf{0}_{3 \times 3n} & \mathbf{0}_{3 \times 3n} & \mathbf{0}_{3 \times 3n} & \mathbf{0}_{3 \times 3n} \\ \mathbf{0}_{1 \times 3} & -\frac{1}{\tau_\beta} & 0 & 0 & \mathbf{0}_{1 \times 3n} & \mathbf{0}_{1 \times 3n} & \mathbf{0}_{1 \times 3n} & \mathbf{0}_{1 \times 3n} \\ \mathbf{0}_{1 \times 3} & 0 & -\frac{1}{\tau_{pr}} & 0 & \mathbf{0}_{1 \times 3n} & \mathbf{0}_{1 \times 3n} & \mathbf{0}_{1 \times 3n} & \mathbf{0}_{1 \times 3n} \\ \mathbf{0}_{1 \times 3} & 0 & 0 & -\frac{1}{\tau_{hs}} & \mathbf{0}_{1 \times 3n} & \mathbf{0}_{1 \times 3n} & \mathbf{0}_{1 \times 3n} & \mathbf{0}_{1 \times 3n} \\ \mathbf{0}_{3n \times 3} & \mathbf{0}_{3n \times 1} & \mathbf{0}_{3n \times 1} & \mathbf{0}_{3n \times 1} & F_{\mathbf{r}_{a_i/O}} & \mathbf{0}_{3n \times 3n} & \mathbf{0}_{3n \times 3n} & \mathbf{0}_{3n \times 3n} \\ \mathbf{0}_{3n \times 3} & \mathbf{0}_{3n \times 1} & \mathbf{0}_{3n \times 1} & \mathbf{0}_{3n \times 1} & \mathbf{0}_{3n \times 3n} & F_{\mathbf{b}_i} & \mathbf{0}_{3n \times 3n} & \mathbf{0}_{3n \times 3n} \\ \mathbf{0}_{3n \times 3} & \mathbf{0}_{3n \times 1} & \mathbf{0}_{3n \times 1} & \mathbf{0}_{3n \times 1} & \mathbf{0}_{3n \times 3n} & \mathbf{0}_{3n \times 3n} & F_{\mathbf{f}_i} & \mathbf{0}_{3n \times 3n} \\ \mathbf{0}_{3n \times 3} & \mathbf{0}_{3n \times 1} & \mathbf{0}_{3n \times 1} & \mathbf{0}_{3n \times 1} & \mathbf{0}_{3n \times 3n} & \mathbf{0}_{3n \times 3n} & \mathbf{0}_{3n \times 3n} & F_{\boldsymbol{\epsilon}_i} \end{bmatrix} \quad \begin{matrix} (6+12n) \times (6+12n) \\ (5.177) \end{matrix}$$

where

$$F_{\mathbf{r}_{a_i/O}} = \left. \frac{\partial \dot{\mathbf{r}}_{a_i/O}}{\partial \mathbf{r}_{a_i/O}} \right|_{\bar{\mathbf{x}}} = -\frac{I_{3n \times 3n}}{\tau_{\mathbf{r}_{a_i/O}}} \quad (5.178)$$

$$F_{\mathbf{b}_i} = \left. \frac{\partial \dot{\mathbf{b}}_i}{\partial \mathbf{b}_i} \right|_{\bar{\mathbf{x}}} = -\frac{I_{3n \times 3n}}{\tau_{\mathbf{b}_i}} \quad (5.179)$$

$$F_{\mathbf{f}_i} = \left. \frac{\partial \dot{\mathbf{f}}_i}{\partial \mathbf{f}_i} \right|_{\bar{\mathbf{x}}} = -\frac{I_{3n \times 3n}}{\tau_{\mathbf{f}_i}} \quad (5.180)$$

$$F_{\boldsymbol{\epsilon}_i} = \left. \frac{\partial \dot{\boldsymbol{\epsilon}}_i}{\partial \boldsymbol{\epsilon}_i} \right|_{\bar{\mathbf{x}}} = -\frac{I_{3n \times 3n}}{\tau_{\boldsymbol{\epsilon}_i}} \quad (5.181)$$

The linearized accelerometer measurements can be summarized as follow

$$\delta \tilde{a}_i^{\tilde{a}_i} = \left[\left. \frac{\partial \mathbf{h}_{3n}}{\partial \mathbf{r}_{CM/E}^I} \right|_{\bar{\mathbf{x}}} \quad \left. \frac{\partial \mathbf{h}_{3n}}{\partial \mathbf{v}_{CM/E}^I} \right|_{\bar{\mathbf{x}}} \quad \left. \frac{\partial \mathbf{h}_{3n}}{\partial \boldsymbol{\theta}_{I \rightarrow B}} \right|_{\bar{\mathbf{x}}} \quad \left. \frac{\partial \mathbf{h}_{3n}}{\partial \boldsymbol{\omega}_{B/I}^B} \right|_{\bar{\mathbf{x}}} \quad \left. \frac{\partial \mathbf{h}_{3n}}{\partial \mathbf{r}_{CM/O}^B} \right|_{\bar{\mathbf{x}}} \quad \left. \frac{\partial \mathbf{h}_{3n}}{\partial \beta} \right|_{\bar{\mathbf{x}}} \right]$$

$$\left. \begin{array}{c} \frac{\partial \mathbf{h}_{3n}}{\partial \rho_r} \Big|_{\bar{\mathbf{x}}} \quad \frac{\partial \mathbf{h}_{3n}}{\partial h_s} \Big|_{\bar{\mathbf{x}}} \quad \frac{\partial \mathbf{h}_{3n}}{\partial \mathbf{r}_{a_i/O}^B} \Big|_{\bar{\mathbf{x}}} \quad \frac{\partial \mathbf{h}_{3n}}{\partial \mathbf{b}_i^{a_i}} \Big|_{\bar{\mathbf{x}}} \quad \frac{\partial \mathbf{h}_{3n}}{\partial \mathbf{f}_i^{a_i}} \Big|_{\bar{\mathbf{x}}} \quad \frac{\partial \mathbf{h}_{3n}}{\partial \boldsymbol{\epsilon}_i^{a_i}} \Big|_{\bar{\mathbf{x}}} \end{array} \right]_{3n \times (18+12n)} \delta \mathbf{x} + \boldsymbol{\eta}_i^{\tilde{a}_i} \quad (5.182)$$

where partials in Eq. 5.182 are given in Section 5.7.

Similarly, the linearized star camera measurements can be summarized as follow

$$\delta \tilde{\mathbf{s}}^{\tilde{s}} = \left[\begin{array}{cccccc} 0_{3 \times 3} & 0_{3 \times 3} & I_{3 \times 3} & 0_{3 \times 3} & 0_{3 \times 3} & 0_{3 \times 1} \\ 0_{3 \times 1} & 0_{3 \times 1} & 0_{3 \times 3n} & 0_{3 \times 3n} & 0_{3 \times 3n} & 0_{3 \times 3n} \end{array} \right]_{3 \times (18+12n)} \delta \mathbf{x} + \boldsymbol{\eta}_{sc}^{\tilde{s}} \quad (5.183)$$

where partials in Eq. 5.183 are given in Section 5.7.

5.9 Summary

In this chapter, the non-linear dynamics and measurement equations for onboard autonomous orbital navigation based on accelerometer measurements were presented. Detailed linearized dynamical and measurement models were provided, along with important equations required to conduct Linear Covariance (LinCov) analysis.

CHAPTER 6

Observability Analysis

6.1 Chapter Overview

This chapter provides a simple, heuristic and intuitive argument for orbit observability based on gravity-gradient measurements. More specifically, a pictorial representation of gravity gradients in a point-mass gravity field is used to show that an onboard measurement of the local gravity gradient can be associated with a specific on-orbit position (with one ambiguity). It is then postulated that position and velocity will be observable if measurements of the local gravity gradient are taken over a period of time.

Results are presented to show that orbital position, velocity, and attitude are all observable using a configuration of six 3-axis accelerometers (i.e., a gradiometer). It is then shown that measurements from just one 3-axis accelerometer can provide orbital and attitude observability.

This chapter is based on the paper presented by Geller and Bhatia at AAS/AIAA Astrodynamics Conference 2018 [46].

6.2 Theoretical Setup

A number of studies have made thorough efforts to analytically and mathematically decode the geophysical, gravitational and spatial information ciphered in the gravity gradient measurements. However, while a gravitational acceleration vector is relatively easy to visualize as an “arrow” with a direction and magnitude, the gravity-gradient tensor is not as easy to visualize. Figure 6.1 (left) shows the gravity field near a point located at a position \mathbf{r}_{cm} from the center of the Earth. An axis of symmetry exists about the radial direction for a point mass gravity field. The difference between the gravity vector at position \mathbf{r} and the gravity vector at a point near \mathbf{r} is shown in Figure 6.1 (right). This picture is a fairly

accurate representation of the gravity gradient tensor for a point mass gravity field: the eigenvectors of the tensor are aligned with the vectors in the figure, the eigenvalues are both positive (tension) and negative (compression), and the sum of the eigenvalues equals zero (note that the third axis, not shown in Figure 6.1, is an axis of compression) [47].

$$\lambda_1 = 2\mu/\|\mathbf{r}\|^3, \quad \lambda_2 = \lambda_3 = -\mu/\|\mathbf{r}\|^3$$

Thus, the 5 independent parameters of the gravity-gradient matrix can then be interpreted as follows: λ_1, λ_2 , two angles defining the direction of the first eigenvector \mathbf{e}_1 , and a third angle defining the direction of the second eigenvector \mathbf{e}_2 (since \mathbf{e}_2 is by definition orthogonal to \mathbf{e}_1). The third eigenvalue is given by $\lambda_3 = -\lambda_1 - \lambda_2$, and the third eigenvector is defined by $\mathbf{e}_3 = \mathbf{e}_1 \times \mathbf{e}_2$ [3].

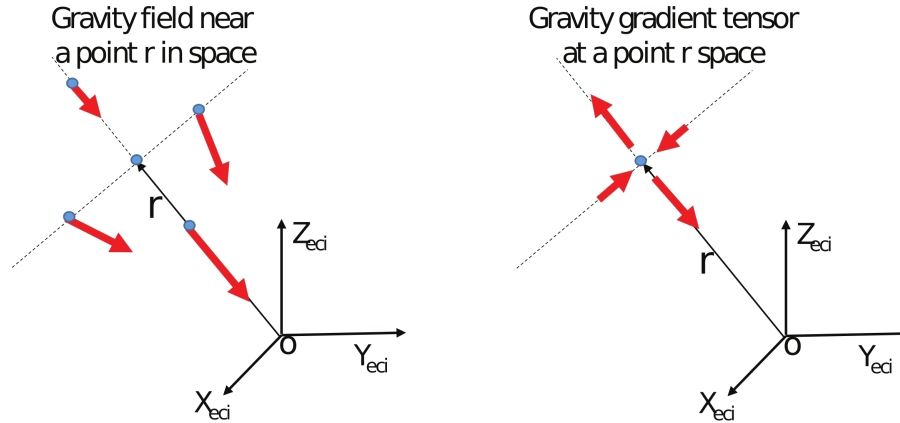


Fig. 6.1: Gravity field near a position \mathbf{r} (left); gravity-gradient tensor at a position \mathbf{r} (right)

Consider a spacecraft with center-of-mass located at a position \mathbf{r}_{cm} in the gravity field as shown in Figure 6.2. If the spacecraft has a single perfect accelerometer located near its center-of-mass, and if the spacecraft is non-rotating and subject only to gravitational acceleration, \mathbf{g} , the measurement obtained from the perfect accelerometer is given by

$$\tilde{\mathbf{a}}_i^b = T_I^b(\boldsymbol{\theta}_I^b) \left[\mathbf{g}^I(\mathbf{r}_{cm/o}^I) - \mathbf{g}^I(\mathbf{r}_{cm/o}^I + \mathbf{r}_{a_i/cm}^I) \right] \quad (6.1)$$

This measurement looks similar to a gravity gradient measurement, but the measurement is a vector while the gravity gradient is a tensor. The accelerometer measurement is actually an approximation of the projection of the gravity gradient tensor onto the direction of $\mathbf{r}_{a_i/cm}^I$

$$\tilde{\mathbf{a}}_i \approx \frac{\partial \mathbf{g}}{\partial \mathbf{r}_{cm/o}^I} \mathbf{r}_{a_i/cm} \quad (6.2)$$

Thus, more than one accelerometer measurement is needed to obtain the local gravity-gradient tensor and its 5 parameters.

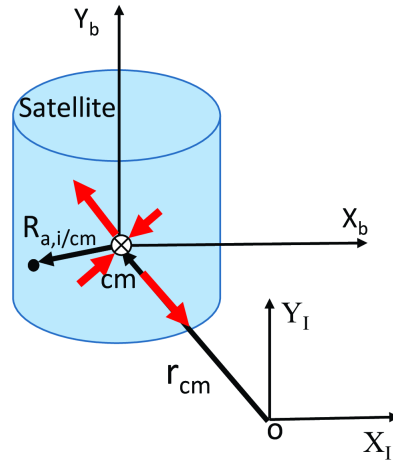


Fig. 6.2: Position of the center-of-mass of a spacecraft with respect to an inertial frame, and position of the i th accelerometer with respect to the center-of-mass .

Figure 6.3 shows a “field” of gravity-gradient tensors for a point-mass gravity model. The field of tensors is symmetric about any plane containing the origin and decreases in magnitude as a function of altitude. Figure 6.3 also shows a non-rotating spacecraft with a known orientation (for example using a star camera) subject only to gravitational forces .

Without loss of generality, it is assumed the vehicle body axes are aligned with the Earth-centered inertial frame.

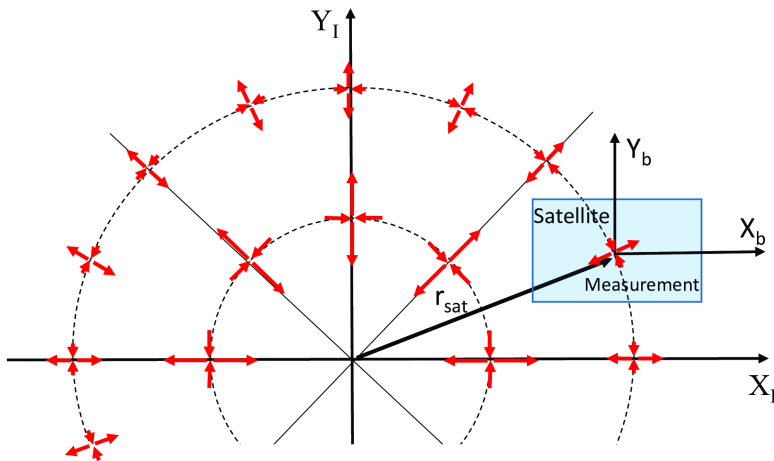


Fig. 6.3: Field of gravity-gradient tensors, and satellite measurement of the gravity gradient tensor in the body frame .

If the spacecraft has a set of perfect accelerometers, a perfect measurement of the gravity-gradient in the body frame can be obtained. Since the orientation of the spacecraft is known, there are only two possible inertial positions in which this gravity gradient tensor measurements could have been obtained, position \mathbf{r}_{sat} , and position $-\mathbf{r}_{sat}$. Hence, position is observable (with one ambiguity) based on one measurement of the gravity-gradient tensor. If two or more measurements of the gravity-gradient tensor separated by Δt seconds are obtained, velocity can be inferred, and complete orbit observability, i.e., position and velocity observability, is achieved.

Regarding the ambiguity in the observed position vector, it is postulated that a unique position, velocity, and therefore orbit, can be determined when a more complex, non-symmetric gravity field is employed.

If these heuristic arguments are applied to the case where both the attitude and orbit are unknown, one can see that full attitude and orbit observability are not possible for a

point-mass gravity field. For example, if the attitude of the spacecraft is unknown, the possible locations where the measured gravity-gradient equals the actual gravity gradient can be anywhere on a sphere of radius $\|\mathbf{r}_{sat}\|$. This is illustrated in Figure 6.4. Thus, the orbit and attitude are probably not observable for a point-mass gravity field.

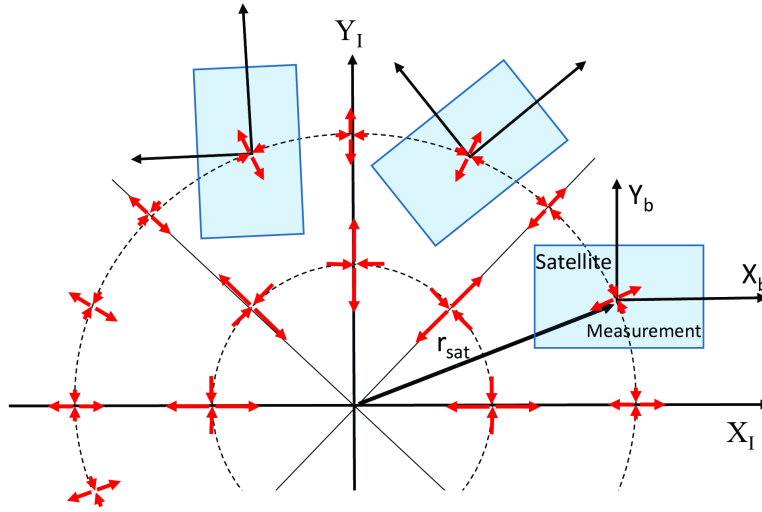


Fig. 6.4: Different satellite orientations with the same measurement of the gravity-gradient tensor in the body frame .

The above arguments however are only heuristic. A more quantitative and definitive approach is taken in the next two sections. In fact, it will be shown that both the attitude and orbit are observable in a a more complex, “lumpy” gravity field.

6.3 Mathematical Setup

In this section, a quantitative standard observability analysis is conducted to demonstrate that three 3-axis onboard accelerometer measurements can provide both orbit and attitude observability, i.e., orbital position, velocity, and attitude observability. It is assumed that the only forces acting on the spacecraft are due to either a simple point-mass gravity model or and $n \times n$ spherical harmonic gravity model. It is also assumed that the angular velocity and angular acceleration of the spacecraft is known and equal to zero.

The analysis is then extended to show that only two, and then only one 3-axis accelerometer is required to obtain full-state, position, velocity, and attitude observability under the given assumptions.

The observability metrics used in this analysis are the rank and condition number of the classical observability Gramian. Special care is taken to ensure the observability Gramian is a well-conditioned matrix.

The simplified dynamics model is defined by the state vector

$$\mathbf{x} = \begin{bmatrix} \mathbf{r}_{cm/o}^I \\ \mathbf{v}_{cm/o}^I \\ \boldsymbol{\theta}_I^b \end{bmatrix} \quad (6.3)$$

where $\mathbf{r}_{cm/o}^I$, $\mathbf{v}_{cm/o}^I$, and $\boldsymbol{\theta}_I^b$ denote the inertial position, velocity, and attitude of the spacecraft, respectively. Since the spacecraft is assumed to be non-rotating, the dynamics model is given by

$$\dot{\mathbf{x}} = f(\mathbf{x}, t) = \begin{bmatrix} \mathbf{v}_{cm/o}^I \\ \mathbf{g}^I(\mathbf{r}_{cm/o}^I) \\ \mathbf{0} \end{bmatrix} \quad (6.4)$$

where $\mathbf{g}^I(\mathbf{r}_{cm/o}^I)$ is the acceleration due to gravity. The 9×9 Jacobian, F , for this system is given by

$$F(t) = \left. \frac{\partial f}{\partial \mathbf{x}} \right|_{\mathbf{x}_n(t)} = \left[\begin{array}{ccc} 0_{3 \times 3} & I_{3 \times 3} & 0_{3 \times 3} \\ \nabla \mathbf{g} & 0_{3 \times 3} & 0_{3 \times 3} \\ 0_{3 \times 3} & 0_{3 \times 3} & 0_{3 \times 3} \end{array} \right] \Bigg|_{\mathbf{x}_n(t)} \quad (6.5)$$

where $\nabla \mathbf{g} = \partial \mathbf{g} / \partial \mathbf{r}_{cm/o}^I$, and the indicated partial derivative is evaluated along a nominal trajectory $\mathbf{x}_n(t)$.

The simplified measurement model for the i th accelerometer is given by

$$\tilde{\mathbf{a}}_i^b = T_I^b(\boldsymbol{\theta}_I^b) \left[\mathbf{g}^I(\mathbf{r}_{cm/o}^I) - \mathbf{g}^I(\mathbf{r}_{cm/o}^I + T_b^I(-\boldsymbol{\theta}_I^b) \mathbf{r}_{ai/cm}^b) \right] + \boldsymbol{\eta}_i^b \quad (6.6)$$

where $\tilde{\mathbf{a}}_i^b$ is the accelerometer measurement in body-fixed frame, $\mathbf{r}_{a_i/cm}^b$ is the position of the accelerometer with respect to the center-of-mass in the body-fixed frame, $T_I^b(\boldsymbol{\theta}_I^b)$ is the inertial to body transformation, $\mathbf{g}^I(\mathbf{r}_{cm/o}^I)$ is the gravitational acceleration at position $\mathbf{r}_{cm/o}^I$, and $\boldsymbol{\eta}_i^b$ is zero mean measurement noise.

The measurement geometry vector is given by

$$\mathbf{h}_i(t_j) = \left. \frac{\partial \tilde{\mathbf{a}}_i^b}{\partial \mathbf{x}} \right|_{\mathbf{x}_n} = \left[\frac{\partial \tilde{\mathbf{a}}_i^b}{\partial \mathbf{r}_{cm/o}^I}, \quad \mathbf{0}_{3 \times 3}, \quad \frac{\partial \tilde{\mathbf{a}}_i^b}{\partial \boldsymbol{\theta}_I^b} \right]_{\mathbf{x}_n(t)} \quad (6.7)$$

where

$$\frac{\partial \tilde{\mathbf{a}}_i^b}{\partial \mathbf{r}_{cm/o}^I} = T_I^b(\boldsymbol{\theta}_I^b) \left[\nabla \mathbf{g}^I(\mathbf{r}_{cm/o}^I) - \nabla \mathbf{g}^I(\mathbf{r}_{cm/o}^I + T_b^I(-\boldsymbol{\theta}_I^b) \mathbf{r}_{a_i/cm}^b) \right] \quad (6.8)$$

$$\frac{\partial \tilde{\mathbf{a}}_i^b}{\partial \boldsymbol{\theta}_I^b} = [M \times] + T_I^b(\boldsymbol{\theta}_I^b) \nabla \mathbf{g}^I(\mathbf{r}_{cm/o}^I + T_b^I(-\boldsymbol{\theta}_I^b) \mathbf{r}_{a_i/cm}^b) T_b^I(-\boldsymbol{\theta}_I^b) [\mathbf{r}_{a_i/cm}^b \times] \quad (6.9)$$

$$M = T_I^b(\boldsymbol{\theta}_I^b) \left[\nabla \mathbf{g}^I(\mathbf{r}_{cm/o}^I) - \nabla \mathbf{g}^I(\mathbf{r}_{cm/o}^I + T_b^I(-\boldsymbol{\theta}_I^b) \mathbf{r}_{a_i/cm}^b) \right]$$

and where the expression $[\mathbf{Z} \times]$ represents a skew-symmetric matrix associated with the vector \mathbf{Z} , i.e., $[\mathbf{Z} \times] \mathbf{a} = \mathbf{Z} \times \mathbf{a}$.

For N accelerometers, the measurement partial is $3N \times 9$ and given by

$$H(t_j) = \begin{bmatrix} \mathbf{h}_1(t_j) \\ \vdots \\ \mathbf{h}_N(t_j) \end{bmatrix} \quad (6.10)$$

Finally, the observability Gramian after m measurements is given by [9]

$$\mathcal{O}(t_m) \triangleq \sum_{j=1}^m \phi^T(t_j, t_0) H^T(t_j) H(t_j) \phi(t_j, t_0) \quad (6.11)$$

where the state transition matrix $\phi(t_j, t_0)$ is computed recursively as

$$\phi(t_j, t_0) = \phi(t_j, t_{j-1}) \phi(t_{j-1}, t_0), \quad \phi(t_0, t_0) = I_{9 \times 9} \quad (6.12)$$

and where

$$\phi(t_j, t_{j-1}) \approx I_{9 \times 9} + F(t_{j-1})\Delta t + F^2(t_{j-1})\Delta t^2/2 + \dots \quad (6.13)$$

Based on this approach, the condition number of the observability Gramian was found to be very large, and it was suspected that the problem was due to the scaling of the problem rather than the matrix actually being near singular (the columns of $\mathbf{h}_i(t_j)$ associated with $\partial \tilde{\mathbf{a}}_i^b / \partial \mathbf{r}_{cm/o}^I$ are many orders of magnitude smaller than the columns associated with $\partial \tilde{\mathbf{a}}_i^b / \partial \boldsymbol{\theta}_I^b$). To solve this, the problem was scaled as follows

$$\bar{\mathbf{x}} = \begin{bmatrix} \mathbf{r}_{cm/o}^I / R_c \\ \mathbf{v}_{cm/o}^I / V_c \\ \boldsymbol{\theta}_I^b \end{bmatrix} \quad (6.14)$$

where R_c and V_c are the mean orbital radius and velocity of the nominal trajectory. Using the scaled state vector $\bar{\mathbf{x}}$ the Jacobian becomes

$$\bar{F} = \left[\begin{array}{ccc} 0_{3 \times 3} & \frac{V_c}{R_c} I_{3 \times 3} & 0_{3 \times 3} \\ \frac{R_c}{V_c} \nabla \mathbf{g} & 0_{3 \times 3} & 0_{3 \times 3} \\ 0_{3 \times 3} & 0_{3 \times 3} & 0_{3 \times 3} \end{array} \right] \bigg|_{\bar{\mathbf{x}}_n(t)} \quad (6.15)$$

and the measurement partial for N accelerometers is given by

$$\bar{H}(t_j) = \begin{bmatrix} \bar{\mathbf{h}}_1(t_j) \\ \vdots \\ \bar{\mathbf{h}}_N(t_j) \end{bmatrix} \quad (6.16)$$

where

$$\bar{\mathbf{h}}_i(t_j) = \frac{\partial \mathbf{a}_i^b}{\partial \bar{\mathbf{x}}} \bigg|_{\bar{\mathbf{x}}_n(t)} = \left[R_c \frac{\partial \tilde{\mathbf{a}}_i^b}{\partial \mathbf{r}_{cm/o}^I}, \quad 0_{3 \times 3}, \quad \frac{\partial \tilde{\mathbf{a}}_i^b}{\partial \boldsymbol{\theta}_I^b} \right]_{\mathbf{x}_n(t)} \quad (6.17)$$

So, in terms of the scaled state vector $\bar{\mathbf{x}}$, the observability Gramian is given by

$$\bar{O}(t_m) \triangleq \sum_{j=1}^m \bar{\phi}^T(t_j, t_0) \bar{H}^T(t_j) \bar{H}(t_j) \bar{\phi}(t_j, t_0) \quad (6.18)$$

where again the state transition matrix $\bar{\phi}(t_j, t_0)$ is computed recursively as

$$\bar{\phi}(t_j, t_0) = \bar{\phi}(t_j, t_{j-1}) \bar{\phi}(t_{j-1}, t_0), \quad \bar{\phi}(t_0, t_0) = I_{9 \times 9} \quad (6.19)$$

and where

$$\bar{\phi}(t_j, t_{j-1}) \approx I_{9 \times 9} + \bar{F}(t_{j-1}) \Delta t + \bar{F}^2(t_{j-1}) \Delta t^2 / 2 + \dots \quad (6.20)$$

6.4 Results

In this section, the rank and condition number of the observability Gramian in Eq. 6.18 are used as a metric to determine orbit and attitude observability. The analysis looks at two different nominal LEO spacecraft orbits, 2 different gravity models, and 3 different accelerometer configurations. In all cases, measurements are taken for 1500 seconds with a sample rate of 30 sec. The nominal vehicle orientation is constant and aligned with the inertial frame. The gravity models are either a point mass gravity model or a 4×4 spherical harmonics model. The LEO orbits have a semi-major axis equal to 7000 km and an inclination of 56 degrees. The first orbit is circular and the second orbit has an eccentricity $e=0.01$.

Three 3-Axis Accelerometers

In this case three 3-axis accelerometers are mounted 0.5 m from the spacecraft center-of-mass along 3 perpendicular axes. The results of the observability analysis are shown below in Table 6.1.

Table 6.1 shows that with three 3-axis accelerometers the orbit and attitude are unobservable for only the circular orbit, point mass gravity model case. This confirms the conclusion drawn at the end Section 6.2. All other cases with three 3-axis accelerometers, including the point mass elliptical orbit case are observable.

Three 3-Axis Accelerometers											
	Point Mass				4 × 4 Spherical				8 × 8 Spherical		
	Rank	Cond #	U/O		Rank	Cond #	U/O		Rank	Cond #	U/O
Circular	8	2.5×10^{16}	U		9	3.9×10^8	O		9	3.6×10^8	O
Elliptical	9	1.0×10^{12}	O		9	3.6×10^8	O		9	3.6×10^8	O

Table 6.1: Orbit and Attitude Observability (O)/Unobservability (U) using three 3-axis accelerometers .

One 3-Axis Accelerometer

In this case one 3-axis accelerometer is mounted 0.5 m from the spacecraft center-of-mass. The results of the observability analysis are shown below in Table 6.2.

One 3-Axis Accelerometer											
	Point Mass				4 × 4 Spherical				8 × 8 Spherical		
	Rank	Cond #	U/O		Rank	Cond #	U/O		Rank	Cond #	U/O
Circular	7	1.6×10^{18}	U		9	1.5×10^9	O		9	1.3×10^9	O
Elliptical	9	5.7×10^{12}	O		9	1.2×10^9	O		9	1.1×10^9	O

Table 6.2: Orbit and Attitude Observability (O)/Unobservability (U) using one 3-axis accelerometer .

The observability results for the one 3-axis accelerometer cases shown in Table 6.2 are the same as the for the three 3-axis accelerometer cases in Table 6.1. However, the condition numbers are all higher indicating weaker observability.

One 2-Axis Accelerometer

In this case one 2-axis accelerometers is mounted 0.5 m from the spacecraft center-of-mass. The results of the observability analysis are shown below in Table 6.3.

One 2-Axis Accelerometer											
	Point Mass				4 × 4 Spherical				8 × 8 Spherical		
	Rank	Cond #	U/O		Rank	Cond #	U/O		Rank	Cond #	U/O
Circular	7	9.6×10^{16}	U		9	1.5×10^{10}	O		9	7.5×10^9	O
Elliptical	9	8.6×10^{12}	O		9	1.1×10^{10}	O		9	6.2×10^9	O

Table 6.3: Orbit and Attitude Observability (O)/Unobservability (U) using one 2-axis accelerometer .

The trend continues for one 2-axis accelerometer, i.e., the observability results are the same, but the conditions numbers are higher indicating still weaker observability.

One Single-Axis Accelerometer

In this case one single-axis accelerometer is mounted 0.5 m from the spacecraft center-of-mass. The results of the observability analysis are shown below in Table 6.4. All cases indicate a lack of observability.

One Single-Axis Accelerometer											
	Point Mass				4 × 4 Spherical				8 × 8 Spherical		
	Rank	Cond #	U/O		Rank	Cond #	U/O		Rank	Cond #	U/O
Circular	6	1.6×10^{34}	U		8	2.4×10^{27}	U		8	2.1×10^{27}	U
Elliptical	6	8.2×10^{33}	U		8	2.4×10^{27}	U		8	4.2×10^{28}	U

Table 6.4: Orbit and Attitude Observability (O)/Unobservability (U) using one single-axis accelerometer .

The above results show that even in the best case, the conditions number are on the order of 10^8 . This relatively high value leads to the suspicion that the inertial attitude is relatively weakly observable. To confirm this, the above observability analysis was repeated with a state vector consisting of only position and velocity. The attitude was assumed to be known. The results of this observability analysis are shown in Table 6.5-6.8 below.

Three 3-Axis Accelerometers											
	Point Mass				4 × 4 Spherical				8 × 8 Spherical		
	Rank	Cond #	U/O		Rank	Cond #	U/O		Rank	Cond #	U/O
Circular	6	110	O		6	110	O		6	110	O
Elliptical	6	106	O		6	106	O		6	106	O

Table 6.5: Orbit-Only Observability (O)/Unobservability (U) using three 3-axis accelerometers .

One 3-Axis Accelerometer											
	Point Mass				4 × 4 Spherical				8 × 8 Spherical		
	Rank	Cond #	U/O		Rank	Cond #	U/O		Rank	Cond #	U/O
Circular	6	357	O		6	359	O		6	359	O
Elliptical	6	345	O		6	347	O		6	347	O

Table 6.6: Orbit-Only Observability (O)/Unobservability (U) using one 3-axis accelerometer

One 2-Axis Accelerometer											
	Point Mass				4 × 4 Spherical				8 × 8 Spherical		
	Rank	Cond #	U/O		Rank	Cond #	U/O		Rank	Cond #	U/O
Circular	6	474	O		6	476	O		6	476	O
Elliptical	6	457	O		6	459	O		6	459	O

Table 6.7: Orbit-Only Observability (O)/Unobservability (U) using one 2-axis accelerometer

One Single-Axis Accelerometer											
	Point Mass				4 × 4 Spherical				8 × 8 Spherical		
	Rank	Cond #	U/O		Rank	Cond #	U/O		Rank	Cond #	U/O
Circular	6	2.1×10^{10}	O		6	2.1×10^{10}	O		6	1.1×10^{10}	O
Elliptical	6	2.0×10^{10}	O		6	2.3×10^{10}	O		6	1.1×10^{10}	O

Table 6.8: Orbit Observability (O)/Unobservability (U) using one single-axis accelerometer

These results show that position and velocity are strongly observable and confirm the suspicion that attitude is relatively weakly observable. Thus, it can be concluded that although it may be theoretically possible to estimate the orbital position, velocity, and attitude using a set of accelerometers, an accurate estimate of attitude may be difficult and require an additional sensor such as a star camera.

6.5 Summary

A preliminary observability analysis shows that in the presence of only gravitational accelerations orbital position, velocity, and attitude are all observable using a configuration of three 3-axis accelerometers. The measurements from just one 3-axis accelerometer, or even one 2-axis accelerometer can provide orbital and attitude observability. The evidence presented in this chapter suggests that the attitude is weakly observable, while the position and velocity are strongly observable.

CHAPTER 7

Linear Covariance (LinCov) Analysis Tool Development

7.1 Chapter Overview

This chapter provides the necessary theoretical background and mathematical equations to develop a Linear Covariance (LinCov) analysis tool. The aim is to introduce the reader to the mathematical process to setup the LinCov analysis tool and conduct a sensitivity analysis. This chapter highlights different error groups, used to interpret the error budget results in Chapter 9.

7.2 LinCov Models - Theory & Setup

Techniques like Monte Carlo analysis and Linear Covariance analysis are extensively used for modeling and simulating a range of possible operational scenarios and thereby enable the study of the effects of significant parameters on the overall mission performance. These techniques are particularly useful for guidance, navigation, and control (GN&C) analysis, and generally include the effects of environment, actuator, and sensor uncertainties, estimation errors, and most importantly, the effect of uncertainties and estimation errors on trajectory and attitude control errors [48].

Despite the initial overhead associated with the development of linear models, LinCov techniques have cost benefits when compared to Monte Carlo analysis [48]. This is because LinCov techniques produce the same statistical results with a single simulation run, thus saving tremendous amount of computational power and time [48]. Since the expected envelope of trajectories about the nominal is often very small for a general orbital dynamics problem, the conditions under which LinCov is valid (e.g. good linear models) are easily satisfied [48].

In a Linear Covariance approach, the system states are segmented into two parts, viz.

filter states and truth states. Further, the covariance of the filter states and the augmented states (truth and filter) are propagated and updated, so as to generate the covariance of the dispersions and navigation errors in a single simulation run.

7.2.1 Propagation

The filter state covariance \hat{P} and the augmented state covariance P_A are propagated as follow [5]

$$\hat{P}(t_{k+1}) = \hat{\phi} \hat{P}(t_k) \hat{\phi}^T + \hat{Q}_d \quad (7.1)$$

$$P_A(t_{k+1}) = \phi P_A(t_k) \phi^T + Q_d \quad (7.2)$$

where $\hat{\phi}$ and ϕ are the filter and augmented state transition matrices, defined as

$$\hat{\phi} = e^{\hat{F}_x dt} \quad (7.3)$$

$$\phi = e \left(\begin{bmatrix} F_x & 0_{z \times \hat{z}} \\ 0_{\hat{z} \times z} & \hat{F}_x \end{bmatrix} dt \right) \quad (7.4)$$

$$\hat{F}_x = \left. \frac{\partial \mathbf{f}}{\partial \hat{\mathbf{x}}} \right|_{\bar{\mathbf{x}}} \quad (7.5)$$

where F_x and \hat{F}_x are the true and filter state Jacobian given by Eq. 5.164 and Eq. 7.5, and z and \hat{z} represent the number of truth and filter states, respectively.

Now since for this study, the filter state model has the same states as the truth state model, and because the only notable difference between two models is the resolution of the gravity model, the partial derivatives needed to compute \hat{F}_x are the same (except the gravity partials) as that needed for F_x , and are given in detail in Chapter 5 and Appendix A.

For this study, the resolution of the truth gravity model has been set to 18×18 , whereas the resolution of the filter gravity model is set to 12×12 . Details about filter and truth models are also noted, alongside the results, in Chapter 9.

In Eq. 7.1 and Eq. 7.2, \hat{Q}_d and Q_d are the filter and augmented process noise covariance matrices for the filter and augmented states, defined as

$$\hat{Q}_d = \text{Diag} \begin{bmatrix} \mathbf{0}_{1 \times 3} & (Q_T + Q_{aero}) \Delta t & \mathbf{0}_{1 \times 3} & Q_R \Delta t & Q_{d_{\mathbf{r}_{CM/O}}} & Q_{d_\beta} \\ & Q_{d_{\rho_r}} & Q_{d_{h_s}} & Q_{d_{\mathbf{r}_{a_i/O}}} & Q_{d_{\mathbf{b}_i}} & Q_{d_{\mathbf{f}_i}} & Q_{d_{\epsilon_i}} \end{bmatrix}_{\hat{z} \times \hat{z}} \quad (7.6)$$

$$Q_d = \begin{bmatrix} \hat{Q}_d & 0_{z \times \hat{z}} \\ 0_{\hat{z} \times z} & 0_{\hat{z} \times \hat{z}} \end{bmatrix}_{(z+\hat{z}) \times (z+\hat{z})} \quad (7.7)$$

In Eq. 7.6, Q_T is the power spectral density (PSD) of the translational disturbance acceleration (m^2/s^3), Q_{aero} is the power spectral density (PSD) of the unmodeled aerodynamic acceleration (m^2/s^3), and Q_R is the power spectral density (PSD) of the rotational disturbance acceleration ($1/s^3$), respectively. The integration/discretization time step is denoted by Δt .

Further, in Eq. 7.6, $Q_{d_{\mathbf{r}_{CM/O}}}$, Q_{d_β} , $Q_{d_{\rho_r}}$, $Q_{d_{h_s}}$, $Q_{d_{\mathbf{r}_{a_i/O}}}$, $Q_{d_{\mathbf{b}_i}}$, $Q_{d_{\mathbf{f}_i}}$, and $Q_{d_{\epsilon_i}}$ are the variance of the linearized unmodeled noise in the center of mass position (m^2), ballistic coefficient (m^4/kg^2), reference atmospheric density (kg^2/m^6), scale height (m^2), i^{th} accelerometer position (m^2), accelerometer bias (m^2/s^4), accelerometer scale factor (unit-less), and accelerometer misalignment (rad^2), respectively. These are defined in Eqs. 5.121, 5.102, 5.104, 5.106, 5.123, 5.125, 5.127, and 5.129, respectively.

7.2.2 Update - Accelerometer Measurements

The filter \hat{P} covariance is updated as follow [5]

$$\hat{P}(t_k^+) = \left[I - \hat{K}(t_k) \hat{H}_{\hat{x}}(t_k) \right] \hat{P}(t_k) \left[I - \hat{K}(t_k) \hat{H}_{\hat{x}}(t_k) \right]^T + \hat{K}(t_k) \hat{R}_a(t_k) \hat{K}^T(t_k) \quad (7.8)$$

$$\hat{K}(t_k) = \hat{P}(t_k) \hat{H}_{\hat{x}}^T(t_k) \left[\hat{H}_{\hat{x}}(t_k) \hat{P}(t_k) \hat{H}_{\hat{x}}^T(t_k) + \hat{R}_a(t_k) \right]^{-1} \quad (7.9)$$

$$\hat{H}_{\hat{x}} = \left. \frac{\partial \mathbf{h}}{\partial \hat{\mathbf{x}}} \right|_{\hat{\mathbf{x}}} \quad (7.10)$$

where $\hat{K}(t_k)$ is the Kalman gain, and $\hat{H}_{\hat{x}}(t_k)$ is the filter measurement partial matrix given by Eq. 7.10 (for accelerometer measurements).

In Eq. 7.8 and Eq. 7.9, the filter measurement noise covariance is denoted by $\hat{R}_a(t_k)$ and is given by

$$E[\hat{\boldsymbol{\eta}}_i^{\tilde{a}_i}(t) \hat{\boldsymbol{\eta}}_i^{\tilde{a}_i}(t')^T] = Q_{\hat{\boldsymbol{\eta}}_i} \delta(t - t') \quad (7.11)$$

$$\hat{R}_a(t_k) = \frac{Q_{\hat{\boldsymbol{\eta}}_i}}{\delta t_{meas}} \quad (7.12)$$

where $\hat{\boldsymbol{\eta}}_i^{\tilde{a}_i}$ is the accelerometer measurement noise, modeled as zero-mean white Gaussian noise, used in the filter model. The strength of the accelerometer measurement noise is denoted by $Q_{\hat{\boldsymbol{\eta}}_i}$, and δt_{meas} is measurement update time in seconds, as used in the filter model. Note the size of $\hat{R}_a(t_k)$ is $3n \times 3n$, where n is the number of accelerometers on-board.

The augmented P_A covariance is updated as follow [5]

$$P_A(t_k^+) = A_k(t_k) P_A(t_k) A_k^T(t_k) + B_k(t_k) R_a(t_k) B_k^T(t_k) \quad (7.13)$$

$$A_k(t_k) = \begin{bmatrix} I_{z \times z} & 0_{z \times \hat{z}} \\ \hat{K}(t_k) H_x(t_k) & I_{\hat{z} \times \hat{z}} - \hat{K}(t_k) \hat{H}_{\hat{x}}(t_k) \end{bmatrix} \quad (7.14)$$

$$B_k(t_k) = \begin{bmatrix} 0_{z \times (z + \hat{z})} \\ \hat{K}(t_k) \end{bmatrix} \quad (7.15)$$

where $H_x(t_k)$ is the truth measurement partial matrix given by Eq. 5.131 (for accelerometer measurements), and $R_a(t_k)$ is the truth measurement noise covariance given by Eq. 5.84 (for accelerometer measurements), respectively. In Eq. 7.14 and Eq. 7.15, z and \hat{z} represent the number of truth and filter states.

As stated in Section 7.2.1, the filter state model has the same states as the truth state model, and because the only notable difference between two models is the resolution of the gravity model, the partial derivatives needed to compute $\hat{H}_{\hat{x}}(t_k)$ are the same (except the gravity partials) as that needed for $H_x(t_k)$, and are given in detail in Chapter 5 and Appendix A.

7.2.3 Update - Star Camera Measurements

The filter \hat{P} covariance is updated as follow [5]

$$\hat{P}(t_k^+) = \left[I - \hat{K}(t_k) \hat{L}_{\hat{x}}(t_k) \right] \hat{P}(t_k) \left[I - \hat{K}(t_k) \hat{L}_{\hat{x}}(t_k) \right]^T + \hat{K}(t_k) \hat{R}_{sc}(t_k) \hat{K}^T(t_k) \quad (7.16)$$

$$\hat{K}(t_k) = \hat{P}(t_k) \hat{L}_{\hat{x}}^T(t_k) \left[\hat{L}_{\hat{x}}(t_k) \hat{P}(t_k) \hat{L}_{\hat{x}}^T(t_k) + \hat{R}_{sc}(t_k) \right]^{-1} \quad (7.17)$$

$$\hat{L}_{\hat{x}} = \left. \frac{\partial \mathbf{l}}{\partial \hat{\mathbf{x}}} \right|_{\bar{\mathbf{x}}} \quad (7.18)$$

where $\hat{K}(t_k)$ is the Kalman gain, and $\hat{L}_{\hat{x}}(t_k)$ is the filter measurement partial matrix given by Eq. 7.18 (for star camera measurements).

In Eq. 7.16 and Eq. 7.17, the filter measurement noise covariance is denoted by $\hat{R}_{sc}(t_k)$ and is given by

$$E[\hat{\boldsymbol{\eta}}_{sc,i}^{\tilde{s}} \hat{\boldsymbol{\eta}}_{sc,j}^{\tilde{s}T}] = Q_{\hat{\boldsymbol{\eta}}_{sc}} \delta_{ij} \quad (7.19)$$

where δ_{ij} is a Kronecker delta function, and $\hat{\boldsymbol{\eta}}_{sc}^{\tilde{s}}$ is a vector of zero-mean white Gaussian noise on the star camera measurements, as used in filter model. The covariance of the measurement noise for the star camera measurements is denoted by $Q_{\hat{\boldsymbol{\eta}}_{sc}}$ (rad^2), i.e.,

$$\hat{R}_{sc}(t_k) = Q_{\hat{\boldsymbol{\eta}}_{sc}} \quad (7.20)$$

Note the size of $\hat{R}_{sc}(t_k)$ is $3n \times 3n$, where n is the number of star cameras on-board.

The augmented P_A covariance is updated as follow [5]

$$P_A(t_k^+) = A_k(t_k) P_A(t_k) A_k^T(t_k) + B_k(t_k) R_{sc}(t_k) B_k^T(t_k) \quad (7.21)$$

$$A_k(t_k) = \begin{bmatrix} I_{z \times z} & 0_{z \times \hat{z}} \\ \hat{K}(t_k) L_x(t_k) & I_{\hat{z} \times \hat{z}} - \hat{K}(t_k) \hat{L}_{\hat{x}}(t_k) \end{bmatrix} \quad (7.22)$$

$$B_k(t_k) = \begin{bmatrix} 0_{z \times (z + \hat{z})} \\ \hat{K}(t_k) \end{bmatrix} \quad (7.23)$$

where $L_x(t_k)$ is the truth measurement partial matrix given by Eq. 5.157 (for star camera measurements), and $R_{sc}(t_k)$ is the truth measurement noise covariance given by Eq. 5.92 (for star camera measurements), respectively. In Eq. 7.22 and Eq. 7.23, z and \hat{z} represent the number of truth and filter states.

As stated in Section 7.2.1, the filter state model has the same states as the truth state model, and because the only notable difference between two models is the resolution of the gravity model, the partial derivatives needed to compute $\hat{L}_{\hat{x}}(t_k)$ are the same (except the gravity partials) as that needed for $L_x(t_k)$, and are given in detail in Chapter 5 and Appendix A.

7.2.4 Performance Evaluation

Covariance of the true navigation state errors P_{true} and covariance of the filter state errors \hat{P} are used to evaluate the performance of the onboard navigation system.

$$P_{true} = \begin{bmatrix} -M_x & I_{\hat{z} \times \hat{z}} \end{bmatrix} P_A \begin{bmatrix} -M_x & I_{\hat{z} \times \hat{z}} \end{bmatrix}^T \quad (7.24)$$

where M_x is the partial with respect to the true state of the mapping function defined as [49]

$$M_x = I_{\hat{z} \times z} \quad (7.25)$$

P_{true} is compared with \hat{P} to determine the performance of the filter. True navigation error provides insight into the navigation performance. The true navigation error is also used for sensitivity analysis, where the simulation is run multiple times with the combination of different error groups switched on/off in the truth model (while the filter model remains unchanged), to compute the error budget or relative contribution of each error group, respectively.

7.3 Error Budget Analysis

Error budget analysis, also known as sensitivity analysis, is a tool to compute the contribution of different sources of error to the total error. This is significant because based on this analysis, individual components of a navigation systems, or GN&C in general, can be adjusted and designed while having permissible and predictable performance, as per mission requirements.

In an error budget analysis, the total error is always equal to the root sum square (RSS) of the individual error sources, provided the error sources are uncorrelated. The selection and classification of the error sources depend entirely on the mission requirements and known/unknown parameters.

For this study, the sources of error have been classified into 9 groups:

1. Spacecraft's initial position and velocity uncertainty - In the plots, shown in later chapters, this group is denoted by an acronym PosVel.
2. Spacecraft's initial orientation and angular velocity uncertainty - In the plots, shown in later chapters, this group is denoted by an acronym AttdAV.
3. Spacecraft's center of mass position uncertainty - In the plots, shown in later chapters, this group is denoted by an acronym COMPos.
4. Translational process noise - In the plots, shown in later chapters, this group is denoted by an acronym QTErr.
5. Rotational process noise - In the plots, shown in later chapters, this group is denoted by an acronym QRErr.
6. Uncertainty in atmospheric model parameters (spacecraft ballistic coefficient, reference atmospheric density, and scale height) - In the plots, shown in later chapters, this group is denoted by an acronym AtmErr.
7. Uncertainty in accelerometer parameters (accelerometer measurement noise, bias, scale factor, and misalignment) - In the plots, shown in later chapters, this group is denoted by an acronym ACErr.
8. Accelerometer position uncertainty - In the plots, shown in later chapters, this group is denoted by an acronym ACPos.
9. Star camera measurement noise - In the plots, shown in later chapters, this group is denoted by an acronym SCNoise.

Uncertainty/Error due to each of the individual groups is switched on for the truth model, while all other sources of error (in truth model) are switched off. The filter model remains unchanged, and the contribution due to this error group on the true navigation error of each state is determined in a single simulation run. Thus, with a single simulation run, the range of acceptable uncertainty in the particular error group, for a given mission requirement, can

be determined. Based on 9 simulation runs, an error budget analysis is conducted and the results are used to design an autonomous orbital navigation system.

Note that this classification of error groups is for this study and is not unique, it depends on the knowledge of the system and mission requirements. However, the error sources must be uncorrelated.

Generally, an additional simulation run with all the errors switched on, for both truth and filter model, to validate the error budget analysis. This process will be explained in Chapter 8.

7.4 Summary

This chapter provided the necessary theoretical background and mathematical equations to develop a Linear Covariance (LinCov) analysis tool. Error budget analysis and the classification of error groups have been discussed.

CHAPTER 8

LinCov Simulation Testing

8.1 Chapter Overview

A thorough examination has been done of the LinCov analysis tool, presented in Chapter 7, and important stages have been documented in this chapter. Developing a simulation always needs extensive testing so as to gain sufficient trust on the mathematical model, its functioning, and corresponding results.

This chapter highlights the steps taken to ensure reasonable and optimal working of the simulation developed for this study. This chapter will help the reader understand different aspects of the LinCov simulation, while convincing the reader of the proper working of mathematical model, and thereby enhancing the trust in the results presented in Chapter 9.

8.2 Reference Trajectory Testing

Spacecraft position, velocity, and orientation results are plotted for the reference trajectory, for various test cases (elucidated in this section) and corresponding results are analyzed. Parameters like LEO orbital elements, spacecraft specifications, and nominal values of atmospheric drag model parameters are given in Tables [8.1-8.2](#).

Name	Value	Units
Semi-major axis (a)	7×10^6	meters (m)
Eccentricity (e)	10^{-2}	unit-less
Inclination (i)	50	degree (deg)
Argument of perifocus (ω)	30	degree (deg)
Right ascension of the ascending node (Ω)	60	degree (deg)
True anomaly (ν)	120	degree (deg)
Numerical integration time-step	10	seconds (s)
Number of orbits simulated	5	unit-less

Table 8.1: LEO Orbital parameters

Parameter Name	Nominal Value	Units	
Spacecraft (s/c) parameters	Radius	0.3	meters (m)
	Mass	406.965	kg
	Coefficient of diffuse reflection	2	unit-less
	Inertia	11.40 (along X-X)	$kg.m^2$
		10.93 (along Y-Y)	$kg.m^2$
		10.93 (along Z-Z)	$kg.m^2$
Coefficient of drag	2	unit-less	
Atmospheric drag parameters	Ballistic number	5.56×10^{-3}	m^2/kg
	Reference atmospheric density	2.80×10^{-12}	kg/m^3
	Reference scale height	58019	meters (m)

Table 8.2: Spacecraft (s/c) Specifications and Nominal Value of Atmospheric Drag Parameters

A number of test cases are run to credibly develop the reference trajectory. In all the test cases, three accelerometers with a baseline of 0.5 meters and measurement update

frequency of 20 seconds are used. A plot of the accelerometer configuration is shown in Figure 8.1.

8.2.1 Test Case 1 - Check Orbital Dynamics

This test case helps ascertain the nominal values of important parameters defining spacecraft's orbit, while all the non-gravitational external forces are switched off and the truth and filter gravity model is set to point mass gravity. Results are presented for a non-rotating spacecraft, with the spacecraft body-fixed frame initially aligned with the ECI frame. For this test case, orbital elements are set as per Table 8.1.

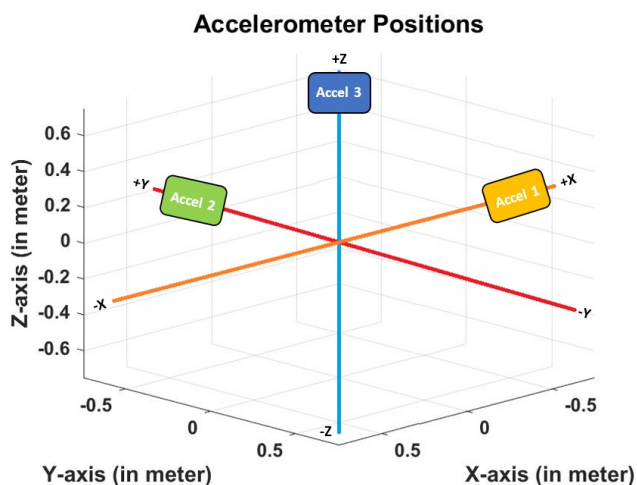


Fig. 8.1: Accelerometer Configuration

As per expectation, orbital elements (except true anomaly) and spacecraft's Euler angles stay constant, and spacecraft's angular velocity is exactly zero. Plots for spacecraft position and accelerometer measurements are shown in Figure 8.2 and Figure 8.3.

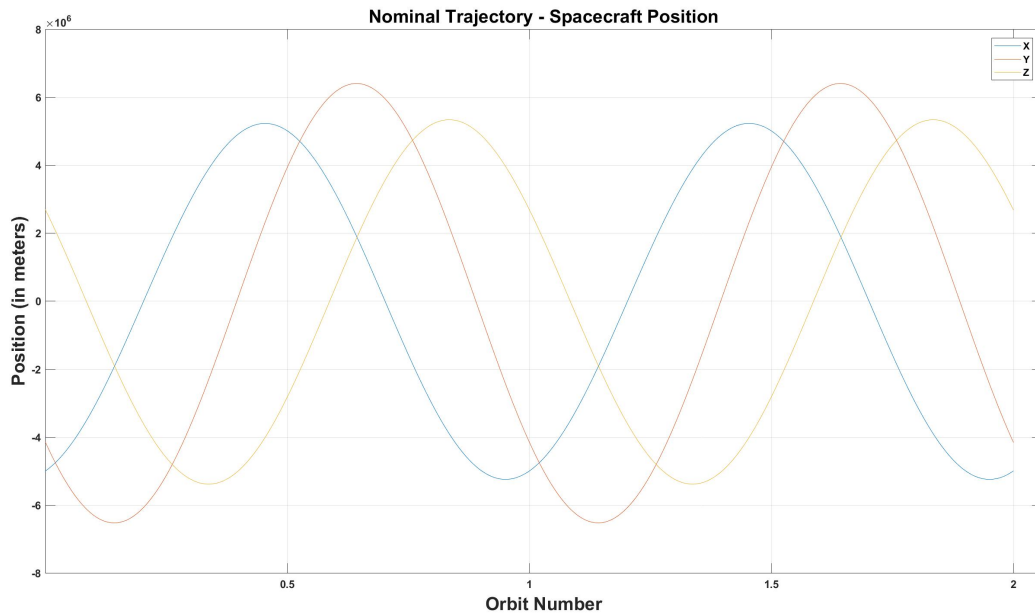


Fig. 8.2: Test case 1 - Spacecraft Position in ECI frame

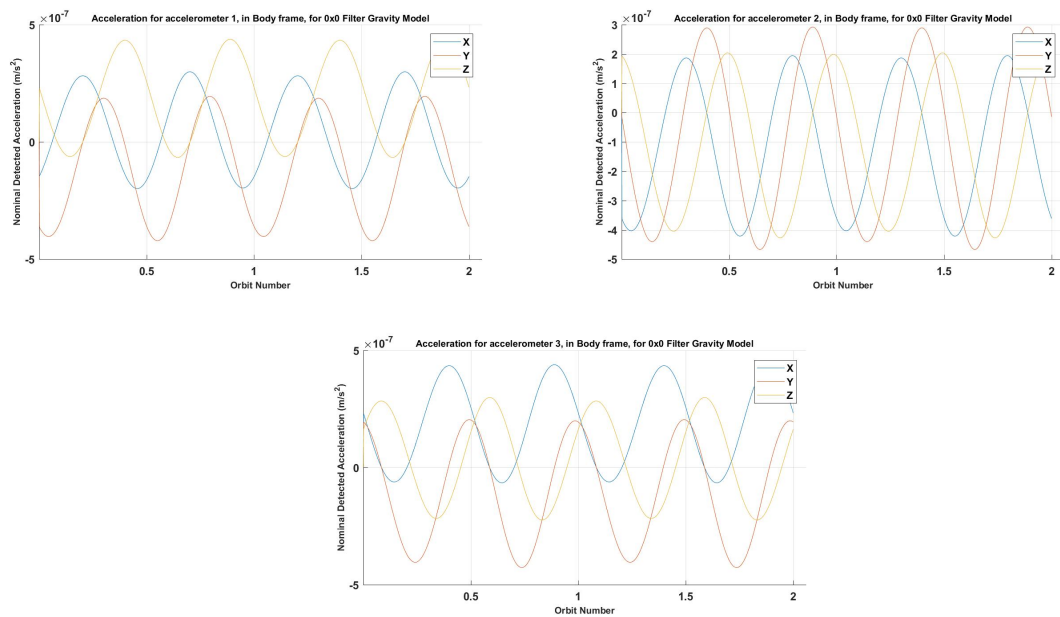


Fig. 8.3: Test case 1 - Accelerometer measurements (in Spacecraft body-fixed reference frame) for accelerometer 1, 2, & 3

8.2.2 Test Case 2 - Check Effect of J2 & Rotating Spacecraft

This test case helps ascertain the effect of the J2 gravity model, and verify the modeling of the spacecraft's attitude and angular velocity. Results are presented for a spacecraft rotating with angular velocity $\omega = \begin{bmatrix} 1 & 0 & 0 \end{bmatrix}$ deg/sec, with the spacecraft body-fixed frame initially aligned with the ECI frame. For this test case, orbital elements are set as per Table 8.1, all the non-gravitational external forces are switched off, and the filter and truth gravity model is set to J2 gravity.

Plots for LEO orbital elements, spacecraft's attitude and accelerometer measurements are shown in Figures 8.4 - 8.6.

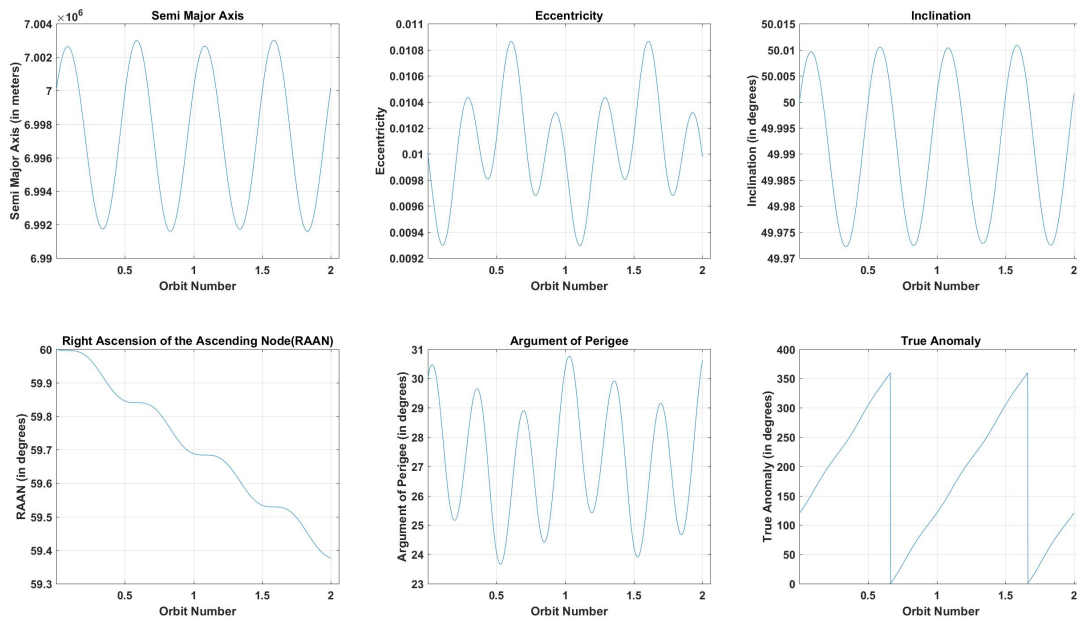


Fig. 8.4: Test case 2 - LEO orbital elements

For this test case, the components of spacecraft's position and velocity are the same as in test case 1, spacecraft's angular velocity is exactly constant, and the oscillation period of the components of Euler angles, denoting spacecraft's attitude, is 360 seconds.

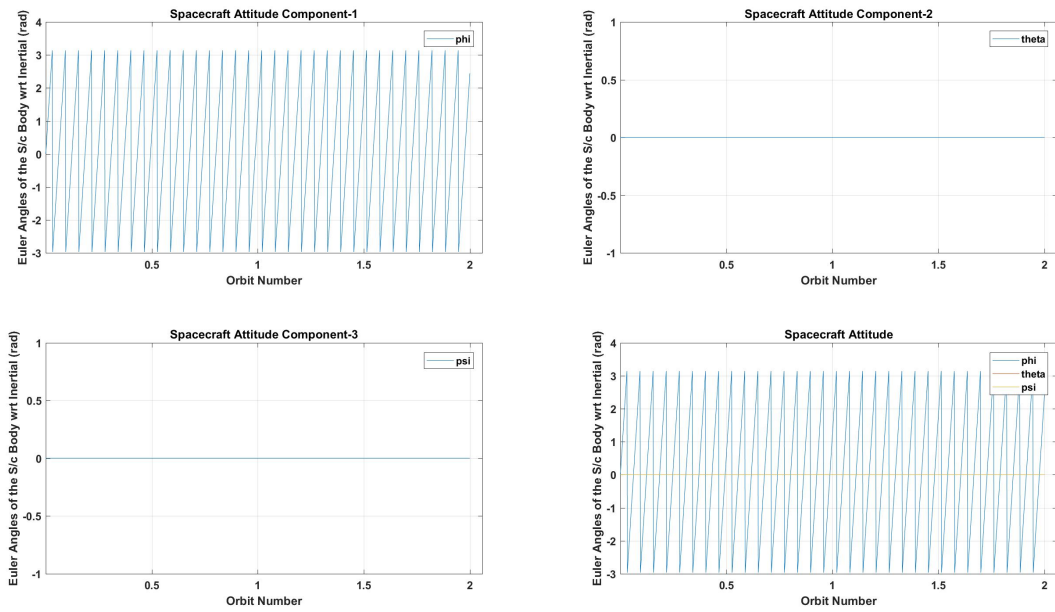


Fig. 8.5: Test case 2 - Euler angles denoting attitude of the spacecraft body-fixed reference frame with respect to the ECI frame

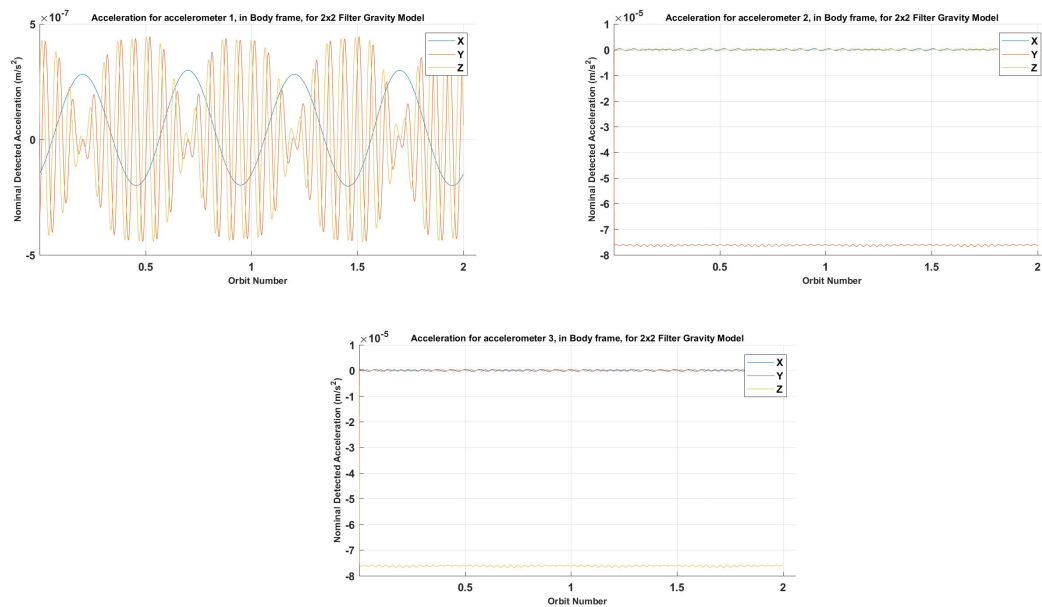


Fig. 8.6: Test case 2 - Accelerometer measurements (in Spacecraft body-fixed reference frame) for accelerometer 1, 2, & 3

8.2.3 Test Case 3 - Check Atmospheric Drag Model

This test case helps evaluate the atmospheric drag model. Results are presented for a spacecraft rotating with angular velocity $\omega = \begin{bmatrix} 1 & 0.1 & 0.05 \end{bmatrix}$ deg/sec, with the spacecraft body-fixed frame initially aligned with the ECI frame. For this test case, orbital elements are set as per Table 8.1 except the eccentricity for the orbit is exactly zero. All the non-gravitational external forces are switched off except translational acceleration due to atmospheric drag, and the filter and truth gravity model is set to point mass gravity.

For this test case, the magnitude of spacecraft's position decreases slowly over time, and the magnitude of the spacecraft's velocity increases slowly over time. Plots for LEO orbital elements, spacecraft's attitude, and accelerometer measurements are shown in Figures 8.7 and Figure 8.9.

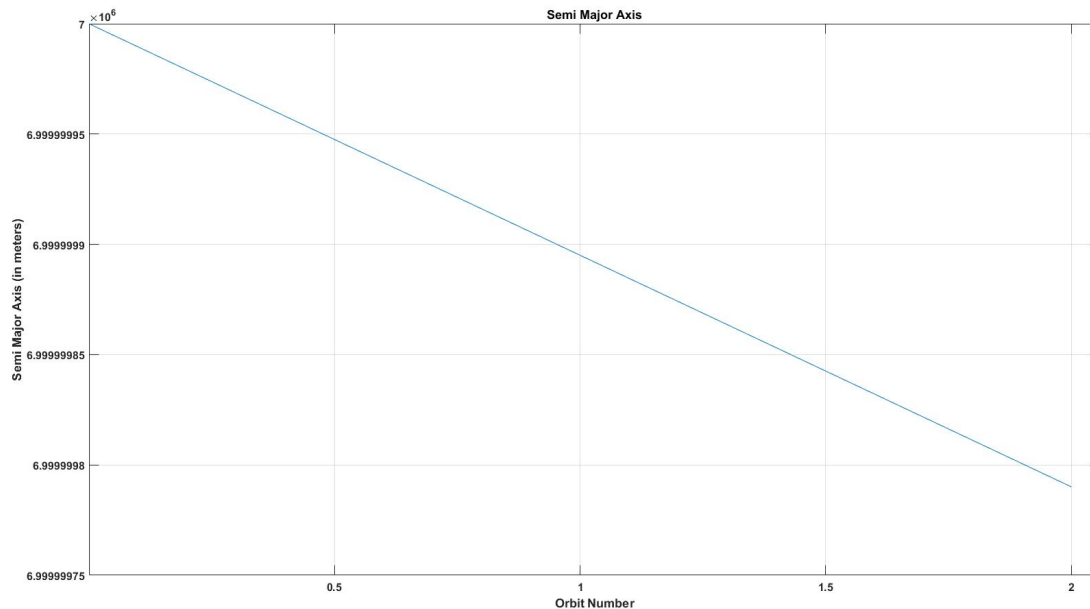


Fig. 8.7: Test case 3 - Change in semi-major axis for the given LEO orbit

Changes in the orbit because of the acceleration due to atmospheric drag are studied. It can be noted that inclination and right ascension of the ascending node stay constant,

and the semi-major axis slightly decreases. Time derivative of the semi-major axis, of a circular orbit, as a function of the acceleration due to atmospheric drag has been derived and presented in Appendix B.

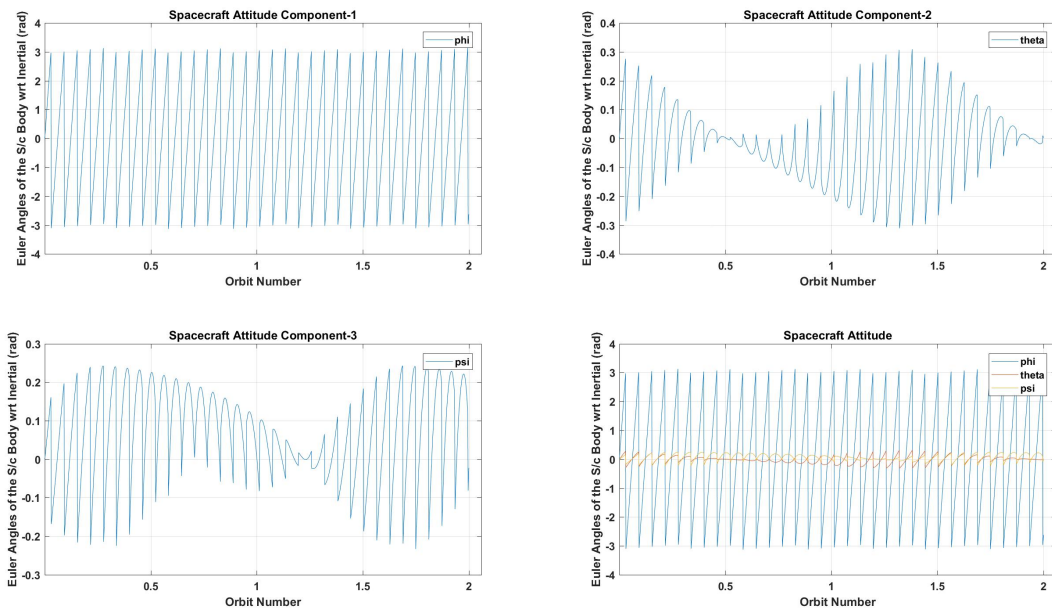


Fig. 8.8: Test case 3 - Euler angles denoting attitude of the spacecraft body-fixed reference frame with respect to the ECI frame

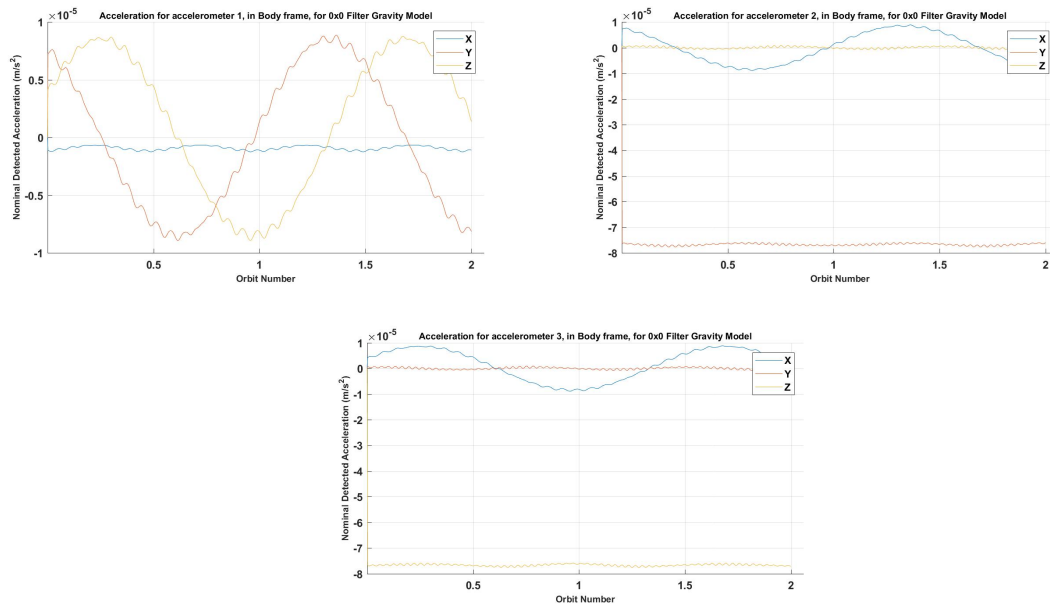


Fig. 8.9: Test case 3 - Accelerometer measurements (in Spacecraft body-fixed reference frame) for accelerometer 1, 2, & 3

8.3 LinCov Propagation Testing

Covariance propagation is an important part of the algorithm for setting up the complete filter. Various test cases have been simulated to debug the propagation algorithm. Two of the most relevant test cases are elucidated in this section and corresponding results are analyzed. Parameters like LEO orbital elements, spacecraft specifications, and nominal values of atmospheric drag model parameters are given in Tables 8.1-8.2. Parameters such as time constants, initial conditions, accelerometer parameters, star camera parameters, and environmental uncertainties are given in Tables 8.3 - 8.7.

Parameter Name	Value	Units
Ballistic number	1000T	seconds (s)
Reference atmospheric density	1000T	seconds (s)
Reference scale height	1000T	seconds (s)
Center of mass (COM) position	T/2	seconds (s)
Accelerometer (AC) position, bias, scale-factor, misalignment	T/2	seconds (s)

Table 8.3: Time Constants (T denotes the orbital period)

Initial Conditions		1 σ Value	Units
Spacecraft (s/c) position	radial	500	meters (m)
	cross-track	1000	meters (m)
	along-track	1000	meters (m)
Spacecraft (s/c) velocity	radial	1.0	m/s
	cross-track	1.0	m/s
	along-track	1.0	m/s
Spacecraft (s/c) attitude	radial	10 ⁻³	radians (rad)
	cross-track	10 ⁻³	radians (rad)
	along-track	10 ⁻³	radians (rad)
Spacecraft (s/c) angular velocity	radial	10 ⁻⁵	rad/s
	cross-track	10 ⁻⁵	rad/s
	along-track	10 ⁻⁵	rad/s

Table 8.4: Initial Conditions - Spacecraft (s/c) position, velocity, attitude, and angular velocity

Parameter Name	Value	Units
Number of accelerometers (AC)	3	unit-less
Accelerometer baseline	0.5	meters (<i>m</i>)
Accelerometer measurement update frequency	20	seconds (<i>s</i>)
Accelerometer measurement noise resolution	10^{-13}	$m/s^2\sqrt{Hz}$
1σ Accelerometer position	10^{-5}	meters (<i>m</i>)
1σ Accelerometer bias	10^{-5}	unit-less
1σ Accelerometer scale-factor	10^{-11}	m/s^2
1σ Accelerometer misalignment	10^{-6}	radians (<i>rad</i>)

Table 8.5: Accelerometer (AC) Parameters

Parameter Name	Value	Units
Number of star cameras (SC)	1	unit-less
Star camera measurement update frequency	20	seconds (<i>s</i>)
Star camera measurement noise resolution	10^{-4}	radians (<i>rad</i>)

Table 8.6: Star Camera (SC) Parameters

Parameter Name	Value	Units
Truth gravity model	18×18	unit-less
Filter gravity model	12×12	unit-less
1σ reference atm. density	2.80×10^{-15}	kg/m^3
1σ reference scale height	58.019	meters (<i>m</i>)
Translational process noise	10^{-10} ($\sim 52 m/rev$ 3σ)	m^2/s^3
Aerodynamic process noise	10^{-10} ($\sim 52 m/rev$ 3σ)	m^2/s^3
Rotational process noise	10^{-16} ($\sim 0.03 rad/rev$ 3σ)	$1/s^3$
1σ spacecraft (s/c) ballistic number	5.56×10^{-6}	m^2/kg
1σ spacecraft (s/c) (COM) position	10^{-4}	meters (<i>m</i>)

Table 8.7: Environmental Uncertainties

In all the test cases, three accelerometers with a baseline of 0.5 meters and measurement update frequency of 20 seconds are used. A plot of the accelerometer configuration is shown in Figure 8.1.

8.3.1 Test Case 1 - Check State Dynamics & Propagation Equations

This test case helps verify the state dynamics and propagation equations by running the simulation without measurement updates and varying uncertainties on individual states. Results are presented for a non-rotating spacecraft with the spacecraft body-fixed frame aligned with the ECI frame. For this test case, orbital elements are set as per Table 8.1, all the non-gravitational external forces are switched off, process noise is zero, and the truth and filter gravity model is set to point mass gravity.

First, all errors/uncertainties on states were set to zero, and as per expectation all the filter navigation errors stay zero. Next, individual state errors are switched on, and it is ascertained that the filter navigation errors behave in accordance with the dynamics. Further, the filter navigation error matches the true navigation error because the filter and truth model are same for this test case. This verifies the state dynamics and propagation equations.

When the spacecraft's position and velocity initial uncertainty is switched on, the filter navigation error grows in accordance with the state dynamics. Next, when spacecraft's attitude and angular velocity initial uncertainty is switched on, the filter navigation error on Euler angles increases while the filter navigation error on angular velocity stays constant.

When the spacecraft's center of mass position initial uncertainty is switched on, the filter navigation error stay constant at the 3σ value. Similarly, when accelerometer position initial uncertainty is switched on, the filter navigation error stays constant at the 3σ value.

When the initial uncertainty on accelerometer bias, misalignment, and scale factor is switched on, the filter navigation error stays constant at the 3σ value. Similarly, when initial uncertainty on ballistic coefficient, reference atmospheric density, and scale height is switched on, the filter navigation error stays constant at the 3σ value.

The reason that the filter navigation error stays constant at the 3σ value for some of the states is because external forces are switched off for this test case and the spacecraft is non-rotating. Changing these conditions changes the trend in filter navigation error, in accordance with the dynamics. This was verified by running this test case again with different conditions, and the state dynamics were verified.

8.3.2 Test Case 2 - Find Appropriate Process Noise

This test case helps to compute the filter navigation error due to the propagation of the process noise. This is important so as to maintain the numerical stability of the filter, while keeping the filter navigation error in check. Results are presented for a non-rotating spacecraft, with the spacecraft body-fixed frame initially aligned with the ECI frame. For this test case, orbital elements are set as per Table 8.1, all the non-gravitational external forces are switched off, and the truth and filter gravity model is set to point mass gravity.

First, the spacecraft's position and velocity initial uncertainty is switched on and the translational process noise is varied until the final navigation error is within required limits. Next, the process is repeated by switching on the initial uncertainty on spacecraft's attitude and angular velocity and the rotational process noise is varied until the final navigation error is within required limits. Thus, an appropriate value for translational and rotational process noise, based on permissible mission requirement and for given initial uncertainty and spacecraft's orbit, is obtained.

This test case is repeated for different gravity models and other varied conditions, so as to be confident on the values selected for translational and rotational process noise.

8.4 LinCov Update Testing

Various test cases have been simulated to debug the update algorithm and set up the complete filter. Three of the most relevant test cases are elucidated in this section and corresponding results are analyzed. Parameters like LEO orbital elements, spacecraft specifications, and nominal value of atmospheric drag model parameters are given in Tables

8.1-8.2. Parameters such as time constants, initial conditions, accelerometer parameters, star camera parameters, and environmental uncertainties are given in Tables 8.3 - 8.7.

In all the test cases, three accelerometers with a baseline of 0.5 meters and measurement update frequency of 20 seconds are used. A plot of the accelerometer configuration is shown in Figure 8.1.

8.4.1 Test Case 1 - Verify State Dynamics & Update Equations

This test case helps verify the state dynamics and update equations by running the simulation with measurement updates and switching uncertainties on individual states on/off. Results are presented for a non-rotating spacecraft with the spacecraft body-fixed frame initially aligned with the ECI frame. For this test case, orbital elements are set as per Table 8.1, all the non-gravitational external forces are switched off, process noise is zero, and the truth and filter gravity model is set to point mass gravity.

First, all errors/uncertainties on states are zero, and as per expectation all the filter navigation errors stay zero. Next, individual state errors are switched on, and it is ascertained that the filter navigation errors converge or approach a steady state value. Further, it is made sure that the filter navigation error matches the true navigation error, because the filter and truth model are same for this test case. This verifies the filter setup, state dynamics and update equations.

When the spacecraft's position and velocity initial uncertainty is switched on, the filter navigation error does converge as per expectation. However, at some time instants, the error is imaginary. This is because the translational process noise is set to zero for this test case, and thus, the filter becomes numerically unstable. This test is repeated with the translational process noise and the results are shown under test case 2.

Similarly, when the spacecraft's attitude and angular velocity initial uncertainty is switched on, then the filter navigation error does converge as per expectation. But the error is again imaginary at some time instants. This is because the rotational process noise is set to zero for this test case, and thus, the filter becomes numerically unstable. This test is repeated with the rotational process noise and the results are shown under test case 2.

Plots for the filter navigation error when spacecraft's center of mass position initial uncertainty is switched on are given in Figure 8.10.

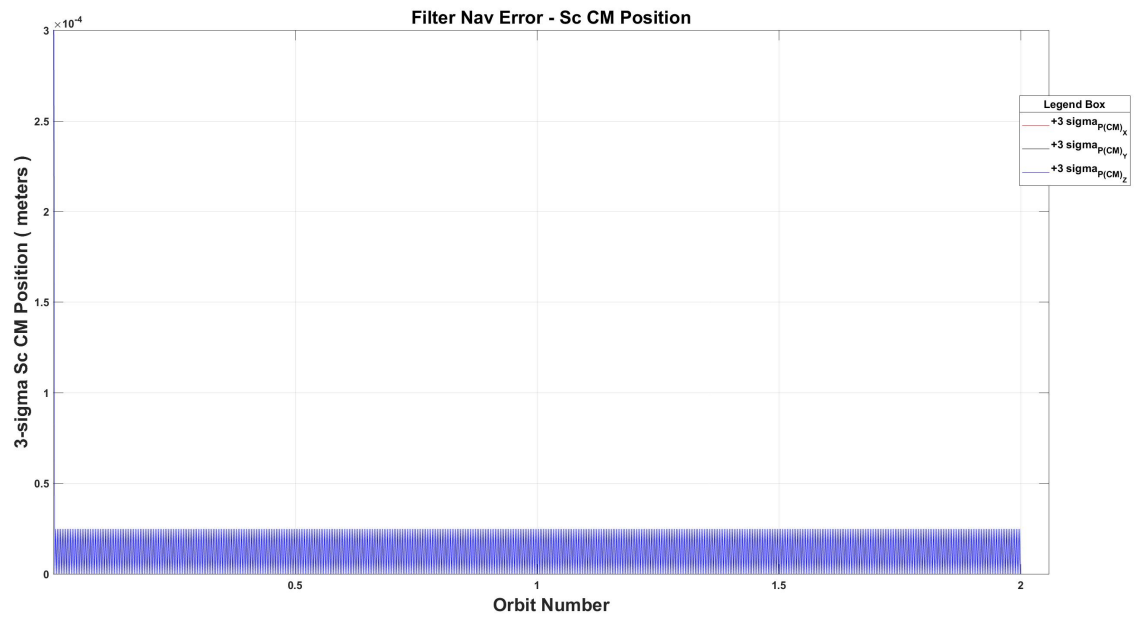
Plots for the filter navigation error when accelerometer position initial uncertainty is switched on are given in Figure 8.11. Filter navigation error on accelerometer 2 position and accelerometer 3 position are similar to that for accelerometer 1.

Plots for the filter navigation error when uncertainty on accelerometer bias, misalignment, and scale factor is switched on, are given in Figure 8.12. Filter navigation error on accelerometer 3 bias, misalignment, and scale factor are similar to that for accelerometer 1. Note that in in Figure 8.12, the estimate for accelerometer misalignment is very poor. Reasons for the same are discussed in Chapter 9.

It is noted that the filter navigation error for ballistic coefficient, reference atmospheric density, and scale height stay zero, even when initial uncertainty on these states are switched on. This is because the external forces (including atmospheric drag) are switched off.

Thus, when the simulation is run again with acceleration due to atmospheric drag switched on, and having initial uncertainty on ballistic coefficient, reference atmospheric density, and scale height switched on, it is noted that the filter navigation errors on these states converge to a steady state value. However, the error is imaginary at some time instants. This is because the aerodynamic process noise is set to zero for this test case, and thus, the filter becomes numerically unstable. This test is repeated with the aerodynamic process noise and the results are shown under test case 2.

(a)



(b)

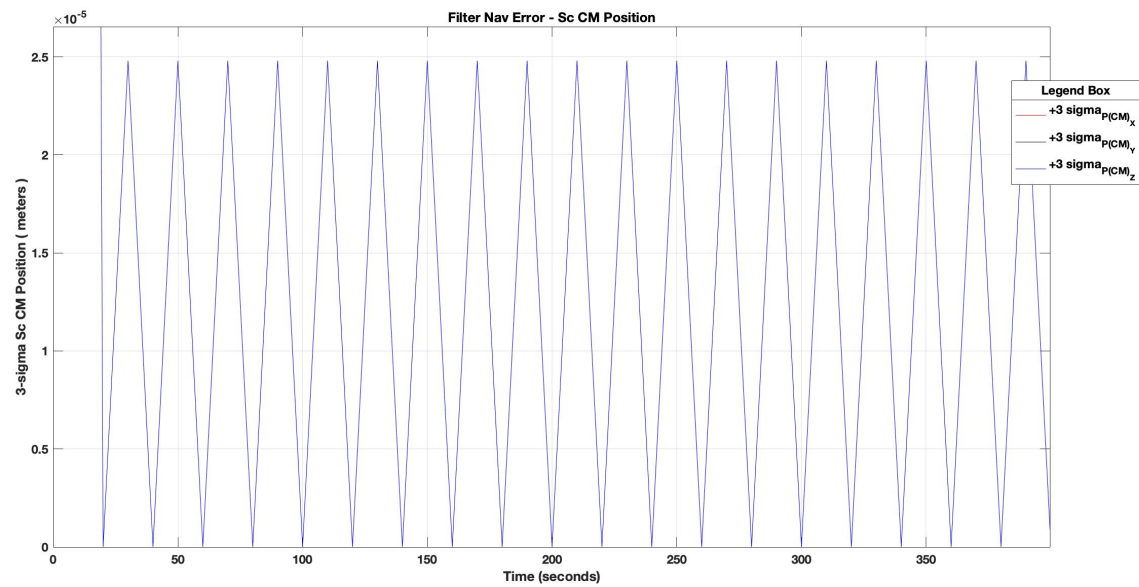
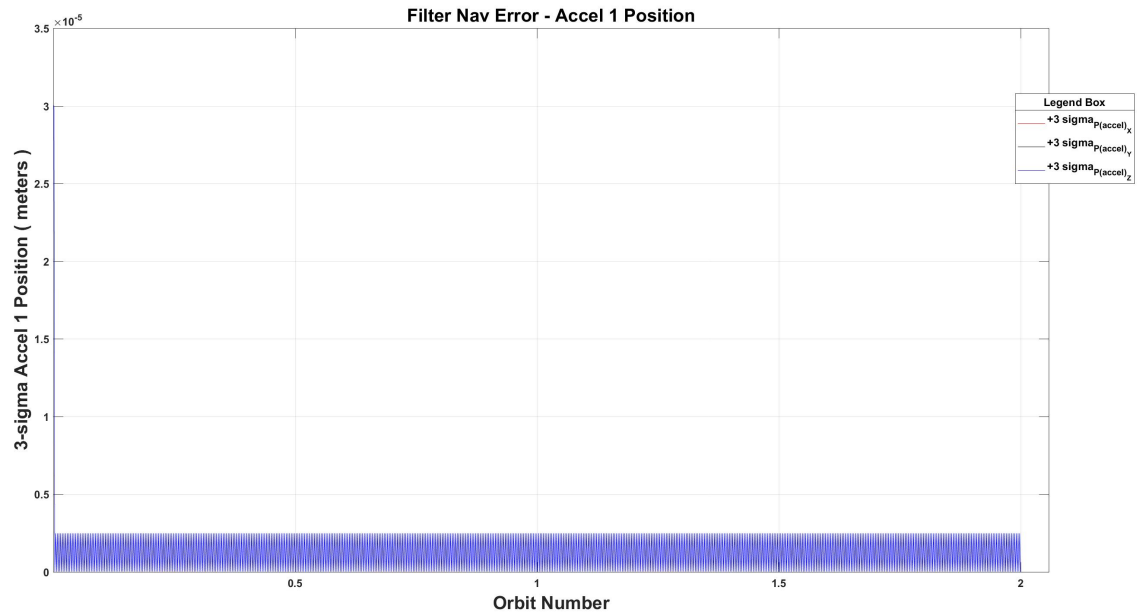


Fig. 8.10: Test case 1 - Spacecraft's center of mass position (with respect to the origin of the spacecraft body-fixed frame and expressed in spacecraft body-fixed frame) filter navigation error - (a) For 2 orbits, (b) Zoomed view for first 350 seconds

(a)



(b)

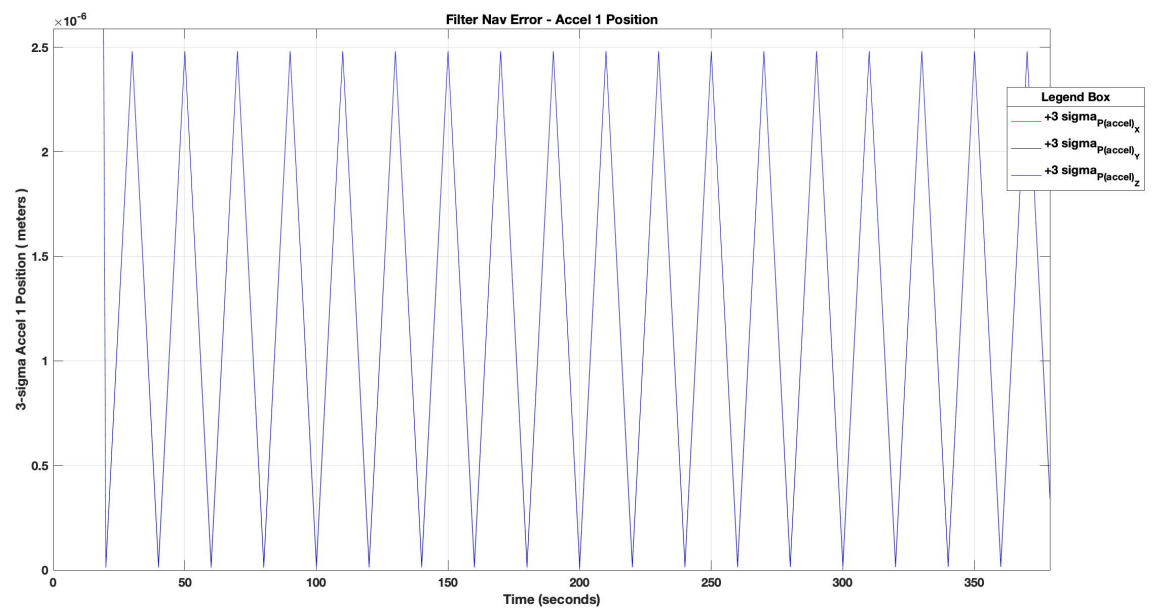
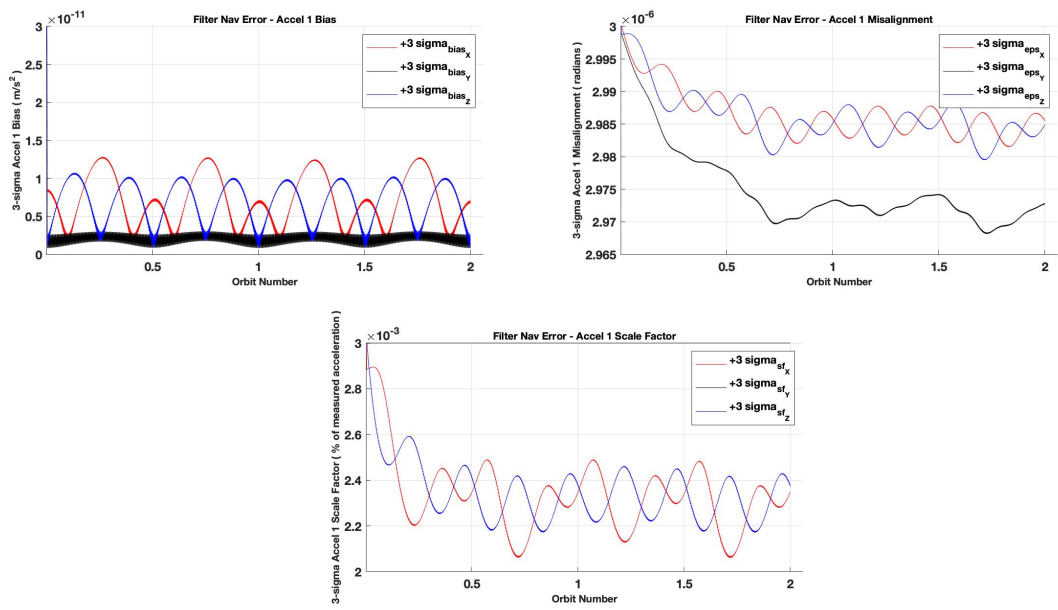


Fig. 8.11: Test case 1 - Accelerometer 1 position (with respect to the origin of the spacecraft body-fixed frame and expressed in spacecraft body-fixed frame) filter navigation error - (a) For 2 orbits, (b) Zoomed view for first 350 seconds

(a)



(b)

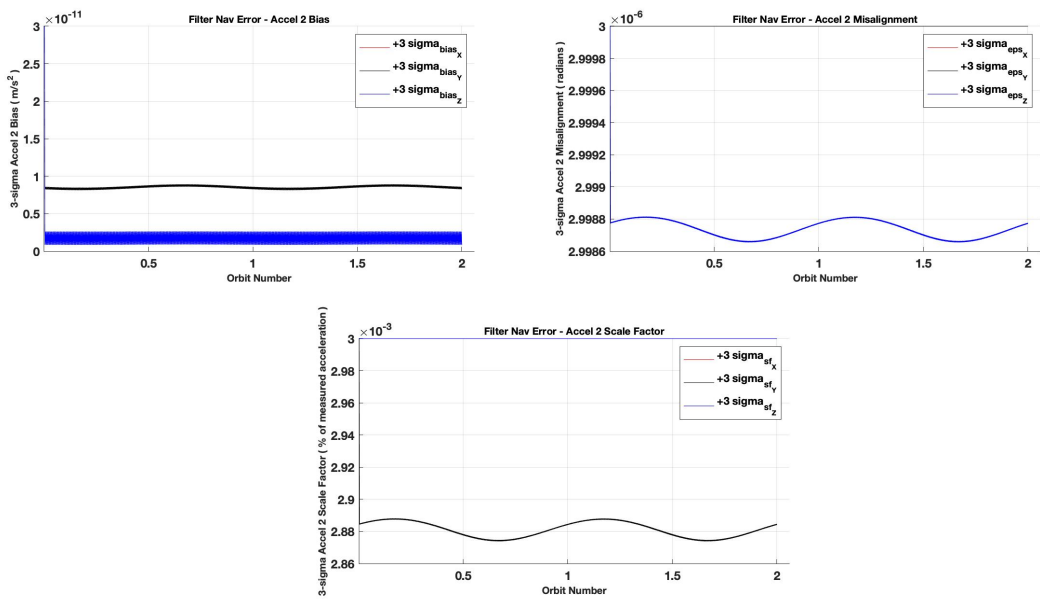


Fig. 8.12: Test case 1 - Accelerometer bias, misalignment, and scale factor (expressed in accelerometer actual reference frame) filter navigation error - (a) For Accelerometer 1, (b) For Accelerometer 2

8.4.2 Test Case 2 - With Process Noise

This test case helps to narrow the initial uncertainties on the states, and to consolidate the process noise power spectral density value selected earlier. Results are presented for a non-rotating spacecraft, with the spacecraft body-fixed frame initially aligned with the ECI frame. For this test case, orbital elements are set as per Table 8.1, all external forces are switched off, and the truth and filter gravity model is set to point mass gravity.

First, when the spacecraft's position and velocity initial uncertainty and the translational process noise are switched on, the filter navigation error converge as per expectation. A plot of spacecraft position, expressed in LVLH frame, is shown in Figure 8.13.

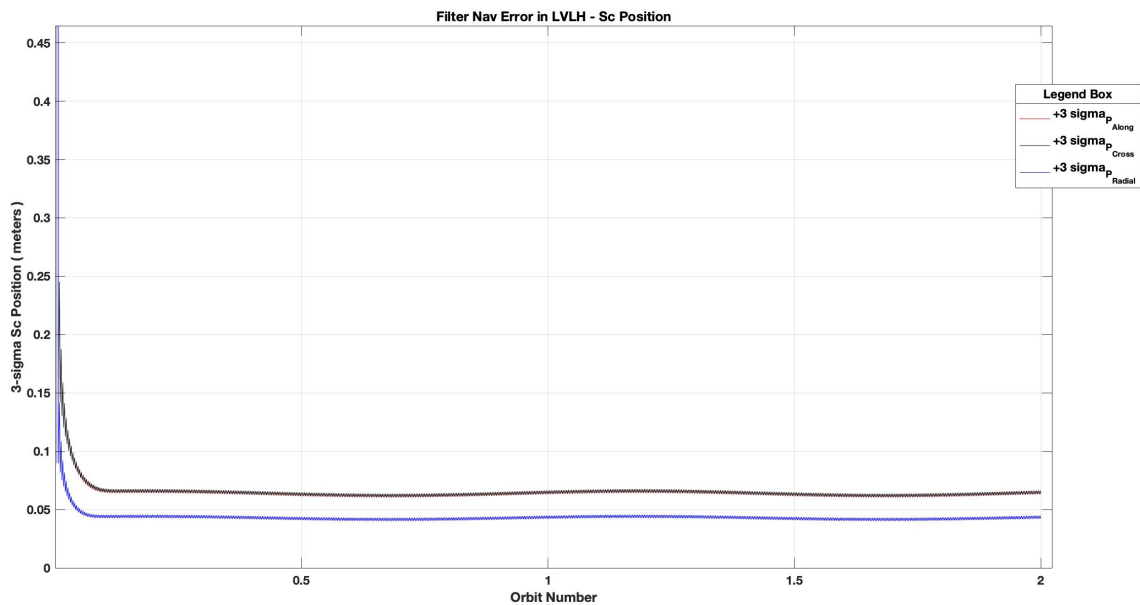


Fig. 8.13: Test case 1 - Spacecraft position (expressed in LVLH frame) filter navigation error

Next, when the spacecraft's attitude and angular velocity initial uncertainty and the rotational process noise are switched on, the filter navigation error converge as per expectation. Plot for spacecraft attitude, expressed in ECI frame, is shown in Figure 8.14.

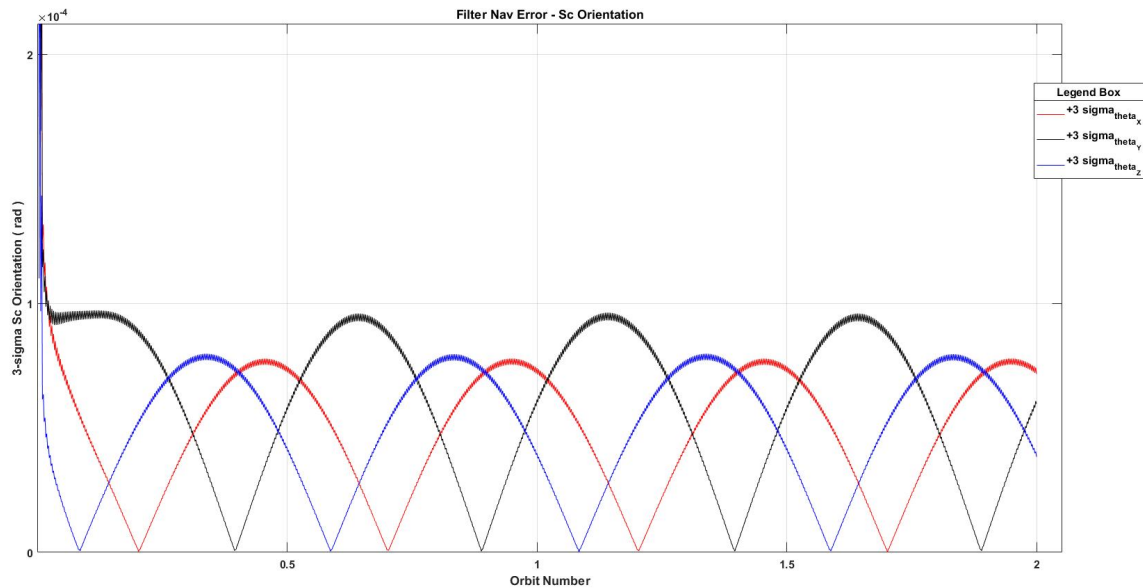


Fig. 8.14: Test case 1 - Spacecraft attitude (expressed in ECI frame) filter navigation error

Finally, when acceleration due to atmospheric drag, initial uncertainty on ballistic coefficient, reference atmospheric density, and scale height, and the aerodynamic process noise are switched on, the filter navigation error converge as per expectation. Plots for ballistic coefficient, reference atmospheric density, and scale height are shown in Figure 8.15.

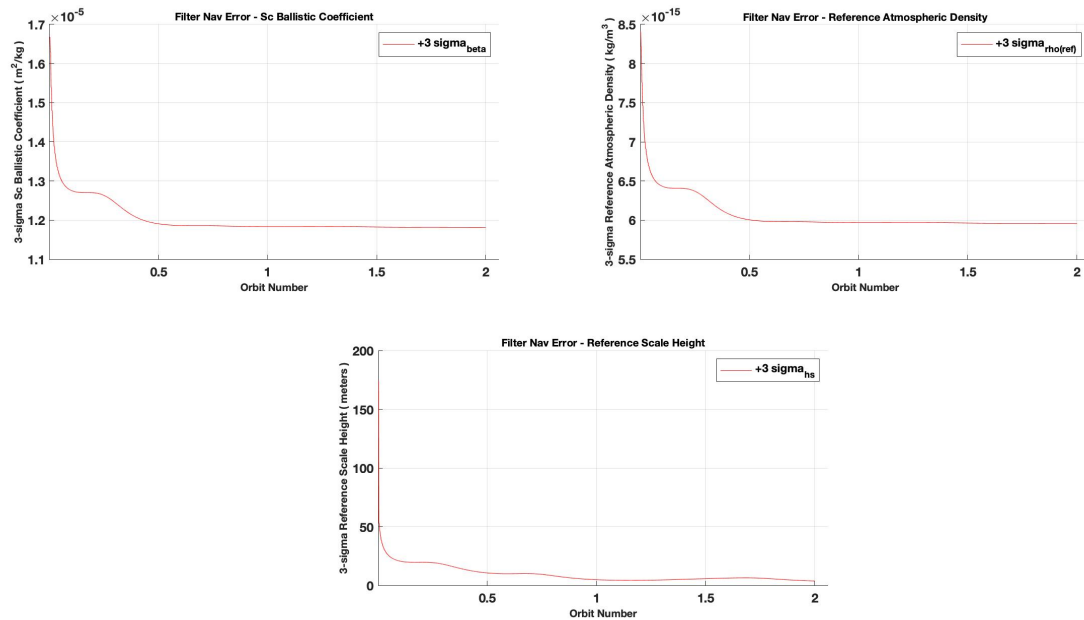


Fig. 8.15: Test case 1 - Filter navigation error on ballistic coefficient, reference atmospheric density, and scale height

This test case was repeated for different gravity models and other varied conditions so as to gain confidence in the values selected for initial uncertainties on the states and the process noise power spectral density value.

8.4.3 Test Case 3 - With Error Groups

After completing the above test cases, the simulation with complete filter setup is run and it is asserted that the filter is working nominally. Next, the simulation is run for different filter and truth gravity models, and again the filter navigation error and true navigation error for all states are closely scrutinized.

Finally, error groups are formed, based on the sources of error to be studied. These error groups consist of one or many uncorrelated filter states. The simulation is run multiple times with the same truth model but different filter model, such that the individual error groups (filter states) are switched on/off. Results from this setup help confirm no correlation

between the selected error groups and nominal working of the LinCov setup.

This test case was repeated for different filter and truth models based on the judgement of the engineer.

8.5 Numerical Instability & Limitations

This section reports about the issues related to the filter numerical instability, its probable causes, and prospective solutions. Numerical stability of the filter is of utmost importance when developing a LinCov simulation, and hence, this section provides an overview on this aspect.

8.5.1 Overview

Kalman filter numerical stability is a widely researched and studied problem. However, due to limited scope of this study, only issues observed during filter setup for this problem will be discussed.

During the simulation development for this study, two major issues resulting in filter numerical instability were observed. The first issue is numerical precision limit of modern day computers. When the filter is setup with initial uncertainty on spacecraft position, velocity, attitude, and angular velocity, it is suspected that the wide range of numerical values result in the breach of numerical precision limit, which in turn results in numerical instability during mathematical operations.

The second issue is the appropriate selection of simulation parameters, like process noise power spectral density, initial uncertainty on states, and sensor parameters. It is suspected that for some scenarios, the simulation is sensitive to the selection of simulation parameters, especially due to very low magnitude of sensor noise and process noise required for this study.

8.5.2 Prospective Solutions

Prospective solutions are suggested for solving numerical instability of the filter. It is suggested that the testing process, presented in this chapter, should be followed thoroughly.

This helps significantly with the appropriate selection of simulation parameters, and in general, promotes healthy algorithm development.

Next, it is believed that a good covariance factorization technique may help solve the issue of numerical precision limit. UDU Covariance Factorization technique may be one of the options. It is used to maintain numerical stability of the filter. In this method, the state covariance P is replaced such that [9, 50]

$$P = UDU^T \quad (8.1)$$

where U is an upper triangular and unitary matrix, and D is a diagonal matrix. Cholesky decomposition algorithm is used to decompose covariance matrix P in the form given in Eq. 8.1 [9, 50]. The flowchart in Figure 8.16 depicts the UDU covariance propagation and update algorithm, equivalent to the system shown in Figure 2.6 [9, 50].

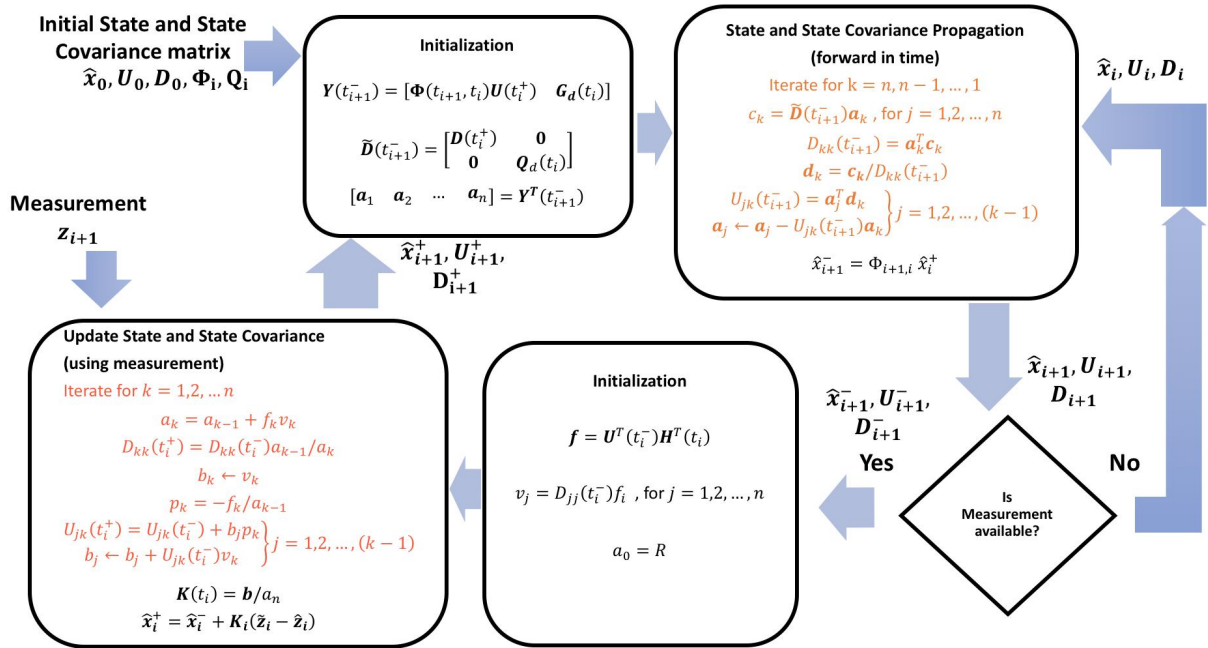


Fig. 8.16: UDU Covariance Propagation and Update Flow Diagram. Based on the algorithm given in Maybeck (1979), Stochastic Models, Estimation, and Control [9]

Another prospective solution is to use variable precision commands (like `vpa` and `digits`) in MATLAB, by performing symbolic mathematical operations for covariance propagation and measurement update equations. This technique increases the computational time and memory requirements.

Finally, another prospective solution may be to normalize the states. This technique was used during the observability analysis for this study, and has been discussed in Chapter 6. Intelligently normalizing the state vector will keep the numerical range within precision limits, without increasing the computational time and memory requirements.

8.6 Summary

This chapter highlighted steps taken to ensure reasonable and optimal working of the simulation. The LinCov analysis tool was thoroughly examined and important test cases have been documented in this chapter. These test cases are an important step towards selecting effective range for the initial values of simulation parameters, while taking into consideration the mission requirements, spacecraft specifications, and spacecraft orbit.

CHAPTER 9

LinCov Simulation Results and Analysis

9.1 Chapter Overview

Based on the framework developed in the preceding chapters, Linear Covariance simulation results are presented and detailed analysis is discussed in this chapter. Effort has been made to reasonably categorize and analyze the results so as to help understand the performance of the system for different configurations.

In the following sections, the initial setup of the simulation parameters is highlighted, and then the results obtained for a Low Earth Orbit (50 degree Inclination) and a polar Low Earth Orbit are presented.

9.2 Initial Setup

Initial setup of the simulation parameters, and the nominal values for initial state errors/uncertainties are presented in this section. Spacecraft specifications, nominal values of atmospheric drag model parameters, initial conditions, time constants, accelerometer parameters, star camera parameters, and environmental uncertainties are given in the Tables [9.1 - 9.6](#).

Parameter Name		Nominal Value	Units
Spacecraft (s/c) parameters	Radius	0.3	meters (<i>m</i>)
	Mass	406.965	<i>kg</i>
	Coefficient of diffuse reflection	2	unit-less
	Inertia	11.40 (along X-X)	<i>kg.m²</i>
		10.93 (along Y-Y)	<i>kg.m²</i>
		10.93 (along Z-Z)	<i>kg.m²</i>
Coefficient of drag	2	unit-less	
Atmospheric drag parameters	Ballistic number	5.56×10^{-3}	<i>m²/kg</i>
	Reference atmospheric density	2.80×10^{-12}	<i>kg/m³</i>
	Reference scale height	58019	meters (<i>m</i>)

Table 9.1: Spacecraft (s/c) Specifications and Nominal Value of Atmospheric Drag Parameters

Initial Conditions		1σ Value	Units
Spacecraft (s/c) position	radial	500	meters (<i>m</i>)
	cross-track	1000	meters (<i>m</i>)
	along-track	1000	meters (<i>m</i>)
Spacecraft (s/c) velocity	radial	1.0	<i>m/s</i>
	cross-track	1.0	<i>m/s</i>
	along-track	1.0	<i>m/s</i>
Spacecraft (s/c) attitude	radial	10^{-3}	radians (<i>rad</i>)
	cross-track	10^{-3}	radians (<i>rad</i>)
	along-track	10^{-3}	radians (<i>rad</i>)
Spacecraft (s/c) angular velocity	radial	10^{-5}	<i>rad/s</i>
	cross-track	10^{-5}	<i>rad/s</i>
	along-track	10^{-5}	<i>rad/s</i>

Table 9.2: Initial Conditions - Spacecraft (s/c) Position, Velocity, Attitude, and Angular Velocity

Parameter Name	Value 1	Value 2	Units
Ballistic number	1000T	1000T	seconds (<i>s</i>)
Reference atmospheric density	1000T	T/2	seconds (<i>s</i>)
Reference scale height	1000T	1000T	seconds (<i>s</i>)
Center of mass (COM) position	T/2	T/2	seconds (<i>s</i>)
Accelerometer (AC) position, bias, scale-factor, misalignment	T/2	T/2	seconds (<i>s</i>)

Table 9.3: Time Constants (T denotes the orbital period)

Parameter Name	High Cost	Moderate Cost	Low Cost	Units
Number of accelerometers (AC)	3, 6	3, 6	3, 6	unit-less
Accelerometer baseline	0.5, 1.0	0.5, 1.0	0.5, 1.0	meters (<i>m</i>)
Accelerometer measurement update frequency	20	20	20	seconds (<i>s</i>)
Accelerometer measurement noise resolution	10^{-13}	10^{-11}	10^{-10}	$m/s^2\sqrt{Hz}$
1σ Accelerometer position	10^{-5}	10^{-4}	10^{-3}	meters (<i>m</i>)
1σ Accelerometer bias	10^{-5}	10^{-4}	10^{-3}	unit-less
1σ Accelerometer scale-factor	10^{-11}	10^{-9}	10^{-7}	m/s^2
1σ Accelerometer misalignment	10^{-6}	10^{-5}	10^{-4}	radians (<i>rad</i>)

Table 9.4: Accelerometer (AC) Parameters

Parameter Name	High Cost	Moderate Cost	Low Cost	Units
Number of star cameras (SC)	1	1	1	unit-less
Star camera measurement update frequency	20	20	20	seconds (<i>s</i>)
Star camera measurement noise resolution	10^{-4}	10^{-4}	10^{-3}	radians (<i>rad</i>)

Table 9.5: Star Camera (SC) Parameters

Parameter Name	High Cost	Moderate Cost	Low Cost	Units
Truth gravity model	18×18	18×18	18×18	unit-less
Filter gravity model	12×12	12×12	12×12	unit-less
1σ reference atm. density	2.80×10^{-15}	2.80×10^{-14}	2.80×10^{-13}	kg/m^3
1σ reference scale height	58.019	580.19	5801.9	meters (m)
Translational process noise	10^{-10} ($\sim 52 \text{ m/rev } 3\sigma$)	10^{-08} ($\sim 520 \text{ m/rev } 3\sigma$)	10^{-08} ($\sim 520 \text{ m/rev } 3\sigma$)	m^2/s^3
Aerodynamic process noise	10^{-10} ($\sim 52 \text{ m/rev } 3\sigma$)	10^{-08} ($\sim 520 \text{ m/rev } 3\sigma$)	10^{-08} ($\sim 520 \text{ m/rev } 3\sigma$)	m^2/s^3
Rotational process noise	10^{-16} ($\sim 0.03 \text{ rad/rev } 3\sigma$)	10^{-14} ($\sim 0.3 \text{ rad/rev } 3\sigma$)	10^{-14} ($\sim 0.3 \text{ rad/rev } 3\sigma$)	$1/s^3$
1σ spacecraft (s/c) ballistic number	5.56×10^{-6}	5.56×10^{-5}	5.56×10^{-4}	m^2/kg
1σ spacecraft (s/c) (COM) position	10^{-4}	10^{-3}	10^{-2}	meters (m)

Table 9.6: Environmental Uncertainties

For the results presented in the forthcoming sections, three accelerometers with a baseline of 0.5 meters and measurement update frequency of 20 seconds are used. A plot of the accelerometer configuration is shown in the Figure 9.1.

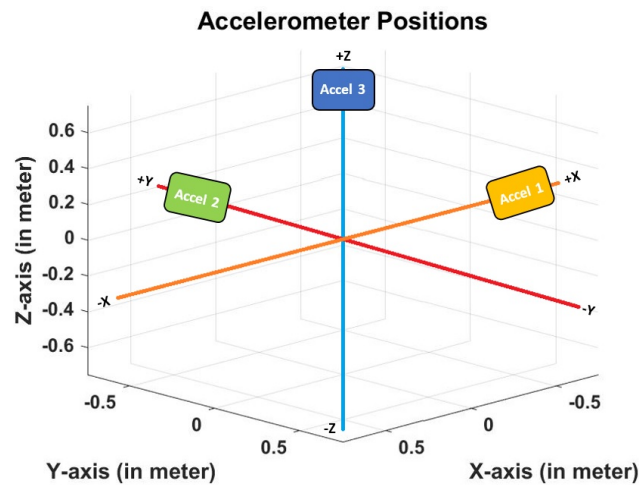


Fig. 9.1: Accelerometer Configuration

Specifications for parameters given above have been set as per the recent advancements made in the development of precision sensors and future projections mentioned in the relevant literature [51, 52, 53, 54].

9.3 Low Earth Orbit (50 degree Inclination)

The reference orbit is defined by the orbital parameters tabulated below

Name	Value	Units
Semi-major axis (a)	7×10^6	meters (m)
Eccentricity (e)	10^{-2}	unit-less
Inclination (i)	50	degree (deg)
Argument of perifocus (ω)	30	degree (deg)
Right ascension of the ascending node (Ω)	60	degree (deg)
True anomaly (ν)	120	degree (deg)
Numerical integration time-step	10	seconds (s)
Number of orbits simulated	5	unit-less

Table 9.7: LEO (50 degree Inclination) Orbital Parameters

9.3.1 Reference Trajectory

Reference trajectory results for a LEO (50 degree Inclination) orbit are presented for 2 orbital periods. Plots have been generated by setting the parameters as per the values given in the Tables 9.1 and 9.7.

Firstly, results are presented for a non-rotating spacecraft which is inertially fixed, i.e., the spacecraft body-fixed frame is initially aligned with the ECI frame. Plots for LEO orbital elements, spacecraft position, spacecraft attitude, and accelerometer measurements are shown in the Figures 9.2 - 9.5.

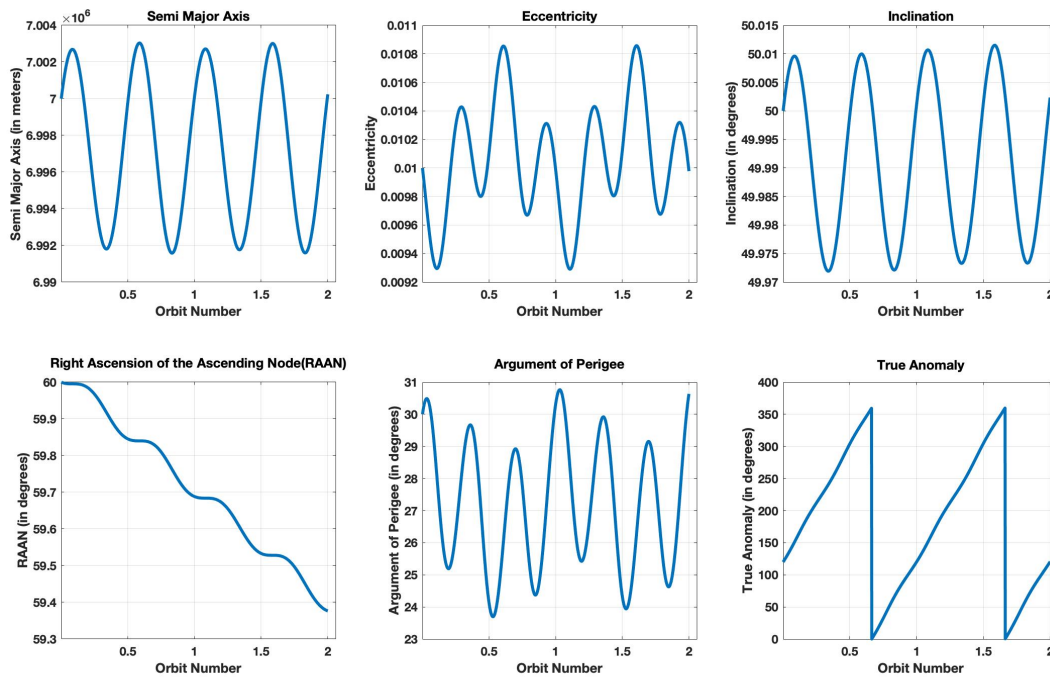


Fig. 9.2: Reference Trajectory (Non-rotating spacecraft) - LEO (50 degree Inclination) orbital elements

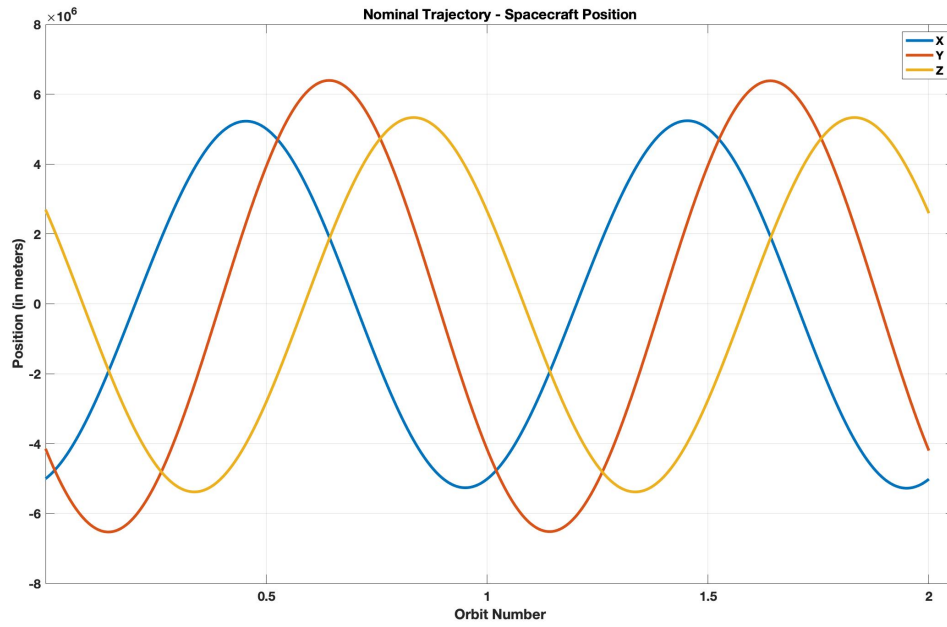


Fig. 9.3: Reference Trajectory (Non-rotating spacecraft) - Spacecraft Position in ECI frame

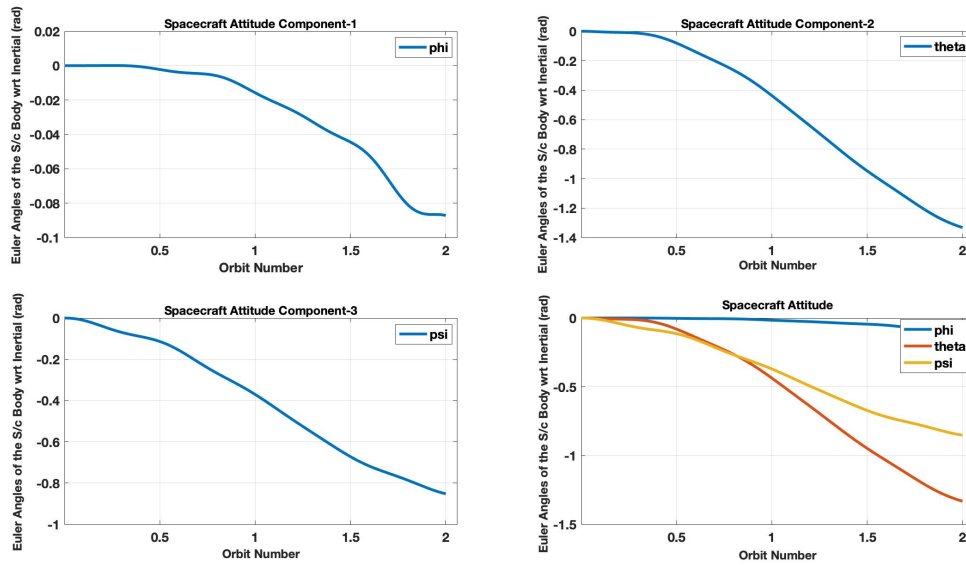


Fig. 9.4: Reference Trajectory (Non-rotating spacecraft) - Euler angles denoting attitude of the spacecraft body-fixed frame with respect to the ECI frame

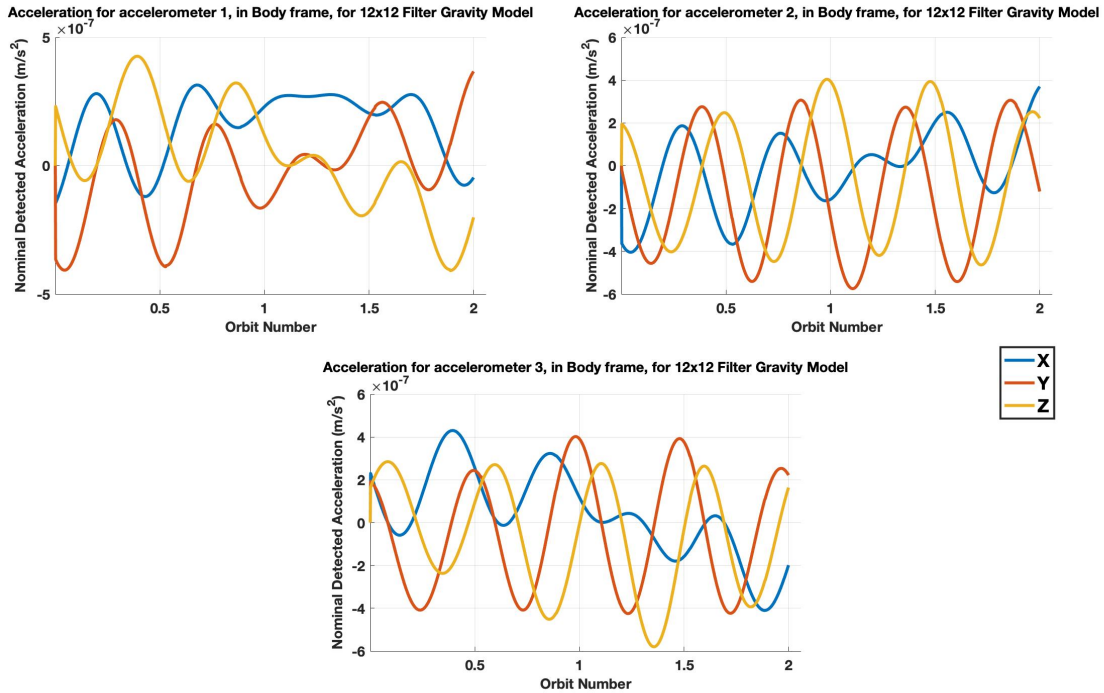


Fig. 9.5: Reference Trajectory (Non-rotating spacecraft) - Accelerometer measurements (in Spacecraft body-fixed frame) for accelerometer 1, 2, & 3

Results are now presented for a rotating spacecraft which is rotating at LVLH rate, Nadir pointing, and the spacecraft body-fixed frame is initially aligned with the LVLH frame.

Since a rotating spacecraft does not affect the translational states, the LEO orbital elements and spacecraft position do not change and the plots are the same as that for the non-rotating spacecraft. Plots for spacecraft attitude and accelerometer measurements are shown in the Figures 9.6 - 9.7.

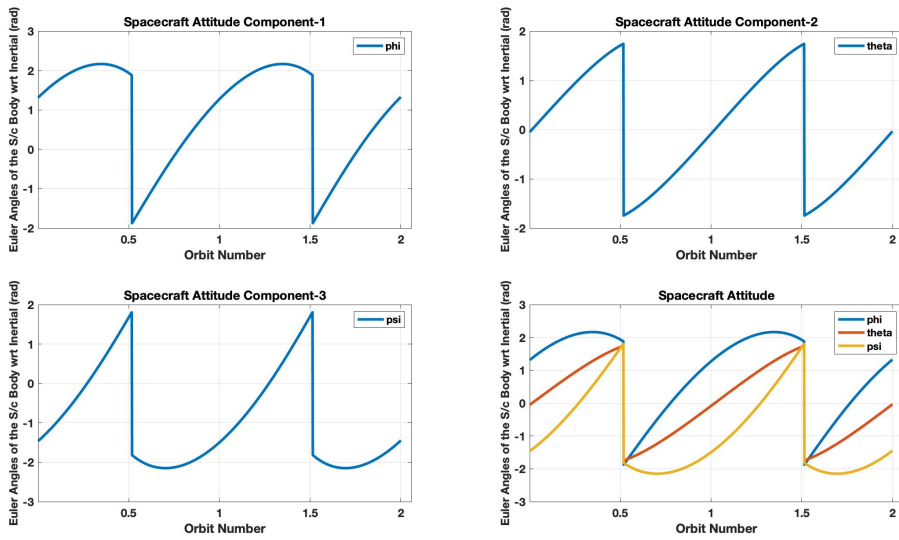


Fig. 9.6: Reference Trajectory (Rotating spacecraft) - Euler angles denoting attitude of the spacecraft body-fixed frame with respect to the ECI frame

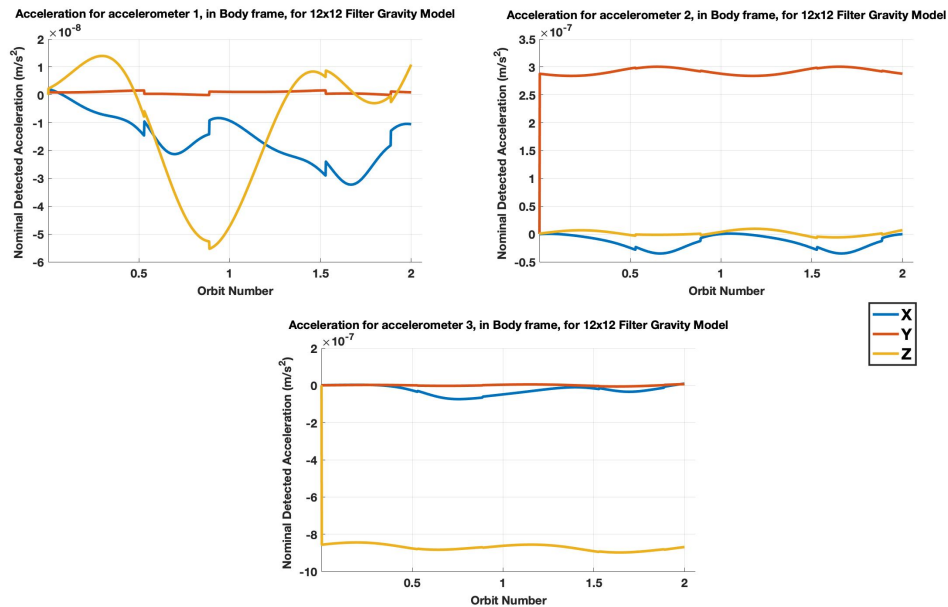


Fig. 9.7: Reference Trajectory (Rotating spacecraft) - Accelerometer measurements (in Spacecraft body-fixed frame) for accelerometer 1, 2, & 3

9.3.2 High Sensor Grade & Precise System Model

In this section, results for high sensor grade and precise system model are presented. To model high sensor grade and precise system model, sensor parameters, environmental uncertainties, and initial 1σ errors for all states are set equal to the values given in the High Cost column of the Tables 9.4, 9.5, and 9.6. Results have been generated by setting the parameters as per the values given in the Tables 9.1, 9.7, and 9.2.

First, the results are presented for three accelerometers, with initial 1σ error on spacecraft position, velocity, attitude, and angular velocity set equal to the values given in Table 9.2, accelerometer parameters are set as per Table 9.4, and the time constants are set as per Value 1 in Table 9.3.

Results for the true navigation error 1σ standard deviation on spacecraft position and attitude are shown in Figures 9.8-9.9. These results are for inertially fixed case, i.e., non-rotating spacecraft.

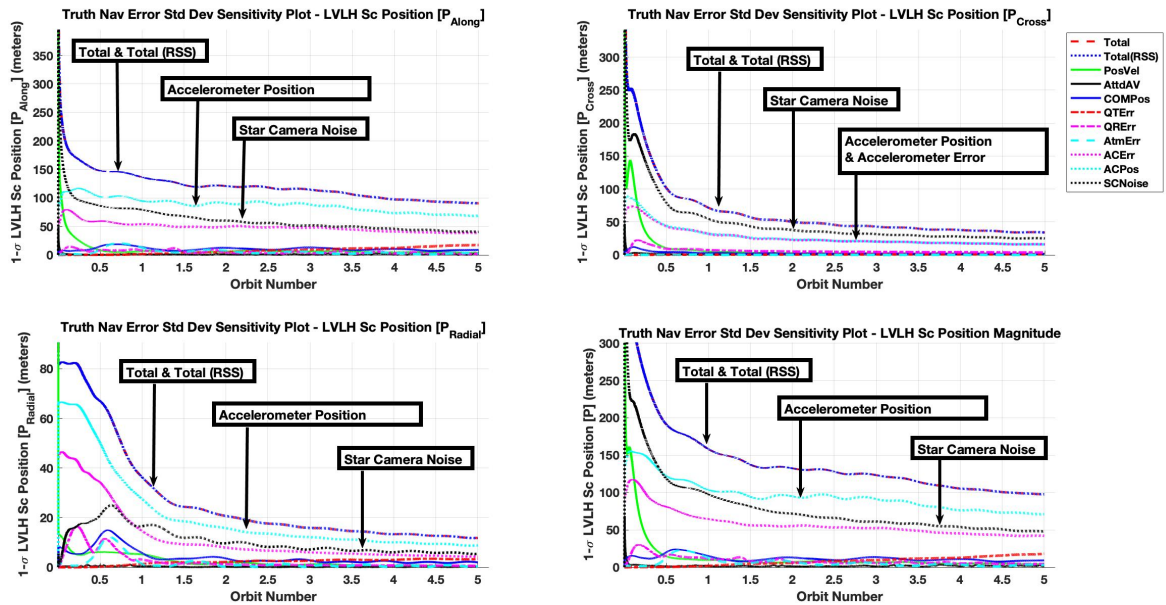


Fig. 9.8: True navigation error 1σ standard deviation on spacecraft position components (expressed in LVLH frame) and magnitude

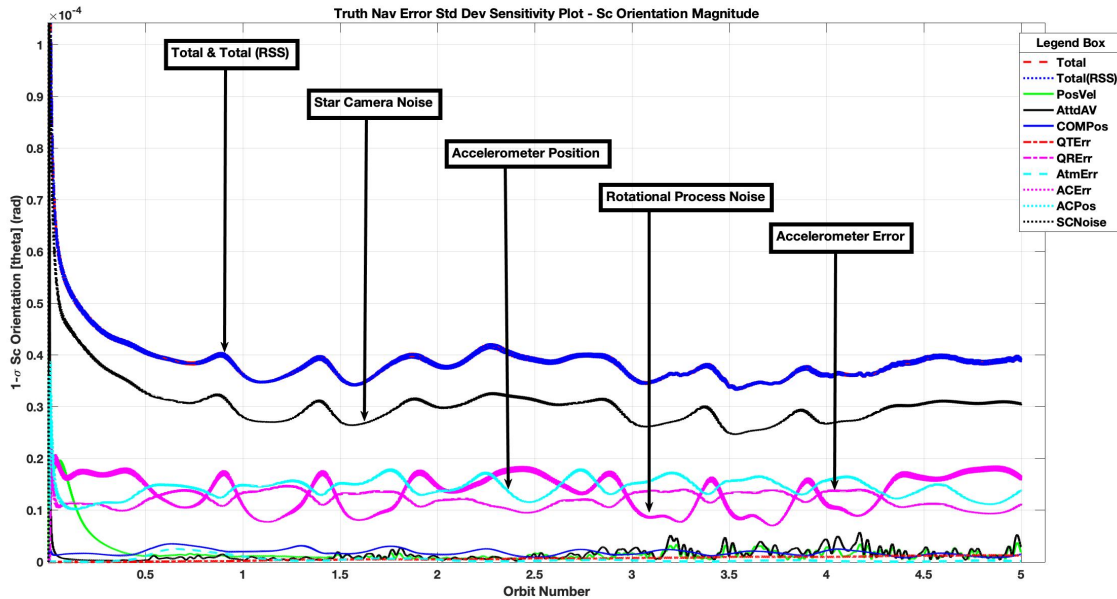


Fig. 9.9: True navigation error 1σ standard deviation on spacecraft attitude magnitude

The true navigation error 1σ standard deviation for all states converge to a steady state value. However, the estimates for accelerometer states are poor, especially accelerometer misalignment. One of the reason for poor estimation of accelerometer states could be weak observability of these states. The error budget results for accelerometer states also reflect this, because the major source of error is accelerometer error.

Further, plots for spacecraft velocity and angular velocity are not shown, as the trend for these states is similar to the trend of the true navigation error for spacecraft position and orientation. All the plots have been annotated to depict the major sources of true navigation error.

Error budget results are summarized in Table 9.8. Note that the total steady-state true navigation error is the RSS of all the error sources.

State Name	Total Steady-State True Navigation Error 1σ	Error Source 1	Error Source 2	Error Source 3	Units
Spacecraft Position Magnitude	105.36	Accelerometer Position - 76.20	Star Camera Noise - 53.89	Accelerometer Error - 45.34	m
Spacecraft Velocity Magnitude	0.11	Accelerometer Position - 0.08	Star Camera Noise - 0.06	Accelerometer Error - 0.05	m/s
Spacecraft Attitude Magnitude	4.032×10^{-5}	Star Camera Noise - 3.137×10^{-5}	Rotational Process Noise - 1.6535×10^{-5}	Accelerometer Position - 1.5211×10^{-5}	rad
Spacecraft Angular Velocity Magnitude	2.0629×10^{-7}	Rotational Process Noise - 1.6269×10^{-7}	Accelerometer Position - 7.4626×10^{-8}	Star Camera Noise - 7.4081×10^{-8}	rad/s
Spacecraft Center of Mass Position Magnitude	2.9021×10^{-5}	Center of Mass Position - 2.4328×10^{-5}	Accelerometer Position - 1.1185×10^{-5}	Accelerometer Error - 8.0496×10^{-6}	m
Spacecraft Ballistic Coefficient	5.1874×10^{-6}	Atmospheric Parameter States - 5.0793×10^{-6}	Center of Mass Position - 1.0083×10^{-6}	Accelerometer Position - 2.0018×10^{-7}	m^2/kg
Reference Atmospheric Density	2.6161×10^{-15}	Atmospheric Parameter States - 2.5616×10^{-15}	Center of Mass Position - 5.0849×10^{-16}	Accelerometer Position - 1.0095×10^{-16}	kg/m^3
Reference Scale Height	28.89	Atmospheric Parameter States - 24.76	Center of Mass Position - 14.65	Accelerometer Position - 1.88	m
Accelerometer 1 Position Magnitude	1.3637×10^{-5}	Accelerometer Position - 1.2657×10^{-5}	Accelerometer Error - 4.3261×10^{-6}	Star Camera Noise - 2.2762×10^{-6}	m
Accelerometer 1 Bias Magnitude	1.4679×10^{-11}	Accelerometer Error - 1.3513×10^{-11}	Accelerometer Position - 5.2064×10^{-12}	Star Camera Noise - 1.985×10^{-12}	m/s^2
Accelerometer 1 Scale Factor Magnitude	1.7139×10^{-5}	Accelerometer Error - 1.7054×10^{-5}	Accelerometer Position - 1.5286×10^{-6}	Star Camera Noise - 6.1338×10^{-7}	% measured acceleration
Accelerometer 1 Misalignment Magnitude	1.7317×10^{-6}	Accelerometer Error - 1.7315×10^{-6}	Accelerometer Position - 2.0949×10^{-8}	Star Camera Noise - 1.0294×10^{-8}	rad

Table 9.8: Error budget of the maximum steady-state true navigation error 1σ standard deviation

Results for the true navigation error 1σ standard deviation on spacecraft position and attitude are shown in Figures 9.10-9.11, for the rotating Nadir pointing spacecraft.

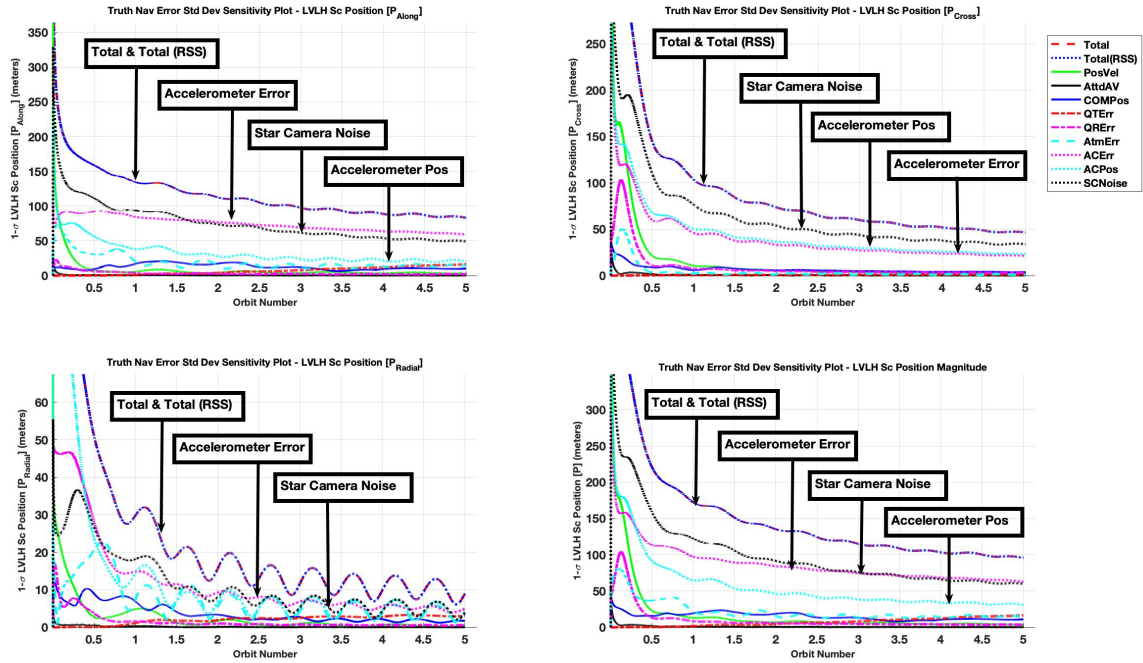


Fig. 9.10: True navigation error 1σ standard deviation on spacecraft position components (expressed in LVLH frame) and magnitude

The true navigation error 1σ standard deviation for all states converge to a steady state value. However, the estimates for accelerometer states are again poor, especially accelerometer misalignment. The reason for poor estimation of accelerometer states is suspected to be weak observability of these states. The error budget results for accelerometer states also reflect this, because the major source of error is accelerometer error.

Further, plots for spacecraft velocity and angular velocity are not shown, as the trend for these states is similar to the trend of the true navigation error for spacecraft position and orientation. All the results have been annotated to depict the major sources of true navigation error.

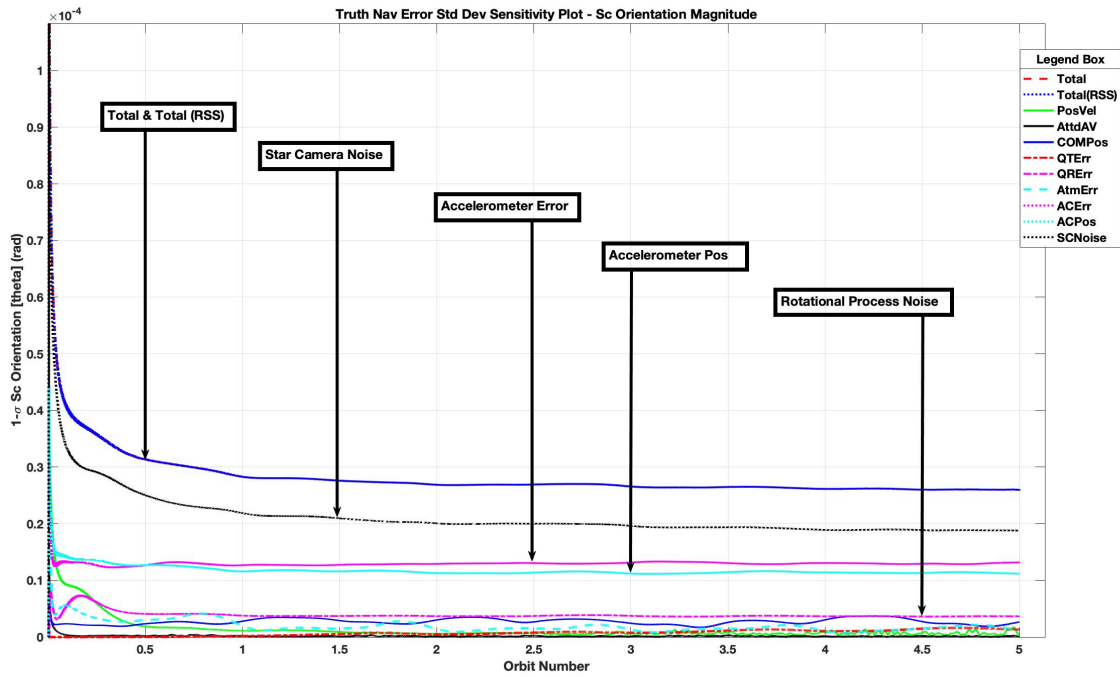


Fig. 9.11: True navigation error 1σ standard deviation on spacecraft attitude magnitude

Error budget results are summarized in Table 9.9. Note that the total steady-state true navigation error is the RSS of all the error sources.

State Name	Total Steady-State True Navigation Error 1σ	Error Source 1	Error Source 2	Error Source 3	Units
Spacecraft Position Magnitude	103.33	Accelerometer Error - 68.32	Star Camera Noise - 66.11	Accelerometer Position - 34.10	m
Spacecraft Velocity Magnitude	0.11	Accelerometer Error - 0.07	Star Camera Noise - 0.07	Accelerometer Position - 0.04	m/s
Spacecraft Attitude Magnitude	2.6354×10^{-5}	Star Camera Noise - 1.8959×10^{-5}	Accelerometer Error - 1.312×10^{-5}	Accelerometer Position - 1.1457×10^{-5}	rad
Spacecraft Angular Velocity Magnitude	7.8497×10^{-8}	Rotational Process Noise - 5.6284×10^{-8}	Accelerometer Error - 3.4877×10^{-8}	Accelerometer Position - 3.1892×10^{-8}	rad/s
Spacecraft Center of Mass Position Magnitude	9.5575×10^{-5}	Center of Mass Position - 9.1158×10^{-5}	Accelerometer Error - 2.3283×10^{-5}	Accelerometer Position - 1.0385×10^{-5}	m
Spacecraft Ballistic Coefficient	4.4676×10^{-6}	Atmospheric Parameter States - 4.1274×10^{-6}	Accelerometer Position - 9.6582×10^{-7}	Star Camera Noise - 9.575×10^{-7}	m^2/kg
Reference Atmospheric Density	2.253×10^{-15}	Atmospheric Parameter States - 2.0815×10^{-15}	Accelerometer Position - 4.8707×10^{-16}	Star Camera Noise - 4.8288×10^{-16}	kg/m^3
Reference Scale Height	14.02	Atmospheric Parameter States - 8.20	Accelerometer Error - 8.09	Accelerometer Position - 5.38	m
Accelerometer 1 Position Magnitude	1.4738×10^{-5}	Accelerometer Position - 1.3958×10^{-5}	Accelerometer Error - 4.1809×10^{-6}	Star Camera Noise - 2.0063×10^{-6}	m
Accelerometer 1 Bias Magnitude	1.4973×10^{-11}	Accelerometer Error - 1.4085×10^{-11}	Accelerometer Position - 3.6982×10^{-12}	Atmospheric Parameter States - 2.302×10^{-12}	m/s^2
Accelerometer 1 Scale Factor Magnitude	1.732×10^{-5}	Accelerometer Error - 1.7319×10^{-5}	Accelerometer Position - 1.0462×10^{-7}	Center of Mass Position - 4.6473×10^{-8}	% measured acceleration
Accelerometer 1 Misalignment Magnitude	1.732×10^{-6}	Accelerometer Error - 1.732×10^{-6}	Accelerometer Position - 1.3432×10^{-9}	Star Camera Noise - 6.0957×10^{-10}	rad

Table 9.9: Error budget of the maximum steady-state true navigation error 1σ standard deviation

The results in Table 9.9 show that the estimates for the spacecraft position, velocity, attitude, angular velocity, and atmospheric parameter states improve marginally for the rotating spacecraft in comparison to that for the non-rotating spacecraft. Whereas, the estimates for spacecraft's center of mass position are marginally better for the non-rotating spacecraft. Estimates for accelerometer states show no change for the rotating spacecraft.

Further, results are generated for a variety of scenarios and the effect of different number

of accelerometers, initial conditions, baseline length, and the time constant are studied. Error budget results for these scenarios are summarized in Tables 9.10-9.27.

The error budget results presented in the following tables help understand the effect of individual simulation parameters on the true navigation error of spacecraft position, velocity, attitude, and angular velocity. This information can be used to model the system based on the mission requirements. For this reason, error budgets for spacecraft position and attitude have been highlighted in each table.

The error budgets presented in this section help study a number of scenarios simultaneously. For example, it can be inferred that to get the best estimate of the spacecraft position for a non-rotating spacecraft, the system may be modeled based on Table 9.22 or Table 9.26. Similarly, an inference can be drawn for a rotating spacecraft. Thus, the error budget tables help provide a sensitivity matrix for multitude scenarios in a concise and compact manner.

Next, the results are presented for six accelerometers, with initial 1σ error on spacecraft position, velocity, attitude, and angular velocity set equal to the values given in Table 9.2, accelerometer parameters are set as per Table 9.4, and the time constants are set as per Value 1 in Table 9.3.

Results for a non-rotating inertially fixed spacecraft are presented in Table 9.10.

State Name	Total Steady-State True Navigation Error 1σ	Error Source 1	Error Source 2	Error Source 3	Units
Spacecraft Position Magnitude	73.03	Star Camera Noise - 49.95	Accelerometer Position - 43.74	Accelerometer Error - 26.64	m
Spacecraft Velocity Magnitude	0.08	Star Camera Noise - 0.05	Accelerometer Position - 0.05	Accelerometer Error - 0.03	m/s
Spacecraft Attitude Magnitude	3.7277×10^{-5}	Star Camera Noise - 3.0113×10^{-5}	Rotational Process Noise - 1.8689×10^{-5}	Accelerometer Position - 8.8692×10^{-6}	rad
Spacecraft Angular Velocity Magnitude	1.9533×10^{-7}	Rotational Process Noise - 1.6825×10^{-7}	Star Camera Noise - 8.0115×10^{-8}	Accelerometer Position - 4.3938×10^{-8}	rad/s

Table 9.10: Error budget of the maximum steady-state true navigation error 1σ standard deviation

Given below in Table 9.11 are the results for the rotating Nadir pointing spacecraft.

State Name	Total Steady-State True Navigation Error 1σ	Error Source 1	Error Source 2	Error Source 3	Units
Spacecraft Position Magnitude	81.49	Star Camera Noise - 59.68	Accelerometer Error - 45.20	Accelerometer Position - 27.61	m
Spacecraft Velocity Magnitude	0.09	Star Camera Noise - 0.06	Accelerometer Error - 0.05	Accelerometer Position - 0.03	m/s
Spacecraft Attitude Magnitude	1.8879×10^{-5}	Star Camera Noise - 1.1838×10^{-5}	Accelerometer Error - 1.098×10^{-5}	Accelerometer Position - 9.3139×10^{-6}	rad
Spacecraft Angular Velocity Magnitude	6.4211×10^{-8}	Rotational Process Noise - 5.514×10^{-8}	Accelerometer Error - 2.3136×10^{-8}	Accelerometer Position - 1.8892×10^{-8}	rad/s

Table 9.11: Error budget of the maximum steady-state true navigation error 1σ standard deviation

The results shown in Tables 9.10 and 9.11 provide evidence that as the number of accelerometers are increased more measurements are received which in turn provides more information about the system dynamics and hence, the state estimation improves.

Next, the results are presented for three accelerometers, with initial 1σ error on position and velocity set to 10% of the values given in Table 9.2, whereas initial 1σ error on spacecraft attitude and angular velocity are set equal to the values given in Table 9.2, accelerometer parameters are set as per Table 9.4, and the time constants are set as per Value 1 in Table 9.3.

Results for a non-rotating inertially fixed spacecraft are presented in Table 9.12.

State Name	Total Steady-State True Navigation Error 1σ	Error Source 1	Error Source 2	Error Source 3	Units
Spacecraft Position Magnitude	101.40	Accelerometer Position - 72.28	Star Camera Noise - 49.72	Accelerometer Error - 42.55	m
Spacecraft Velocity Magnitude	0.11	Accelerometer Position - 0.08	Star Camera Noise - 0.05	Accelerometer Error - 0.04	m/s
Spacecraft Attitude Magnitude	4.0263×10^{-5}	Star Camera Noise - 3.1284×10^{-5}	Rotational Process Noise - 1.6534×10^{-5}	Accelerometer Position - 1.5201×10^{-5}	rad
Spacecraft Angular Velocity Magnitude	2.0484×10^{-7}	Rotational Process Noise - 1.6306×10^{-7}	Accelerometer Position - 7.4244×10^{-8}	Star Camera Noise - 7.4002×10^{-8}	rad/s

Table 9.12: Error budget of the maximum steady-state true navigation error 1σ standard deviation

Given below in Table 9.13 are the results for the rotating Nadir pointing spacecraft.

State Name	Total Steady-State True Navigation Error 1σ	Error Source 1	Error Source 2	Error Source 3	Units
Spacecraft Position Magnitude	98.71	Accelerometer Error - 65.06	Star Camera Noise - 59.33	Accelerometer Position - 30.24	m
Spacecraft Velocity Magnitude	0.10	Accelerometer Error - 0.07	Star Camera Noise - 0.06	Accelerometer Position - 0.03	m/s
Spacecraft Attitude Magnitude	2.6198×10^{-5}	Star Camera Noise - 1.8744×10^{-5}	Accelerometer Error - 1.3065×10^{-5}	Accelerometer Position - 1.1395×10^{-5}	rad
Spacecraft Angular Velocity Magnitude	7.8223×10^{-8}	Rotational Process Noise - 5.6276×10^{-8}	Accelerometer Error - 3.4754×10^{-8}	Accelerometer Position - 3.175×10^{-8}	rad/s

Table 9.13: Error budget of the maximum steady-state true navigation error 1σ standard deviation

Next, the results are presented for six accelerometers, with initial 1σ error on position and velocity set to 10% of the values given in Table 9.2, whereas initial 1σ error on spacecraft attitude and angular velocity are set equal to the values given in Table 9.2, accelerometer parameters are set as per Table 9.4, and the time constants are set as per Value 1 in Table 9.3.

Results for a non-rotating inertially fixed spacecraft are presented in Table 9.14.

State Name	Total Steady-State True Navigation Error 1σ	Error Source 1	Error Source 2	Error Source 3	Units
Spacecraft Position Magnitude	71.00	Star Camera Noise - 46.83	Accelerometer Position - 42.00	Accelerometer Error - 25.38	m
Spacecraft Velocity Magnitude	0.07	Star Camera Noise - 0.05	Accelerometer Position - 0.04	Accelerometer Error - 0.03	m/s
Spacecraft Attitude Magnitude	3.7228×10^{-5}	Star Camera Noise - 3.0069×10^{-5}	Rotational Process Noise - 1.8707×10^{-5}	Accelerometer Position - 8.8164×10^{-6}	rad
Spacecraft Angular Velocity Magnitude	1.9483×10^{-7}	Rotational Process Noise - 1.6835×10^{-7}	Star Camera Noise - 8.0106×10^{-8}	Accelerometer Position - 4.381×10^{-8}	rad/s

Table 9.14: Error budget of the maximum steady-state true navigation error 1σ standard deviation

Given below in Table 9.15 are the results for the rotating Nadir pointing spacecraft.

State Name	Total Steady-State True Navigation Error 1σ	Error Source 1	Error Source 2	Error Source 3	Units
Spacecraft Position Magnitude	78.31	Star Camera Noise - 54.76	Accelerometer Error - 42.64	Accelerometer Position - 25.79	m
Spacecraft Velocity Magnitude	0.08	Star Camera Noise - 0.06	Accelerometer Error - 0.05	Accelerometer Position - 0.03	m/s
Spacecraft Attitude Magnitude	1.8729×10^{-5}	Star Camera Noise - 1.158×10^{-5}	Accelerometer Error - 1.0941×10^{-5}	Accelerometer Position - 9.2656×10^{-6}	rad
Spacecraft Angular Velocity Magnitude	6.4031×10^{-8}	Rotational Process Noise - 5.514×10^{-8}	Accelerometer Error - 2.3105×10^{-8}	Accelerometer Position - 1.8867×10^{-8}	rad/s

Table 9.15: Error budget of the maximum steady-state true navigation error 1σ standard deviation

The results shown in Tables 9.12 - 9.15 provide evidence that the filter performance is nominal as the filter converge to the same steady state values for different initial conditions. This is because as the measurements are received over time, the error due to the initial uncertainty shrinks and eventually a steady state is achieved.

Results are now presented for three accelerometers, with initial 1σ error on spacecraft position, velocity, attitude, and angular velocity set equal to the values given in Table 9.2,

accelerometer parameters are set as per Table 9.4, and the time constants are set as per Value 2 in Table 9.3.

Results for a non-rotating inertially fixed spacecraft are presented in Table 9.16 .

State Name	Total Steady-State True Navigation Error 1σ	Error Source 1	Error Source 2	Error Source 3	Units
Spacecraft Position Magnitude	105.38	Accelerometer Position - 76.25	Star Camera Noise - 53.90	Accelerometer Error - 45.36	m
Spacecraft Velocity Magnitude	0.11	Accelerometer Position - 0.08	Star Camera Noise - 0.06	Accelerometer Error - 0.05	m/s
Spacecraft Attitude Magnitude	4.0321×10^{-5}	Star Camera Noise - 3.1371×10^{-5}	Rotational Process Noise - 1.6535×10^{-5}	Accelerometer Position - 1.5215×10^{-5}	rad
Spacecraft Angular Velocity Magnitude	2.0629×10^{-7}	Rotational Process Noise - 1.6269×10^{-7}	Accelerometer Position - 7.4634×10^{-8}	Star Camera Noise - 7.4082×10^{-8}	rad/s

Table 9.16: Error budget of the maximum steady-state true navigation error 1σ standard deviation

Given below in Table 9.17 are the results for the rotating Nadir pointing spacecraft.

State Name	Total Steady-State True Navigation Error 1σ	Error Source 1	Error Source 2	Error Source 3	Units
Spacecraft Position Magnitude	107.08	Accelerometer Error - 70.12	Star Camera Noise - 67.06	Accelerometer Position - 36.32	m
Spacecraft Velocity Magnitude	0.11	Accelerometer Error - 0.07	Star Camera Noise - 0.07	Accelerometer Position - 0.04	m/s
Spacecraft Attitude Magnitude	2.6817×10^{-5}	Star Camera Noise - 1.9347×10^{-5}	Accelerometer Error - 1.3375×10^{-5}	Accelerometer Position - 1.1764×10^{-5}	rad
Spacecraft Angular Velocity Magnitude	7.9939×10^{-8}	Rotational Process Noise - 5.6577×10^{-8}	Accelerometer Error - 3.6936×10^{-8}	Accelerometer Position - 3.298×10^{-8}	rad/s

Table 9.17: Error budget of the maximum steady-state true navigation error 1σ standard deviation

Given below in Table 9.18 are the results for six accelerometers, with initial 1σ error on spacecraft position, velocity, attitude, and angular velocity set equal to the values given

in Table 9.2, accelerometer parameters are set as per Table 9.4, and the time constants are set as per Value 2 in Table 9.3.

Results for a non-rotating inertially fixed spacecraft are presented in Table 9.18.

State Name	Total Steady-State True Navigation Error 1σ	Error Source 1	Error Source 2	Error Source 3	Units
Spacecraft Position Magnitude	73.03	Star Camera Noise - 49.95	Accelerometer Position - 43.74	Accelerometer Error - 26.64	m
Spacecraft Velocity Magnitude	0.08	Star Camera Noise - 0.05	Accelerometer Position - 0.05	Accelerometer Error - 0.03	m/s
Spacecraft Attitude Magnitude	3.7277×10^{-5}	Star Camera Noise - 3.0113×10^{-5}	Rotational Process Noise - 1.8689×10^{-5}	Accelerometer Position - 8.8691×10^{-6}	rad
Spacecraft Angular Velocity Magnitude	1.9533×10^{-7}	Rotational Process Noise - 1.6825×10^{-7}	Star Camera Noise - 8.0115×10^{-8}	Accelerometer Position - 4.3938×10^{-8}	rad/s

Table 9.18: Error budget of the maximum steady-state true navigation error 1σ standard deviation

Results for the rotating Nadir pointing spacecraft are presented in Table 9.19 .

State Name	Total Steady-State True Navigation Error 1σ	Error Source 1	Error Source 2	Error Source 3	Units
Spacecraft Position Magnitude	82.64	Star Camera Noise - 59.99	Accelerometer Error - 45.46	Accelerometer Position - 29.04	m
Spacecraft Velocity Magnitude	0.09	Star Camera Noise - 0.06	Accelerometer Error - 0.05	Accelerometer Position - 0.03	m/s
Spacecraft Attitude Magnitude	1.8911×10^{-5}	Star Camera Noise - 1.1851×10^{-5}	Accelerometer Error - 1.0979×10^{-5}	Accelerometer Position - 9.3432×10^{-6}	rad
Spacecraft Angular Velocity Magnitude	6.4213×10^{-8}	Rotational Process Noise - 5.514×10^{-8}	Accelerometer Error - 2.3136×10^{-8}	Accelerometer Position - 1.8893×10^{-8}	rad/s

Table 9.19: Error budget of the maximum steady-state true navigation error 1σ standard deviation

The results shown in Tables 9.16 - 9.19 depict the effect of the smaller time constant on the reference atmospheric density state. And when these results are compared with that

shown in Tables 9.8 - 9.11, it is inferred that there is no effect on spacecraft position, velocity, attitude, and angular velocity states for the non-rotating inertially fixed case. While the effect is minimal on these states for rotating Nadir pointing spacecraft.

Further, results are presented for three accelerometers with accelerometer baseline length set to 1 meters. Initial 1σ error on spacecraft position, velocity, attitude, and angular velocity is set equal to the values given in Table 9.2, accelerometer parameters are set as per Table 9.4, and the time constants are set as per Value 1 in Table 9.3.

Results for a non-rotating inertially fixed spacecraft are presented in Table 9.20 .

State Name	Total Steady-State True Navigation Error 1σ	Error Source 1	Error Source 2	Error Source 3	Units
Spacecraft Position Magnitude	70.78	Star Camera Noise - 49.96	Accelerometer Position - 40.48	Accelerometer Error - 25.31	m
Spacecraft Velocity Magnitude	0.07	Star Camera Noise - 0.05	Accelerometer Position - 0.04	Accelerometer Error - 0.03	m/s
Spacecraft Attitude Magnitude	3.6786×10^{-5}	Star Camera Noise - 2.991×10^{-5}	Rotational Process Noise - 1.8757×10^{-5}	Accelerometer Position - 7.4131×10^{-6}	rad
Spacecraft Angular Velocity Magnitude	1.92×10^{-7}	Rotational Process Noise - 1.6647×10^{-7}	Star Camera Noise - 7.9806×10^{-8}	Accelerometer Position - 3.7199×10^{-8}	rad/s

Table 9.20: Error budget of the maximum steady-state true navigation error 1σ standard deviation

Given below in Table 9.21 are the results for the rotating Nadir pointing spacecraft.

State Name	Total Steady-State True Navigation Error 1σ	Error Source 1	Error Source 2	Error Source 3	Units
Spacecraft Position Magnitude	76.40	Star Camera Noise - 59.28	Accelerometer Error - 37.60	Accelerometer Position - 24.68	m
Spacecraft Velocity Magnitude	0.08	Star Camera Noise - 0.06	Accelerometer Error - 0.04	Accelerometer Position - 0.02	m/s
Spacecraft Attitude Magnitude	1.8675×10^{-5}	Star Camera Noise - 1.1923×10^{-5}	Accelerometer Error - 1.0168×10^{-5}	Accelerometer Position - 9.2134×10^{-6}	rad
Spacecraft Angular Velocity Magnitude	6.4362×10^{-8}	Rotational Process Noise - 5.516×10^{-8}	Accelerometer Error - 2.1396×10^{-8}	Accelerometer Position - 1.9501×10^{-8}	rad/s

Table 9.21: Error budget of the maximum steady-state true navigation error 1σ standard deviation

Next, results are presented for six accelerometers with accelerometer baseline length set to 1 meters. Initial 1σ error on spacecraft position, velocity, attitude, and angular velocity is set equal to the values given in Table 9.2, accelerometer parameters are set as per Table 9.4, and the time constants are set as per Value 1 in Table 9.3.

Results for a non-rotating inertially fixed spacecraft are presented in Table 9.22 .

State Name	Total Steady-State True Navigation Error 1σ	Error Source 1	Error Source 2	Error Source 3	Units
Spacecraft Position Magnitude	57.19	Star Camera Noise - 47.22	Accelerometer Position - 24.23	Accelerometer Error - 15.66	m
Spacecraft Velocity Magnitude	0.06	Star Camera Noise - 0.05	Accelerometer Position - 0.03	Accelerometer Error - 0.02	m/s
Spacecraft Attitude Magnitude	3.5802×10^{-5}	Star Camera Noise - 2.9382×10^{-5}	Rotational Process Noise - 1.8717×10^{-5}	Accelerometer Position - 5.8003×10^{-6}	rad
Spacecraft Angular Velocity Magnitude	1.9346×10^{-7}	Rotational Process Noise - 1.1682×10^{-7}	Initial Spacecraft Position & Velocity - 9.0593×10^{-8}	Initial Attitude & Angular Velocity - 6.8368×10^{-8}	rad/s

Table 9.22: Error budget of the maximum steady-state true navigation error 1σ standard deviation

Given below in Table 9.23 are the results for the rotating Nadir pointing spacecraft.

State Name	Total Steady-State True Navigation Error 1σ	Error Source 1	Error Source 2	Error Source 3	Units
Spacecraft Position Magnitude	64.44	Star Camera Noise - 51.48	Accelerometer Error - 25.47	Accelerometer Position - 25.17	m
Spacecraft Velocity Magnitude	0.07	Star Camera Noise - 0.05	Accelerometer Error - 0.03	Accelerometer Position - 0.03	m/s
Spacecraft Attitude Magnitude	1.2384×10^{-5}	Accelerometer Error - 7.358×10^{-6}	Star Camera Noise - 7.1157×10^{-6}	Accelerometer Position - 6.4502×10^{-6}	rad
Spacecraft Angular Velocity Magnitude	5.8077×10^{-8}	Rotational Process Noise - 5.4991×10^{-8}	Accelerometer Error - 1.3288×10^{-8}	Accelerometer Position - 1.087×10^{-8}	rad/s

Table 9.23: Error budget of the maximum steady-state true navigation error 1σ standard deviation

The results shown in Tables 9.20 - 9.23 provide evidence for the effect of the increase in the baseline length of the on-board accelerometers. As expected, the increase in baseline length improves the resolution of the accelerometer measurements and hence, the filter performance improves.

Next, results are presented for three accelerometers with accelerometer baseline length set to 1 meters. Initial 1σ error on spacecraft position, velocity, attitude, and angular velocity is set equal to the values given in Table 9.2, accelerometer parameters are set as per Table 9.4, and the time constants are set as per Value 2 in Table 9.3.

Results for a non-rotating inertially fixed spacecraft are presented in Table 9.24 .

State Name	Total Steady-State True Navigation Error 1σ	Error Source 1	Error Source 2	Error Source 3	Units
Spacecraft Position Magnitude	70.79	Star Camera Noise - 49.96	Accelerometer Position - 40.51	Accelerometer Error - 25.32	m
Spacecraft Velocity Magnitude	0.07	Star Camera Noise - 0.05	Accelerometer Position - 0.04	Accelerometer Error - 0.03	m/s
Spacecraft Attitude Magnitude	3.6786×10^{-5}	Star Camera Noise - 2.991×10^{-5}	Rotational Process Noise - 1.8757×10^{-5}	Accelerometer Position - 7.4139×10^{-6}	rad
Spacecraft Angular Velocity Magnitude	1.92×10^{-7}	Rotational Process Noise - 1.6647×10^{-7}	Star Camera Noise - 7.9806×10^{-8}	Accelerometer Position - 3.72×10^{-8}	rad/s

Table 9.24: Error budget of the maximum steady-state true navigation error 1σ standard deviation

And similarly, given below in Table 9.25 are the results for the rotating Nadir pointing spacecraft.

State Name	Total Steady-State True Navigation Error 1σ	Error Source 1	Error Source 2	Error Source 3	Units
Spacecraft Position Magnitude	78.21	Star Camera Noise - 59.65	Accelerometer Error - 38.39	Accelerometer Position - 26.67	m
Spacecraft Velocity Magnitude	0.08	Star Camera Noise - 0.06	Accelerometer Error - 0.04	Accelerometer Position - 0.03	m/s
Spacecraft Attitude Magnitude	1.9144×10^{-5}	Star Camera Noise - 1.2179×10^{-5}	Accelerometer Error - 1.0457×10^{-5}	Accelerometer Position - 9.4771×10^{-6}	rad
Spacecraft Angular Velocity Magnitude	6.5095×10^{-8}	Rotational Process Noise - 5.5289×10^{-8}	Accelerometer Error - 2.2618×10^{-8}	Accelerometer Position - 2.0186×10^{-8}	rad/s

Table 9.25: Error budget of the maximum steady-state true navigation error 1σ standard deviation

Results are now presented for six accelerometers with accelerometer baseline length set to 1 meters. Initial 1σ error on spacecraft position, velocity, attitude, and angular velocity is set equal to the values given in Table 9.2, accelerometer parameters are set as per Table 9.4, and the time constants are set as per Value 2 in Table 9.3.

Results for a non-rotating inertially fixed spacecraft are given in Table 9.26.

State Name	Total Steady-State True Navigation Error 1σ	Error Source 1	Error Source 2	Error Source 3	Units
Spacecraft Position Magnitude	57.19	Star Camera Noise - 47.22	Accelerometer Position - 24.23	Accelerometer Error - 15.66	m
Spacecraft Velocity Magnitude	0.06	Star Camera Noise - 0.05	Accelerometer Position - 0.03	Accelerometer Error - 0.02	m/s
Spacecraft Attitude Magnitude	3.5802×10^{-5}	Star Camera Noise - 2.9382×10^{-5}	Rotational Process Noise - 1.8717×10^{-5}	Accelerometer Position - 5.8003×10^{-6}	rad
Spacecraft Angular Velocity Magnitude	1.9346×10^{-7}	Rotational Process Noise - 1.1682×10^{-7}	Initial Spacecraft Position & Velocity - 9.0593×10^{-8}	Initial Attitude & Angular Velocity - 6.8367×10^{-8}	rad/s

Table 9.26: Error budget of the maximum steady-state true navigation error 1σ standard deviation

Given below in Table 9.27 are the results for the rotating Nadir pointing spacecraft.

State Name	Total Steady-State True Navigation Error 1σ	Error Source 1	Error Source 2	Error Source 3	Units
Spacecraft Position Magnitude	64.95	Star Camera Noise - 51.58	Accelerometer Position - 26.00	Accelerometer Error - 25.56	m
Spacecraft Velocity Magnitude	0.07	Star Camera Noise - 0.05	Accelerometer Position - 0.03	Accelerometer Error - 0.03	m/s
Spacecraft Attitude Magnitude	1.2408×10^{-5}	Star Camera Noise - 7.1239×10^{-6}	Accelerometer Error - 7.3604×10^{-6}	Accelerometer Position - 6.4785×10^{-6}	rad
Spacecraft Angular Velocity Magnitude	5.8078×10^{-8}	Rotational Process Noise - 5.4991×10^{-8}	Accelerometer Error - 1.3288×10^{-8}	Accelerometer Position - 1.0871×10^{-8}	rad/s

Table 9.27: Error budget of the maximum steady-state true navigation error 1σ standard deviation

The results shown in Tables 9.24 - 9.27 provide evidence for the combined effect of the increase in the baseline length of the on-board accelerometers and the smaller time constant on the reference atmospheric density state.

9.3.3 Moderate Sensor Grade & Moderately Precise System Model

In this section, results for moderate sensor grade and moderately precise system model are presented. To model moderate sensor grade and moderately precise system model, sensor parameters, environmental uncertainties, and initial 1σ error for all states are set equal to the values given in the Moderate Cost column of the Tables 9.4, 9.5, and 9.6. Results have been generated by setting the parameters as per the values given in the Tables 9.1, 9.7, and 9.2.

Results are presented for three accelerometers, with initial 1σ error on spacecraft position, velocity, attitude, and angular velocity set equal to the values given in Table 9.2, accelerometer parameters are set as per Table 9.4, and the time constants are set as per Value 1 in Table 9.3.

Results for the true navigation error 1σ standard deviation on spacecraft position and attitude are shown in Figures 9.12-9.13, for the non-rotating inertially fixed spacecraft.

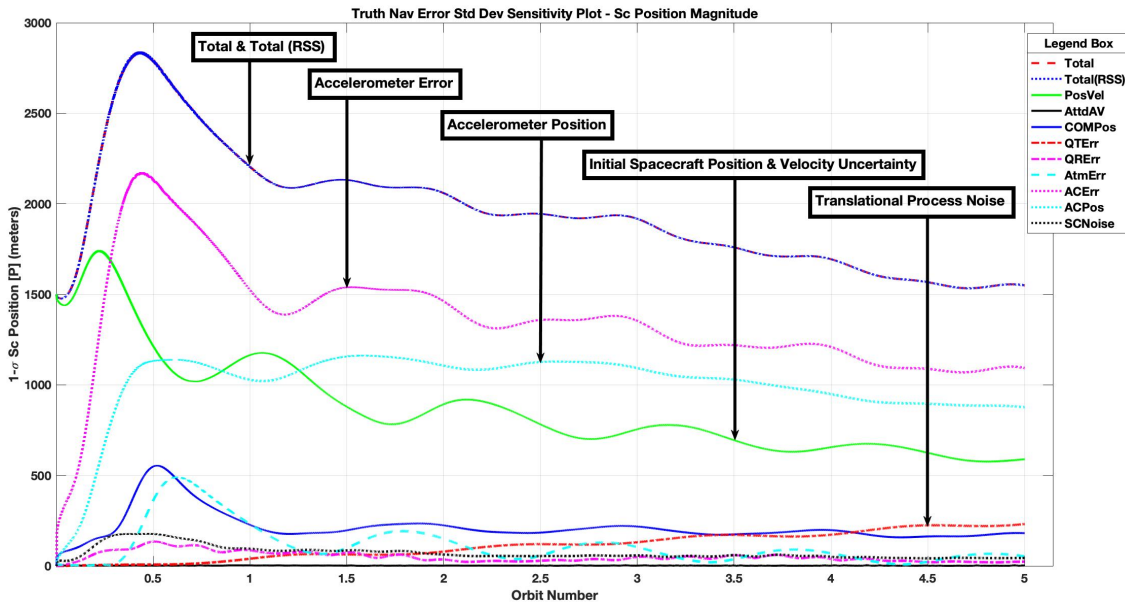


Fig. 9.12: True navigation error 1σ standard deviation on spacecraft position magnitude

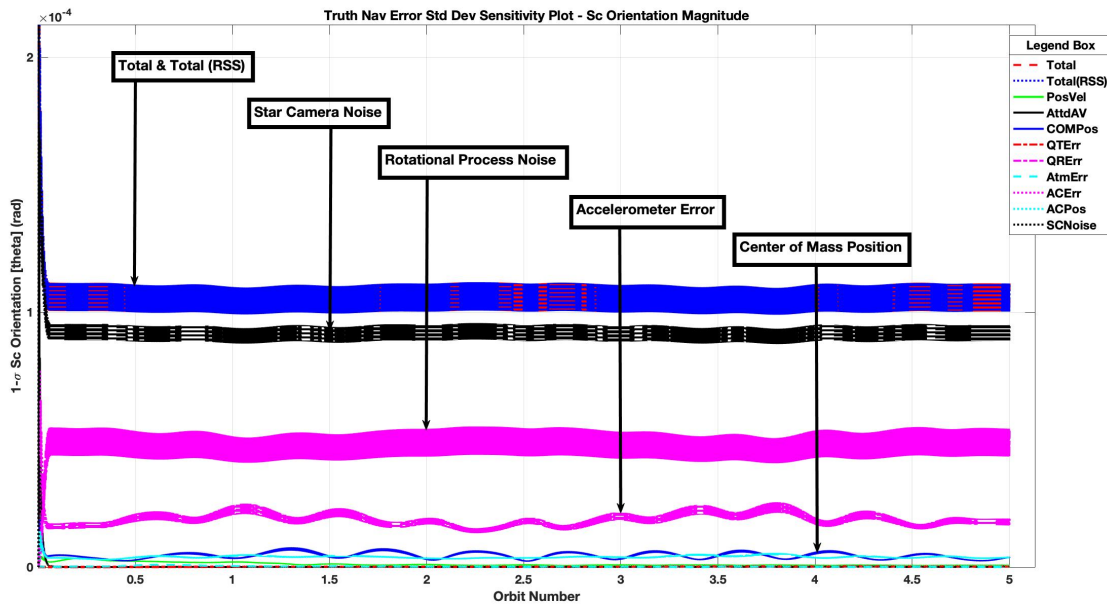


Fig. 9.13: True navigation error 1σ standard deviation on spacecraft attitude magnitude

Results for spacecraft velocity and angular velocity are not shown, as the trend for these states is similar to the trend of the true navigation error for spacecraft position and orientation. All results have been annotated to depict the major sources of true navigation error.

Error budget results are summarized in Table 9.28. Note that the total steady-state true navigation error is the RSS of all the error sources.

State Name	Total Steady-State True Navigation Error 1σ	Error Source 1	Error Source 2	Error Source 3	Units
Spacecraft Position Magnitude	1694.09	Accelerometer Error - 1209.09	Accelerometer Position - 948.85	Initial Spacecraft Position & Velocity - 655.89	m
Spacecraft Velocity Magnitude	1.73	Accelerometer Error - 1.21	Accelerometer Position - 1.00	Initial Spacecraft Position & Velocity - 0.69	m/s
Spacecraft Attitude Magnitude	1.1157×10^{-4}	Star Camera Noise - 9.5402×10^{-5}	Rotational Process Noise - 5.4931×10^{-5}	Accelerometer Error - 1.6873×10^{-5}	rad
Spacecraft Angular Velocity Magnitude	1.7159×10^{-6}	Rotational Process Noise - 1.4929×10^{-6}	Star Camera Noise - 8.0764×10^{-7}	Accelerometer Error - 2.3239×10^{-7}	rad/s

Table 9.28: Error budget of the maximum steady-state true navigation error 1σ standard deviation

Results for the true navigation error 1σ standard deviation on spacecraft position and attitude are shown in Figures 9.14-9.15, for the rotating Nadir pointing spacecraft.

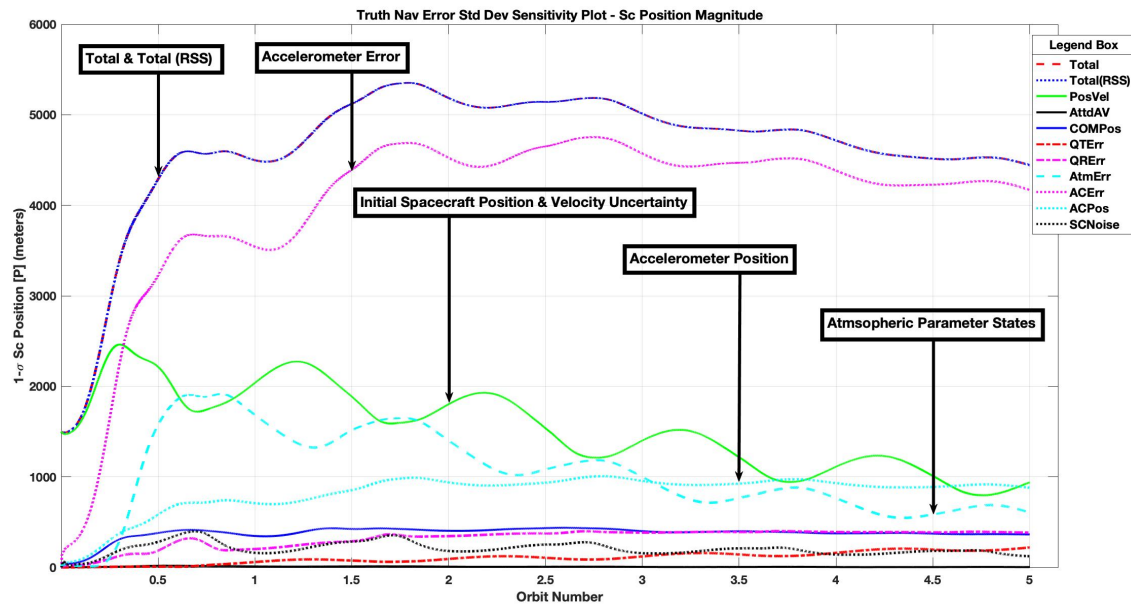


Fig. 9.14: True navigation error 1σ standard deviation on spacecraft position magnitude

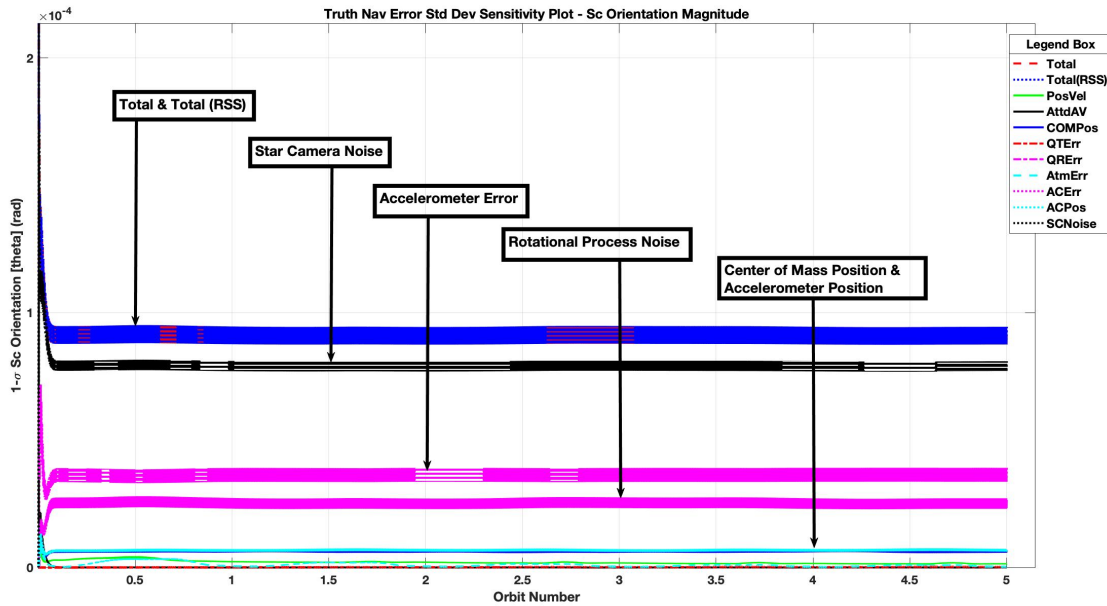


Fig. 9.15: True navigation error 1σ standard deviation on spacecraft attitude magnitude

Plots for spacecraft velocity and angular velocity are not shown, as the trend for these states is similar to the trend of the true navigation error for spacecraft position and orientation. All results have been annotated to depict the major sources of true navigation error.

Error budget results are summarized in Table 9.29. Note that the total steady-state true navigation error is the RSS of all the error sources.

The results for the moderate sensor grade and moderately precise system model depict the effect of lower sensor grade on the true navigation error of spacecraft position, velocity, attitude, and angular velocity. The accelerometer error is now a major source of error, and thus system should be designed accordingly.

State Name	Total Steady-State True Navigation Error 1σ	Error Source 1	Error Source 2	Error Source 3	Units
Spacecraft Position Magnitude	4716.33	Accelerometer Error - 4383.03	Initial Spacecraft Position & Velocity - 1114.52	Accelerometer Position - 930.85	m
Spacecraft Velocity Magnitude	4.99	Accelerometer Error - 4.65	Initial Spacecraft Position & Velocity - 1.18	Accelerometer Position - 0.99	m/s
Spacecraft Attitude Magnitude	9.4514×10^{-5}	Star Camera Noise - 8.0989×10^{-5}	Accelerometer Error - 3.9108×10^{-5}	Rotational Process Noise - 2.7155×10^{-5}	rad
Spacecraft Angular Velocity Magnitude	1.1643×10^{-6}	Rotational Process Noise - 7.6322×10^{-7}	Accelerometer Error - 6.9076×10^{-7}	Star Camera Noise - 5.0861×10^{-7}	rad/s

Table 9.29: Error budget of the maximum steady-state true navigation error 1σ standard deviation

9.3.4 Low Sensor Grade & Less Precise System Model

In this section, results for low sensor grade and less precise system model are discussed. To model low sensor grade and less precise system model, sensor parameters, environmental uncertainties, and initial 1σ error for all states are set equal to the values given in the Low Cost column of the Tables 9.4, 9.5, and 9.6. Plots were generated by setting the parameters as per the values given in the Tables 9.1, 9.7, and 9.2.

Results were generated for three accelerometers, with initial 1σ error on spacecraft position, velocity, attitude, and angular velocity set equal to the values given in Table 9.2, accelerometer parameters are set as per Table 9.4, and the time constants are set as per Value 1 in Table 9.3. In both cases, non-rotating inertially fixed spacecraft or rotating radially pointing spacecraft, true navigation error for spacecraft position and velocity diverge, and the estimation of these states is not feasible. The major source of error is due to the low grade sensor model and its associated accelerometer error. Though estimation of spacecraft attitude and angular velocity is still possible because of the star camera measurements.

9.4 Polar Low Earth Orbit (P-LEO)

Reference orbit is defined by the orbital parameters tabulated below

Name	Value	Units
Semi-major axis (a)	7080136.3	meters (m)
Eccentricity (e)	1.37×10^{-4}	unit-less
Inclination (i)	98.2194	degree (deg)
Argument of perifocus (ω)	89.4379	degree (deg)
Right ascension of the ascending node (Ω)	298.3267	degree (deg)
True anomaly (ν)	0	degree (deg)
Numerical integration time-step	10	seconds (s)
Number of orbits simulated	5	unit-less

Table 9.30: Polar LEO Orbital Parameters

9.4.1 Reference Trajectory

Reference trajectory results for a polar LEO orbit are presented for 2 orbital periods. Plots have been generated by setting the parameters as per the values given in the Tables [9.1](#) and [9.30](#).

Firstly, for a non-rotating spacecraft which is inertially fixed, i.e., the spacecraft body-fixed frame is initially aligned with the ECI frame. Plots for LEO orbital elements, spacecraft position, spacecraft attitude, and accelerometer measurements are shown in the Figures [9.16](#) - [9.19](#).

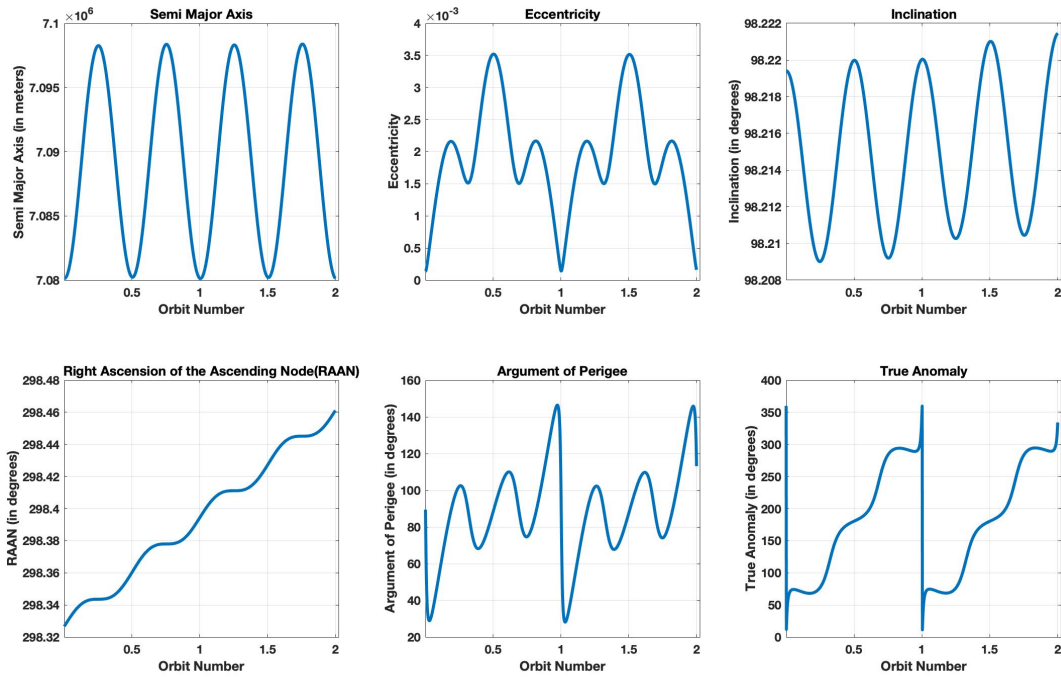


Fig. 9.16: Reference Trajectory (Non-rotating spacecraft) - Polar LEO orbital elements

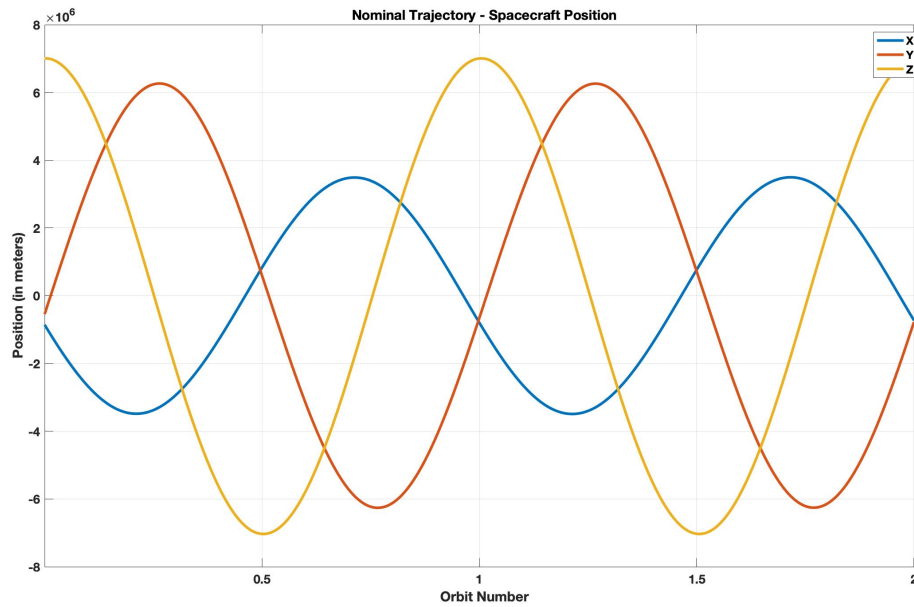


Fig. 9.17: Reference Trajectory (Non-rotating spacecraft) - Spacecraft Position in ECI frame

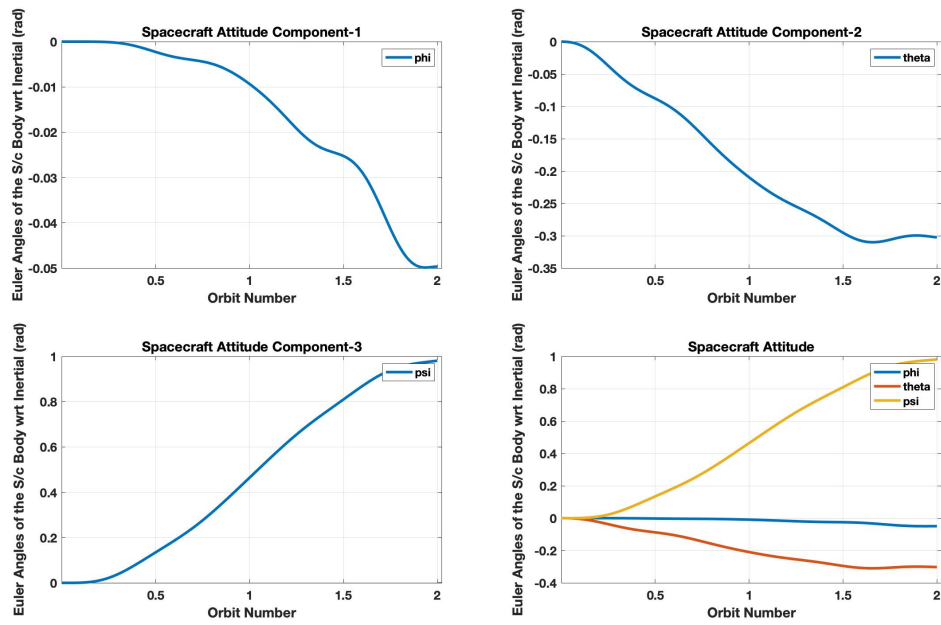


Fig. 9.18: Reference Trajectory (Non-rotating spacecraft) - Euler angles denoting attitude of the spacecraft body-fixed frame with respect to the ECI frame

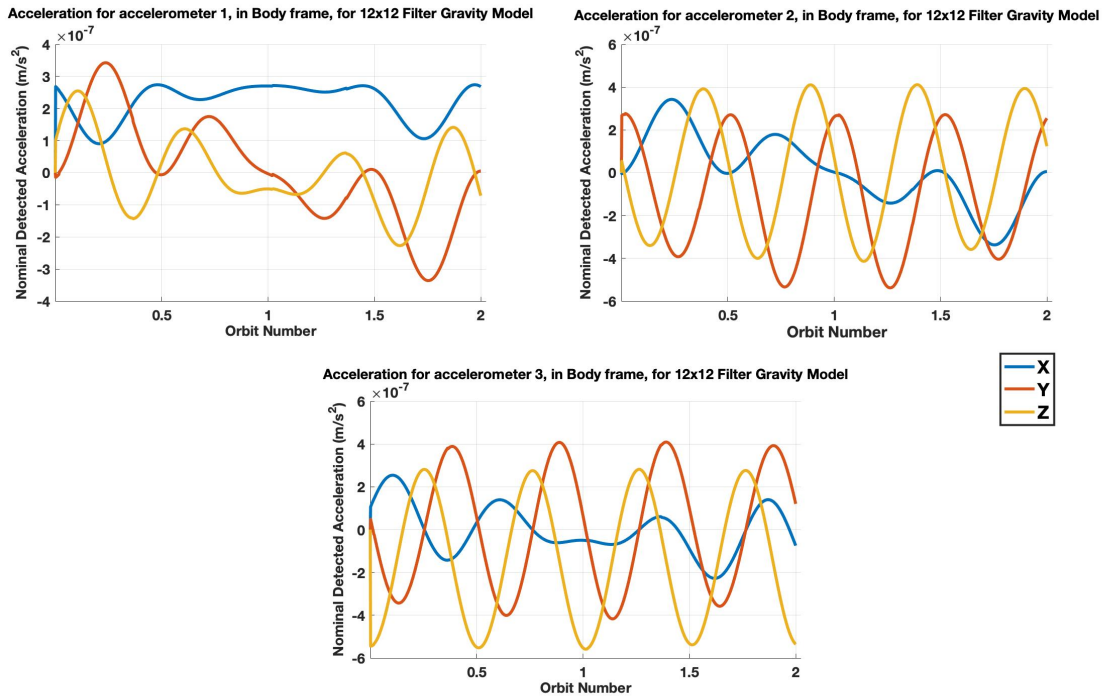


Fig. 9.19: Reference Trajectory (Non-rotating spacecraft) - Accelerometer measurements (in Spacecraft body-fixed frame) for accelerometer 1, 2, & 3

Results are now presented for a rotating spacecraft which is rotating at LVLH rate, such that the spacecraft is radially pointing and the spacecraft body-fixed frame is initially aligned with the LVLH frame.

Since a rotating spacecraft do not affects the translational states, the LEO orbital elements and spacecraft position do not change and the plots are the same as that for the non-rotating spacecraft. Plots for spacecraft attitude and accelerometer measurements are shown in the Figures 9.20 - 9.21.

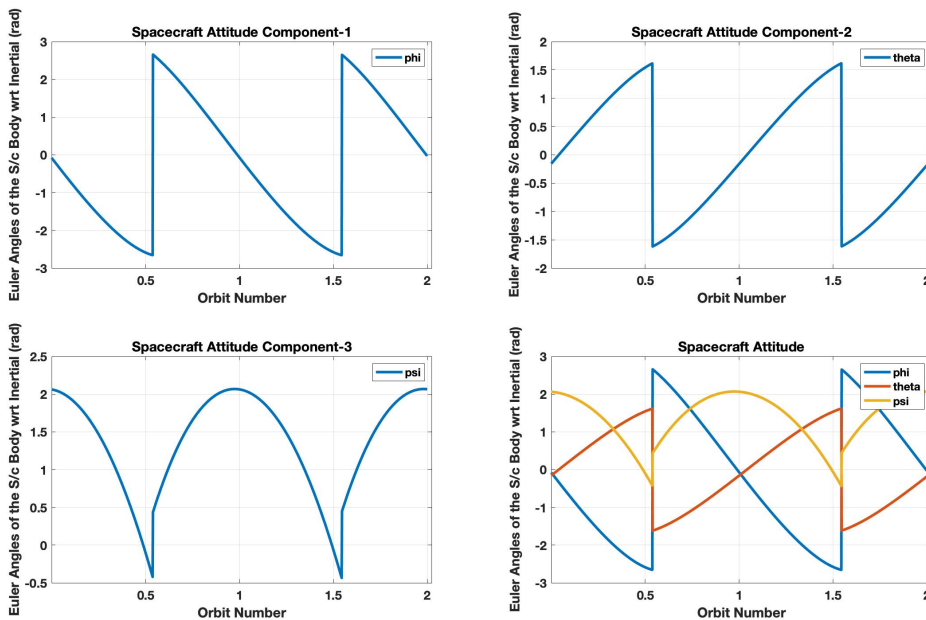


Fig. 9.20: Reference Trajectory (Rotating spacecraft) - Euler angles denoting attitude of the spacecraft body-fixed frame with respect to the ECI frame

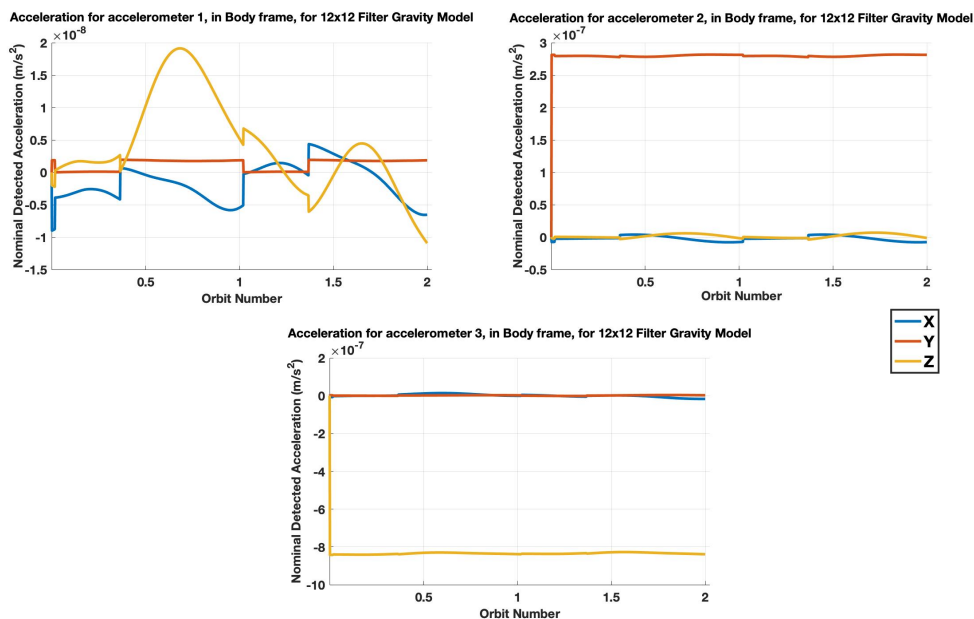


Fig. 9.21: Reference Trajectory (Rotating spacecraft) - Accelerometer measurements (in Spacecraft body-fixed frame) for accelerometer 1, 2, & 3

9.4.2 High Sensor Grade & Precise System Model

In this section, results for high sensor grade and precise system model are presented. To model high sensor grade and precise system model, sensor parameters, environmental uncertainties, and initial 1σ error for all states are set equal to the values given in the High Cost column of the Tables 9.4, 9.5 (except the star camera noise is set equal to 10^{-5} rad), and 9.6. Plots have been generated by setting the parameters as per the values given in the Tables 9.1, 9.30, and 9.2.

First, the results are presented for three accelerometers, with initial 1σ error on spacecraft position, velocity, attitude, and angular velocity set equal to the values given in Table 9.2, accelerometer parameters are set as per Table 9.4, and the time constants are set as per Value 1 in Table 9.3.

Plots for the true navigation error 1σ standard deviation on spacecraft position and attitude are shown in Figures 9.22-9.23, for the non-rotating inertially fixed spacecraft.

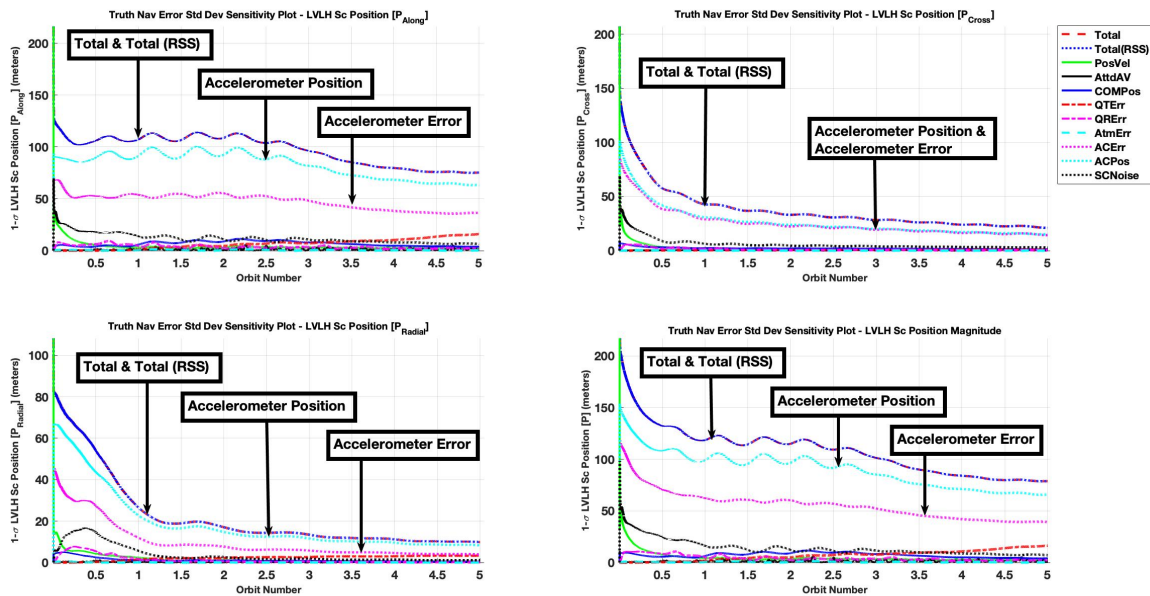


Fig. 9.22: True navigation error 1σ standard deviation on spacecraft position components (expressed in LVLH frame) and magnitude

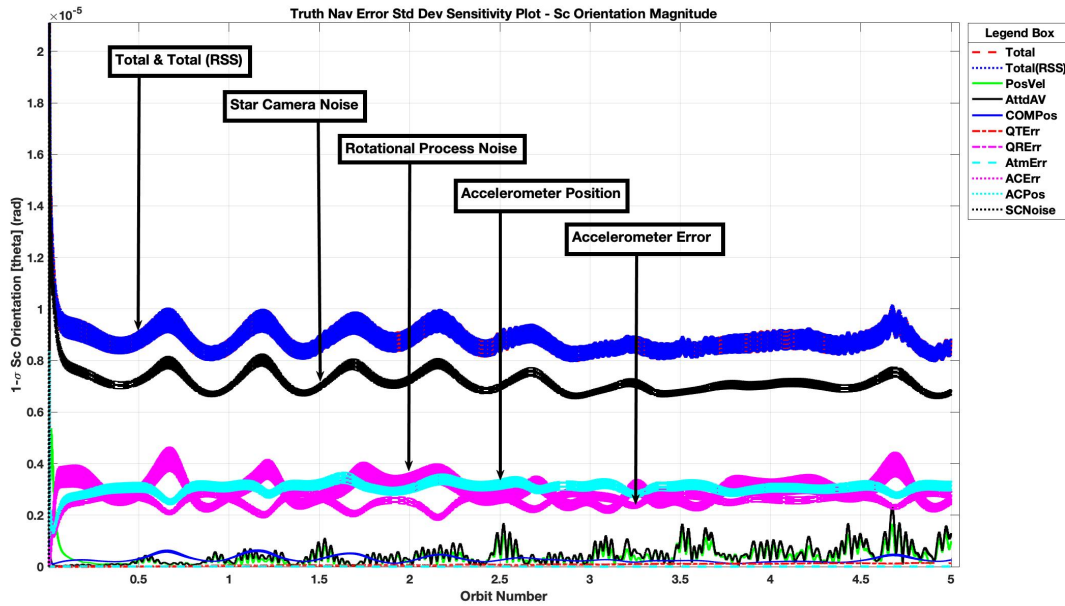


Fig. 9.23: True navigation error 1σ standard deviation on spacecraft attitude magnitude

The true navigation error 1σ standard deviation for all states converge to a steady state value. However, the estimates for the accelerometer states are poor, especially accelerometer misalignment. One of the reason for poor estimation of accelerometer states could be weak observability of these states. The error budget results for accelerometer states also reflect this, because the major source of error is accelerometer error.

Further, plots for spacecraft velocity and angular velocity are not shown, as the trend for these states is similar to the trend of the true navigation error for spacecraft position and orientation. All the plots have been annotated to depict the major sources of true navigation error.

Error budget results are summarized in Table 9.31. Note that the total steady-state true navigation error is the RSS of all the error sources.

State Name	Total Steady-State True Navigation Error 1σ	Error Source 1	Error Source 2	Error Source 3	Units
Spacecraft Position Magnitude	84.07	Accelerometer Position - 71.16	Accelerometer Error - 41.94	Translational Process Noise - 10.79	m
Spacecraft Velocity Magnitude	0.09	Accelerometer Position - 0.07	Accelerometer Error - 0.04	Translational Process Noise - 0.01	m/s
Spacecraft Attitude Magnitude	1.0178×10^{-5}	Star Camera Noise - 7.7697×10^{-6}	Rotational Process Noise - 4.4302×10^{-6}	Accelerometer Position - 2.9721×10^{-6}	rad
Spacecraft Angular Velocity Magnitude	1.5876×10^{-7}	Rotational Process Noise - 1.3008×10^{-7}	Star Camera Noise - 6.3519×10^{-8}	Accelerometer Position - 4.2393×10^{-8}	rad/s
Spacecraft Center of Mass Position Magnitude	2.1616×10^{-5}	Center of Mass Position - 1.537×10^{-5}	Accelerometer Position - 1.0175×10^{-5}	Accelerometer Error - 7.9652×10^{-6}	m
Spacecraft Ballistic Coefficient	5.531×10^{-6}	Atmospheric Parameter States - 5.512×10^{-6}	Center of Mass Position - 4.5661×10^{-7}	Accelerometer Error - 3.4767×10^{-8}	m^2/kg
Reference Atmospheric Density	2.7894×10^{-15}	Atmospheric Parameter States - 2.7797×10^{-15}	Center of Mass Position - 2.3027×10^{-16}	Accelerometer Error - 1.7533×10^{-17}	kg/m^3
Reference Scale Height	49.26	Atmospheric Parameter States - 42.05	Center of Mass Position - 25.55	Accelerometer Error - 1.78	m
Accelerometer 1 Position Magnitude	1.3077×10^{-5}	Accelerometer Position - 1.2001×10^{-5}	Accelerometer Error - 4.9376×10^{-6}	Star Camera Noise - 1.1928×10^{-6}	m
Accelerometer 1 Bias Magnitude	1.396×10^{-11}	Accelerometer Error - 1.2608×10^{-11}	Accelerometer Position - 5.6991×10^{-12}	Star Camera Noise - 1.3312×10^{-12}	m/s^2
Accelerometer 1 Scale Factor Magnitude	1.715×10^{-5}	Accelerometer Error - 1.708×10^{-5}	Accelerometer Position - 1.4898×10^{-6}	Star Camera Noise - 3.0164×10^{-7}	% measured acceleration
Accelerometer 1 Misalignment Magnitude	1.7317×10^{-6}	Accelerometer Error - 1.7316×10^{-6}	Accelerometer Position - 2.0336×10^{-8}	Star Camera Noise - 3.1591×10^{-9}	rad

Table 9.31: Error budget of the maximum steady-state true navigation error 1σ standard deviation

Results for the true navigation error 1σ standard deviation on spacecraft position and attitude are shown in Figures 9.24-9.25, for the rotating Nadir pointing spacecraft.

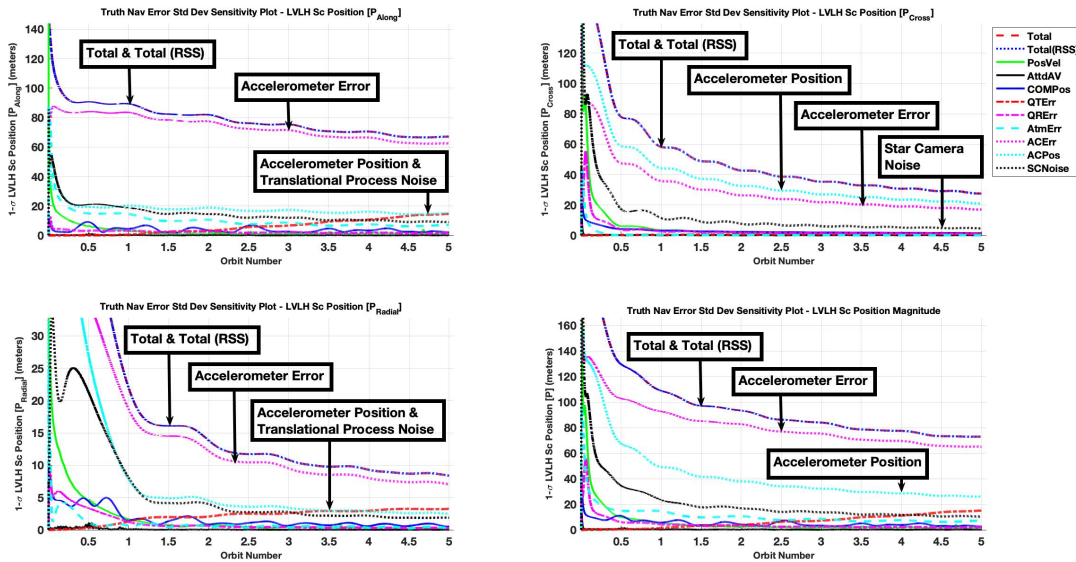


Fig. 9.24: True navigation error 1σ standard deviation on spacecraft position components (expressed in LVLH frame) and magnitude

The true navigation error 1σ standard deviation for all states converge to a steady state value. However, the estimates for accelerometer states are poor, especially accelerometer misalignment. One of the reason for poor estimation of accelerometer states is suspected to be weak observability of these states. The error budget results for accelerometer states also reflect this, and the major source of error is accelerometer error.

Further, plots for spacecraft velocity and angular velocity are not shown, as the trend for these states is similar to the trend of the true navigation error for spacecraft position and orientation. All the plots have been annotated to depict the major sources of true navigation error.

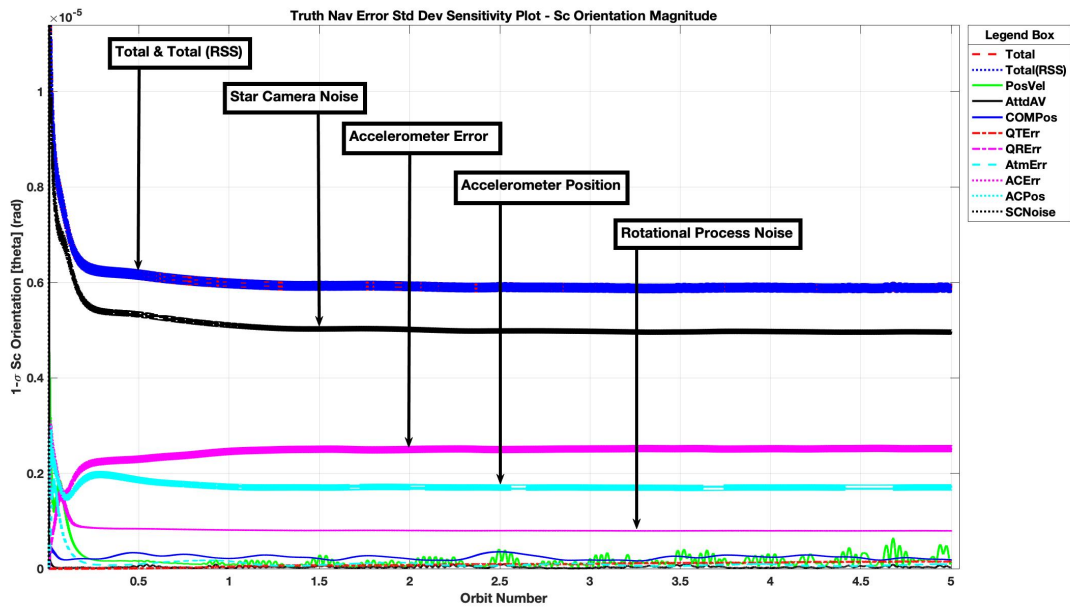


Fig. 9.25: True navigation error 1σ standard deviation on spacecraft attitude magnitude

Error budget results are summarized in Table 9.32. Note that the total steady-state true navigation error is the RSS of all the error sources.

State Name	Total Steady-State True Navigation Error 1σ	Error Source 1	Error Source 2	Error Source 3	Units
Spacecraft Position Magnitude	77.54	Accelerometer Error - 69.63	Accelerometer Position - 28.61	Star Camera Noise - 11.69	m
Spacecraft Velocity Magnitude	0.08	Accelerometer Error - 0.07	Accelerometer Position - 0.03	Star Camera Noise - 0.01	m/s
Spacecraft Attitude Magnitude	6.0128×10^{-6}	Star Camera Noise - 5.0169×10^{-6}	Accelerometer Error - 2.5929×10^{-6}	Accelerometer Position - 1.7653×10^{-6}	rad
Spacecraft Angular Velocity Magnitude	6.3451×10^{-8}	Rotational Process Noise - 5.5115×10^{-8}	Accelerometer Error - 2.0514×10^{-8}	Accelerometer Position - 1.7138×10^{-8}	rad/s
Spacecraft Center of Mass Position Magnitude	9.9749×10^{-5}	Center of Mass Position - 9.7875×10^{-5}	Accelerometer Error - 1.6542×10^{-5}	Accelerometer Position - 8.3993×10^{-6}	m
Spacecraft Ballistic Coefficient	5.4604×10^{-6}	Atmospheric Parameter States - 5.4472×10^{-6}	Accelerometer Error - 3.6283×10^{-7}	Star Camera Noise - 6.5728×10^{-8}	m^2/kg
Reference Atmospheric Density	2.7537×10^{-15}	Atmospheric Parameter States - 2.7471×10^{-15}	Accelerometer Error - 1.8298×10^{-16}	Star Camera Noise - 3.3147×10^{-17}	kg/m^3
Reference Scale Height	20.91	Atmospheric Parameter States - 15.80	Accelerometer Error - 13.40	Accelerometer Position - 2.06	m
Accelerometer 1 Position Magnitude	1.4449×10^{-5}	Accelerometer Position - 1.3613×10^{-5}	Accelerometer Error - 4.7149×10^{-6}	Star Camera Noise - 9.0417×10^{-7}	m
Accelerometer 1 Bias Magnitude	1.4065×10^{-11}	Accelerometer Error - 1.3159×10^{-11}	Accelerometer Position - 4.4388×10^{-12}	Star Camera Noise - 1.5972×10^{-12}	m/s^2
Accelerometer 1 Scale Factor Magnitude	1.732×10^{-5}	Accelerometer Error - 1.732×10^{-5}	Accelerometer Position - 4.3466×10^{-8}	Star Camera Noise - 1.4338×10^{-8}	% measured acceleration
Accelerometer 1 Misalignment Magnitude	1.7321×10^{-6}	Accelerometer Error - 1.732×10^{-6}	Accelerometer Position - 9.1923×10^{-10}	Star Camera Noise - 2.8236×10^{-10}	rad

Table 9.32: Error budget of the maximum steady-state true navigation error 1σ standard deviation

The results in Table 9.32 show that the estimates for the spacecraft position, velocity, attitude, angular velocity, and atmospheric parameter states improve marginally for the rotating spacecraft in comparison to that for the non-rotating spacecraft. Whereas, the estimates for spacecraft's center of mass position are marginally better for the non-rotating spacecraft. Estimates for accelerometer states show no change for the rotating spacecraft.

Further, results are generated for six on-board accelerometers. The initial 1σ error on

spacecraft position, velocity, attitude, and angular velocity set equal to the values given in Table 9.2, accelerometer parameters are set as per Table 9.4, and the time constants are set as per Value 1 in Table 9.3.

Results for a non-rotating inertially fixed spacecraft are shown in Table 9.33 .

State Name	Total Steady-State True Navigation Error 1σ	Error Source 1	Error Source 2	Error Source 3	Units
Spacecraft Position Magnitude	53.23	Accelerometer Position - 44.30	Accelerometer Error - 25.68	Translational Process Noise - 11.83	m
Spacecraft Velocity Magnitude	0.06	Accelerometer Position - 0.05	Accelerometer Error - 0.03	Translational Process Noise - 0.01	m/s
Spacecraft Attitude Magnitude	8.9524×10^{-6}	Star Camera Noise - 6.6234×10^{-6}	Rotational Process Noise - 3.1183×10^{-6}	Initial Attitude & Angular Velocity - 2.8897×10^{-6}	rad
Spacecraft Angular Velocity Magnitude	1.3031×10^{-7}	Rotational Process Noise - 1.0133×10^{-7}	Accelerometer Position - 4.9386×10^{-8}	Star Camera Noise - 4.3681×10^{-8}	rad/s

Table 9.33: Error budget of the maximum steady-state true navigation error 1σ standard deviation

Given below in Table 9.34 are the results for the rotating Nadir pointing spacecraft.

State Name	Total Steady-State True Navigation Error 1σ	Error Source 1	Error Source 2	Error Source 3	Units
Spacecraft Position Magnitude	51.14	Accelerometer Error - 45.08	Accelerometer Position - 18.68	Rotational Process Noise - 11.04	m
Spacecraft Velocity Magnitude	0.05	Accelerometer Error - 0.05	Accelerometer Position - 0.02	Rotational Process Noise - 0.01	m/s
Spacecraft Attitude Magnitude	5.217×10^{-6}	Star Camera Noise - 4.2429×10^{-6}	Accelerometer Error - 2.3255×10^{-6}	Accelerometer Position - 1.6034×10^{-6}	rad
Spacecraft Angular Velocity Magnitude	5.8758×10^{-8}	Rotational Process Noise - 5.4932×10^{-8}	Accelerometer Error - 1.3865×10^{-8}	Accelerometer Position - 1.1368×10^{-8}	rad/s

Table 9.34: Error budget of the maximum steady-state true navigation error 1σ standard deviation

Thus, above results show how increasing the number of on-board accelerometers can improve the performance of the autonomous orbital navigation system.

Above scenarios for high sensor grade and precise system model in P-LEO were repeated with star camera noise of 10^{-4} radians and nominal results were obtained.

9.4.3 Moderate Sensor Grade & Moderately Precise System Model

In this section, results for moderate sensor grade and moderately precise system model are presented. To model moderate sensor grade and moderately precise system model, sensor parameters, environmental uncertainties, and initial 1σ error for all states are set equal to the values given in the Moderate Cost column of the Tables 9.4, 9.5, and 9.6. Plots have been generated by setting the parameters as per the values given in the Tables 9.1, 9.30, and 9.2.

Results are presented for three accelerometers, with initial 1σ error on spacecraft position, velocity, attitude, and angular velocity set equal to the values given in Table 9.2, accelerometer parameters are set as per Table 9.4, and the time constants are set as per Value 1 in Table 9.3.

Results for the true navigation error 1σ standard deviation on spacecraft position and attitude are shown in Figures 9.26-9.27, for the non-rotating inertially fixed spacecraft.

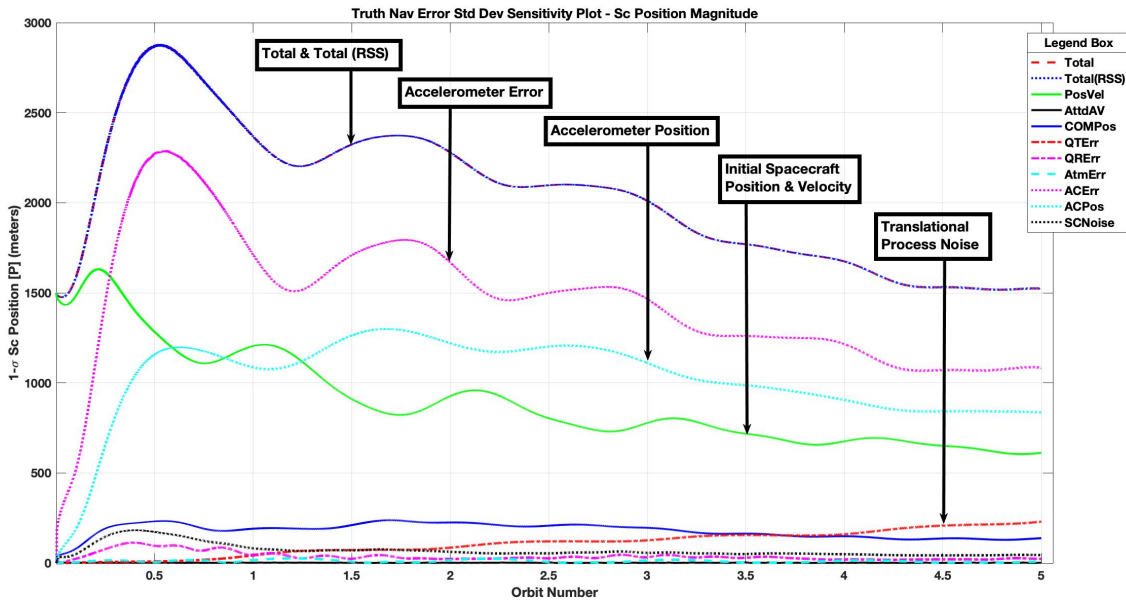


Fig. 9.26: True navigation error 1σ standard deviation on spacecraft position magnitude

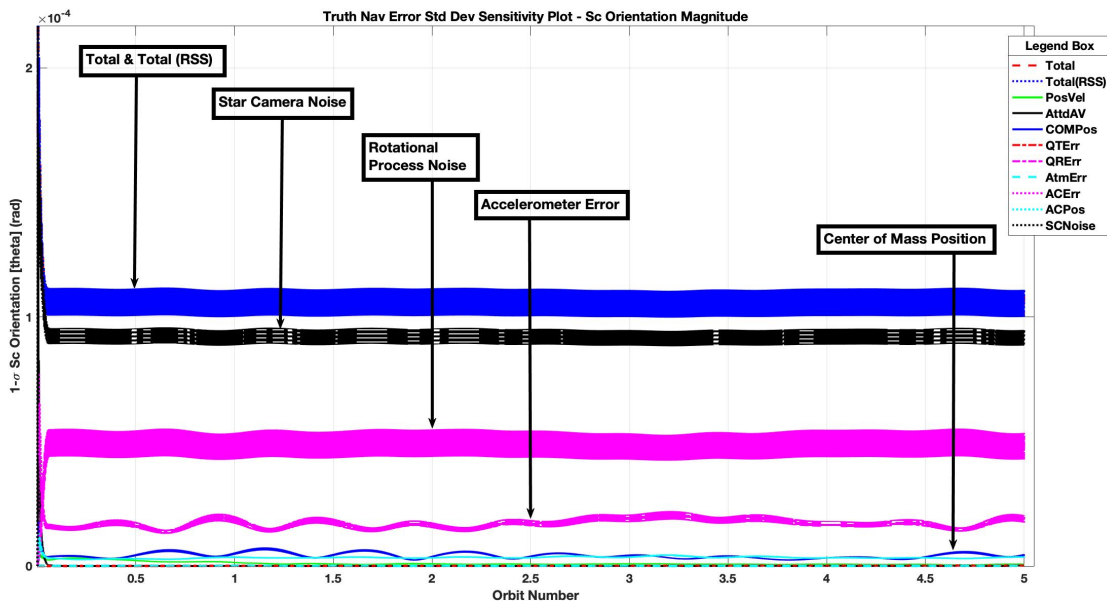


Fig. 9.27: True navigation error 1σ standard deviation on spacecraft attitude magnitude

Results for spacecraft velocity and angular velocity are not shown, as the trend for these states is similar to the trend of the true navigation error for spacecraft position and orientation. All results have been annotated to depict the major sources of true navigation error.

Error budget results are summarized in Table 9.35. Note that the total steady-state true navigation error is the RSS of all the error sources.

State Name	Total Steady-State True Navigation Error 1σ	Error Source 1	Error Source 2	Error Source 3	Units
Spacecraft Position Magnitude	1674.72	Accelerometer Error - 1215.51	Accelerometer Position - 905.49	Initial Spacecraft Position & Velocity - 675.80	m
Spacecraft Velocity Magnitude	1.69	Accelerometer Error - 1.20	Accelerometer Position - 0.94	Initial Spacecraft Position & Velocity - 0.71	m/s
Spacecraft Attitude Magnitude	1.1176×10^{-4}	Star Camera Noise - 9.5687×10^{-5}	Rotational Process Noise - 5.5203×10^{-5}	Accelerometer Error - 1.5547×10^{-5}	rad
Spacecraft Angular Velocity Magnitude	1.7175×10^{-6}	Rotational Process Noise - 1.4937×10^{-6}	Star Camera Noise - 8.1276×10^{-7}	Accelerometer Error - 2.1324×10^{-7}	rad/s

Table 9.35: Error budget of the maximum steady-state true navigation error 1σ standard deviation

Results for the true navigation error 1σ standard deviation on spacecraft position and attitude are shown in Figures 9.28-9.29, for the rotating Nadir pointing spacecraft.

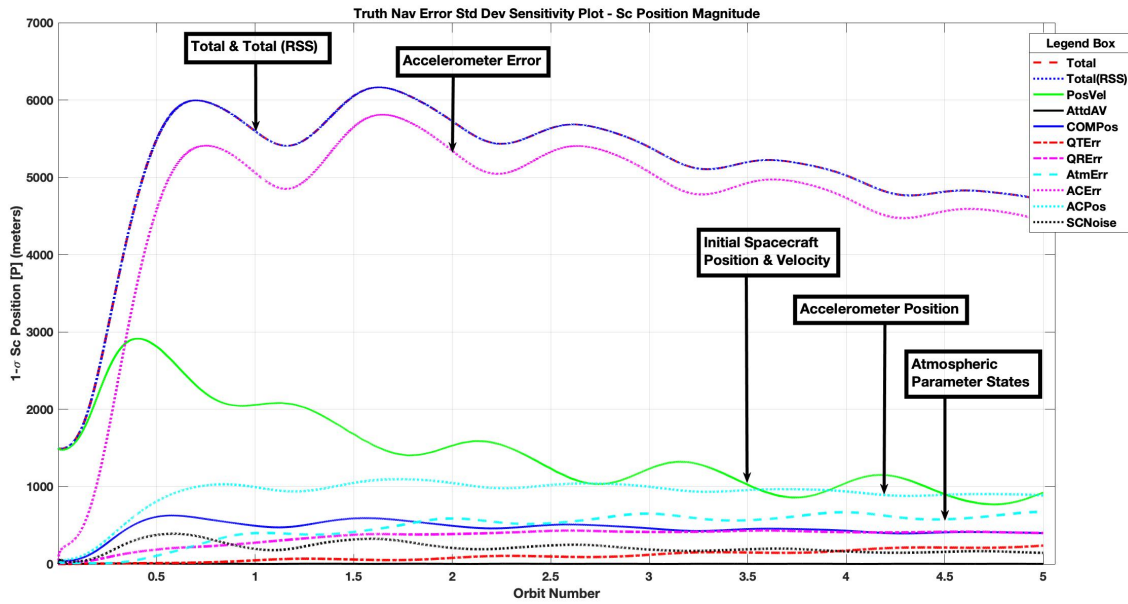


Fig. 9.28: True navigation error 1σ standard deviation on spacecraft position magnitude

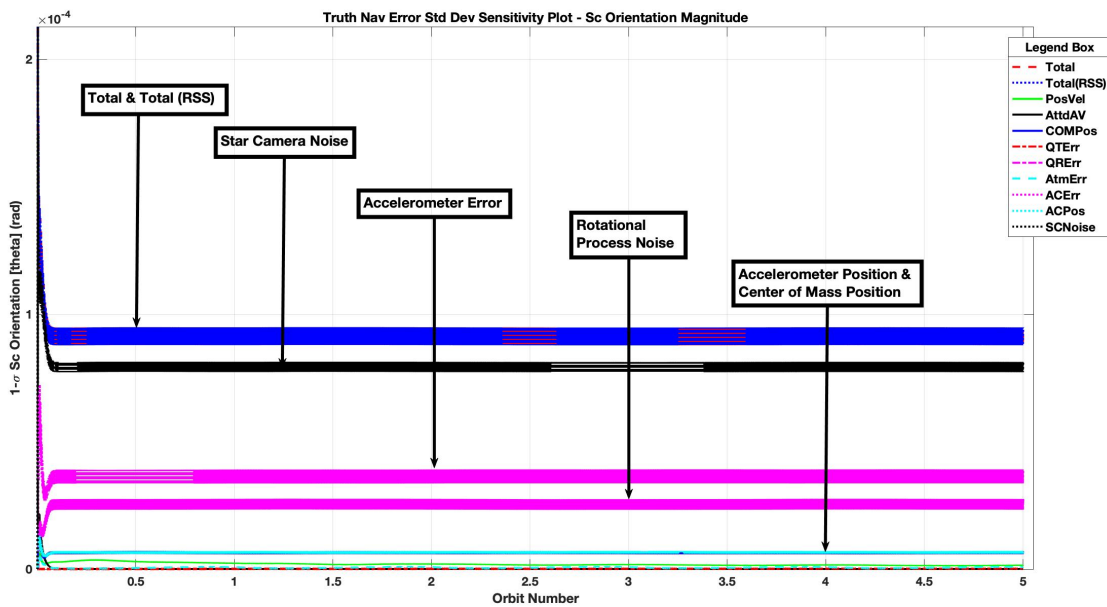


Fig. 9.29: True navigation error 1σ standard deviation on spacecraft attitude magnitude

Plots for spacecraft velocity and angular velocity are not shown, as the trend for these states is similar to the trend of the true navigation error for spacecraft position and orientation. All results have been annotated to depict the major sources of true navigation error.

Error budget results are summarized in Table 9.36. Note that the total steady-state true navigation error is the RSS of all the error sources.

The results for the moderate sensor grade and moderately precise system model depict the effect of lower sensor grade on the true navigation error of spacecraft position, velocity, attitude, and angular velocity. The accelerometer error is now a major source of error, and thus system should be designed accordingly.

State Name	Total Steady-State True Navigation Error 1σ	Error Source 1	Error Source 2	Error Source 3	Units
Spacecraft Position Magnitude	5023.55	Accelerometer Error - 4732.04	Initial Spacecraft Position & Velocity - 1050.85	Accelerometer Position - 937.91	m
Spacecraft Velocity Magnitude	5.23	Accelerometer Error - 4.94	Initial Spacecraft Position & Velocity - 1.05	Accelerometer Position - 0.97	m/s
Spacecraft Attitude Magnitude	9.4872×10^{-5}	Star Camera Noise - 8.1314×10^{-5}	Accelerometer Error - 3.9116×10^{-5}	Rotational Process Noise - 2.7547×10^{-5}	rad
Spacecraft Angular Velocity Magnitude	1.1735×10^{-6}	Rotational Process Noise - 7.7067×10^{-7}	Accelerometer Error - 6.9462×10^{-7}	Star Camera Noise - 5.1386×10^{-7}	rad/s

Table 9.36: Error budget of the maximum steady-state true navigation error 1σ standard deviation

9.4.4 Low Sensor Grade & Less Precise System Model

In this section, results for low sensor grade and less precise system model are discussed. To model low sensor grade and less precise system model, sensor parameters, environmental uncertainties, and initial 1σ error for all states are set equal to the values given in the Low Cost column of the Tables 9.4, 9.5, and 9.6. Plots were generated by setting the parameters

as per the values given in the Tables 9.1, 9.30, and 9.2.

Results were generated for three accelerometers, with initial 1σ error on spacecraft position, velocity, attitude, and angular velocity set equal to the values given in Table 9.2, accelerometer parameters are set as per Table 9.4, and the time constants are set as per Value 1 in Table 9.3. In both cases, non-rotating inertially fixed spacecraft or rotating radially pointing spacecraft, true navigation error for spacecraft position and velocity diverge, and the estimation of these states is not feasible. The major source of error is due to the low grade sensor model and its associated accelerometer error. Though estimation of spacecraft attitude and angular velocity is still possible because of the star camera measurements.

9.5 Summary

Linear Covariance simulation results for a LEO (50 degree Inclination) and a polar LEO orbits were presented and detailed analysis was conducted. Results have been categorized, so as to help understand the performance of the system for different configurations.

A number of simulation parameters were studied and corresponding error budget analysis has been shown. For improving the performance of the system, high sensor grade and precise system model is recommended. Additionally, filter performance improves when the number of on-board accelerometers is increased. Filter performance is better for 1 meter baseline length accelerometer configuration in comparison to that for 0.5 meter baseline length accelerometer configuration.

Further, major source of error for most of the scenarios has been sensor errors (like accelerometer error, accelerometer position uncertainty or star camera noise). This is an important result as it highlights the sensor specifications to be improved, so as to reduce the final navigation error.

CHAPTER 10

Conclusion

10.1 Summary of the Contributions & Results

LinCov results for a spacecraft in a LEO (50 degree Inclination) and a polar LEO orbits have been presented, analyzed, and discussed in detail. Key contributions from this study are noted to be the development of mathematical measurement model of electrostatic accelerometers, observability analysis for the autonomous navigation system, and the error budget results for a spacecraft in LEO regime.

An extensive detail about the existing technology and literature background of gravity gradiometry and spacecraft navigation has been discussed. Detailed problem setup and LinCov tool development has been presented along with mathematical model for measurements and state dynamics. Observability analysis was conducted and the results were presented, so as to corroborate the idea of autonomous orbital navigation with advanced accelerometers.

Observability of spacecraft position, velocity, and attitude was proven for a configuration of three 3-axis accelerometers. Feasibility of autonomous orbital navigation was established.

Error budget analysis for a non-rotating and a rotating spacecraft, in a low Earth orbit (50 degree Inclination) and polar low Earth orbit, was conducted and results were documented. A number of scenarios were discussed and contributions due to specific error sources were identified.

Results were analyzed for three different sensor grades, and it was shown that the performance of the high sensor grade and precise system model satisfies the requirements for autonomous orbital navigation. Additionally, filter performance was shown to improve when the number of on-board accelerometers is increased. Filter performance was shown to be better for 1 meter baseline length accelerometer configuration in comparison to that for

0.5 meter baseline length accelerometer configuration. It has also been noted that estimation of accelerometer scale-factor and misalignment is poor, for all the scenarios.

Further, major source of error for most of the scenarios has been sensor errors (like accelerometer error, accelerometer position uncertainty or star camera noise). This is an important result as it highlights the sensor specifications to be improved, so as to reduce the final navigation error.

This research highlighted the ultra-precise sensitivity requirements needed to generate accelerometer measurements and in turn use the information to navigate autonomously in space.

In summary, the objective of the research as stated in the first chapter of this dissertation has been accomplished.

The objective of this research is to use the Linear Covariance theory to investigate the feasibility and sensitivity requirements for an autonomous orbit determination using advanced accelerometer measurements and onboard gravity field maps, for different sensor and orbit configurations.

10.2 Proposed Future Work

This research presented an idea and a feasibility study along with the sensitivity requirements for developing an autonomous orbital navigation system based on ultra-precise accelerometers. To extend this idea of developing an autonomous orbital navigation system into reality, a detailed analysis and intensive study of the hardware of these ultra-precise sensors is needed.

Results presented in this study can be used to perform a detailed analysis by expanding the number of parameters and including uncertainties in the gravity field model and Earth model. Further, a suite of sensors can be included and different permutations can be tested accordingly.

Monte Carlo analysis can be conducted and an analysis may be performed in order to test and validate the linearized models. Different types of gravity models can be studied

and an effort may be made towards determining computationally efficient method to store high-fidelity gravity maps on-board.

REFERENCES

- [1] Veryaskin, A. V., *Gravity, Magnetic and Electromagnetic Gradiometry*, 2053-2571, Morgan & Claypool Publishers, 2018.
- [2] Richeson, J. A., *Gravity gradiometer aided inertial navigation within non-GNSS environments*, Phd thesis, University of Maryland, College Park, 2008, Copyright - Database copyright ProQuest LLC; Last updated - 2016-05-27.
- [3] Chen, P., Sun, X., and Han, C., "Gravity gradient tensor eigendecomposition for spacecraft positioning," *Journal of Guidance, Control, and Dynamics*, Vol. 38, No. 11, 2015, pp. 2200–2206.
- [4] Evstifeev, M., "The state of the art in the development of onboard gravity gradiometers," *Gyroscopy and Navigation*, Vol. 8, No. 1, 2017, pp. 68–79.
- [5] Christensen, R. S. and Geller, D., "Linear covariance techniques for closed-loop guidance navigation and control system design and analysis," *Proceedings of the Institution of Mechanical Engineers, Part G: Journal of Aerospace Engineering*, Vol. 228, No. 1, 2014, pp. 44–65.
- [6] Cesare, S., "Performance requirements and budgets for the gradiometric mission. Technical Note," Technical report, GOC-TN-AI-0027, Alenia Spazio, Turin, Italy, 2002.
- [7] Grewal, M. S., Weill, L. R., and Andrews, A. P., *Global positioning systems, inertial navigation, and integration*, John Wiley & Sons, 2007.
- [8] Bond, V. and Allman, M., *Modern Astrodynamics: Fundamentals and Perturbation Methods*, Cambridge studies in advanced mathematics, Princeton University Press, 1996.
- [9] Maybeck, P., *Stochastic Models, Estimation and Control*, No. 1 in Mathematics in science and engineering, Academic Press, 1979.
- [10] DiFrancesco, D., Meyer, T., Christensen, A., and FitzGerald, D., "Gravity gradiometry—today and tomorrow," 2009.
- [11] Király, P., "Eötvös and STEP," *Proceedings of the STEP (Satellite Test of the Equivalence Principle) Symposium (esa WPP-115), Noordwijk, The Netherlands, July 1996*, pp. 399–406.
- [12] Gray, S. D., Parmentola, J. A., and LeSchack, R., "Estimating the weight of very heavy objects with a gravity gradiometer," *Journal of Physics D: Applied Physics*, Vol. 28, No. 11, 1995, pp. 2378.
- [13] Hofmann-Wellenhof, B. and Moritz, H., *Physical geodesy*, Springer Science & Business Media, 2006.

- [14] Argentiero, P. and Garza-Robles, R., "A spacecraft-borne gradiometer mission analysis," 1976.
- [15] Jekeli, C., "Gravity, Gradiometry," *Encyclopedia of solid earth geophysics*, Springer, 2011, pp. 547–561.
- [16] Sonnabend, D. and Born, G. H., "Measuring attitude with a gradiometer," 1994.
- [17] Pedersen, L. and Rasmussen, T., "The gradient tensor of potential field anomalies: Some implications on data collection and data processing of maps," *Geophysics*, Vol. 55, No. 12, 1990, pp. 1558–1566.
- [18] Jekeli, C., "A review of gravity gradiometer survey system data analyses," *GEO-PHYSICS*, Vol. 58, No. 4, 1993, pp. 508–514.
- [19] DiFrancesco, D., Grierson, A., Kaputa, D., and Meyer, T., "Gravity gradiometer systems—advances and challenges," *Geophysical Prospecting*, Vol. 57, No. 4, 2009, pp. 615–623.
- [20] Wells, W. C., "Spaceborne gravity gradiometers," 1984.
- [21] Bell, R. E., "Gravity gradiometry," *Scientific American*, Vol. 278, No. 6, 1998, pp. 74–79.
- [22] Mahadeswaraswamy, C., *Atom interferometric gravity gradiometer: Disturbance compensation and mobile gradiometry*, Ph.D. thesis, Stanford University, 2009.
- [23] Forward, R. L., "Review of Artificial Satellite Gravity Gradiometer Techniques for Geodesy." Tech. rep., HUGHES RESEARCH LABS MALIBU CA, 1973.
- [24] Paik, H. and Morgan, S., "Superconducting gravity gradiometer mission." *Relativistic Gravitational Experiments in Space*, 1993.
- [25] Carraz, O., Siemes, C., Massotti, L., Haagmans, R., and Silvestrin, P., "A spaceborne gravity gradiometer concept based on cold atom interferometers for measuring Earth gravity field," *Microgravity Science and Technology*, Vol. 26, No. 3, 2014, pp. 139–145.
- [26] Affleck, C. A. and Jircitano, A., "Passive gravity gradiometer navigation system," *Position Location and Navigation Symposium, 1990. Record. The 1990's-A Decade of Excellence in the Navigation Sciences. IEEE PLANS'90.*, 1990, pp. 60–66.
- [27] Sun, X., Chen, P., Macabiau, C., and Han, C., "Autonomous orbit determination via kalman filtering of gravity gradients," *IEEE Transactions on Aerospace and Electronic Systems*, Vol. 52, No. 5, October 2016, pp. 2436–2451.
- [28] Sun, X., Chen, P., Macabiau, C., and Han, C., "Low-Earth Orbit Determination from Gravity Gradient Measurements," *Acta Astronautica*, Vol. 123, 2016, pp. 350 – 362, Special Section: Selected Papers from the International Workshop on Satellite Constellations and Formation Flying 2015.

- [29] Bobojć, A. and Drożyner, A., “Satellite orbit determination using satellite gravity gradiometry observations in GOCE mission perspective,” *Advances in Geosciences*, Vol. 1, 2003, pp. 109–112.
- [30] Pei, C., Tengda, S., and Xiucong, S., “Autonomous orbit determination using epoch-differenced gravity gradients and starlight refraction,” *Chinese Journal of Aeronautics*, Vol. 30, No. 5, 2017, pp. 1740–1749.
- [31] Markley, F. and Crassidis, J., *Fundamentals of Spacecraft Attitude Determination and Control*, Space Technology Library, Springer New York, 2014.
- [32] Mohinder, S. and Augus, P., *Kalman Filtering: Theory and Practice with MATLAB*, Wiley-IEEE Press, 2001.
- [33] Kalman, R. E., “A new approach to linear filtering and prediction problems,” *Journal of basic Engineering*, Vol. 82, No. 1, 1960, pp. 35–45.
- [34] Vallado, D. A., *Fundamentals of astrodynamics and applications*, Vol. 12, Springer Science & Business Media, 2001.
- [35] Noureldin, A., Karamat, T. B., and Georgy, J., *Fundamentals of inertial navigation, satellite-based positioning and their integration*, Springer Science & Business Media, 2012.
- [36] Pilinski, M. and Palo, S., “An innovative method for measuring drag on small satellites,” 2009.
- [37] Vetter, J. R., “The evolution of Earth gravitational models used in astrodynamics.” *Johns Hopkins APL Technical Digest*, Vol. 15, 1994, pp. 319–335.
- [38] Carroll, K. and Faber, D., “Asteroid Orbital Gravity Gradiometry,” *Lunar and Planetary Science Conference*, Vol. 49, 2018.
- [39] Roithmayr, C. M., “Contribution of zonal harmonics to gravitational moment,” 1990.
- [40] Roithmayr, C. M., “Contributions of spherical harmonics to magnetic and gravitational fields,” 2004.
- [41] Takahashi, Y., Busch, M. W., and Scheeres, D., “Spin state and moment of inertia characterization of 4179 Toutatis,” *The Astronomical Journal*, Vol. 146, No. 4, 2013, pp. 95.
- [42] Marsh, J., Lerch, F., Putney, B., Christodoulidis, D., Smith, D., Felsentreger, T., Sanchez, B., Klosko, S., Pavlis, E., Martin, T., et al., “A new gravitational model for the Earth from satellite tracking data: GEM-T1,” *Journal of Geophysical Research: Solid Earth*, Vol. 93, No. B6, 1988, pp. 6169–6215.
- [43] Wertz, J., *Spacecraft Attitude Determination and Control*, Astrophysics and Space Science Library, Springer Netherlands, 1978.

- [44] Lefferts, E. J., Markley, F. L., and Shuster, M. D., “Kalman filtering for spacecraft attitude estimation,” *Journal of Guidance, Control, and Dynamics*, Vol. 5, No. 5, 1982, pp. 417–429.
- [45] Pittelkau, M. E., “Rotation vector in attitude estimation,” *Journal of Guidance, Control, and Dynamics*, Vol. 26, No. 6, 2003, pp. 855–860.
- [46] Geller, D. K. and Bhatia, R., “Orbit and Attitude Observability Using Accelerometer Measurements,” AAS 18-301, AAS/AIAA Astrodynamics Conference, Snowbird, Utah, Aug. 2018.
- [47] Carroll, K. and Faber, D., “Tidal acceleration gravity gradiometry for measuring asteroid gravity field from orbit,” 2018.
- [48] Geller, D. K., “Linear covariance techniques for orbital rendezvous analysis and autonomous onboard mission planning,” *Journal of Guidance, Control, and Dynamics*, Vol. 29, No. 6, 2006, pp. 1404–1414.
- [49] Christensen, R. S., *Linear covariance analysis for gimballed pointing systems*, Utah State University, 2013.
- [50] Bierman, G. J., *Factorization methods for discrete sequential estimation*, Courier Corporation, 2006.
- [51] Zhu, Z., Zhou, Z., Cai, L., Bai, Y., and Luo, J., “Electrostatic gravity gradiometer design for the future mission,” *Advances in Space Research*, Vol. 51, No. 12, 2013, pp. 2269–2276.
- [52] Kasevich, M., “Cold Atom Navigation Sensors,” *Proceedings of the Stanford PNT Challenges and Opportunities Symposium, Stanford*. Available at: <http://scpnt.stanford.edu/pnt/pnt2007.html>, 2007.
- [53] Kasevich, M., “Navigation, Gravitation and Cosmology with Cold Atom Sensors,” *International Workshop on Advances in precision tests and experimental gravitation in space Florence, ITALY*, 2006, pp. 28–30.
- [54] Silvestrin, P., Aguirre, M., Massotti, L., Leone, B., Cesare, S., Kern, M., and Haagsmans, R., “The future of the satellite gravimetry after the GOCE mission,” *Geodesy for Planet Earth*, Springer, 2012, pp. 223–230.

APPENDICES

APPENDIX A

Matrix Partial Derivatives

A.1 Overview

This appendix highlights some additional partial derivatives used in Chapter 5.

A.2 Partial Of Gravitational Acceleration With Respect To Spacecraft Position

$$\left. \frac{\partial \mathbf{g}_E^I(\mathbf{r}_{CM/E}^I)}{\partial \mathbf{r}_{CM/E}^I} \right|_{\bar{\mathbf{x}}} = \nabla \mathbf{g}_E^I(\bar{\mathbf{r}}_{CM/E}^I) \quad (\text{A.1})$$

A.3 Partial Of Acceleration Due To Atmospheric Drag With Respect To Spacecraft Position

$$\left. \frac{\partial \mathbf{a}_{aero}^I}{\partial \mathbf{r}_{CM/E}^I} \right|_{\bar{\mathbf{x}}} = \frac{1}{2} \bar{\rho}_r e^{-\left(\frac{\|\bar{\mathbf{r}}_{CM/E}^I\|}{h_s} - h_{ref}\right)} \bar{\beta} \left\| \bar{\mathbf{v}}_{CM/E}^I \right\| \bar{\mathbf{v}}_{CM/E}^I \frac{\hat{\mathbf{i}}_{\bar{\mathbf{r}}_{CM/E}^I}^T}{\bar{h}_s} \quad (\text{A.2})$$

A.4 Partial Of Acceleration Due To Atmospheric Drag With Respect To Spacecraft Velocity

$$\left. \frac{\partial \mathbf{a}_{aero}^I}{\partial \mathbf{v}_{CM/E}^I} \right|_{\bar{\mathbf{x}}} = -\frac{1}{2} \bar{\rho}_r e^{-\left(\frac{\|\bar{\mathbf{r}}_{CM/E}^I\|}{h_s} - h_{ref}\right)} \bar{\beta} \left(\bar{\mathbf{v}}_{CM/E}^I \hat{\mathbf{i}}_{\bar{\mathbf{v}}_{CM/E}^I}^T + \left\| \bar{\mathbf{v}}_{CM/E}^I \right\| I_{3 \times 3} \right) \quad (\text{A.3})$$

A.5 Partial Of Acceleration Due To Atmospheric Drag With Respect To Spacecraft Ballistic Coefficient

$$\left. \frac{\partial \mathbf{a}_{aero}^I}{\partial \beta} \right|_{\bar{\mathbf{x}}} = -\frac{1}{2} \bar{\rho}_r e^{-\left(\frac{\|\bar{\mathbf{r}}_{CM/E}^I\|}{h_s} - h_{ref}\right)} \left\| \bar{\mathbf{v}}_{CM/E}^I \right\| \bar{\mathbf{v}}_{CM/E}^I \quad (\text{A.4})$$

A.6 Partial Of Acceleration Due To Atmospheric Drag With Respect To Reference Atmospheric Density

$$\left. \frac{\partial \mathbf{a}_{aero}^I}{\partial \rho_r} \right|_{\bar{\mathbf{x}}} = -\frac{1}{2} e^{-\frac{(\|\bar{\mathbf{r}}_{CM/E}^I\| - h_{ref})}{h_s}} \bar{\beta} \|\bar{\mathbf{v}}_{CM/E}^I\| \bar{\mathbf{v}}_{CM/E}^I \quad (\text{A.5})$$

A.7 Partial Of Acceleration Due To Atmospheric Drag With Respect To Scale Height

$$\left. \frac{\partial \mathbf{a}_{aero}^I}{\partial h_s} \right|_{\bar{\mathbf{x}}} = -\frac{(\|\bar{\mathbf{r}}_{CM/E}^I\| - h_{ref})}{2\bar{h}_s^2} \bar{\rho}_r e^{-\frac{(\|\bar{\mathbf{r}}_{CM/E}^I\| - h_{ref})}{h_s}} \bar{\beta} \|\bar{\mathbf{v}}_{CM/E}^I\| \bar{\mathbf{v}}_{CM/E}^I \quad (\text{A.6})$$

A.8 Partial Of Solar Radiation Pressure Perturbation With Respect To Spacecraft Position

Solar radiation pressure perturbation partial, with respect to spacecraft position in inertial frame, is computed as follow

$$\left. \frac{\partial \mathbf{a}_{SRP}^I}{\partial \mathbf{r}_{CM/E}^I} \right|_{\bar{\mathbf{x}}} = \frac{F_e}{c} \left[\frac{3}{r_{sc} \rho_{sc}} \right] \left[\frac{1}{4} + \frac{1}{9} c_d \right] \left[\frac{\partial \left(\frac{\mathbf{r}_{CM/E}^I - \boldsymbol{\rho}_{Sun}}{\|\mathbf{r}_{CM/E}^I - \boldsymbol{\rho}_{Sun}\|} \right)}{\partial \mathbf{r}_{CM/E}^I} \right]_{\bar{\mathbf{x}}} \quad (\text{A.7})$$

$$\left. \frac{\partial \mathbf{a}_{SRP}^I}{\partial \mathbf{r}_{CM/E}^I} \right|_{\bar{\mathbf{x}}} = \frac{F_e}{c \|\bar{\mathbf{r}}_{CM/E}^I - \boldsymbol{\rho}_{Sun}\|} \left[\frac{3}{r_{sc} \rho_{sc}} \right] \left[\frac{1}{4} + \frac{1}{9} c_d \right] \left[I_{3 \times 3} - \hat{\mathbf{i}}_{CM/Sun}^I \left(\hat{\mathbf{i}}_{CM/Sun}^I \right)^T \right] \quad (\text{A.8})$$

where $\hat{\mathbf{i}}_{CM/Sun}^I$ is the unit vector defined as

$$\hat{\mathbf{i}}_{CM/Sun}^I = \frac{\bar{\mathbf{r}}_{CM/E}^I - \boldsymbol{\rho}_{Sun}}{\|\bar{\mathbf{r}}_{CM/E}^I - \boldsymbol{\rho}_{Sun}\|} \quad (\text{A.9})$$

A.9 Partial Of Third-Body Perturbation With Respect To Spacecraft Position

Third-body perturbation partial, with respect to spacecraft position in inertial frame, is computed as follow

$$\left. \frac{\partial \mathbf{a}_{3rd}^I}{\partial \mathbf{r}_{CM/E}^I} \right|_{\bar{\mathbf{x}}} = \left. \frac{-Gm_{3rd} \partial \left(\frac{\mathbf{r}_{CM/E}^I - \boldsymbol{\rho}_{3rd}}{\|\mathbf{r}_{CM/E}^I - \boldsymbol{\rho}_{3rd}\|^3} + \frac{\boldsymbol{\rho}_{3rd}}{\|\boldsymbol{\rho}_{3rd}\|^3} \right)}{\partial \mathbf{r}_{CM/E}^I} \right|_{\bar{\mathbf{x}}} \quad (\text{A.10})$$

$$\left. \frac{\partial \mathbf{a}_{3rd}^I}{\partial \mathbf{r}_{CM/E}^I} \right|_{\bar{\mathbf{x}}} = \frac{-Gm_{3rd}}{\|\bar{\mathbf{r}}_{CM/E}^I - \boldsymbol{\rho}_{3rd}\|^3} \left[I_{3 \times 3} - 3\hat{\mathbf{i}}_{CM/3rd}^I \left(\hat{\mathbf{i}}_{CM/3rd}^I \right)^T \right] \quad (\text{A.11})$$

where m_{3rd} is the mass of the third-body (Sun, Moon, etc.), and $\hat{\mathbf{i}}_{CM/3rd}^I$ is the unit vector defined as

$$\hat{\mathbf{i}}_{CM/3rd}^I = \frac{\bar{\mathbf{r}}_{CM/E}^I - \boldsymbol{\rho}_{3rd}}{\|\bar{\mathbf{r}}_{CM/E}^I - \boldsymbol{\rho}_{3rd}\|} \quad (\text{A.12})$$

A.10 Partial Of Gravity Gradient Torque With Respect To Spacecraft Position

Gravity gradient torque partial with respect to spacecraft position is computed as follow

$$\left. \frac{\partial M_{gg}}{\partial \mathbf{r}_{CM/E}^I} \right|_{\bar{\mathbf{x}}} = \left. \frac{\partial \left\{ \frac{3\mu}{\|\mathbf{r}_{CM/E}^B\|^5} \left(\mathbf{r}_{CM/E}^B \times \left[J\mathbf{r}_{CM/E}^B \right] \right) \right\}}{\partial \mathbf{r}_{CM/E}^I} \right|_{\bar{\mathbf{x}}} \quad (\text{A.13})$$

$$\left. \frac{\partial M_{gg}}{\partial \mathbf{r}_{CM/E}^I} \right|_{\bar{\mathbf{x}}} = 3\mu \left[\mathbf{r}_{CM/E}^B \times \left(J\mathbf{r}_{CM/E}^B \right) \right] \frac{\partial \left(\frac{1}{\|\mathbf{r}_{CM/E}^B\|^5} \right)}{\partial \|\mathbf{r}_{CM/E}^B\|} \frac{\partial \|\mathbf{r}_{CM/E}^B\|}{\partial \mathbf{r}_{CM/E}^B} \frac{\partial \mathbf{r}_{CM/E}^B}{\partial \mathbf{r}_{CM/E}^I} \Bigg|_{\bar{\mathbf{x}}}$$

$$\frac{-3\mu \left[\left(J\bar{\mathbf{r}}_{CM/E}^B \right) \times \right]}{\|\mathbf{r}_{CM/E}^B\|^5} \frac{\partial \mathbf{r}_{CM/E}^B}{\partial \mathbf{r}_{CM/E}^B} \frac{\partial \mathbf{r}_{CM/E}^B}{\partial \mathbf{r}_{CM/E}^I} \Bigg|_{\bar{\mathbf{x}}} + \frac{\left[\bar{\mathbf{r}}_{CM/E}^B \times \right] J}{\|\mathbf{r}_{CM/E}^B\|^5} \frac{\partial \mathbf{r}_{CM/E}^B}{\partial \mathbf{r}_{CM/E}^B} \frac{\partial \mathbf{r}_{CM/E}^B}{\partial \mathbf{r}_{CM/E}^I} \Bigg|_{\bar{\mathbf{x}}} \quad (\text{A.14})$$

$$\begin{aligned} \left. \frac{\partial M_{gg}}{\partial \mathbf{r}_{CM/E}^I} \right|_{\bar{\mathbf{x}}} &= \frac{-3\mu}{\|\bar{\mathbf{r}}_{CM/E}^B\|^5} \left\{ \frac{5 \left[\bar{\mathbf{r}}_{CM/E}^B \times \left(J \bar{\mathbf{r}}_{CM/E}^B \right) \right] \hat{\mathbf{i}}_{\bar{\mathbf{r}}_{CM/E}^B}^T}{\|\bar{\mathbf{r}}_{CM/E}^B\|} + \left[\left(J \bar{\mathbf{r}}_{CM/E}^B \right) \times \right. \right. \\ &\quad \left. \left. - \left[\bar{\mathbf{r}}_{CM/E}^B \times \right] J \right\} T_{I \rightarrow B} \end{aligned} \quad (\text{A.15})$$

A.11 Partial Of Gravity Gradient Torque With Respect To Spacecraft Rotation Vector

Gravity gradient torque partial with respect to rotation vector is computed as follow

$$\left. \frac{\partial M_{gg}}{\partial \boldsymbol{\theta}} \right|_{\bar{\mathbf{x}}} = \left. \frac{\partial \left\{ \frac{3\mu}{\|\mathbf{r}_{CM/E}^B\|^5} \left(\mathbf{r}_{CM/E}^B \times \left[J \mathbf{r}_{CM/E}^B \right] \right) \right\}}{\partial \boldsymbol{\theta}} \right|_{\bar{\mathbf{x}}} \quad (\text{A.16})$$

$$\begin{aligned} \left. \frac{\partial M_{gg}}{\partial \boldsymbol{\theta}} \right|_{\bar{\mathbf{x}}} &= 3\mu \left(\mathbf{r}_{CM/E}^B \times \left[J \mathbf{r}_{CM/E}^B \right] \right) \frac{\partial \left(\frac{1}{\|\mathbf{r}_{CM/E}^B\|^5} \right)}{\partial \|\mathbf{r}_{CM/E}^B\|} \frac{\partial \|\mathbf{r}_{CM/E}^B\|}{\partial \boldsymbol{\theta}} \Bigg|_{\bar{\mathbf{x}}} \\ &+ \frac{-3\mu \left[\left(J \bar{\mathbf{r}}_{CM/E}^B \right) \times \right] \partial \mathbf{r}_{CM/E}^B}{\|\mathbf{r}_{CM/E}^B\|^5 \partial \boldsymbol{\theta}} \Bigg|_{\bar{\mathbf{x}}} + \frac{3\mu \left(\left[\bar{\mathbf{r}}_{CM/E}^B \times \right] J \right) \partial \mathbf{r}_{CM/E}^B}{\|\mathbf{r}_{CM/E}^B\|^5 \partial \boldsymbol{\theta}} \Bigg|_{\bar{\mathbf{x}}} \end{aligned} \quad (\text{A.17})$$

Since, $\frac{\partial \|\mathbf{r}_{CM/E}^B\|}{\partial \boldsymbol{\theta}} = 0$

$$\left. \frac{\partial M_{gg}}{\partial \boldsymbol{\theta}} \right|_{\bar{\mathbf{x}}} = \frac{-3\mu \left[\left(J \bar{\mathbf{r}}_{CM/E}^B \right) \times \right] \partial \mathbf{r}_{CM/E}^B}{\|\mathbf{r}_{CM/E}^B\|^5 \partial \boldsymbol{\theta}} \Bigg|_{\bar{\mathbf{x}}} + \frac{3\mu \left[\bar{\mathbf{r}}_{CM/E}^B \times \right] J \partial \mathbf{r}_{CM/E}^B}{\|\mathbf{r}_{CM/E}^B\|^5 \partial \boldsymbol{\theta}} \Bigg|_{\bar{\mathbf{x}}} \quad (\text{A.18})$$

To compute $\left. \frac{\partial(\mathbf{r}_{CM/E}^B)}{\partial\boldsymbol{\theta}_{I \rightarrow B}} \right|_{\bar{\mathbf{x}}}$, Eq. A.16 is linearized, such that for small rotations ($\delta\boldsymbol{\theta}$)

$$T_{I \rightarrow B} = (I - [\delta\boldsymbol{\theta} \times]) T_{I \rightarrow \bar{B}} \quad (\text{A.19})$$

$$\mathbf{r}_{CM/E}^B = T_{I \rightarrow B} \left(\mathbf{r}_{CM/E}^I \right) \quad (\text{A.20})$$

$$\mathbf{r}_{CM/E}^B = (I_{3 \times 3} - [\delta\boldsymbol{\theta} \times]) T_{I \rightarrow \bar{B}} \left(\mathbf{r}_{CM/E}^I \right) \quad (\text{A.21})$$

Expanding right hand side in Eq. A.21

$$\mathbf{r}_{CM/E}^B = T_{I \rightarrow \bar{B}} \left(\mathbf{r}_{CM/E}^I \right) - [\delta\boldsymbol{\theta} \times] T_{I \rightarrow \bar{B}} \left(\mathbf{r}_{CM/E}^I \right) \quad (\text{A.22})$$

$$\mathbf{r}_{CM/E}^B = T_{I \rightarrow \bar{B}} \left(\mathbf{r}_{CM/E}^I \right) + \left[\left\{ T_{I \rightarrow \bar{B}} \left(\mathbf{r}_{CM/E}^I \right) \right\} \times \right] \delta\boldsymbol{\theta} \quad (\text{A.23})$$

Extracting the first order term from Eq. A.23, gives

$$\left. \frac{\partial \mathbf{r}_{CM/E}^B}{\partial \boldsymbol{\theta}} \right|_{\bar{\boldsymbol{\theta}}} = \left[\bar{\mathbf{r}}_{CM/E}^B \times \right] \quad (\text{A.24})$$

Substituting Eq. A.24 in Eq. A.18, the partial derivative of the gravity gradient torque can be written as follow

$$\left. \frac{\partial M_{gg}}{\partial \boldsymbol{\theta}} \right|_{\bar{\mathbf{x}}} = \frac{-3\mu}{\left\| \mathbf{r}_{CM/E}^B \right\|^5} \left\{ \left[\left(J \bar{\mathbf{r}}_{CM/E}^B \right) \times \right] - \left[\bar{\mathbf{r}}_{CM/E}^B \times \right] J \right\} \left[\bar{\mathbf{r}}_{CM/E}^B \times \right] \quad (\text{A.25})$$

A.12 Partial of Accelerometer Measurement With Respect To Spacecraft Rotation Vector

Accelerometer measurement in spacecraft body-fixed frame, is given as

$$\begin{aligned} \mathbf{a}_{d_i}^B = T_{I \rightarrow B} \left\{ \mathbf{g}^I \left(\mathbf{r}_{CM/E}^I \right) - \mathbf{g}^I \left(\mathbf{r}_{CM/E}^I + T_{B \rightarrow I} \left[\mathbf{r}_{a_i/O}^B - \mathbf{r}_{CM/O}^B \right] \right) + \mathbf{a}_{aero}^I + \mathbf{a}_{SRP}^I \right\} \\ + \boldsymbol{\omega}_{B/I}^B \times \left(\boldsymbol{\omega}_{B/I}^B \times \left[\mathbf{r}_{a_i/O}^B - \mathbf{r}_{CM/O}^B \right] \right) \end{aligned} \quad (\text{A.26})$$

To compute $\left. \frac{\partial \mathbf{a}_{d_i}^B}{\partial \boldsymbol{\theta}_{I \rightarrow B}} \right|_{\bar{\mathbf{x}}}$, Eq. A.26 is linearized, such that for small rotations ($\delta \boldsymbol{\theta}$)

$$\boldsymbol{\theta}_{I \rightarrow B} \approx \boldsymbol{\theta}_{I \rightarrow \bar{B}} + \delta \boldsymbol{\theta} \quad (\text{A.27})$$

$$T_{I \rightarrow B}(\boldsymbol{\theta}_{I \rightarrow B}) = (I - [\delta \boldsymbol{\theta} \times]) T_{I \rightarrow \bar{B}} \quad (\text{A.28})$$

$$\mathbf{a}_{d_i}^B = (I_{3 \times 3} - [\delta \boldsymbol{\theta} \times]) T_{I \rightarrow \bar{B}}(\boldsymbol{\theta}) \mathbf{a}_{d_i}^I(\boldsymbol{\theta} + \delta \boldsymbol{\theta}) \quad (\text{A.29})$$

$$\mathbf{a}_{d_i}^B = (I_{3 \times 3} - [\delta \boldsymbol{\theta} \times]) T_{I \rightarrow \bar{B}}(\boldsymbol{\theta}) \left[\mathbf{a}_{d_i}^I(\boldsymbol{\theta}) + \left. \frac{\partial \mathbf{a}_{d_i}^I}{\partial \boldsymbol{\theta}} \right|_{\bar{\mathbf{x}}} \delta \boldsymbol{\theta} \right] \quad (\text{A.30})$$

Expanding right hand side in Eq. A.30

$$\mathbf{a}_{d_i}^B = T_{I \rightarrow \bar{B}}(\boldsymbol{\theta}) \mathbf{a}_{d_i}^I(\boldsymbol{\theta}) - [\delta \boldsymbol{\theta} \times] T_{I \rightarrow \bar{B}}(\boldsymbol{\theta}) \mathbf{a}_{d_i}^I(\boldsymbol{\theta}) +$$

$$T_{I \rightarrow \bar{B}}(\boldsymbol{\theta}) \left. \frac{\partial \mathbf{a}_{d_i}^I}{\partial \boldsymbol{\theta}} \right|_{\bar{\mathbf{x}}} \delta \boldsymbol{\theta} - [\delta \boldsymbol{\theta} \times] T_{I \rightarrow \bar{B}}(\boldsymbol{\theta}) \left. \frac{\partial \mathbf{a}_{d_i}^I}{\partial \boldsymbol{\theta}} \right|_{\bar{\mathbf{x}}} \delta \boldsymbol{\theta} \quad (\text{A.31})$$

Ignoring second order term in $\delta \boldsymbol{\theta}$

$$\mathbf{a}_{d_i}^B = T_{I \rightarrow \bar{B}}(\boldsymbol{\theta}) \mathbf{a}_{d_i}^I(\boldsymbol{\theta}) + \left\{ [(T_{I \rightarrow \bar{B}}(\boldsymbol{\theta}) \mathbf{a}_{d_i}^I(\boldsymbol{\theta})) \times] + T_{I \rightarrow \bar{B}}(\boldsymbol{\theta}) \left. \frac{\partial \mathbf{a}_{d_i}^I}{\partial \boldsymbol{\theta}} \right|_{\bar{\mathbf{x}}} \right\} \delta \boldsymbol{\theta} \quad (\text{A.32})$$

Extracting the first order term from Eq. A.32, gives

$$\left. \frac{\partial \mathbf{a}_{d_i}^B}{\partial \boldsymbol{\theta}} \right|_{\bar{\mathbf{x}}} = [\{T_{I \rightarrow \bar{B}}(\bar{\boldsymbol{\theta}}) \bar{\mathbf{a}}_{d_i}^I(\bar{\boldsymbol{\theta}})\} \times] + T_{I \rightarrow \bar{B}}(\bar{\boldsymbol{\theta}}) \left. \frac{\partial \mathbf{a}_{d_i}^I}{\partial \boldsymbol{\theta}} \right|_{\bar{\mathbf{x}}} \quad (\text{A.33})$$

To evaluate $\left. \frac{\partial \mathbf{a}_{d_i}^I}{\partial \boldsymbol{\theta}} \right|_{\bar{\mathbf{x}}}$, differentiate both sides of $\mathbf{a}_{d_i}^I = \mathbf{g}^I(\mathbf{r}_{CM/E}^I) - \mathbf{g}^I(\mathbf{r}_{CM/E}^I + T_{I \rightarrow B}^T[\mathbf{r}_{a_i/CM}^B])$ with respect to $\boldsymbol{\theta}$. Since, $\frac{\partial \{\mathbf{g}^I(\mathbf{r}_{CM/E}^I)\}}{\partial \boldsymbol{\theta}}$ is not a function of $\boldsymbol{\theta}$, this implies

$$\left. \frac{\partial \mathbf{a}_{d_i}^I}{\partial \boldsymbol{\theta}} \right|_{\bar{\mathbf{x}}} = - \frac{\partial \left\{ \mathbf{g}^I(\mathbf{r}_{CM/E}^I + T_{I \rightarrow B}^T[\mathbf{r}_{a_i/CM}^B]) \right\}}{\partial \boldsymbol{\theta}} \quad (\text{A.34})$$

Since, $\mathbf{r}_{a_i/E}^I = \mathbf{r}_{CM/E}^I + T_{I \rightarrow B}^T[\mathbf{r}_{a_i/CM}^B]$, using chain rule

$$\left. \frac{\partial \mathbf{a}_{d_i}^I}{\partial \boldsymbol{\theta}} \right|_{\bar{\mathbf{x}}} = - \frac{\partial \left\{ \mathbf{g}^I(\mathbf{r}_{a_i/E}^I) \right\}}{\partial \mathbf{r}_{a_i/E}^I} \frac{\partial (\mathbf{r}_{a_i/E}^I)}{\partial \boldsymbol{\theta}} \quad (\text{A.35})$$

Noting that $\frac{\partial \{\mathbf{g}^I(\mathbf{r}_{a_i/E}^I)\}}{\partial \mathbf{r}_{a_i/E}^I}$ is equal to the gravity gradient $\nabla \mathbf{g}^I(\mathbf{r}_{a_i/E}^I)$, at the i^{th} accelerometer position

$$\left. \frac{\partial \mathbf{a}_{d_i}^I}{\partial \boldsymbol{\theta}} \right|_{\bar{\mathbf{x}}} = - \nabla \bar{\mathbf{g}}^I(\bar{\mathbf{r}}_{a_i/E}^I) \frac{\partial (\mathbf{r}_{a_i/E}^I)}{\partial \boldsymbol{\theta}} \quad (\text{A.36})$$

Substituting $\mathbf{r}_{a_i/E}^I = \mathbf{r}_{CM/E}^I + T_{I \rightarrow B}^T[\mathbf{r}_{a_i/CM}^B]$ in Eq. A.36

$$\left. \frac{\partial \mathbf{a}_{d_i}^I}{\partial \boldsymbol{\theta}} \right|_{\bar{\mathbf{x}}} = - \nabla \bar{\mathbf{g}}^I(\bar{\mathbf{r}}_{a_i/E}^I) \frac{\partial (T_{I \rightarrow B}^T[\mathbf{r}_{a_i/CM}^B])}{\partial \boldsymbol{\theta}} \quad (\text{A.37})$$

To evaluate $\left. \frac{\partial (T_{I \rightarrow B}^T[\mathbf{r}_{a_i/CM}^B])}{\partial \boldsymbol{\theta}} \right|_{\bar{\mathbf{x}}}$, using the linearization method, such that

$$T_{I \rightarrow B}^T(\boldsymbol{\theta}) = T_{I \rightarrow B}^T(\boldsymbol{\theta}_{I \rightarrow \bar{B}} + \delta \boldsymbol{\theta}) \quad (\text{A.38})$$

$$T_{I \rightarrow B}^T(\boldsymbol{\theta}) = T_{B \rightarrow I}(-\boldsymbol{\theta}_{I \rightarrow \bar{B}} - \boldsymbol{\delta\theta}) \quad (\text{A.39})$$

Using the cascading property of the transformation matrix

$$T_{I \rightarrow B}^T(\boldsymbol{\theta}) = T_{\bar{B} \rightarrow I}(-\boldsymbol{\theta}) T_{B \rightarrow \bar{B}}(-\boldsymbol{\delta\theta}) \quad (\text{A.40})$$

For small angle rotations, approximating $T_{B \rightarrow \bar{B}}(-\boldsymbol{\delta\theta}) = (I_{3 \times 3} + [\boldsymbol{\delta\theta} \times])$

$$T_{I \rightarrow B}^T \left[\mathbf{r}_{a_i/CM}^B \right] = T_{I \rightarrow \bar{B}}^T (I_{3 \times 3} + [\boldsymbol{\delta\theta} \times]) \left[\mathbf{r}_{a_i/CM}^B \right] \quad (\text{A.41})$$

On expanding the right hand side

$$T_{I \rightarrow B}^T(\boldsymbol{\theta}) \left[\mathbf{r}_{a_i/CM}^B \right] = T_{I \rightarrow B_N}^T(\boldsymbol{\theta}_N) \left[\mathbf{r}_{a_i/CM}^B \right] + T_{I \rightarrow B_N}^T(\boldsymbol{\theta}_N) [\boldsymbol{\delta\theta} \times] \left[\mathbf{r}_{a_i/CM}^B \right] \quad (\text{A.42})$$

$$T_{I \rightarrow B}^T(\boldsymbol{\theta}) \left[\mathbf{r}_{a_i/CM}^B \right] = T_{I \rightarrow \bar{B}}^T(\boldsymbol{\theta}) \left[\mathbf{r}_{a_i/CM}^B \right] - T_{I \rightarrow \bar{B}}^T(\boldsymbol{\theta}) \left[\mathbf{r}_{a_i/CM}^B \times \right] \boldsymbol{\delta\theta} \quad (\text{A.43})$$

Ignoring the nominal term and extracting the first order term from Eq. A.43, yields

$$\left. \frac{\partial \left(T_{I \rightarrow B}^T(\boldsymbol{\theta}) \left[\mathbf{r}_{a_i/CM}^B \right] \right)}{\partial \boldsymbol{\theta}} \right|_{\bar{\mathbf{x}}} = -T_{I \rightarrow \bar{B}}^T(\bar{\boldsymbol{\theta}}) \left[\bar{\mathbf{r}}_{a_i/CM}^B \times \right] \quad (\text{A.44})$$

Substituting the result from Eq. A.44 in Eq. A.37, gives

$$\left. \frac{\partial \mathbf{a}_{d_i}^I}{\partial \boldsymbol{\theta}} \right|_{\bar{\mathbf{x}}} = \nabla \bar{\mathbf{g}}^I \left(\bar{\mathbf{r}}_{a_i/E}^I \right) T_{I \rightarrow \bar{B}}^T(\bar{\boldsymbol{\theta}}) \left[\bar{\mathbf{r}}_{a_i/CM}^B \times \right] \quad (\text{A.45})$$

Substituting the result from Eq. A.45 in Eq. A.33, gives

$$\left. \frac{\partial \mathbf{a}_{d_i}^B}{\partial \boldsymbol{\theta}} \right|_{\bar{\mathbf{x}}} = [\{T_{I \rightarrow \bar{B}}(\bar{\boldsymbol{\theta}}) \bar{\mathbf{a}}_{d_i}^I(\bar{\boldsymbol{\theta}})\} \times] + T_{I \rightarrow \bar{B}}(\bar{\boldsymbol{\theta}}) \nabla \bar{\mathbf{g}}^I(\bar{\mathbf{r}}_{a_i/E}^I) T_{I \rightarrow \bar{B}}^T(\bar{\boldsymbol{\theta}}) [\bar{\mathbf{r}}_{a_i/CM}^B \times] \quad (\text{A.46})$$

A.13 Partial Of Acceleration Measurement With Respect To Spacecraft Angular Velocity

Partial of accelerometer measurement with respect to spacecraft angular velocity is given as

$$\left. \frac{\partial \mathbf{a}_{d_i}^I}{\partial \boldsymbol{\omega}_{B/I}^B} \right|_{\bar{\mathbf{x}}} = T_{B \rightarrow I}(\mathbf{q}_{B \rightarrow I}) \left. \frac{\partial \left[\boldsymbol{\omega}_{B/I}^B \times \left(\boldsymbol{\omega}_{B/I}^B \times \left(\mathbf{r}_{a_i/O}^B - \mathbf{r}_{CM/O}^B \right) \right) \right]}{\partial \boldsymbol{\omega}_{B/I}^B} \right|_{\bar{\mathbf{x}}} \quad (\text{A.47})$$

$$\begin{aligned} \left. \frac{\partial \mathbf{a}_{d_i}^I}{\partial \boldsymbol{\omega}_{B/I}^B} \right|_{\bar{\mathbf{x}}} &= -T_{B \rightarrow I} \left[\frac{\partial \left\{ \boldsymbol{\omega}_{B/I}^B \times \left(\left[\mathbf{r}_{a_i/O}^B - \mathbf{r}_{CM/O}^B \right] \times \boldsymbol{\omega}_{B/I}^B \right) \right\}}{\partial \boldsymbol{\omega}_{B/I}^B} \right]_{\bar{\mathbf{x}}} \\ &+ \left. \frac{\partial \left\{ \left(\boldsymbol{\omega}_{B/I}^B \times \left[\mathbf{r}_{a_i/O}^B - \mathbf{r}_{CM/O}^B \right] \right) \times \boldsymbol{\omega}_{B/I}^B \right\}}{\partial \boldsymbol{\omega}_{B/I}^B} \right]_{\bar{\mathbf{x}}} \end{aligned} \quad (\text{A.48})$$

$$\left. \frac{\partial \mathbf{a}_{d_i}^I}{\partial \boldsymbol{\omega}_{B/I}^B} \right|_{\bar{\mathbf{x}}} = -T_{B \rightarrow I} \left\{ \left[\left(\bar{\boldsymbol{\omega}}_{B/I}^B \times \left[\bar{\mathbf{r}}_{a_i/O}^B - \bar{\mathbf{r}}_{CM/O}^B \right] \right) \times \right] + \left[\bar{\boldsymbol{\omega}}_{B/I}^B \times \right] \left[\left(\bar{\mathbf{r}}_{a_i/O}^B - \bar{\mathbf{r}}_{CM/O}^B \right) \times \right] \right\} \quad (\text{A.49})$$

A.14 Partial Of Accelerometer Measurement With Respect To Spacecraft's Center Of Mass Position

Partial of accelerometer measurement with respect to spacecraft's center of mass position, in spacecraft body-fixed frame and with respect to the origin of spacecraft body-fixed frame, is given as

$$\begin{aligned} \left. \frac{\partial \mathbf{a}_{d_i}^I}{\partial \mathbf{r}_{CM/O}^B} \right|_{\bar{\mathbf{x}}} &= - \left. \frac{\partial \left\{ \mathbf{g}^I \left(\mathbf{r}_{CM/E}^I + T_{B \rightarrow I}(\mathbf{q}_{B \rightarrow I}) \left[\mathbf{r}_{a_i/O}^B - \mathbf{r}_{CM/O}^B \right] \right) \right\}}{\partial \mathbf{r}_{CM/O}^B} \right|_{\bar{\mathbf{x}}} \\ &+ T_{B \rightarrow I}(\mathbf{q}_{B \rightarrow I}) \left. \frac{\partial \left\{ \boldsymbol{\omega}_{B/I}^B \times \left(\boldsymbol{\omega}_{B/I}^B \times \left[\mathbf{r}_{a_i/O}^B - \mathbf{r}_{CM/O}^B \right] \right) \right\}}{\partial \mathbf{r}_{CM/O}^B} \right|_{\bar{\mathbf{x}}} \end{aligned} \quad (\text{A.50})$$

$$\begin{aligned} \left. \frac{\partial \mathbf{a}_{d_i}^I}{\partial \mathbf{r}_{CM/O}^B} \right|_{\bar{\mathbf{x}}} &= - \left. \frac{\partial \left\{ \mathbf{g}^I \left(\bar{\mathbf{r}}_{a_i/E}^I \right) \right\}}{\partial \bar{\mathbf{r}}_{a_i/E}^I} \right|_{\bar{\mathbf{x}}} \left. \frac{\partial \left(\mathbf{r}_{a_i/E}^I \right)}{\partial \mathbf{r}_{CM/O}^B} \right|_{\bar{\mathbf{x}}} \\ &+ T_{B \rightarrow I}(\bar{\mathbf{q}}_{B \rightarrow I}) \left(\left. \frac{\partial \left\{ \left[\bar{\boldsymbol{\omega}}_{B/I}^B \times \right] \left[\bar{\boldsymbol{\omega}}_{B/I}^B \times \right] \left[\mathbf{r}_{a_i/O}^B - \mathbf{r}_{CM/O}^B \right] \right\}}{\partial \mathbf{r}_{CM/O}^B} \right|_{\bar{\mathbf{x}}} \right) \end{aligned} \quad (\text{A.51})$$

$$\left. \frac{\partial \mathbf{a}_{d_i}^I}{\partial \mathbf{r}_{CM/O}^B} \right|_{\bar{\mathbf{x}}} = \nabla \bar{\mathbf{g}}^I \left(\bar{\mathbf{r}}_{a_i/E}^I \right) T_{B \rightarrow I} - T_{B \rightarrow I} \left(\left[\bar{\boldsymbol{\omega}}_{B/I}^B \times \right] \left[\bar{\boldsymbol{\omega}}_{B/I}^B \times \right] \right) \quad (\text{A.52})$$

A.15 Partial Of Accelerometer Measurement With Respect To Accelerometer Position

Partial of accelerometer measurement with respect to the i^{th} accelerometer position, in spacecraft body-fixed frame and with respect to the origin of the spacecraft body-fixed frame $\left(\mathbf{r}_{a_i/O}^B \right)$, is given as

$$\left. \frac{\partial \mathbf{a}_{d_i}^I}{\partial \mathbf{r}_{a_i/O}^B} \right|_{\bar{\mathbf{x}}} = - \left. \frac{\partial \left\{ \mathbf{g}^I \left(\mathbf{r}_{CM/E}^I + T_{B \rightarrow I}(\mathbf{q}_{B \rightarrow I}) \left[\mathbf{r}_{a_i/O}^B - \mathbf{r}_{CM/O}^B \right] \right) \right\}}{\partial \mathbf{r}_{a_i/O}^B} \right|_{\bar{\mathbf{x}}}$$

$$+ T_{B \rightarrow I} (\mathbf{q}_{B \rightarrow I}) \frac{\partial \left\{ \boldsymbol{\omega}_{B/I}^B \times \left(\boldsymbol{\omega}_{B/I}^B \times \left[\mathbf{r}_{a_i/O}^B - \mathbf{r}_{CM/O}^B \right] \right) \right\}}{\partial \mathbf{r}_{a_i/O}^B} \Bigg|_{\bar{\mathbf{x}}} \quad (\text{A.53})$$

$$\frac{\partial \mathbf{a}_{d_i}^I}{\partial \mathbf{r}_{a_i/O}^B} \Bigg|_{\bar{\mathbf{x}}} = - \frac{\partial \left\{ \mathbf{g}^I \left(\bar{\mathbf{r}}_{a_i/E}^I \right) \right\}}{\partial \mathbf{r}_{a_i/E}^I} \Bigg|_{\bar{\mathbf{x}}} \frac{\partial \left(\mathbf{r}_{a_i/E}^I \right)}{\partial \mathbf{r}_{a_i/O}^B} \Bigg|_{\bar{\mathbf{x}}}$$

$$+ T_{B \rightarrow I} \left(\frac{\partial \left\{ \left[\bar{\boldsymbol{\omega}}_{B/I}^B \times \right] \left[\bar{\boldsymbol{\omega}}_{B/I}^B \times \right] \left[\mathbf{r}_{a_i/O}^B - \mathbf{r}_{CM/O}^B \right] \right\}}{\partial \mathbf{r}_{a_i/O}^B} \Bigg|_{\bar{\mathbf{x}}} \right) \quad (\text{A.54})$$

$$\frac{\partial \mathbf{a}_{d_i}^I}{\partial \mathbf{r}_{a_i/O}^B} \Bigg|_{\bar{\mathbf{x}}} = -\nabla \bar{\mathbf{g}}^I \left(\bar{\mathbf{r}}_{a_i/E}^I \right) T_{B \rightarrow I} + T_{B \rightarrow I} \left(\left[\bar{\boldsymbol{\omega}}_{B/I}^B \times \right] \left[\bar{\boldsymbol{\omega}}_{B/I}^B \times \right] \right) \quad (\text{A.55})$$

APPENDIX B

Semi-Major Axis Time Derivative

B.1 Overview

This appendix provides the detailed derivation of the time derivative of the semi-major axis for a circular orbit, when atmospheric drag acts on the spacecraft.

B.2 Derivation

Total Energy of an orbit is given as

$$\frac{\mathbf{v} \cdot \mathbf{v}}{2} - \frac{\mu}{\sqrt{\mathbf{r} \cdot \mathbf{r}}} = -\frac{\mu}{2a} = \xi \quad (\text{B.1})$$

where ξ denotes the total energy, \mathbf{r} and \mathbf{v} are position and velocity of the object in orbit, μ is the standard gravitational parameter of the primary body, and a is the semi-major axis of the orbit, respectively.

Now to compute the change in semi-major axis, due to atmospheric drag, taking the time derivative of both sides of Eq. B.1

$$\frac{\partial}{\partial t} \left(\frac{\mathbf{v} \cdot \mathbf{v}}{2} - \frac{\mu}{\sqrt{\mathbf{r} \cdot \mathbf{r}}} \right) = -\frac{\mu}{2} \frac{\partial}{\partial t} \left(\frac{1}{a} \right) \quad (\text{B.2})$$

$$\dot{\mathbf{v}} \cdot \mathbf{v} + \frac{\mu (\dot{\mathbf{r}} \cdot \mathbf{r})}{(\mathbf{r} \cdot \mathbf{r})^{3/2}} = \frac{\mu \dot{a}}{2a^2} \quad (\text{B.3})$$

Since, $\dot{\mathbf{v}} = -\frac{\mu}{(\mathbf{r} \cdot \mathbf{r})^{3/2}} \mathbf{r} + \mathbf{a}_{drag}$ and $\mathbf{v} = \dot{\mathbf{r}}$

$$-\frac{\mu}{(\mathbf{r} \cdot \mathbf{r})^{3/2}} \mathbf{r} \cdot \dot{\mathbf{r}} + \mathbf{a}_{drag} \cdot \dot{\mathbf{r}} + \frac{\mu (\dot{\mathbf{r}} \cdot \mathbf{r})}{(\mathbf{r} \cdot \mathbf{r})^{3/2}} = \frac{\mu \dot{a}}{2a^2} \quad (\text{B.4})$$

$$\frac{\mu (\dot{\mathbf{r}} \cdot \mathbf{r})}{\sqrt{\mathbf{r} \cdot \mathbf{r}}} \left(-\frac{1}{\mathbf{r} \cdot \mathbf{r}} + \frac{1}{\mathbf{r} \cdot \mathbf{r}} \right) + \mathbf{a}_{drag} \cdot \dot{\mathbf{r}} = \frac{\mu \dot{a}}{2a^2} \quad (\text{B.5})$$

$$\dot{a} = \frac{(2a^2) \mathbf{a}_{drag} \cdot \dot{\mathbf{r}}}{\mu} \quad (\text{B.6})$$

Since, mean motion n is given as

$$n = \sqrt{\frac{\mu}{a^3}} \quad (\text{B.7})$$

$$\dot{a} = \frac{2\mathbf{a}_{drag} \cdot \dot{\mathbf{r}}}{n^2 a} \quad (\text{B.8})$$

Now, for a circular orbit $\dot{\mathbf{r}}_{circ} = \sqrt{\frac{\mu}{\mathbf{r} \cdot \mathbf{r}}} = \sqrt{\frac{2\mu}{a}}$

$$\dot{a}_{circ} = \frac{(2a^2) \mathbf{a}_{drag} \cdot \sqrt{\frac{2\mu}{a}}}{\mu} \quad (\text{B.9})$$

$$\dot{a}_{circ} = (2\sqrt{2}) \mathbf{a}_{drag} \sqrt{\frac{a^3}{\mu}} \quad (\text{B.10})$$

Thus, the time derivative of the semi-major axis (circular orbit) as a function of the acceleration due to atmospheric drag, is given as

$$\dot{a}_{circ} = \frac{(2\sqrt{2}) \mathbf{a}_{drag}}{n} \quad (\text{B.11})$$

CURRICULUM VITAE

Rachit Bhatia

Education

- **Doctor of Philosophy (Ph.D.) - Aerospace Engineering** **Aug'15 - Aug'19**
Utah State University (USU), Logan, Utah
 - Research Area: Spacecraft Guidance, Navigation and Control
 - Research Topic: Revolution in Autonomous Orbital Navigation (RAON)
 - Faculty Advisor: Dr. David Geller
- **Masters in Science (M.S.) - Mechanical Engineering** **Aug'15 - May'19**
Utah State University (USU), Logan, Utah
- **Bachelor of Technology (B.Tech.) - Mechanical Engineering** **Aug'10 - July'14**
SRM University, Chennai, Tamil Nadu

Publications

- Geller, D. K. and Bhatia, R., "Orbit and Attitude Observability Using Accelerometer Measurements," AAS 18-301, AAS/AIAA Astrodynamics Conference, Snowbird, Utah, Aug. 2018.
- Bhatia, R. and Geller, D. K., "RAON: Revolution in Autonomous Orbital Navigation," AAS 18-080, AAS Guidance and Control Conference, Breckenridge, CO, Feb. 2018.

- Bhatia, R. and Geller, D. K., “Autonomous Navigation using Gravity Gradient Measurements,” Contribution 187 in Session 15, 9th-IAASS Conference, Toulouse, France, Oct. 2017.

Prominent Research Projects & Presentations

- *RELATIVE STATE ESTIMATION FOR AUTOMATIC CARRIER LANDING* **Fall’18**
 - Develop mathematical model to process Line of Sight (LOS) & GPS measurements on-board unmanned aerial vehicle.
 - Conduct Monte-Carlo analysis to determine the sensor & dynamical requirements to land a UAV on an aircraft carrier.
- *THRUST REQUIREMENT STUDY FOR STATION-KEEPING ABOUT THE EM LAGRANGE POINTS* **Fall’16**
 - LQR Controller developed to analyze the thrust required for station-keeping about all five Earth Moon Lagrange Points.
- *INITIAL ORBIT DETERMINATION OF GEO RSO’S FROM EARTH MOON L1-HALO ORBIT* **Spring’16**
 - Implement Batch Process technique to study feasibility of a mission to observe residential space objects in GEO using angles only measurement from optical observatory stationed at Earth-Moon L1 point.

Skills

Programming Languages: Python (Basic Level) C++

Software: STK (AGI) CREO 2.0 MATLAB/Simulink Auto-Desk Inventor

Engineering: Optimal Sequential Filtering Optimal Estimation Theory

Linear Covariance Theory Linear & Non-linear Controls Theory Monte-Carlo Analysis

Astrodynamics Attitude Determination & Control Simultaneous Localization & Mapping (SLAM)

Experience

- **Graduate Research Assistant - Utah State University (Logan, Utah)** **Aug'15 - Aug'19**
 - Develop and utilize tools like Extended Kalman Filter (EKF), observability analysis, Linear Covariance, and Monte-Carlo to solve problems related to spacecraft guidance, navigation, and controls (GN&C).
 - Working on project to investigate autonomous orbital navigation using precision sensors. Involves development and evaluation of sensor measurement models and dynamics.

- **Team Member (Simulation & Orbital Dynamics) - Get Away Special Team (USU, Logan-Utah)** **May'16 - May'19**
 - Work with undergraduate student team on Microgravity Satellite Project to develop a CubeSat & demonstrate passive attitude stabilization using a UV cured AeroBoom.
 - Develop the orbit determination simulation & conduct orbital dynamics analysis of a single 1U CubeSat.

- **Team Member - Space Exploration Project Group at Space Generation Advisory Council (SGAC)** **May'18 - Present**
 - Discuss and collaborate on projects related to space exploration and advanced space technology.

- **Graduate Teaching Assistant - Utah State University (Logan, Utah)** **Fall'16**
 - Served as Teaching Assistant for Advanced Dynamics (MAE3320).
 - Responsibilities include assisting 60 undergraduate students, hold help sessions, and grade student assignments.

Outstanding Achievements

- 2017**
 - *Graduate Student Fellowship (GSF)*
 - Awarded by International Space Safety Foundation (ISSF).
 - \$1,000 funding is provided towards the selected research project.

- Batch 2015-2019**
 - *Presidential Doctoral Research Fellow (PDRF)*
 - Awarded by Department of Mechanical and Aerospace Engineering (MAE) at Utah State University (Logan, Utah).
 - PDRF is the top graduate fellowship award offered at the Utah State University.

Relevant Coursework

Core Courses: Aerodynamics(Dr. Robert E. Spall) Dynamics of Space Flight(Dr. Kohei Fujimoto) Spacecraft Navigation(Dr. David K. Geller) Advanced Astrodynamics, Theory and Applications(Dr. David K. Geller) Optimal Spacecraft Guidance(Dr. Rees Fullmer)

Advanced Math Courses: Mathematical Methods for Signals and Systems(Dr. Todd K. Moon) Introduction to Theory and Application of Nonlinear Dynamical Systems(Dr. Brynja Kohler) Optimal Estimation of Aerospace Systems(Dr. Randall Christensen)

Technical Electives: Orbital Debris(Dr. Kohei Fujimoto) Monte Carlo and Linear Covariance Analysis(Dr. David K. Geller) Linear Multivariable Control(Dr. Rajnikant Sharma) Spacecraft Attitude Control, Theory and Applications(Bryan Bingham) Nonlinear/Adaptive Control(Dr. Randall Christensen)